

Development of a high-cadence, high-precision solar imaging polarimeter with application to the FSP prototype

Der Fakultät für Elektrotechnik, Informationstechnik, Physik
der Technischen Universität Carolo-Wilhelmina zu Braunschweig
zur Erlangung des Grades eines
der Ingenieurwissenschaften (Dr.-Ing.)

genehmigte Dissertation

von Francisco Andrés Iglesias
aus Mendoza, Argentinien

eingereicht am: 12. April 2016

mündliche Prüfung am: 29. April 2016

1. Referent: Prof. Dr.-Ing. Harald Michalik
2. Referent: Prof. Dr. Sami K. Solanki

Druckjahr: 2016

Bibliografische Information der Deutschen Nationalbibliothek

Die Deutsche Nationalbibliothek verzeichnet diese Publikation in der Deutschen Nationalbibliografie; detaillierte bibliografische Daten sind im Internet über <http://dnb.d-nb.de> abrufbar.

Cover: High-cadence, MOMFBD-restored measurement of a solar pore acquired with the FSP (top and bottom left). The Grey scale in the normalized Stokes V ranges from -23 to 10% . FSP modulator (top right) and the pnCCD camera (bottom right). Cover by www.behance.net/birpip

ISBN 978-3-944072-50-0

uni-edition GmbH 2016

<http://www.uni-edition.de>

© Francisco Andrés Iglesias



This work is distributed under a
Creative Commons Attribution 3.0 License

Printed in Germany

Vorveröffentlichungen der Dissertation

Teilergebnisse aus dieser Arbeit wurden mit Genehmigung der Fakultät für Elektrotechnik, Informationstechnik, Physik, vertreten durch den Betreuer der Arbeit, in folgenden Beiträgen vorab veröffentlicht:

Publikationen

Iglesias, F. A., Feller, A., Nagaraju, K. and Solanki, S. K., 2016, *High-resolution, high-sensitivity, ground-based solar spectropolarimetry with a new fast imaging polarimeter*, Astronomy and Astrophysics, Volume 590, A89.

Iglesias, F. A., Feller, A. and Nagaraju, K., 2015, *Smear correction of highly-variable, frame-transfer-CCD images with application to polarimetry*, Applied Optics, Volume 54, Issue 19, p. 5970.

Tagungsbeiträge

Iglesias, F. A., Feller, A., Nagaraju, K. and Solanki, S. K., 2016, *Fast Solar Polarimeter: Prototype characterization and first results*, ASP Conference Series, Volume 504, p. 325.

Feller, A., Iglesias, F. A., Nagaraju, K., Solanki, S. K. and Ihle, S., 2014, *Fast Solar Polarimeter: Description and First Results*, ASP Conference Series, Volume 489, p. 271.

To my family and María Belén Tomaselli

Contents

List of Figures	xii
List of Tables	xiii
Summary	xvi
Kurzfassung	xviii
1 Introduction	1
1.1 Objectives	3
1.2 Outline	4
2 Background	7
2.1 Introduction to solar spectropolarimetry	7
2.1.1 Description of polarized light and its transformations	7
2.1.2 Generation and transformation of polarized light	10
2.1.3 Solar spectropolarimetry	16
2.1.4 Data requirements in high-resolution solar polarimetry	17
2.2 Solar polarimeters	20
2.2.1 Measurement technique	20
2.2.2 Polarization modulators	23
2.2.3 Wavelength discrimination	25
2.2.4 Scientific cameras	27
2.3 Polarimetric effects of atmospheric seeing and image motion	32
2.3.1 Description of atmospheric seeing and image motion	32
2.3.2 Polarimetric effects in the different modulation schemes	36
2.3.3 Image restoration	40
3 High-cadence, ground-based polarimetry	45
3.1 Main properties of a high-cadence polarimeter	45
3.1.1 Camera requirements	47
3.1.2 Polarization modulator requirements	50
3.2 The Fast Solar Polarimeter Prototype	51
3.2.1 Cameras used in ground-based polarimeters: state-of-the-art	52
3.2.2 System overview	54

4	Characterization and optimization of an FLC-based polarization modulator	59
4.1	Main design features	59
4.2	Efficiencies optimization	62
4.2.1	Step 1: FLCs characterization	63
4.2.2	Step 2: First optimization and SRs characterization	66
4.2.3	Step 3: Final optimization and results	67
4.3	Polarimetric calibration	68
4.3.1	Spatial dependence	70
4.3.2	Spectral dependence	71
4.3.3	Modulation frequency dependence	72
4.3.4	Thermal dependence	73
5	Characterization and optimization of a pnCCD camera for fast imaging polarimetry	75
5.1	Design and specifications	75
5.1.1	pnCCD sensor and readout electronics	76
5.1.2	pnCCD camera	77
5.2	Camera-modulator synchronization and camera calibration	78
5.2.1	Frame transfer model	80
5.2.2	Frame transfer correction	83
5.3	Gain and linearity	86
5.4	Camera noise	89
5.4.1	Common mode correction	89
5.4.2	Total camera noise	91
5.4.3	Exposure time stability	91
5.4.4	Readout and quantization noise	92
5.4.5	Dark noise, offset and dynamic range	92
5.5	Photon-noise limited regime	93
6	First light measurements	97
6.1	Data acquisition and reduction	97
6.1.1	Intensity calibration	97
6.1.2	Polarimetric calibration	99
6.1.3	Frame accumulation and polarimetric normalization	99
6.1.4	Instrumental polarization	100
6.1.5	Image restoration with MOMFBD	101
6.2	Measurements in spectrograph mode	103
6.2.1	Low SNR regime: Second solar spectrum of Ca I	104
6.3	Measurements in filtergraph mode	104
6.3.1	Low SNR regime: Fe I scan of the quiet sun	105
6.3.2	High SNR regime: Fe I scan of an active region	109
6.4	Performance evaluation	110
6.4.1	pnCCD camera issues	110
6.4.2	Image restoration and signal amplitude	113
6.4.3	Polarimetric sensitivity	115
6.4.4	Measurements of the magnetically insensitive 557.6 nm line	116

6.4.5	Spatial resolution and seeing induced crosstalk	118
7	Concluding remarks and prospects	123
7.1	The Fast Solar Polarimeter II	125
	Acronyms	128
	Nomenclature	133
	Bibliography	135
	Acknowledgements	145
	Curriculum Vitae and publications	148

List of Figures

1.1	Examples of solar activity and its effects on Earth	2
2.1	Processes that can generate or modify polarization	10
2.2	Example of scattering polarization signals in the solar atmosphere	13
2.3	Example of Zeeman polarization signals in a sunspot	15
2.4	Remote diagnosis of the solar atmosphere using ground-based, spectropolarimetric measurements	17
2.5	Intrinsic trade-offs in high-resolution, solar spectropolarimetry	20
2.6	Basic architecture of a scientific camera	28
2.7	Comparison between CMOS and CCD image sensors	28
2.8	Measured power spectrum of seeing-induced image motion	37
2.9	Simulated SIC considering high-order aberrations and the AO effect . . .	41
3.1	Rolling shutter implications in high-cadence polarimetry.	49
3.2	Comparison of the frame rate and modulation frequency of the solar polarimeters listed in Table 3.2	55
3.3	Components of the FSP	56
3.4	Retardance dispersion of the achromatic QWP in the PSG of FSP	56
4.1	FSP modulator package.	60
4.2	Sensitivity of the total polarimetric efficiency to variations in the FLCs switching angles and the retardances of all components.	63
4.3	FLCs characterization results.	65
4.4	Measured and modeled FSP polarimetric efficiencies.	68
4.5	Example FSP calibration measurements.	70
4.6	Spatial variation of the FSP modulation matrix due to errors during calibration.	72
4.7	Measured dispersion of the FSP modulation matrix.	73
4.8	Measured variation of the FSP polarimetric efficiencies with modulation frequency.	74
4.9	Measured modulator housing temperature.	74
5.1	pnCCD sensor used in FSP	78
5.2	pnCCD camera system used in FSP	79
5.3	Frame transfer and camera-modulator synchronization.	81
5.4	Errors in the desmeared images due to uncertainties in the final condition	84
5.5	Error propagation in the desmearing algorithm	85

5.6	Frame transfer artifact correction.	86
5.7	Measured pnCCD camera gain.	87
5.8	Measured pnCCD non-linearities.	88
5.9	Polarimetric errors introduced by second order non-linearities and residual offsets in the pnCCD camera.	89
5.10	Common mode artifact correction	91
5.11	Measured readout plus residual common mode noise of the pnCCD camera.	93
5.12	Bias frame of the pnCCD camera.	94
5.13	Integration time versus total camera noise	95
6.1	Frame accumulation and polarimetric normalization	100
6.2	FSP setup during the first light measurements with the VTT echelle spectrograph.	104
6.3	Ca I second solar spectrum measured with Fast Solar Polarimeter (FSP).	106
6.4	FSP setup during the first light measurements with the TESOS filtergraph at the VTT.	107
6.5	Quiet Sun scan of the Fe I 630.2 nm spectral line.	108
6.6	MOMFBD restored quiet Sun scan of the Fe I 630.2 nm spectral line.	109
6.7	Active region scan of the Fe I 630.2 nm spectral line measured with FSP.	111
6.8	MOMFBD-restored active region scan of Fe I spectral line.	112
6.9	Detail of the MOMFBD-restored active region scan of the Fe I 630.2 nm spectral line.	113
6.10	Effects of FSP cadence and duty cycle on image restoration.	115
6.11	Measurements of the non-magnetic 557.6 nm line.	117
6.12	Seeing induced crosstalk in normalized Stokes Q images.	120
6.13	Measured artifact level in individual Stokes Q measurements.	121
6.14	Effects of the modulation frequency, duty cycle and image restoration on the SIC level.	122

List of Tables

2.1	Basic camera characteristics and performance specifications	30
2.2	Comparison of the main properties of CMOS and CCD sensors	31
3.1	Summary of the most relevant properties of a ground-based polarimeter that aims for high-sensitivity and high spatial resolution	46
3.2	Comparison of the detector-related properties for eight state-of-the-art, full-stokes, ground-based, solar polarimeters working in the visible part of the spectrum.	53
4.1	Measured FLCs dispersion constants	64
4.2	Measured FLCs switching time	66
4.3	Measured SRs dispersion constants	67
4.4	Properties of the optical components in FSP modulator	67
4.5	Sensitivity of the total polarimetric efficiency to variations in the position angles.	68
4.6	Example FSP modulation matrix.	69
4.7	Maximum allowed variations of the modulation matrix elements.	71
4.8	Variation of the FSP modulation matrix with modulation frequency.	74
4.9	Simulated thermal variation of the FSP modulation matrix.	74
6.1	Different approaches to restore FSP data with MOMFBD.	102
6.2	Data specification of the Ca I second solar spectrum measured with FSP .	105
6.3	Data specification for the Fe I scan of the quiet sun measured with FSP . .	107
6.4	Data specification for active region scan in Fe I measured with FSP	110

Summary

Many open questions in solar physics demand the acquisition of spectropolarimetric measurements of solar light, involving challenging requirements in terms of spatial, spectral and temporal resolution, and polarimetric sensitivity. There are important motives to try acquiring such measurements from the ground instead of using a space-based observatory, e.g. the larger available apertures. However, a major impediment to reach the requirements are the effects of atmospheric seeing. The most important effects are the reduction of spatial resolution, and the introduction of spurious polarimetric signals (denoted as seeing induced crosstalk, SIC) caused by variable seeing induced image aberrations, and the fact that polarimetric measurements are based on time differential photometry.

Standard numeric techniques used to correct for seeing induced image aberrations, require short exposure times (<10 ms). In addition, a fundamental solution to reduce SIC is to increase the modulation frequency of the polarimeter beyond the values defined by the typical seeing coherence time (>100 Hz). The two aforementioned properties can be met by a high-cadence polarimeter. This thesis describes the development of such a polarimeter and presents the results obtained with a specific instrument, namely the prototype of the Fast Solar Polarimeter (FSP). FSP is based on a high-cadence (up to 800 fps) camera and a polarization modulator with ferro-electric liquid crystals (FLCs). The camera is custom-made, using a frame-transfer, back-illuminated pn-type CCD (pnCCD) sensor, that has high sensitivity, and provides almost 100 % duty cycle.

We have characterized and integrated the components of the modulator package, using a model-based optimization procedure to derive the position angles and retardances of the components that minimize the dispersion of the polarimetric efficiencies. We have obtained a variation of 20 % of the total polarimetric efficiency, in the 400 to 700 nm wavelength range. In addition, the characterization results of the integrated modulator package allowed us to derive basic calibration and operational requirements. We have also characterized the pnCCD camera and we have proven that it is suitable to be used for high-cadence, high-sensitivity polarimetry. This includes selecting a specific synchronization between camera and modulator—which allowed us to develop a numeric technique for correcting image smearing post-acquisition—and addressing the effects of non-linearities, residual offsets, common-mode noise and readout noise of the camera.

The FSP instrumental concept was validated during five campaigns carried out in the years 2013 to 2015 at the 68 cm German Vacuum Tower Telescope of the El Teide observatory on Tenerife. We have measured the second solar spectrum of Ca I 422.7 nm with a polarimetric sensitivity of 8×10^{-5} , and we have detected sub-arcsec bipolar transversal Zeeman signals of the quiet Sun at the 1×10^{-3} level, using the TESOS filtergraph tuned to the Fe I 630.2 nm spectral line. In addition we have found that the high cadence and duty cycle of FSP allows the restoration of the Stokes images by means of a multi-object

multi-frame blind deconvolution, using only the narrow-band science data, consisting of individual short exposure (2.5 ms) frames with low signal to noise ratio. We have studied the residual level of seeing induced crosstalk (SIC) using non-modulated filtergraph measurements. At a modulation frequency of 100 Hz, if no image restoration is used, SIC is below the 7×10^{-5} noise level after averaging ~ 8 min of quiet-Sun Stokes images. On the other hand, after restoring 1.16 min of the same measurements, we found traces of SIC at the noise level of 4×10^{-4} only in the edges of the images, where the performance of the adaptive optics and image restoration are reduced due to seeing anisoplanatism.

The techniques and methods studied and/or developed in this work are of relevance for any project addressing the development of high-cadence, high-sensitivity imaging polarimetry.

Kurzfassung

Viele offene Fragen in der Sonnenphysik erfordern Spektropolarimetrie mit hohen Anforderungen an die räumliche, spektrale und zeitliche Auflösung, sowie an die polarimetrische Genauigkeit. Es gibt gute Argumente warum man solche Messungen an bodengebundenen Teleskopen durchführt und nicht im Weltraum, z.B. wegen der größeren Apertur von bodengebundenen Teleskopen. Ein Nachteil von bodengebundenen Beobachtungen ist allerdings der Einfluss von atmosphärischer Turbulenz (Seeing). Seeing beeinträchtigt die räumliche Auflösung und verursacht falsche Polarisations-signale, sogenannten Seeing Induced Crosstalk (SIC). Der SIC ist bedingt durch eine zeitliche Änderung der optischen Aberrationen während der Polarisationsmessung, welche ihrerseits auf einer zeitlichen Abfolge von differenziellen Intensitätsmessungen beruht.

Typische numerische Algorithmen zur Korrektur von seeingbedingten Aberrationen verlangen nach Einzelbildern mit kurzen Belichtungszeiten (< 10 ms). Darüber hinaus besteht eine grundlegende Lösung für das Problem des SIC darin das Polarimeter bei Modulationsperioden unterhalb der typischen Korrelationszeitskala des Seeings zu betreiben. Dies entspricht Modulationsfrequenzen oberhalb von 100 Hz. Alle die genannten Anforderungen können durch ein schnelles Polarimeter erfüllt werden. Diese Dissertation beschreibt die Entwicklung eines schnellen Polarimeters sowie die Resultate die mit dem Prototypen des "Fast Solar Polarimeter" (FSP) erzielt wurden. Das FSP besteht aus einer schnellen (bis zu 800 fps) Kamera und einem Polarisationsmodulator aus ferroelektrischen Flüssigkristallen (FLCs). Die Kamera ist eine Spezialanfertigung basierend auf einem rückseitenbeleuchteten pn-Typ CCD (pnCCD) Sensor mit Frame Transfer. Dieser Sensor hat eine sehr hohe Empfindlichkeit und ermöglicht den Betrieb bei einem Arbeitszyklus von nahezu 100 %.

Die Komponenten des Modulators wurden einzeln charakterisiert und mit Hilfe eines Modells in Bezug auf Positionswinkel und Verzögerungen dahingehend optimiert, dass eine möglichst hohe und achromatische polarimetrische Effizienz erreicht wird. Es ist hierbei gelungen, die Schwankung der gesamten polarimetrischen Effizienz über den spektralen Arbeitsbereich von 400 bis 700 nm unterhalb von 20 % zu halten. Darüber hinaus hat die sorgfältige Charakterisierung des Modulators es erlaubt, die Anforderungen an dessen Kalibration und Betriebsstabilität zu definieren, welche eingehalten werden müssen, um die angestrebte polarimetrische Genauigkeit zu erreichen. Des Weiteren wurde die pnCCD Kamera charakterisiert und es konnte gezeigt werden, dass diese in der Tat geeignet ist für schnelle Polarimetrie mit der geforderten Genauigkeit. Die Arbeiten in Bezug auf die Kamera beinhalteten weiter eine Optimierung der Synchronisierung mit dem Modulator sowie die Ausarbeitung und die Verifizierung eines Algorithmus zur numerischen Korrektur der durch den Frame Transfer verursachten Bildverschmierung. Weiter wurde der Einfluss von verschiedenen kamerabezogenen Effekten auf die Polari-

sationsmessung untersucht: Nichtlinearität, residuale Offsets, sowie Common-Mode und Ausleserauschen.

Fünf Beobachtungskampagnen haben es erlaubt das FSP Konzept zu validieren. Diese Kampagnen wurden in den Jahren 2013-2015 am deutschen 68 cm Vakuum-Turm-Teleskop (VTT) des Teide Observatoriums auf Teneriffa durchgeführt. Am Gitterspektrographen des VTT wurde unter anderem das Streupolarisationsspektrum (das sogenannte zweite Sonnenspektrum) der Ca I 422.7 nm Spektralline mit einer polarimetrischen Empfindlichkeit von 8×10^{-5} gemessen. Am TESOS Filtergraphen des VTT wurden unter anderem die schwachen (Amplitude um 1×10^{-3}), kleinskaligen (< 1 Bogensekunde) horizontalen Magnetfelder der ruhigen Sonne mittels des transversalen Zeeman Effekts in der Fe I 630.2 nm Spektralline gemessen. Weiter konnte gezeigt werden, dass die hohe Kadenz und der hohe Arbeitszyklus des FSP die Rekonstruktion von Stokes Bildern mit hoher Qualität erlauben. Dabei werden, im Gegensatz zu anderen Instrumenten indessen ein zusätzlicher Breitbandkanal zum Einsatz kommt, nur die schmalbandigen und kurzzeitig belichteten (2.5 ms) Bilder der pnCCD Kamera des FSP verwendet. Auf diese Weise können differentielle Fehler zwischen zwei unterschiedlichen Bildkanälen ausgeschlossen werden. Die Rekonstruktion basiert auf dem "Multi-Object Multi-Frame Blind Deconvolution" (MOMFBD) Algorithmus.

Bei einer Modulationsfrequenz von 100 Hz, und ohne Bildrekonstruktion, liegt die Amplitude des SIC unterhalb des Rauschlevels von 7×10^{-5} , welcher nach einer Integrationszeit von etwa 8 min in der ruhigen Sonne erreicht wurde. Andererseits, nach Bildrekonstruktion eines Datensatzes aus der gleichen Beobachtung, entsprechend einer Integrationszeit von 1.16 min, wurden Signaturen von SIC knapp oberhalb des Rauschlevels von 4×10^{-4} beobachtet. Allerdings ist der SIC hier auf die Randbereiche der Stokes Bilder beschränkt wo die Güte der adaptiven Optik und der Bildrekonstruktion wegen Anisoplanatismus und Randeffekten eingeschränkt ist.

Die Techniken und Methoden die in dieser Dissertation studiert und in der Praxis erprobt wurden sind von allgemeiner Bedeutung für Projekte, die sich mit hochgenauer bildgebender Polarimetrie mit hoher Kadenz beschäftigen.

1 Introduction

Even though the Sun is a common, middle-aged star, it is very special to human kind. Our home planet lies within the realm of the Sun. This is true not only from a gravitational point of view—with more than 99.8 % of the solar system mass concentrated in its star (Woolfson 2000)—but also in terms of energy flow. The Sun has provided the majority of the Earth's energy input uninterruptedly during billions of years, allowing among others things the evolution of life as we know it.

Our host star is also special from an astronomical point of view, it is the only star that we can resolve, even in a very demanding definition of the term. State-of-the-art observatories can reach a spatial resolution that corresponds to only 5×10^{-5} of the solar diameter approximately (some 70 km!). The ability to investigate and in particular to image the fine details of the Sun, has radically changed the early human conception of a static and quiet star. Our present understanding involves a highly dynamic and active Sun, with many phenomena that span a wide range of temporal, spatial and energetic scales. From the more regular eleven-years cycle of the sunspots (see, e.g. Solanki 2003) to the unpredictable coronal mass ejections (see Fig. 1.1), and the fast (tens of minutes) solar flares (Stix 2002, Ch. 9). This diverse solar activity strongly influences the vicinity of Earth, including its magnetosphere and upper atmosphere. Such an influence became socially relevant with the advent of electricity-based and specially space-based technologies, promoting among others the development of the space weather sciences (Bothmer and Daglis 2007, Ch. 2). The effects of solar activity include not only the beautiful polar auroras (see Fig.1.1), but also more harmful phenomena such as the injection of high-energy particles in low orbits, which can damage spacecrafts, artificial satellites or hazard astronauts during spacewalks; the induction of electric currents in long power lines or oil pipes located in high-latitude regions, which can destroy transformers or sensing and protection systems; the interference of satellite or aircraft communication; and the interruption or performance reduction of global navigation systems (Bothmer and Daglis 2007).

The main driver of the solar activity is the Sun's magnetic field (Stix 2002, Ch. 8), therefore a detailed study of its generation and interaction with solar matter, is of paramount importance to both general society and to the scientific community. Given the large distances and very hazardous conditions of the near-sun environment, in-situ measurements of magnetic fields in the solar surface, or lower atmosphere, are not yet possible. As a result, remote sensing tools have been developed to estimate the solar magnetic fields from Earth or near-Earth space using a combination of spectropolarimetric measurements of the incoming solar light and polarized radiative transfer theory (see e.g. del Toro Iniesta 2003). The solar magnetic fields extend along spatial scales that range from tens of km to hundreds of Mm; change in time intervals that can last few seconds to several years; and have strengths ranging from tens to thousands of Gauss (Stix 2002, Ch.

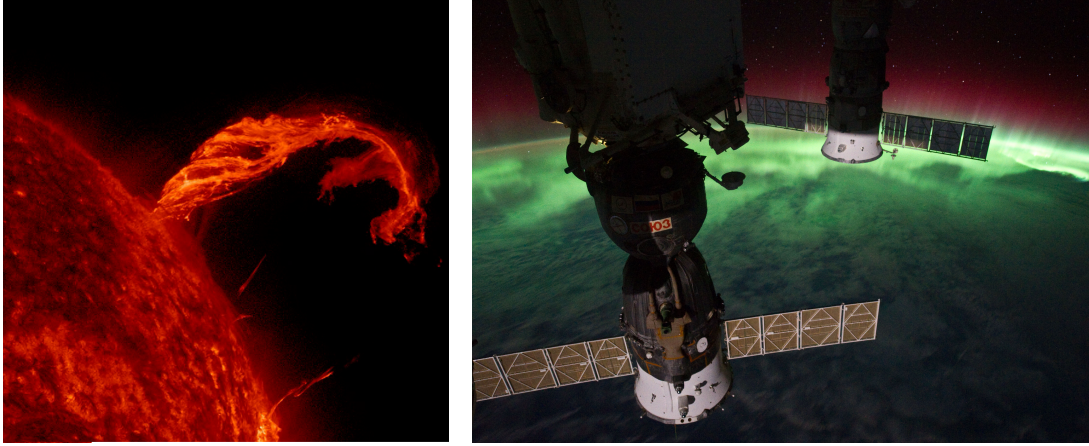


Figure 1.1. Examples of solar activity and its effects on Earth: An eruptive prominence is blown out of the Sun (left), carrying a huge amount of charged particles and magnetic field towards the interplanetary medium. If the ejected particles reach the Earth's magnetosphere under the appropriate conditions, they can penetrate and excite the gases in the atmosphere producing an aurora at high latitudes. However, the same source that produced the beautiful aurora Australis glowing in green and red over New Zealand (right), can also harm equipment and personnel (during space walks) of the International Space Station, from where the picture displayed rightmost was acquired. Credits: Solar Dynamics Observatory, NASA (left) and members of the International Space Station expedition 29, NASA (right).

8). As a consequence, remote estimations of the distribution and evolution of the fastest, smallest and weakest solar fields requires spectropolarimetric imaging systems with high spectral ($\text{m}\text{\AA}$), spatial (arcsec) and temporal (s) resolution along with very low noise (10^{-3} to 10^{-5} of the continuum intensity).

The location of the observatory, in space or on the ground, establishes important differences that affect the ultimate performance and costs of the spectropolarimeter. The most relevant, to achieve the above-stated polarimetric requirements, are the effects of atmospheric seeing. When observing from the Earth's surface, the originally plain wavefronts of the incoming solar light are distorted by the random fluctuations of the refractive index in the atmosphere. Due to the differential and non simultaneous nature of polarization measurements, seeing effects include not only the well known degradation of the image quality, but also the introduction of spurious polarization signals known as seeing induced crosstalk (SIC).

Carrying out high-precision, high-resolution solar polarimetry from the ground requires, among others, the minimization of seeing aberrations and SIC. The latter can be achieved, for instruments that use a temporal modulation scheme, by adopting a fast modulation frequency. This translates into the necessity of using high-cadence (>400 fps) scientific cameras. To fight seeing aberrations, adaptive optics (AO) systems and post-facto, image restoration techniques are routinely used in modern solar facilities. Short exposure times (~ 10 ms) are a requirement to optimally apply image restoration (Löfdahl et al. 2007) as for example a multi-object multi-frame blind deconvolution (MOMFBD). On the other hand, the low photon flux that ultimately reaches each resolution element of the detector, along with the dynamic nature of the solar signals, impose a very low figure (few tens of photoelectrons) for the camera noise specifications.

In this way, the development of high-precision, high-resolution solar polarimeters is strongly coupled to the development of fast, low-noise detectors. Moreover, only recent technological developments in complementary metal-oxide-semiconductor (CMOS) sensors or charge-coupled devices (CCDs) and their readout electronics, have allowed us to get close to the performance requirements derived from the most demanding open questions in modern solar spectropolarimetry.

1.1 Objectives

All the main goals of this thesis are related to the instrumental challenges that arise during the development of a state-of-the-art, ground-based, solar polarimeter. A particular focus is on the relatively unexplored case of high-cadence solar polarimetry, by means of the development and validation of a specific instrument: The prototype of the FSP. The main goals of this work are:

- (g1) Integration, characterization and optimization of a polarization modulator based on ferro-electric liquid crystals (FLCs), to be used for fast modulation and high-resolution polarimetry.
- (g2) Characterization and optimization of a custom-made, pn-type CCD (pnCCD) camera to be used in high-cadence polarimetry.
- (g3) Integration, testing and validation of the FSP as a complete system.
- (g4) Application of image restoration to high-cadence polarimetric data, to improve spatial resolution and signal to noise ratio (SNR).

The most important questions that arise from the above-described goals, involve the evaluation of the effects introduced by the pnCCD camera, never used in visible polarimetry before; and the FLC-based modulator on the polarimeter's performance. The principal contributions of the author are related to the quantification of such effects and the development of the necessary criteria and techniques to mitigate them when relevant. Since a measurement instrument can only accomplish its purpose when all its components are working properly and in harmony, from hardware to software, there is in addition a set of secondary tasks that need to be carried out when trying to fulfill the listed objectives. The most relevant contributions derived from this thesis are enumerated below.

- (c1) *Measurement and analysis of the properties of an FLC-based, polarization modulator and optimization of its polarimetric efficiencies in a high-cadence regime.* This includes the derivation of calibration requirements from the spatial, thermal, spectral and temporal characterization of the modulation matrix. Also the application of a model-based optimization procedure during design and assembly in order to obtain wide-band polarimetric efficiencies. (c1) is related to (g1) and (g3).
- (c2) *Measurement and analysis of the relevant properties of a pnCCD camera and selection of a camera-modulator synchronization strategy.* This involves the quantification of the polarimetric artifacts introduced by the camera, as well as of the effects of the camera noise properties on the instrumental performance. This contribution

includes: (a) the selection of a camera-modulator synchronization strategy; (b) the development of a novel technique to numerically correct the smearing artifacts due to the shutter-less operation of frame transfer sensors, for the case of highly-variable scenes; and (c) analysis of the common mode artifact correction. (c2) is related to (g2) and (g3).

(c3) *Integration and validation of the FSP as a complete system.* This includes the development of the reduction pipeline that implements all the calibration steps, derived from the results in (c1) and (c2), necessary to obtain science ready data. It also implies executing the relevant tasks, e.g. integration with post focus-instruments, required to acquire the first light measurements at the solar telescope; as well as the evaluation of the results to quantify the instrumental performance. (c4) is related to (g3).

(c4) *First restoration of high-cadence, spectropolarimetric data by means of a MOMFBD.* This involves the application of MOMFBD to spectropolarimetric data that have an exposure time (2.5 ms) shorter than the decorrelation time of day-time seeing (~ 20 ms), near 100 % duty cycle (*DC*) and very low sensor noise ($\sim 4.9 e^-$ rms); a regime not reachable with others solar polarimeters. (c5) is related to (g4).

1.2 Outline

The rest of the manuscript is organized as follows:

Chapter 2 reviews the fundamental concepts relevant to the subjects presented in this thesis. It covers the basics of solar imaging polarimetry, including polarized light characterization and generation, a brief overview of remote solar atmospheric diagnosis and a detailed description of the main components of solar polarimeters. A limited introduction to atmospheric seeing and its polarimetric effects is also given here. Finally the problem of solar image restoration by means of a MOMFBD is briefly presented.

Chapter 3 firstly discusses the case of high-cadence, solar polarimetry by detailing its main advantages, challenges and the derived requirements on the modulator package and the scientific camera used to obtain high-resolution, high-sensitivity observations from the ground. Secondly, the FSP is presented including its science goals and main specifications in order to point out its pros and cons with respect to other state-of-the-art, ground-based, solar polarimeters that also operate in the visible part of the spectrum.

Chapter 4 details the development of an FLC-based polarization modulator package that operates at 100 Hz modulation frequency, and is optimized to obtain balanced and achromatic polarimetric efficiencies in the 400 nm to 700 nm wavelength range. Mechanical, optical, thermal and dynamical design descriptions and characterization results are presented. The latter are used to define calibration requirements and to develop the data reduction routines in Chapter 6.

- Chapter 5** presents the characterization and optimization of a pnCCD camera to be used for high-cadence, solar polarimetry. After a review of the camera design and structure, a given modulator-camera synchronization strategy is selected to develop a numeric technique to correct for frame transfer artifacts. The camera noise, gain and dark current are measured and its impact on polarimetric precision is evaluated. Additionally, the common mode artifact is analyzed and its correction discussed.
- Chapter 6** describes some of the first-light measurements, carried out with FSP at the 68 cm Vacuum Tower Telescope (VTT), and discusses its results. Firstly, the main aspects of the data reduction pipeline developed by the author are presented. Secondly, a brief discussion of the different approaches to apply MOMFBD to the high-cadence data, is presented. Thirdly, three observational results are shown for spectrograph and filtergraph modes. Finally, the performance and limitations of FSP are discussed after estimating the residual SIC, and reporting the results of the measurements of the non-magnetic 557.6 nm absorption line.
- Chapter 7** summarizes the main contributions and results of the thesis. A short description of the second phase of the FSP project is also given.

2 Background

The development of a solar polarimeter requires understanding the synergy of different topics, including the physics of polarized light, the engineering behind the main devices that allow measuring polarization and the post-facto treatment of the raw data. This chapter reviews these topics, in order to establish the necessary terminology and definitions, required to present the work developed in the rest of the thesis.

Section 2.1 introduces the formalism needed to describe quasi-monochromatic, partially polarized light and the natural mechanisms, relevant to solar physics, that generate it. Additionally, it briefly describes the usage of polarimetry in modern solar physics and what are the typical data requirements and challenges that arise from it. Section 2.2 details the different measurement techniques and the components that form an imaging solar spectropolarimeter, including the polarization modulator, the scientific camera and the wavelength discriminator. The polarimetric effects of the atmospheric seeing and image motion, crucial for ground based instruments, are addressed in section 2.3. Where, in addition, the problem of restoring seeing-degraded solar images is briefly discussed; focusing on a particular technique, namely MOMFBD.

2.1 Introduction to solar spectropolarimetry

2.1.1 Description of polarized light and its transformations

Measuring polarization of light implies characterizing the behavior of the electric field vector as the wave propagates. For the case of a transversal —the propagation mode in free space— monochromatic wave, such a behavior is described by the well known polarization ellipse (see e.g. Goldstein 2003, Ch. 3). Moreover, only three real parameters are required to completely define the polarization ellipse, namely, the amplitude of the two components of the electric field (\mathbf{E}) that are orthogonal to the propagation direction, and the phase difference between them.

However, the amplitude-based description mentioned above, is not complete, e.g. it can not describe unpolarized light, and has limited practical relevance. The main reasons of the latter are (a) that monochromatic (strictly time and space periodic) waves do not exist in nature; (b) that the optical electric field describes a full ellipse in time-scales that are too short to access with current detection technology (see below); and (c) that devices capable of quantifying optical radiation are sensitive to the field volume energy ($\propto |\mathbf{E}|^2$) and not to its amplitude. Due to the aforementioned reasons, a description of the polarization of polychromatic (in particular quasi-monochromatic) radiation, in terms of observable (measurable) quantities is required. Such a formalism was introduced by G.

G. Stokes in 1852, and is summarized below.

The x component of the complex electric field, E_x , belonging to a quasi-monochromatic¹, transversal, plane wave propagating in the z direction; can be expressed as a monochromatic, plane wave that is slowly modulated in amplitude as follows

$$E_x(z, t) = [\xi_x(t)e^{i\delta_x(t)}]e^{i(kz - \omega_0 t)}, \quad (2.1)$$

where t is time, i the imaginary unit, ω_0 the mean frequency, k the wave number; and $\xi_x(t)$ and $\delta_x(t)$ are the module and phase of the complex modulating function—that determines the spectral content of the wave— respectively.

Since in practice a polarimetric measurement requires a time interval that is much longer than the mean period (or the coherence time) of the optical wave, a temporal average of the polarization ellipse will be actually registered during any experiment, e.g. the mean period is 1.6×10^{-15} s for a mean wavelength of 500 nm. After applying such a temporal average, the equation of the polarization ellipse can be expressed in terms of measurable quantities as (see e.g. Goldstein 2003, Ch. 4)

$$I^2 \geq Q^2 + U^2 + V^2, \quad (2.2)$$

where,

$$I = \langle E_x E_x^* \rangle + \langle E_y E_y^* \rangle = \langle \xi_x^2(t) \rangle + \langle \xi_y^2(t) \rangle, \quad (2.3)$$

$$Q = \langle E_x E_x^* \rangle - \langle E_y E_y^* \rangle = \langle \xi_x^2(t) \rangle - \langle \xi_y^2(t) \rangle, \quad (2.4)$$

$$U = \langle E_x E_y^* \rangle + \langle E_y E_x^* \rangle = 2\langle \xi_x(t)\xi_y(t)\cos(\delta(t)) \rangle, \quad (2.5)$$

$$V = i(\langle E_x E_y^* \rangle - \langle E_y E_x^* \rangle) = 2\langle \xi_x(t)\xi_y(t)\sin(\delta(t)) \rangle, \quad (2.6)$$

$\delta = \delta_x - \delta_y$ and $\langle \rangle$ denotes the average operation. Note that we have dropped the dependences on t and z in E_x and E_y for clarity. However, we preserved the temporal dependence in all the ξ and δ , to empathize that the wave is not monochromatic and thus it can be partially polarized².

The four terms introduced in Eq. 2.2, the so called Stokes parameters, are quadratic forms of the electric field and thus have units of intensity, i.e. they are the measurable aspects of the polarization ellipse. They are referred to as Stokes I parameter, that gives the total intensity of the beam; Stokes Q parameter, that gives the amount of linear 0° or 90° polarization; Stokes U parameter, that gives the amount of linear 45° or -45° polarization; and Stokes V parameter, that gives the amount of right or left handed circular polarization. The Stokes parameters are usually arranged in the so called Stokes vector (**S**) as follows

$$\mathbf{S} = [I, Q, U, V]^T = [S_0, S_1, S_2, S_3]^T, \quad (2.7)$$

¹With a spectral bandwidth negligible compared to its mean frequency.

²Since the measured signal is the result of the incoherent average of many uncorrelated photons (which are always totally polarized), it can present zero polarization—i.e. there is no statistical preference for any polarization state— or partial polarization. The latter means that, after averaging the polarization state of all the considered photons, a fraction of them (given by the polarization degree) are not canceled out. Such an incoherent superposition, can not be described by the *Jones calculus* because the Jones vectors preserve the phases of the individual photons, and thus their average is equivalent to the coherent superposition (see e.g. Stenflo 1994, Ch. 2 for a definition of Jones calculus).

where the superscript T denotes the transpose. In Eq. 2.6, we have also introduced an alternative notation of \mathbf{S} , i.e. using S_0, S_1, S_2 and S_3 ; both notations shall be used indistinguishably across the manuscript.

The Stokes formalism provides a concise representation of unpolarized ($Q = U = V = 0$), partially polarized ($I^2 > Q^2 + U^2 + V^2$) and totally polarized ($I^2 = Q^2 + U^2 + V^2$) light. Moreover, it readily describes the polarization state (\mathbf{S}) of a beam resulting from the combination of two uncorrelated beams ($\mathbf{S}^{(0)}$ and $\mathbf{S}^{(1)}$) as a simple addition ($\mathbf{S} = \mathbf{S}^{(0)} + \mathbf{S}^{(1)}$).

The modification of the polarization state of a beam, resulting from its interaction with matter, can be conveniently expressed as a linear transformation of the initial Stokes vector, $\mathbf{S}^{(0)}$, defined by a 4×4 Mueller matrix (\mathbf{M}) as follows³

$$\mathbf{S} = \mathbf{M}\mathbf{S}^{(0)}. \quad (2.8)$$

If N of such a transformations —each defined by \mathbf{M}_n , with $n \in \{0, 1, \dots, N-1\}$ and $n=0$ being the first one applied— act on a beam with initial Stokes vector $\mathbf{S}^{(0)}$, the resulting polarization state, \mathbf{S} , is given by

$$\mathbf{S} = \left(\prod_{n=N-1}^0 \mathbf{M}_n \right) \mathbf{S}^{(0)}. \quad (2.9)$$

To facilitate the interpretation of a physically meaningful \mathbf{M} , let us differentiate its elements in terms of its diattenuation 3-vector (\mathbf{h}), polarizance 3-vector (\mathbf{v}) and 3×3 rotation matrix (\mathbf{R}). Following del Toro Iniesta (2003), we can re-write Eq. 2.8 as

$$g \begin{bmatrix} 1 \\ \mathbf{p} \end{bmatrix} = M_{0,0} \begin{bmatrix} 1 & \mathbf{h}^T \\ \mathbf{v} & \mathbf{R} \end{bmatrix} \begin{bmatrix} 1 \\ \mathbf{p}^{(0)} \end{bmatrix}, \quad (2.10)$$

where $M_{0,0}$ is the first element of \mathbf{M} , the polarization vector (\mathbf{p}) is defined as

$$\mathbf{p} = \left[\frac{Q}{I}, \frac{U}{I}, \frac{V}{I} \right]^T = [q, u, v]^T \text{ with } 0 \leq |\mathbf{p}| \leq 1, \quad (2.11)$$

and g is the gain of the optical system. In Eq. 2.11, we have also introduced an alternative notation of \mathbf{p} using the short forms for the normalized Stokes parameters, namely q, u and v .

A given 4×4 matrix is a Mueller matrix if it defines a transformation that is closed in the Stokes vectors space, i.e. if the \mathbf{S} obtained from Eq. 2.8 satisfies Eq. 2.2. To do so, $M_{0,0} \geq 0$ to ensure a positive output intensity for an unpolarized ($\mathbf{p}^{(0)} = 0$, also called natural) input; \mathbf{h} has to belong to the Poincaré sphere⁴ to ensure $I/I^{(0)} \geq 0$; and \mathbf{v} has to belong to the Poincaré sphere because $\mathbf{p} = \mathbf{v}$ for a natural input.

A useful Mueller matrix is the one that produces a rotation of the reference frame in the transversal plane of the wave, i.e. it does not modify circular polarization values (V).

³This matrix approach, introduced by Hans Mueller in 1940s, satisfactorily describes the polarimetric effects of most of the optical components found in solar telescopes, spectrographs and polarimeters. Moreover it also sets the basis for the description of the polarimetric effects of stellar atmospheres.

⁴A unitary sphere introduced by Henri Poincaré to visually represent the polarization state of a beam, and simplify the calculus of its modifications when interacting with polarizing elements (see e.g. Goldstein 2003, Ch. 12).

For a rotation of an angle θ , measured counterclockwise from the Stokes Q direction, such a matrix is defined as (del Toro Iniesta 2003)

$$\mathbf{M}_{rot}(\theta) = \begin{bmatrix} 1 & 0 & 0 & 0 \\ 0 & c_2 & s_2 & 0 \\ 0 & -s_2 & c_2 & 0 \\ 0 & 0 & 0 & 1 \end{bmatrix}, \quad (2.12)$$

where $c_2 = \cos(2\theta)$ and $s_2 = \sin(2\theta)$. Note that, \mathbf{M}_{rot} is a \mathbb{R}^4 rotation matrix, i.e. $\mathbf{M}_{rot}\mathbf{M}_{rot}^T = \mathbf{M}_{rot}^T\mathbf{M}_{rot} = \mathbb{1}$, where $\mathbb{1}$ is the identity matrix. After rotation, the new Stokes vector and Mueller matrix are given by

$$\mathbf{S} = \mathbf{M}_{rot}\mathbf{S}^{(0)} \quad \text{and} \quad \mathbf{M} = \mathbf{M}_{rot}^T\mathbf{M}^{(0)}\mathbf{M}_{rot} \quad (2.13)$$

2.1.2 Generation and transformation of polarized light

There are many radiation-matter interaction processes that can generate polarized light or modify its polarization state (see e.g. Sascha 2014). Polarization is a highly geometrical phenomenon that arises from the fact that light is asymmetric, i.e. it propagates transversally in free space, therefore the processes that generate polarization are associated to asymmetries in the source-observer system. The most common processes are summarized in Fig. 2.1 along with some examples of their occurrence in the context of solar spectropolarimetry. As can be appreciated there, some polarizing processes take place in the Sun (these can potentially be used to retrieve solar properties) and some others occur at an instrumental level (these can be used to detect polarization or, ironically, may make this task difficult). The following list briefly details only the mechanisms that are relevant to this work.

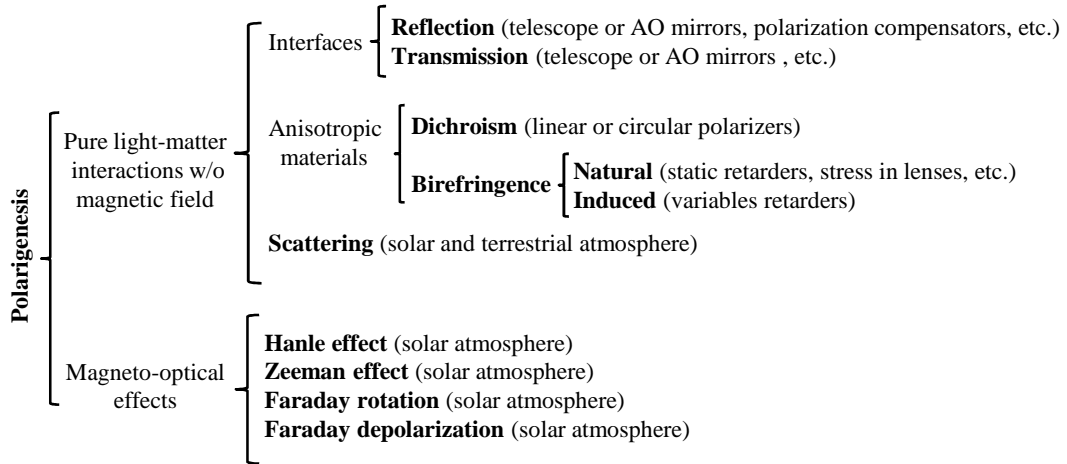


Figure 2.1. Processes that can generate or modify polarization. Some examples of their occurrence, in the context of solar spectropolarimetry, are given in parentheses.

1. *Dichroism* (a.k.a diattenuation), denotes the asymmetric absorption of the two orthogonal polarization states of the incoming beam. It is a consequence of the

anisotropic electric properties of a material, and is commonly used to manufacture polarizers. In particular, a partial linear polarizer has a high transmittance, k_{0° , of the \mathbf{E} component that is parallel to its optical axis; and a lower transmittance, k_{90° , of the orthogonal component. Denoting $\alpha = k_{0^\circ}^2 + k_{90^\circ}^2$, $\beta = (k_{0^\circ}^2 - k_{90^\circ}^2)/\alpha$ and $\gamma = 2k_{0^\circ}k_{90^\circ}/\alpha$; the polarimetric action of a partial linear polarizer, with its optical axis forming an angle θ relative to the Stokes Q direction, can be characterized by its Mueller matrix, \mathbf{M}_{pol} , as follows (del Toro Iniesta 2003)

$$\mathbf{M}_{pol}(\theta, k_{0^\circ}, k_{90^\circ}) = \frac{\alpha}{2} \begin{bmatrix} 1 & \beta c_2 & \beta s_2 & 0 \\ \beta c_2 & c_2^2 + \gamma s_2^2 & (1 - \gamma)s_2 c_2 & 0 \\ \beta s_2 & (1 - \gamma)s_2 c_2 & s_2^2 + \gamma c_2^2 & 0 \\ 0 & 0 & 0 & \gamma \end{bmatrix}. \quad (2.14)$$

If $k_{0^\circ} = 1$ and $k_{90^\circ} = 0$, \mathbf{M}_{pol} reduces to the case of an ideal linear polarizer with Mueller matrix \mathbf{M}_{pol} , given by

$$\mathbf{M}_{pol}(\theta) = \frac{1}{2} \begin{bmatrix} 1 & c_2 & s_2 & 0 \\ c_2 & c_2^2 & s_2 c_2 & 0 \\ s_2 & s_2 c_2 & s_2^2 & 0 \\ 0 & 0 & 0 & 0 \end{bmatrix}. \quad (2.15)$$

Note that, a perfect linear polarizer produces a linearly polarized output beam for any value of the input Stokes vector, i.e. $\mathbf{v} \neq 0$ and the last row of \mathbf{M}_{pol} is null. The same device can also be used as a *linear polarization analyzer*, i.e. its \mathbf{h} produces an output Stokes I , that is sensitive to the values of Stokes Q and U of the input beam (see Sect. 2.2.1).

2. *Birefringence* is a consequence of the anisotropic electric response (refractive index) of a given material, i.e. the dielectric tensor written in the principal frame of reference, is a 3×3 diagonal matrix with different diagonal elements. If only two out of the three principal refractive indexes of the dielectric tensor are equal, the material is called *uniaxial*. Disc-shaped optical components made of uniaxial materials, are typically characterized by the position angle of its optical axis (θ) and a retardance (δ) given by

$$\delta = 2\pi \frac{(n_o - n_e)thick}{\lambda}, \quad (2.16)$$

where *thick* is the geometrical thickness of the disc; n_o and n_e are the ordinary (corresponding to the two directions perpendicular to the optical axis) and extraordinary (corresponding to the direction of the optical axis) refractive indexes respectively; and λ is the wavelength of the wave in vacuum (del Toro Iniesta 2003, Ch. 4). When light hits normally such a device, the component of the \mathbf{E} that is perpendicular to the optical axis experiences a phase lag with respect to the component parallel to it given by δ , modifying in this way the polarization state of the beam.

Birefringence can be natural or induced, and is commonly exploited to manufacture retarders. Natural birefringence appears in materials that are formed by non-isotropic crystals, such as Calcite, $LiNbO_3$ (uniaxial) or mica (biaxial) (Goldstein 2003, Ch. 24). Birefringence may be induced or modified, i.e. the values of δ or

θ can be changed using electric fields (as in an FLC or nematic LC) or pressure waves (as in piezo-elastic crystals). Regardless of its kind, the polarimetric action of a retarder can be characterized for a given δ and θ using its Mueller matrix, \mathbf{M}_{ret} , given by (del Toro Iniesta 2003)

$$\mathbf{M}_{ret}(\theta, \delta) = \begin{bmatrix} 1 & 0 & 0 & 0 \\ 0 & c_2^2 + s_2^2 \cos(\delta) & [1 - \cos(\delta)]s_2c_2 & -s_2 \sin(\delta) \\ 0 & [1 - \cos(\delta)]s_2c_2 & s_2^2 + c_2^2 \cos(\delta) & c_2 \sin(\delta) \\ 0 & s_2 \sin(\delta) & -s_2 \sin(\delta) & \cos(\delta) \end{bmatrix}. \quad (2.17)$$

If $\delta = \pi/2$, the retarder is called a *quarter-wave plate (QWP)*. Analogously, if $\delta = \pi$, the retarder is called a *half-wave plate (HWP)*. Note that, a linear retarder does not modify the polarization degree of a beam, i.e. $\mathbf{v} = \mathbf{h} = 0$, it only introduces a rotation of the incoming \mathbf{p} , i.e. the matrix \mathbf{R} is a \mathbb{R}^3 rotation matrix.

3. *Scattering polarization* is produced when an incident, anisotropic radiation field is scattered by matter (Goldstein 2003, Ch. 20). The phenomenon can be understood in terms of classical electrodynamics by assuming that the scattering material is composed of elemental electric dipoles (representing e.g. the electrons, atomic nuclei, molecules, etc.) that are excited by the incoming transversal waves, and reradiate only in directions perpendicular to their longitudinal axes. For the case of Thomson and Rayleigh scattering, the polarization state of the beam scattered at an angle θ relative to the propagation direction of the incoming beam, can be obtained using the Mueller matrix of the process (Goldstein 2003, Ch. 20)

$$\mathbf{M}_{sca}(\theta) = \kappa_{sca} \begin{bmatrix} 1 + \cos^2(\theta) & \sin^2(\theta) & 0 & 0 \\ \sin^2(\theta) & 1 + \cos^2(\theta) & 0 & 0 \\ 0 & 0 & 2 \cos(\theta) & 0 \\ 0 & 0 & 0 & 2 \cos(\theta) \end{bmatrix}, \quad (2.18)$$

where Stokes Q is defined perpendicular to the plane of scattering and κ_{sca} is a constant independent of the wavelength of the incoming beam (λ) for Thomson scattering, or, a function proportional to $1/\lambda^4$ for Rayleigh scattering. Since the polarizance vector of \mathbf{M}_{sca} is not null, the scattering process acts as a polarizer, i.e. the scattered light will be linearly polarized even for the case of unpolarized incoming radiation. The polarization degree depends on the scattering angle, being zero for forward ($\theta = 0^\circ$) and backwards ($\theta = 180^\circ$) scattering, and maximum for $\theta = 90^\circ$.

The Earth's atmosphere is anisotropically illuminated by the distant Sun, as a consequence, molecular Rayleigh scattering produces not only a blue —see the resulting Stokes I parameter for an unpolarized input in Eq 2.18— but also a linearly polarized sky. Fortunately the net sky polarization in the direction of the Sun ($\theta = 0^\circ$) is very low and can be neglected when doing solar polarimetry from the ground.

Scattering polarization takes place also in the solar atmosphere due to the anisotropic radiation field, i.e. the incident light has a preferred radial direction, giving rise to a net linear polarization signal predominantly oriented parallel to the solar limb (see e.g. Stenflo 2013). Since the scattering angle viewed by a distant observer tends

to 90° towards the solar limb, the larger scattering polarization signals are found there. However, even the largest signals are relatively small ($\sim 10^{-3}$) due to the averaged contribution of a wide range of scattering angles and other quantum effects introduced by the scattering in bound-bound transitions of atoms (that deviate from the dipole approximation given above, Stenflo 2013). A spectral atlas of Stokes Q/I due to scattering polarization near the solar limb, presents a behavior that strongly differs from the intensity solar spectrum. Therefore, it is usually referred to as the *second solar spectrum* (Stenflo and Keller 1997), see Fig. 2.2.

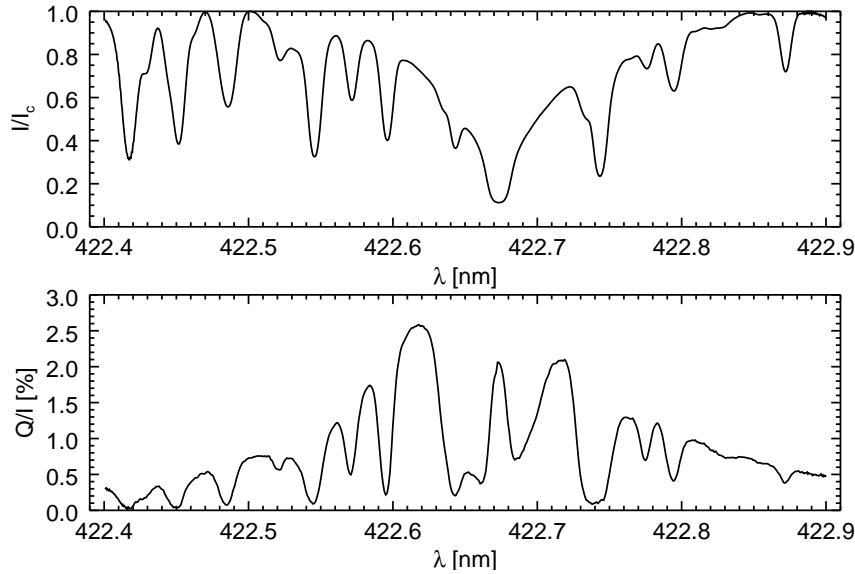


Figure 2.2. Example of scattering polarization signals in the solar atmosphere. The upper panel shows a portion of the normalized intensity spectrum recorded near the solar limb. The light is also linearly polarized due to scattering in the solar atmosphere, as the Stokes Q/I measurements presented in the lower panel exemplify. The spectral behavior of both signals is so different, that the bottom case is usually referred to as the second solar spectrum. These measurements are part of a full spectral atlas that covers the visible and UV ranges published by Gandorfer (2000, 2002, 2005).

4. *Hanle effect.* The presence of a magnetic field (\mathbf{B}) modifies the scattering polarization process. This can be partially understood as a randomization of the elemental dipoles orientations between the excitation and emission stages, that derives in the reduction of the resulting net linear polarization. The *Hanle effect*—which may also produce a rotation of the plane of polarization (Hanle 1924)—can be used to probe the solar magnetic fields in certain spectral lines (Stenflo 1982).
5. *The Zeeman effect* refers to the splitting of the energy levels of an atom due to the influence of an external \mathbf{B} (see e.g. del Toro Iniesta 2003, Ch. 8 and references therein). An energy level with total angular momentum quantum number j , splits in to $(2j + 1)$ sub-levels, each with a different magnetic quantum number (m). The energy difference between the sub-levels is proportional to $|\mathbf{B}|$ and the magnetic sensitivity of the level, the so called Landé factor. When light interacts with matter, an absorption or emission spectral line is formed if the electrons of the constituent

atoms change between two energy levels due to the absorption or emission of photons respectively. In the presence of a magnetic field, each of the two energy levels involved will often split into many sub-levels, resulting in multiple possible transitions. As a consequence, the original spectral line will be split into multiple lines (Zeeman components) according to how many of the energy transitions are allowed, i.e. fulfill angular momentum conservation as expressed by the selection rules of m ($\Delta m = 0, \pm 1$), of j ($\Delta j = \pm 1$), of the spin angular momentum quantum number ($\Delta s = 0$) and of the orbital angular momentum quantum number ($\Delta l = 0, \pm 1$). The different Zeeman components can be separated into three groups, the π components which correspond to $\Delta m = 0$ and therefore present no (net) shift, with respect to the $\mathbf{B} = 0$ case, and are linearly polarized; the σ_b components, which correspond to $\Delta m = +1$ and thus are shifted to the blue and elliptically polarized; and the σ_r components, which correspond to $\Delta m = -1$ and thus are shifted to the red and also elliptically polarized, however with opposite ellipticity.

When treating the *normal Zeeman effect*, i.e. the triplet produced by the transitions between energy levels with $j = 0$ and $j = 1$, the spectral splitting of the components ($\Delta\lambda_z$) is a function of the wavelength of the line (λ) and the Landé factor of the atomic transition (g), namely

$$\Delta\lambda_z = \kappa_z g \lambda^2 |\mathbf{B}|. \quad (2.19)$$

where $\kappa_z = 4.67 \times 10^{-13} \text{ \AA}^{-1} \text{ G}^{-1}$. Eq. 2.19 can be used to estimate $|\mathbf{B}|$ if the resulting $\Delta\lambda_z$ is larger than the line width⁵. In addition, Eq. 2.19 can be used to approximate the average displacement of the group of σ -components with respect to the line center in the *anomalous Zeeman effect*, if g is replaced by the so called effective Landé factor (Reiners 2012).

As pointed out above, the Zeeman components are not only shifted in the spectrum but also polarized. For the special case of \mathbf{B} oriented perpendicular to the line of sight (LOS), the resulting π , σ_r and σ_b components are linearly polarized (*transversal Zeeman effect*). On the other hand, for the case of \mathbf{B} parallel to the LOS, the resulting σ_r and σ_b components are circularly polarized, while the π components vanish (*longitudinal Zeeman effect*).

The detailed spectral behavior of the Zeeman polarization signals can be approximated for weak fields, i.e. where the resulting $\Delta\lambda_z$ is smaller than the line width, if an homogeneous \mathbf{B} —oriented with inclination angle γ and azimuth angle χ , measured with respect to the LOS and to the defined Stokes Q direction respectively—and a static absorbing (or emitting) medium are assumed. The resulting Stokes vector for unpolarized incident radiation, can then be estimated using the well known

⁵This is generally the case for long optical wavelengths (if \mathbf{B} is strong enough), because the (thermal) Doppler broadening of the lines scales with λ , while $\Delta\lambda_z$ scales with λ^2 .

weak field approximation (see e.g. Stenflo 2013)

$$I \approx I^{(0)}, \quad (2.20)$$

$$Q \approx -\kappa_z^2 g^2 \lambda^4 \cos(2\chi) \sin^2(\gamma) |\mathbf{B}|^2 \frac{\partial^2 I}{\partial \lambda^2}, \quad (2.21)$$

$$U \approx -\kappa_z^2 g^2 \lambda^4 \sin(2\chi) \sin^2(\gamma) |\mathbf{B}|^2 \frac{\partial^2 I}{\partial \lambda^2}, \quad (2.22)$$

$$V \approx -\kappa_z g \lambda^2 \cos(\gamma) |\mathbf{B}| \frac{\partial I}{\partial \lambda}, \quad (2.23)$$

were $I^{(0)}$ is the Stokes I parameter that would be produced if $\mathbf{B} = 0$. While the above-given approximations for Stokes I and V are generally valid, the expressions for Q and U are restricted only to weak spectral lines (where no Zeeman saturation is present). Note that, Stokes V is directly proportional to the longitudinal component of \mathbf{B} (Eq. 2.23). On the other hand, Stokes Q and U depend non-linearly on the transversal component of \mathbf{B} (Eq. 2.21 and 2.22). In the Sun, the Zeeman effect is one of the most important sources of polarized radiation, and certainly the cornerstone of remote, solar magnetometry techniques (see Sect. 2.1.3). Different from the scattering or Hanle case, the Zeeman polarization signals can be relatively large (up to $\sim 40\%$) in solar active regions, where \mathbf{B} can reach few kG (see Fig. 2.3). On the other hand, the Zeeman signals of spatially unresolved, longitudinal magnetic fields of opposite polarities will tend to cancel out (something that does not occur with Hanle signals), complicating the estimation of faint, small scale fields.

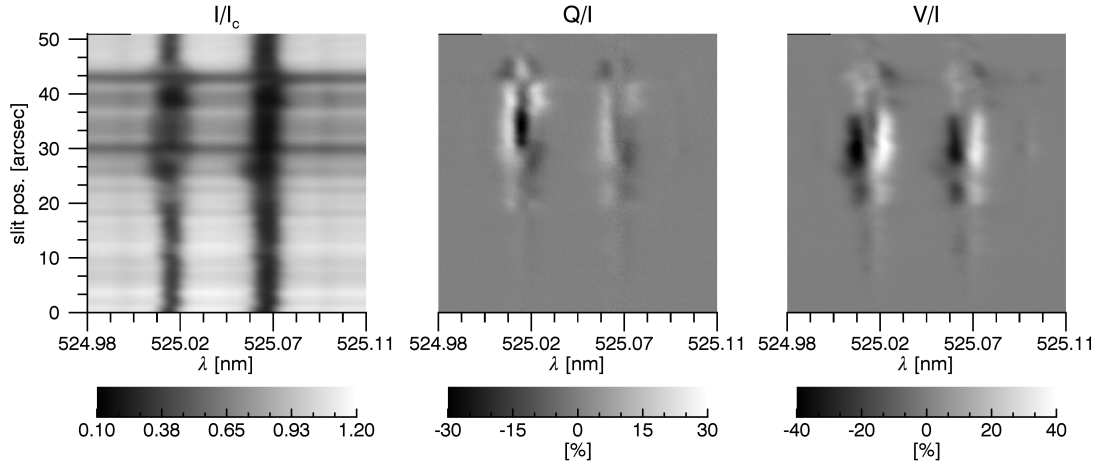


Figure 2.3. Example of Zeeman polarization signals in a sunspot. The light from the solar scene is passed through a slit (vertical axis in the images) to eliminate one spatial dimension and replace it with the spectral information (horizontal axis in the images) using a diffraction grating. The strongest magnetic fields are located from 26 to 43 arcsec approximately, where also the largest Zeeman broadening (see Stokes I/I_c) and polarization signals (see Stokes Q/I and V/I) are present. Note that, the spectral dependence of the polarization signals given by Eq. 2.21 and 2.23 are generally satisfied. The images were acquired with FSP.

2.1.3 Solar spectropolarimetry

Solar spectropolarimetry refers to the measurement of the polarization state of solar light as function of its wavelength. In general, the aim of these kind of measurements is the quantification of different physical variables of interest in the Sun, particularly in its atmosphere. Many such variables, most notably the solar magnetic field, are of crucial importance to understand the solar dynamics and the plethora of phenomena that arise from the Sun and influence the whole solar system (see Ch. 1). Therefore solar spectropolarimetry is a key resource to solar system sciences such as Solar physics, planetary sciences and Earth climate.

The above-mentioned measurement and analysis procedure, usually denoted as atmospheric diagnosis, is summarized by the sketch presented in Fig. 2.4, for the specific case in which ground-based observations are employed. The light radiated from the base of the solar photosphere⁶ (assumed to be unpolarized) interacts with the material of the solar atmosphere. For visible and infra red (IR) wavelengths, the majority of absorption spectral lines are formed by interactions with the plasma of the photosphere and lower chromosphere. Further absorption and emission spectral lines are also formed higher in the chromosphere and in the corona, mostly in the ultra violet (UV) and shorter wavelengths. When radiation leaves the solar atmosphere, it carries information about the environment, e.g. magnetic field, line of sight velocity of the plasma (v_{los}), etc., in which the spectral lines are formed. Such an information is imprinted in the polarization state of the light and its spectral dependence (denoted with Stokes vector \mathbf{S}_\odot), thanks to the Zeeman, Doppler and Hanle effects among others (see Sect 2.1.2).

After traveling through the optically thin interplanetary medium, light reaches the Earth's atmosphere. There, atmospheric seeing aberrates the solar image, resulting in a reduction of spatial resolution and other issues (see Sect. 2.3.1). The aberrated solar scene, \mathbf{S}_{tel} , is then observed with a ground-based telescope, usually equipped with an AO system to partially correct the seeing effects. The polarimeter receives light, \mathbf{S} , at the scientific focus of the telescope, that may differ from \mathbf{S}_{tel} due to spurious instrumental polarization. The first block of the polarimeter, performs a modulation in order to encode the incoming polarization information in fluctuations of its output intensity (denoted as $I(\mathbf{S})$). The intensities are then recorded by a scientific camera (denoted as $\hat{I}(\mathbf{S})$), after previous selection of the desired spectral range by means of a wavelength discrimination system, e.g. a filter or a spectrograph.

Once the raw data is acquired, a first set of basic reduction steps, e.g. demodulation, are applied to retrieve the best possible estimation of \mathbf{S} , $\hat{\mathbf{S}}$. Additional processing of the data is also done to eliminate the telescope and AO polarimetric effects, and further reduce the seeing aberrations, in order to recover \mathbf{S}_\odot . The estimated solar signal, $\hat{\mathbf{S}}_\odot$, is used in the last step to perform a spectropolarimetric inversion. The latter provides, through an iterative model-fitting process, a quantitative estimation of the physical variables at the

⁶The solar atmosphere is divided in four layers. The lowest, *photosphere*, a few hundred km thick layer which defines the visible surface of the star, i.e. the effective temperature at the photosphere (~ 5778 K) is equal to the temperature of a black body radiating the same total energy as the Sun. Above the photosphere lies the *chromosphere*, which extends for some 2000 km and presents a small temperature increase (from 4000 to 7000 K approximately). In between the chromosphere and the 1 MK *corona*, there is a thin *transition region* that presents also an abrupt decrease in density (see e.g. Stix 2002, Ch. 4 and 9 for extra details).

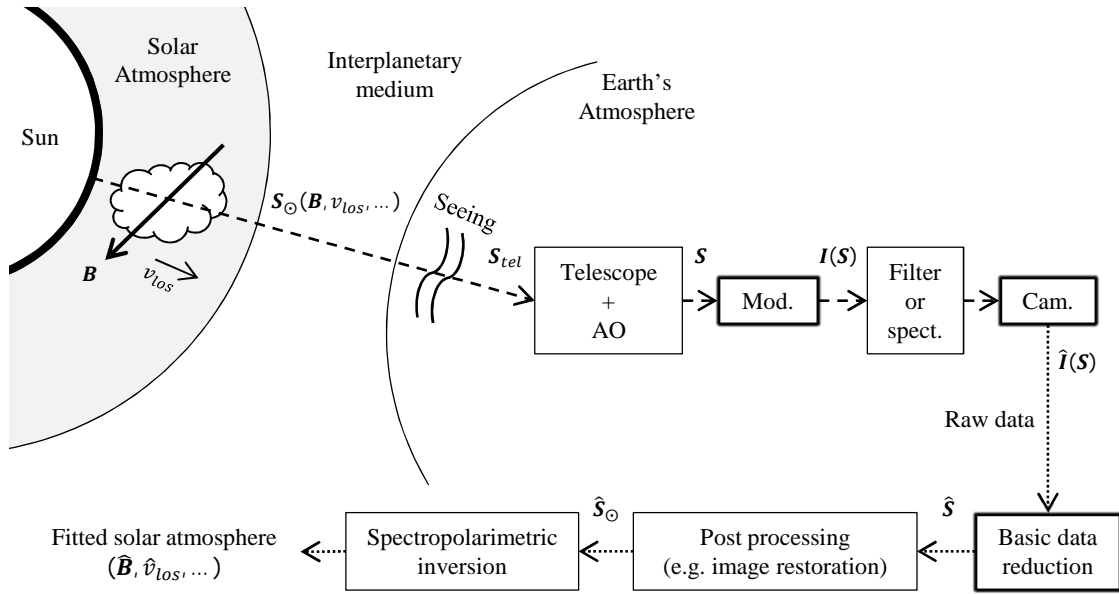


Figure 2.4. Remote diagnosis of the solar atmosphere using ground-based, spectropolarimetric measurements. The dashed lines mark the light path, while the dotted lines show the data flux. The rectangular boxes represent different hardware and/or software systems that process light or data. The polarimeter (central topic of this thesis) is composed by the polarization modulator (Mod.), the scientific camera (Cam.) and the associated, basic data reduction procedures (all denoted by boxes with thick borders). See the text for extra details.

solar atmosphere, e.g. \mathbf{B} , v_{los} , etc.

As can be appreciated, the solar atmospheric diagnosis involves many subsystems and processes, some of which are strongly model dependent. Therefore the term remote measurement has to be used with care in this context (remote estimation is more adequate). When the main variable of interest is the magnetic field, the above-described process is usually denoted as solar magnetometry.

The solar spectropolarimeter is one of the key components required to acquire the data used for the atmospheric diagnosis. In Fig 2.4, the spectropolarimeter is formed by the combination of the polarimeter (boxes with thick borders) and the wavelength discriminator instrument (filter or spectrograph). The main focus of this work is the development of a novel polarimeter, both the hardware and the necessary data reduction routines that lead to a reliable detection of the incoming Stokes vector. Some points regarding the post processing steps, such as image restoration, are also addressed.

2.1.4 Data requirements in high-resolution solar polarimetry

The quality of a solar spectropolarimetric measurement is usually quantified using four numbers, namely, the spatial⁷ ($\Delta\alpha$), spectral ($\Delta\lambda$) and temporal (Δt) resolution elements; and the noise level in the normalized Stokes images, also called *polarimetric sensitivity*⁸.

⁷A square spatial resolution element is assumed here, and in the rest of the thesis, unless the contrary is explicitly specified.

⁸Note that, we do not mention accuracy, i.e. systematic deviations from the true value. The main reasons for this are that accuracies in the $\sim 1\%$ level are typically obtained, and that the normalized solar signals are

The latter is equal to the noise to signal ratio (NSR) of the corresponding intensity images, divided by the so called polarimetric efficiencies (see Sect. 2.2.1 for a definition), thus we use the NSR in the following analysis. In addition, we consider here only polarimeters that are able to measure the full Stokes vector.

Many open questions in modern solar physics impose challenging requirements on the current and upcoming solar telescopes and spectropolarimeters (Kleint and Gandorfer 2015). Four examples of such questions that particularly push the instrumental limits are summarized in the following list.

- Quantification of the horizontal component of the faint —with a mean strength of ~ 100 G— quiet Sun \mathbf{B} of the photosphere. The latter is crucial to determine whether the small-scale fields are more horizontal or vertical, or more importantly, if the quiet Sun magnetic fields dominate the total magnetic flux of the Sun (Almeida and González 2011).
- Quantification of the turbulent \mathbf{B} . The limited spatial resolution of current observations, plus the cancellation effect of the Zeeman signals when the magnetic field is randomly oriented, put the Hanle effect in an advantage point to diagnose small-scale turbulent fields (possibly related to the quiet Sun fields of the previous point). The latter requires the detection of the faint scattering polarization signals (see sect. 2.1.2) at small spatial scales (Trujillo Bueno et al. 2004).
- Quantification and structure of the faint chromospheric \mathbf{B} . The fields at the chromosphere are generally weaker, and the spectral line selection is more limited in terms of Landé factors, than in the photosphere. The latter results in faint Zeeman signals which also change faster due to the larger chromospheric sound speed (Kleint and Gandorfer 2015).
- Polarimetry of fast events, such as flares, require spectropolarimeters that can perform full-Stokes measurements within a second (Kleint and Gandorfer 2015).

Clearly, not all the aforementioned examples (and other open questions not mentioned here) impose the same specifications on the required spectropolarimetric data. However, it is possible to define rough values for the instrumental requirements that characterize most of the state-of-the-art (or under development), high-resolution, high-sensitivity solar spectropolarimeters. These are, $\Delta\alpha_{goal} \sim 0.2$ arcsec, $\Delta\lambda_{goal} \sim 20$ mÅ and $NSR_{goal} \sim 10^{-4}$. The definition of Δt_{goal} is more case dependent, because it is strongly related to the achievable NSR and $\Delta\alpha$, this is detailed below.

There are intrinsic trade-offs that arise from the data requirements specified above, these are related to the fact that high-resolution imaging of dynamic solar signals is photon starved (see e.g. Stenflo 1999). Let us consider the detection, at a given wavelength (λ_0), of a polarimetric feature that evolves only spatially on the solar surface with an angular speed v ; using a resolution element $[\Delta\alpha, \Delta t, \Delta\lambda]$ and aiming for a given NSR . In order to avoid spatial smearing, the detection should be faster than the time the feature takes to cross one spatial resolution element, i.e. the *maximum* measurement time is limited by

$$\Delta t \leq \Delta\alpha/v. \quad (2.24)$$

also small and quantified relative to the nearest unpolarized continuum portion of the spectrum. Thus, in the absence of artifacts and assuming typical instrumental polarization ($<5\%$); the noise level becomes the relevant quantity to determine the minimum detectable signal.

Note that we have neglected any other phenomenon that may lead to a reduction of the spatial resolution, most notably the atmospheric seeing (see Sect 2.3.1).

On the other hand, assuming the instrument is photon noise (N_p) limited⁹, the *minimum* time required to reach the desired NSR is related to the effective photon flux illuminating the detector (Φ) by

$$\Delta t \geq 12/(NSR^2 \Phi \Delta \alpha^2), \quad (2.25)$$

where we have assumed, for simplicity, ideal polarimetric efficiencies for the modulator (equal to $1/\sqrt{3}$, see Sect. 2.2.1), ideal quantum efficiency (QE) for the detector, and that the image is critically sampled, i.e. the angular pixel size is half the angular spatial resolution. An estimation of Φ , given in terms of the solar spectral irradiance (Γ)¹⁰ and telescope aperture (\mathbb{D}), is

$$\Phi = \kappa_\Phi \Gamma \lambda_0^2 \mathbb{D}^2 \text{ photon s}^{-1} \text{ arcsec}^{-2}, \quad (2.26)$$

where $\kappa_\Phi = 273.33 \text{ photon J}^{-1} \text{ nm}^{-1} \text{ arcsec}^{-2}$, and we have assumed a resolving power of 250 000 ($\Delta \lambda = 20 \text{ m\AA}$ at $\lambda_0 = 500 \text{ nm}$) and a total throughput of the system of 10 %.

Under the afore mentioned assumptions, Eq. 2.24 to 2.26, define a limit for the possible combinations of $\Delta \alpha$ and NSR that can be simultaneously satisfied, given a \mathbb{D} and a λ_0 , namely

$$NSR \geq \left(\frac{12\nu}{\kappa_\Phi \Gamma \lambda_0^2 \mathbb{D}^2 \Delta \alpha^3} \right)^{1/2}. \quad (2.27)$$

Fig. 2.5 shows plots of the minimum NSR , defined by Eq. 2.27, versus $\Delta \alpha$ for different \mathbb{D} and λ_0 , using $\nu = 10 \text{ km s}^{-1}$ (which corresponds roughly to the sound speed in the solar photosphere). The values for NSR_{goal} and $\Delta \alpha_{goal}$ are identified by a black circle. Let us take as an example the case of $\mathbb{D} = 1.5 \text{ m}$ (the approximate value for the biggest solar telescopes currently in operation) and $\lambda_0 = 500 \text{ nm}$. Here, even when the diffraction limit of the telescope allows resolving features of 0.2 arcsec , the spatial smearing due to evolution makes this only possible for a maximum integration time of 14.5 s . The latter in turn, imposes $NSR > 3 \times 10^{-4}$, due to the photo collecting power of the considered aperture. Therefore, the measurement regime defined by NSR_{goal} and $\Delta \alpha_{goal}$ can not be reached with a 1.5 m telescope. Only an increase in \mathbb{D} , e.g. to the 4 m of the largest solar telescope to operate in the near future, can (barely) allow the acquisition of such a measurement. We have to point out that the present analysis is based on the assumption that only a single long exposure measurement is acquired, or equivalently, that many short-exposures measurements are blindly accumulated in order to reduce NSR . Other techniques, e.g. feature-tracking-based averaging, may be used to minimize spatial smearing due to the signal evolution, i.e. to obtain a better dependence of NSR vs. Δt than that given by Eq. 2.25.

⁹This means that the dominant noise source in the images is the Poissonian shot noise —with mean value $\langle N_p \rangle$ and variance $\sigma_p^2 = \langle N_p \rangle$ — associated to the photo-electrons generation in the detector.

¹⁰In the following example, we use the values of the ground spectral irradiance, with units of $\text{J s}^{-1} \text{ m}^{-2} \text{ nm}^{-1}$, reported in <http://redc.nrel.gov/solar/spectra/am1.5/astmg173/astmg173.html>

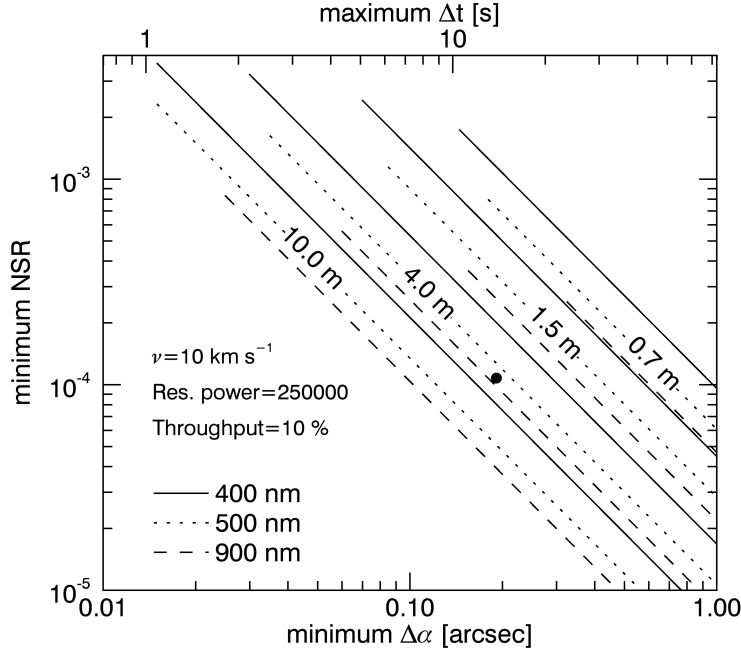


Figure 2.5. Intrinsic trade-offs in high-resolution, solar spectropolarimetry. The minimum achievable NSR imposed by solar evolution, i.e. Eq. 2.27, is plotted versus the angular resolution ($\Delta\alpha$) for four telescope apertures (numbers inside each group of three curves) and three wavelengths (different line-styles, see legend). Each curve is cut at its corresponding diffraction-limited resolution. A representative value for the goal in state-of-the-art, high-resolution, high-sensitivity, solar spectropolarimetry is also given for comparison (black circle with coordinates 1×10^{-4} and 0.2 arcsec). The assumed transversal speed of the signal on the solar surface (ν), spectral resolving power and total throughput of the system, are annotated in the plot.

2.2 Solar polarimeters

2.2.1 Measurement technique

Since optical detectors are only sensitive to the light intensity, any polarization measurement at this wavelengths requires the encoding, or modulation, of the polarization information in to intensity. This defines the two basic components of a Stokes polarimeter¹¹, namely the polarization modulator and the scientific camera (see Fig. 2.4). Moreover, it also implies that more than one intensity measurement is required to measure the polarization state of a beam.

Performing the polarization modulation involves the usage of analyzers, i.e. a device with a Mueller matrix that has a non-null diattenuation vector (\mathbf{h}). The measured intensity (\hat{I}) at the output of an analyzer, illuminated by a beam with polarization state \mathbf{S} , is given by (see Eq. 2.8 and 2.10)

$$\hat{I}(\mathbf{u}) = M_{0,0}[1, \mathbf{h}^T(\mathbf{u})]\mathbf{S}, \quad (2.28)$$

where we have made explicit that \mathbf{h} changes with respect to the independent variables of

¹¹There is a difference between Stokes polarimetry, i.e. the measurement of the \mathbf{S} of a beam, and Mueller matrix polarimetry, i.e. the measurement of the \mathbf{M} of a given material or process.

the modulation (\mathbf{u}), and so does the measured \hat{I} . To obtain an analyzer that has an output intensity sensitive to the four Stokes parameters of the input, one or many retarders (see Eq. 2.17) followed by a linear polarizer (see Eq. 2.14) need to be used, i.e. the analyzer has $\mathbf{M}_{ana} = \mathbf{M}_{ppol}(\theta_{ret})\mathbf{M}_{ret}(\theta_{ppol}, \delta)$ for the case of a single retarder. As a consequence, the basic variables that can be modified in order to change $\mathbf{h}(\mathbf{u})$, and produce the modulation, are the retardances (δ) and the position angles (θ_{ret} and θ_{ppol}).

In general, \mathbf{h} will be restricted to a finite set of discrete values, the so called *modulation states*, defined at different \mathbf{u} , i.e. $\mathbf{u} \in \{\mathbf{u}_0, \mathbf{u}_1, \dots, \mathbf{u}_{N_{mod}-1}\}$. In this case, a full polarimetric measurement requires the synchronous acquisition of N_{mod} intensity measurements, one per each modulation state, that can be collected in a vector $\hat{\mathbf{I}} = [\hat{I}_0, \hat{I}_1, \dots, \hat{I}_{N_{mod}-1}]$, given by

$$\hat{\mathbf{I}} = \mathbf{O}\mathbf{S}, \quad (2.29)$$

where the *modulation matrix* (\mathbf{O}) is

$$\mathbf{O} = \begin{bmatrix} 1 & \mathbf{h}^T(\mathbf{u}_0) \\ 1 & \mathbf{h}^T(\mathbf{u}_1) \\ \vdots & \vdots \\ 1 & \mathbf{h}^T(\mathbf{u}_{N_{mod}-1}) \end{bmatrix}, \quad (2.30)$$

and we have assumed that \mathbf{S} does not change with \mathbf{u} , and that $M_{0,0} = 1$ because its value does not affect the measured \mathbf{p} .

In order to solve the linear system given by Eq. 2.29 and retrieve the full \mathbf{S} , at least four independent measurements are needed ($N_{mod} = 4$). Such a solution can be expressed as

$$\hat{\mathbf{S}} = \mathbf{D}\hat{\mathbf{I}}, \quad (2.31)$$

where, ideally, the *demodulation matrix* (\mathbf{D}) is given by $\mathbf{D} = \mathbf{O}^{-1}$ and is exactly known. In practice this is not the case due to imperfect calibration and noise among others, that is the reason to differentiate between the measured Stokes vector, $\hat{\mathbf{S}}$, and the true \mathbf{S} .

Error propagation in Eq. 2.31, leads to the definition of the useful polarimetric efficiencies vector (ϵ); which has elements ϵ_i , that are related to the elements of \mathbf{D} , $D_{i,j}$, through (Collados 1999)

$$\epsilon_i = \frac{1}{\sqrt{N_{mod} \sum_{j=0}^{N_{mod}-1} D_{i,j}^2}} = \frac{\sigma / \sqrt{N_{mod}}}{\sigma_i}, \quad (2.32)$$

where $i \in \{0, 1, 2, 3\}$, σ is the uncertainty in the measured $\hat{\mathbf{I}}$ (assuming the same value for all its components) and σ_i is the uncertainty in the measured \hat{S}_i . Note that, the ϵ defined above quantifies how the noise obtained by simply averaging the N_{mod} measurements, $\sigma / \sqrt{N_{mod}}$, compares to the noise in the retrieved Stokes parameter, σ_i . The latter allows the comparison of the noise properties in different *modulation schemes*, i.e. systems with different N_{mod} . The total polarimetric efficiency is defined as,

$$\epsilon_{total} = \sqrt{\epsilon_1^2 + \epsilon_2^2 + \epsilon_3^2}. \quad (2.33)$$

The relevant quantities when doing solar polarimetry, are the uncertainties in the normalized Stokes parameters, these are given by

$$\sigma_{i/0}^2 = \left(-\frac{\hat{S}_i}{\hat{S}_0^2} \sigma_0 \right)^2 + \left(\frac{1}{\hat{S}_0} \sigma_i \right)^2 \approx \left(\frac{1}{\hat{S}_0} \sigma_i \right)^2, \quad (2.34)$$

where the approximation was done assuming $\hat{S}_i/\hat{S}_0 \ll 1$, as is the case for many solar targets (see Sect. 2.1.2). Replacing Eq. 2.32 in 2.34, we get that $\sigma_{i/0}$ is given by the NSR in the averaged N_{mod} elements of $\hat{\mathbf{I}}, \langle \hat{I} \rangle$, scaled by the polarimetric efficiency

$$\sigma_{i/0} \approx \frac{1}{\epsilon_i \sqrt{N_{mod}}} \frac{\sigma}{\hat{S}_0} \approx \frac{1}{\epsilon_i} \frac{\sigma / \sqrt{N_{mod}}}{\langle \hat{I} \rangle}, \quad (2.35)$$

where we have used the fact that, for the weakly polarized scene assumed, $\hat{S}_0 \approx \langle \hat{I} \rangle$.

An ideal analyzer has $|\mathbf{h}(\mathbf{u})| = 1$. Any given modulation scheme that uses ideal components would reach a maximum ϵ_{ideal} that satisfies,

$$\epsilon_{ideal,0} = 1 \quad \text{and} \quad \sqrt{\epsilon_{ideal,1}^2 + \epsilon_{ideal,2}^2 + \epsilon_{ideal,3}^2} = 1. \quad (2.36)$$

Or, equivalently, it has an associated polarimetric efficiencies matrix,

$$\mathbf{A} = \mathbf{O}^T \mathbf{O}, \quad (2.37)$$

that is diagonal, with the main diagonal equal to $N_{mod}\epsilon_{ideal}$ (del Toro Iniesta and Collados 2000). Note that, Eq. 2.36 implies that the efficiencies of an ideal and *balanced modulator*, i.e. with equal efficiencies in Stokes Q, U and V , are

$$\epsilon_{bal} = \left[1, \frac{1}{\sqrt{3}}, \frac{1}{\sqrt{3}}, \frac{1}{\sqrt{3}} \right]. \quad (2.38)$$

Ideal modulators can not be achieved in practice, because the analyzer elements are not perfect retarders and polarizers. In this case, Eq. 2.36 does not hold and matrix \mathbf{A} is not diagonal. The latter gives a general guide to design efficient modulators, namely, the more diagonal the matrix \mathbf{A} is, the closer is the system to its ideal behavior.

Finally, the definition of ϵ given in Eq. 2.32, allows responding to the question of what is the best \mathbf{D} to use in Eq. 2.31 when $N_{mod} > 4$, and thus the system given by Eq. 2.29 becomes overdetermined. If the maximization of the resulting ϵ is the driving criterion, then \mathbf{D} has to fulfill (del Toro Iniesta and Collados 2000)

$$\mathbf{D} = (\mathbf{O}^T \mathbf{O})^{-1} \mathbf{O}^T = \mathbf{A} \mathbf{O}^T. \quad (2.39)$$

Of particular interest is the fact that, computing \mathbf{D} using Eq. 2.39, is equivalent to its derivation using the singular value decomposition (SVD) method (see e.g. Press et al. 2007b, Ch. 2.6) to find the pseudo-inverse of \mathbf{O} (Collados 1999). This is because SVD minimizes the sum of the squared coefficients of \mathbf{D} and thus maximizes the ϵ .

2.2.2 Polarization modulators

Depending on which are the independent variables used to modulate the output intensity of the polarization analyzer, different instrumental concepts can be envisioned (see e.g. del Toro Iniesta 2003, Ch. 4). The list below describes the main modulation techniques employed in solar polarimeters, including the technologies used to implement them.

1. *Temporal modulation*: In this case $\mathbf{u} = t$ (see Eq. 2.28), thus the different intensity measurements are acquired at different instants of time. If the time interval between consecutive intensity measurements is $1/(f_{mod}N_{mod})$, then we call f_{mod} the *modulation frequency*. The temporal modulation can be implemented using the following devices.
 - (a) *Rotating retarder*: If the retarder of the analyzer is motorized, it can be rotated at a fixed angular speed, say ω . This produces a linear variation of the position angle of its optical axis with time, i.e. $\theta_{ret}(t) = \omega t$, and thus a temporal modulation of the analyzer diattenuation vector. Rotating retarders have been widely used in the first generations of ground-based, imaging polarimeters. However, moving parts restrict the maximum f_{mod} and, in combination with misalignments, produce image wobbling that can severely harm spatial resolution (Stenflo 1994, Ch. 13). There are, however, some techniques to reduce wobbling that had led to rotating-retarder polarimeters that can achieve high spatial resolution, e.g. Lites et al. (2013).
 - (b) *Electro-optical retarder*: These are devices with induced birefringence (see Sect. 2.1.2) that allow a controlled modification of their δ or θ_{ret} by the application of an external electric field (del Toro Iniesta 2003, Ch. 4). The most commonly used for solar polarimetry are:
 - *Piezo-elastic modulators* (PEMs, Stenflo and Povel 1985) are made of a piece of glass in which a standing acoustic wave is established, by means of an electro-acoustic transducer, at the resonance frequency (~ 50 kHz) of the glass plate. This produces a continuous temporal modulation of the δ at the same frequency, while keeping the θ_{ret} fixed. They can be used in the vacuum UV and IR (Stenflo 1994, Ch. 13). A full-Stokes, PEM-based modulator, which requires the synchronization of two PEMs, has not been achieved in practice due to frequency stability issues, see e.g. Gandorfer (1999).
 - *Nematic liquid crystals* can be confined in a thin layer between two glass plates to form a variable retarder. The application of an external voltage modifies the aspect ratio of the individual birefringent crystals (see Sect. 2.1.2) allowing for slow ($f_{mod} \approx 20$ Hz), continuous modulation of the device δ (del Toro Iniesta 2003, Ch.). Crystal-based devices whose δ can be controlled, such as nematic liquid crystals, are usually called liquid crystal variable retarders (LCVRs).
 - *Ferro-electric liquid crystals* can also be contained in thin layers to produce variable retarders. Here the external field imposed produces the re-orientation of the uniaxial birefringent crystals, which modifies θ_{ret} of the

device between two positions, that differ $\Theta \approx 45^\circ$ from each other (where Θ is called the FLC switching angle). δ is controlled by the thickness of the layer ($\sim 2 \mu\text{m}$), which can be tuned to produce a half-wave plate at a given central wavelength, λ_0 (Gandorfer 1999). Two FLCs can be used in combination with two static retarders (SRs) to efficiently modulate the full Stokes vector up to $f_{mod} \approx 1 \text{ kHz}$, in the visible portion of the spectrum (from 400 to 700 nm approximately, see Gandorfer 1999). Such a design has been adopted in many current solar polarimeters.

The wavelength dependence of δ in FLCs is considerable, and has been studied by Gisler et al. (2003). They proposed the following model for the dispersion law of birefringence, at a given temperature and expressed in fractions of λ

$$\delta(\lambda) = \left(\delta_0 \lambda_0 - \frac{C}{\lambda_0^2} \right) \frac{1}{\lambda} + \frac{C}{\lambda^3}, \quad (2.40)$$

where C is the dispersion constant and δ_0 is the retardance value at the central wavelength, λ_0 , e.g. equal to 0.5 and 0.25 for ideal half-wave and quarter-wave plates respectively.

Both δ and Θ are temperature (T) dependent in FLCs. The latter is the stronger effect and can be modeled by (Gisler et al. 2003)

$$\Theta(T) = C_{T1} \sqrt{C_{T2} - T}, \quad (2.41)$$

where C_{T1} and C_{T2} are two constants.

2. *Spatial modulation*: In this case $\mathbf{u} = x$ (see Eq. 2.28), therefore the different intensity measurements are acquired simultaneously at different positions. This type of modulators can be implemented by means of the following two devices.

- (a) *Birefringent plate*: If a block of birefringent material is cut in such a way that its optical axis forms an oblique angle with respect to an incident beam, it will produce a separation of such a beam in one ordinary and one extraordinary component (see Sect. 2.1.2). While the ordinary ray is not deviated from the incident direction, the extraordinary is refracted at an oblique angle. The latter leads to the formation of two rays at the output of the block (del Toro Iniesta 2003, Ch. 4). The two most commonly used devices are the *Savart plate*, where two birefringent plates are properly placed to separate the incoming beam into two output rays that experience the same phase lag and have parallel propagation directions; and the *Wollaston plate* where the output beams have different output angles. The polarimetric action of both devices can be modeled by two Mueller matrices, one per output ray, that correspond to two linear polarizers with orthogonal optical axes (antiparallel \mathbf{h} and \mathbf{v}). Therefore, they form spatial modulators, that can be used to illuminate different sections of a single detector simultaneously due to the small separation of the output beams. The Savart plate is used close to the detector (focal plane) while the Wollaston plate is used in collimated setups (close to a pupil).

- (b) *Polarizing beam splitter*: Discrete spatial modulation can also be achieved with a block of birefringent material, that has been cut diagonally and stuck

back using a special cement. The refractive index of the cement produces total reflexion of the ordinary beam that is deviated orthogonally from the incident direction. The extraordinary beam is refracted in the diagonal interface continuing its propagation with unaffected direction. The polarimetric action of such a beam splitter is modeled by two Mueller matrices, one for each output ray, that correspond to two linear polarizers with orthogonal optical axes (antiparallel \mathbf{h} and \mathbf{v}). The polarizing beam splitter can be used together with two detectors, or a single detector plus the appropriate optics, to record simultaneously two orthogonal polarization states.

3. *Spatio-temporal modulation*: A combination of temporal and spatial modulation is applied in the dual beam and beam exchange techniques.

- (a) *Dual beam*: In this common scheme (Lites 1987, Collados 1999), a temporal modulator is followed by a double birefringent plate or a polarizing beam splitter. Two simultaneous measurements with orthogonal polarization are acquired for every state of the temporal modulator (using either two cameras or two parts of the same sensor). After the appropriate combination of the simultaneous measurements, the SIC can be reduced provided that beam imbalances are controlled (see Sect. 2.3.2).
- (b) *Beam exchange*: Same as the dual beam, except that, an extra measurement is acquired after exchanging the beams that reach the two cameras. This reduces the effects of beam imbalances with respect to the dual beam technique (see Sect. 2.3.2). For example, Bianda et al. (1998) use a manually-rotated half-wave plate in combination with a polarizing beam splitter to implement the beam exchange. They simultaneously image Stokes $I+Q$ and $I-Q$ on different sections of a single sensor. After this first exposure, they manually rotate the retarder to switch the polarization states of the output beams and expose again. Similar implementations can be done using electro-optical retarders such as FLCs in order to increase the temporal modulation frequency.

2.2.3 Wavelength discrimination

Most of the physical phenomena that modify the polarization of light are strongly wavelength dependent (see Sect. 2.1.2). In particular, accurate measurements of solar Zeeman or scattering polarization signals, require resolving spectral features that are much narrower than the width of a single absorption or emission line, i.e. $\ll 1 \text{ \AA}$. As a consequence, the device used for wavelength discrimination along with the polarimeter (see Fig. 2.4) is of paramount importance.

There are three solutions developed to solve the fundamental problem of imaging the two spatial plus one spectral dimensions in to a bi-dimensional intensity detector. The main difference between them is what dimensions are simultaneously imaged, and which are multiplexed in time. This affects the properties of the resulting data, i.e. simultaneity, resolution, field of view (*FOV*) and spectral range. Any of the three approaches can be combined with a temporally or spatially modulated polarimeter to form a spectropolarimeter. In the former case, the simultaneity in the dimension that is time-multiplexed

is diminished, due to the time the polarimeter takes to acquire all the modulation states. For this and other reasons, some of the requirements for wavelength discriminators are generally stricter if they are used for spectropolarimetry than those used for simple spectroscopy, e.g. duty cycle. Further details on each of the three solutions, as they are implemented in solar spectropolarimeters, are given below.

1. *Spectrograph + slit based scanner*: In this case the spectral dimension, including one or more spectral lines, plus one of the spatial dimensions are simultaneously imaged on the detector. Thus the remaining spatial dimension is multiplexed in time. This is typically accomplished by first selecting an unidimensional region from the *FOV* using a slit¹². The light from the slit is then fed to a spectrograph in order to produce an image containing the spectral plus spatial information along the slit. To acquire the remaining spatial information, the slit is moved in discrete steps to scan the *FOV* (see e.g. Beck et al. 2005a and Sankarasubramanian et al. 2004 for two solar applications). Solar spectrograph-based systems are usually built using echelle diffraction gratings¹³ and have high resolving power (up to 800 000, Kentischer et al. 1998). On the other hand, the resulting data is not spatially coherent. It follows that moving or extended signals may not be properly sampled, that the resulting spatial resolution is usually worse than with the other approaches (due to the limited accuracy of the scanning system) and that each slit exposure is affected by a different realization of the atmospheric seeing (see Sect. 2.3.1). The latter greatly complicates any post-facto restoration of the acquired images (see Sect. 2.3.3).
2. *Tunable filtergraph*: Using a tunable filter, both spatial dimensions can be simultaneously imaged on the detector. In order to obtain the spectral information, the filter has to be successively re-tuned in discrete wavelength steps. Generally less than 20 points are recorded per spectral line (Kentischer et al. 1998). For that reason, the detection of spectrally complex signals is commonly done with spectrograph-based systems. On the other hand, the spatial coherence of the data acquired with a filtergraph allows a better study of moving solar signals that are spatially extended, as well as allowing the application of post-facto image restoration to improve the spatial resolution in ground-based observatories. The most common tunable filters used in high-resolution spectropolarimeters use one or multiple Fabry-Pérot etalons¹⁴ (e.g. Bello González and Kneer 2008 and Martínez Pillet et al. 2011) because they can be tuned in a short time (<1 s, Kentischer et al. 1998) and provide

¹²The slit thickness corresponds typically to the diffraction limit of the telescope.

¹³A diffraction grating is a dispersive element that features a periodic (with spacing d) distribution of N thin grooves. The achievable resolving power of the grating is given by Nm , where m is the interference order. Analogously, the angle of dispersion for a wavelength λ_0 and normal incidence, is $\arcsin(m\lambda_0/d)$. Therefore, observing at high orders is desirable, however, only a fraction of the incoming light is put in any given order. To solve this issue, and allow spectroscopy of faint sources, an *echelle* grating has specially shaped grooves that ensure that most of the incoming light is output to a given high (e.g. 1000) order (Born and Wolf 1999, Ch. 8).

¹⁴A Fabry-Pérot etalon is a resonant cavity formed by two highly parallel ($\lambda/200$) reflecting surfaces. The transmission spectrum presents periodic resonance peaks every $\Delta\lambda_{FSR}$, the so called free spectral range. The full-width at half maximum ($\Delta\lambda_{FWHM}$) is related to the reflectivity (ref) by $\Delta\lambda_{FWHM}/\Delta\lambda_{FSR} = \pi\sqrt{ref}/(1 - ref)$, i.e. the higher the ref , the better the *finesse* or separation of the transmission peaks. The location of the peaks can be changed by re-tuning the etalon, i.e. modifying the separation between the reflective surfaces using piezoelectric actuators. Errors in the cavity thickness produce random shifts of the transmission

high transmission and spectral resolution. The etalons cavity is usually filled with air or $LiNbO_3$. In order to keep a stable transmission profile, the surfaces of each etalon have to remain parallel and the refractive index in the interior of the cavity has to be constant (only relevant for $LiNbO_3$). To ensure this, each etalon is located in a sealed cell and a closed-loop system is adopted to control the surfaces separation, and allow accurate tuning (Cavallini 2006).

3. *Integral field solutions:* In this approach all the three dimensions are simultaneously imaged on a single detector at the expense of a reduced *FOV* or spectral range (given a sampling and detector size). This can be accomplished by dividing the *FOV* using many optical fibers and then feed them to one or many slit-based spectrographs, by re-imaging the *FOV* using an array of micro-lenses to shrink the pixels and then feed them to a single spectrograph, or by using an image slicer to separate the *FOV* in slices and then feed a spectrograph. The above-mentioned approaches are currently under development and have not been fully tested in solar applications (Kleint and Gandorfer 2015).

2.2.4 Scientific cameras

The intensity at the output of the polarization modulator package, after being filtered by the wavelength discriminator, is synchronously detected using a scientific digital camera (see Fig. 2.4 and Sect. 2.2.1). A scientific camera differs from other kind of cameras in its specifications, which tend to be more strict and push the state-of-the-art in design and manufacturing processes. The main goal of the camera is to reliably quantify the number of photons that hit the detector during the exposure time. To do so, the camera has two main components, namely, the image sensor and its associated front-end electronics (see Fig. 2.6). The main task of the image sensor is the generation of an analog output voltage that is a function of the number of detected photons. Meanwhile, the front-end electronics takes care of the generation of all the signals required for the sensor operation, and to process its output. This includes the supply voltages (implemented by dedicated supply circuitry), ensuring stability and noise isolation; the amplification and/or digitalization of the sensor output via analog to digital converters (ADCs); and the generation of the clocking and control signals to operate the sensor, ADCs and supply circuit. The latter is the task of the digital control electronics, which can be implemented via ASIC, FPGA, microcontroller or microprocessor-based systems. Each of these alternatives presents different pros and cons in design time, cost, flexibility and performance. The architecture presented in Fig. 2.6 is by no means strict, e.g. many components of the front-end electronics can be implemented monolithically in the sensor (specially in CMOS devices). Additionally, some cameras may require extra or fewer components to operate.

The two main sensor technologies used in digital cameras are CMOS (see e.g. Hoffman et al. 2005, Bigas et al. 2006, and references therein) and CCD (see e.g. Janesick 2001, Howell 2006, and references therein). There is a plethora of different implementations and subtypes of both CCD and CMOS, that can be found in the extensive literature

profiles across the *FOV* when the etalon is used in a telecentric setup (close to focus). The latter is not present in a collimated setup (close to a pupil), however, a radial blue shift of the transmission peaks across the *FOV* appears in this case (Feller 2007).

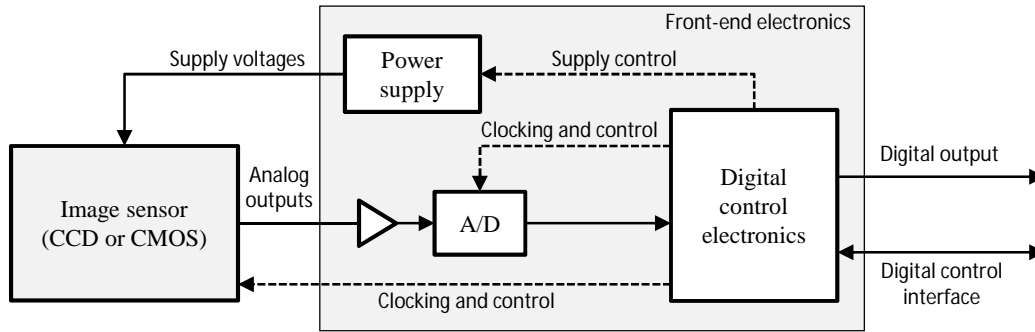


Figure 2.6. Basic architecture of a scientific camera. The two main components are the image sensor and the front end electronics which provides all the required supply and clocking signals as well as the data flow control. Adapted from Piqueras (2013).

available on these topics. Thus, the following explanation intends only to illustrate the fundamental working principles. Both types of sensors perform the same three basic steps: *charge generation* via the photoelectric effect, *charge accumulation* during the exposure time and *charge to voltage conversion* using a capacitance. The main difference between both approaches, is how and where each of this steps takes place in the detector (Fig. 2.7).

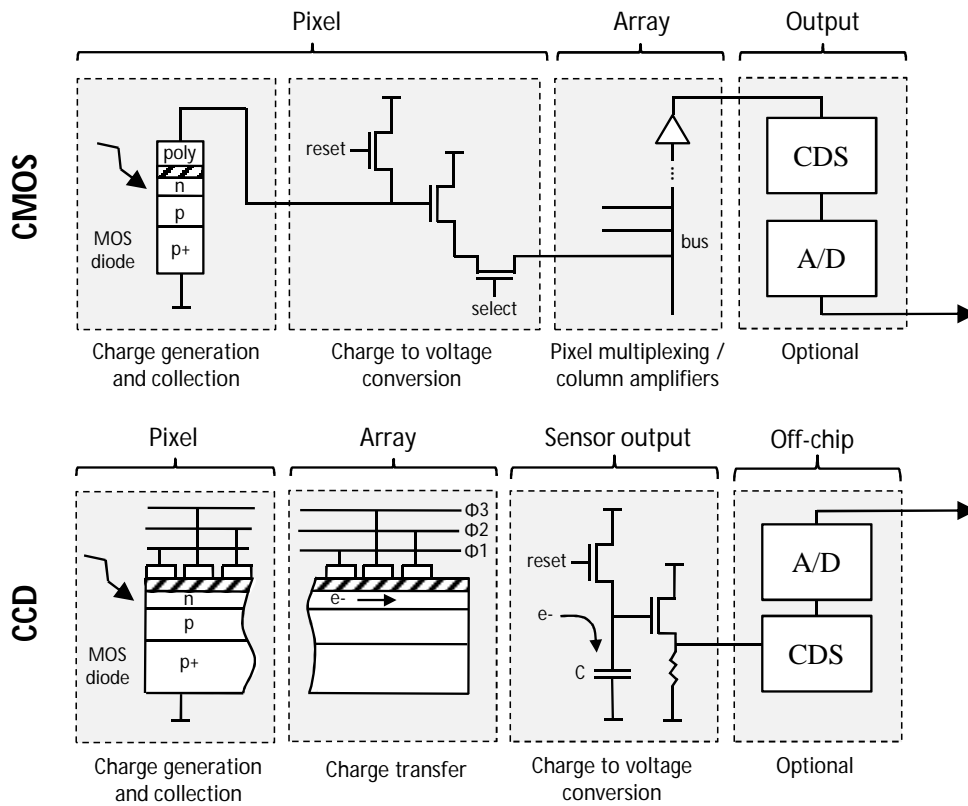


Figure 2.7. Comparison between CMOS and CCD image sensors. The two sketches show conceptual diagrams for the fundamental steps performed by the CMOS (top) and CCD (bottom) approaches. Adapted from Hoffman et al. (2005), Piqueras (2013) and Janesick (2001).

CMOS sensors perform the charge generation, collection and conversion to voltage within a single pixel. Further signal processing steps, such as amplification or multi-sampling¹⁵, can be also embedded to produce an *active pixel structure*. The voltages of the matrix are then read by multiplexing each pixel to common buffers, which are terminated in amplifiers. The detailed addressing process, number of buffers and amplifiers, depends on the specific sensor design. Further stages, used to implement CDS and to allocate the ADCs, can be optionally placed at the sensor level.

On the other hand, CCDs perform only the charge generation and accumulation steps on the pixel level. As a consequence, the charges need to be transferred row-wise, using the shift-register structure of the sensor, after every exposure. At the end of the columns, the charges are typically loaded in a transversal register that shifts them towards the readout node —where the charge to voltage conversion and amplification occur— one pixel at a time. Multiple transversal registers and/or output channels are also commonly used to increase the readout speed.

Before performing any comparison between the performances of the CCD and CMOS technologies; let us collect and define in Table 2.1, the camera characteristics and performance specifications that will be used during the rest of this thesis.

The spectral range of the *QE* in CCDs is mostly limited to that of silicon¹⁶, i.e. typically from 300 to 1100 nm plus the x-rays, provided that proper anti-reflective coatings are applied. CMOS devices can have an extended working range due to the possibility of using a non-silicon layer as photosensitive material, connected —usually using iridium or indium bumps— to a silicon layer where the readout integrated circuitry of each pixel is located. Such an *hybrid* CMOS can be sensitive up to 10 μm (Hoffman et al. 2005).

If the sensor is *front illuminated*, the gate structure, electrodes and other circuitry (in CMOS) present there, reduce the *FF*. The spectral response is also limited in this case, mainly because short wavelengths (<400 nm) are strongly absorbed and reflected by the poly-silicon gate structure (Janesick 2001, Sect 1.2.2.1). To increase the UV response, the gate can be coated with a phosphor (that re-radiates at longer wavelengths) or a *back illuminated* sensor can be employed. The latter option is very efficient because in addition a 100 % *FF* can be reached. However, back illumination requires thinning the sensor substrate (to allow the photons reaching the collecting area near the gate) and a more complicated manufacturing process (Janesick 2001, Sect. 1.1.2).

The literature is full of good comparisons between the properties of CMOS and CCD technologies, e.g. Janesick et al. (2006, 2007), Magnan (2003). Some of the most important differences between the two technologies are summarized in Table 2.2. We have highlighted using italics the sensor properties that are more relevant to ground-based solar polarimetry. These will be discussed in detail in the following chapters, particularly

¹⁵ Fixed pattern noise (FPN) —mostly due to dark current non-uniformity (*DCNU*, see Table 2.1)— is one of the main disadvantages in CMOS devices; because of the manufacturing-induced differences in the circuitry of each pixel. An effective way to reduce FPN and reset noise (due to the *kTC* noise of the sense capacitance and reset pulse feed-through) in CMOS and CCD sensors, is sampling the pixel signal multiple times during the readout. One of the simplest way to do the latter is correlated double sampling (CDS), here the sensing node is sampled twice. A first time after the reset and the second time after the exposure is finished. The two samples are then subtracted to eliminate low frequency noise and any offset, producing essentially a band-pass effect (Hoffman et al. 2005, Janesick 2001).

¹⁶Some CCDs have been produced using *Germanium*, they have an extended spectral response up to 1.6 μm . However, they present other issues like large dark currents (Janesick 2001, Sect. 1.2.2.1).

2 Background

Parameter	Symbol	Unit	Definition and responsible components or processes
Sensor area	$N_{col} \times N_{row}$	pixel ²	The sensor area and aspect ratio are defined during the design stage.
Pixel area	A_{pixel}	μm ²	The total area occupied by each pixel is defined during the design stage.
Frame rate	FR	fps ; Hz	Number of frames that can be read out per second. It is influenced by the readout electronics, ADCs and the charge transfer speed (in CCDs).
Duty cycle	DC	%	Equal to the product of the frame rate and the exposure time. It is affected by the readout electronics and shutter strategy.
ADC resolution	N_{adc}	bit	Length of the ADC word.
Sensitivity	$QE \times FF$	%	The filling factor (FF , ratio of the photosensitive to the total area of the pixel) is mainly influenced by the designs of the pixel (gate size, extra circuitry, etc.) and sensor (back or front illuminated, routing, etc.). The QE (fraction of incident photons that produce photo-electrons) is given by the photosensitive material and anti-reflective coating among others.
Non-linearity	NL	%	Quantifies how much the sensor output deviates from a linear function of the exposure time. Mainly influenced by the pixel structure and readout electronics.
Full well charge	FWC	e^-	The amount of electrons that can be collected by a pixel before it saturates, i.e. its output does not increase with an increase of the exposure time. It is determined by the pixel and sensor structure as well as the readout electronics.
Conversion gain	G	DN / e^-	Number of digital counts produced per each photo-electron. Mostly given by the sensing node capacity, readout electronics and ADCs. Generally configurable.
Dark current	i_d	$e^- s^{-1}$	Flux of thermal charges created in the sensor. The sensor temperature, pixel size and material strongly influence its value.
Dark current non-uniformity	$DCNU$	%	Pixel to pixel variations of the i_d after calibration. Mainly given by the manufacturing tolerances and readout circuitry. It is an additive noise source.
Photon response non-uniformity	$PRNU$	%	Pixel to pixel variations of the photon response (G , QE , etc.) after calibration (multiplicative noise). Given by the manufacturing tolerances and readout circuitry.
Read out noise rms value	σ_{ro}	e^- rms	Noise in a zero-exposure frame. Given mostly by the readout circuitry.
Quantization noise rms value	σ_{adc}	e^- rms	Quantization plus other noise sources introduced by the ADCs. It is an important contributor to σ_{ro} . Given by N_{adc} and the ADCs circuitry.
Dark noise rms value	σ_d	e^- rms	Poissonian noise produced by i_d .

Table 2.1. Basic camera characteristics and performance specifications. The last column gives a short definition and a summary of the main responsible components or processes for each feature. See e.g. Janesick (2001) for more detailed definitions.

in Sect. 3.1.1 and Ch. 5. Note that, CCDs tend to perform typically better in the sensor properties that are determinant for low-light scientific imaging (such as high-resolution, solar spectropolarimetry).

Property	CCD	CMOS
<i>Noise</i> ⁽¹⁾	Typically lower due to the low dark current and readout noise.	Higher, e.g. the quality of the readout circuits in each pixel produce higher FPN and reset noise.
<i>Linearity</i>	Better.	Worse, due to the signal dependence of the readout circuit gain.
<i>Sensitivity</i>	Higher	Lower.
<i>Shutter</i>	Mechanical or electronic snapshot (frame transfer or interline).	Electronic snapshot or rolling shutter.
Cost	Higher	Lower. Benefits from computer CMOS industry.
Mass/size	Higher.	Lower. Monolithic integration of much of the front-end electronics is possible.
Power consumption	Higher. Needs many, relatively high voltages for charge transferring.	Lower. Only a single CMOS voltage is required.
Radiation tolerance	Lower due to the creation of charge traps.	Higher because no charge transfer is needed.
Heritage	Long heritage (since 1975) specially in the scientific community.	Serious competitors since the 90's. Very strong growth in recent years due to the push of massive commercial applications.
Misc.	No built-in signal processing. May suffer from smearing, pixel blooming and charge transfer inefficiency.	Only a single clock is needed. Random or selective readout is possible.

¹ The root mean squared (rms) value of the total camera noise, σ_{cam} , is equal to $\sqrt{\sigma_{ro}^2 + \sigma_d^2}$.

Table 2.2. Comparison of the main properties of CMOS and CCD sensors. The properties highlighted in *italic* are more critical for ground-based solar polarimetry.

The CMOS architecture has in principle many advantages with respect to the CCD approach, e.g. built-in signal processing capabilities. However, CCDs have been superior in overall still image quality, and thus the preferred option in many scientific applications, since their first astronomical usages in the mid 70's. Up to recently, the noise, sensitivity and dynamic range of state-of-the-art scientific CCDs, could not be simultaneously achieved by CMOS sensors (Bigas et al. 2006). This is mainly due to the quality and

size of the readout circuits that the CMOS manufacturing process can achieve within the reduced space of a single pixel. Regardless of this, CMOS sensors have made their way (since the early 90's) into many commercial and scientific applications that benefit from its advantages; most notably low power consumption and radiation tolerance (of particular importance in space-based imaging systems, see e.g. Piqueras 2013).

In the last decade, the synergy between the manufacturing processes of CMOS sensors and other massive commercial industries (personal computers, mobile devices, etc.) have produced enormous improvements in some sensor parameters that are critical for scientific applications (sensitivity and noise). Sometimes reaching and surpassing the most demanding CCD benchmarks (Janesick et al. 2013). Nowadays the performance difference between the two technologies is narrow and is getting narrower every year. The huge variety of sensors design, configurations and performances; make any weighing between the CCD and CMOS solutions strongly dependent on the application, manufacturer availability and budget, even within the scientific imaging sector.

2.3 Polarimetric effects of atmospheric seeing and image motion

The location of the solar observatory strongly influences the properties of the resulting spectropolarimetric data. Space-based observatories can, among others, detect portions of the spectrum absorbed by Earth's atmosphere (such as the UV regime); observe the Sun 24 hours uninterruptedly (in some cases); and avoid the image aberrations introduced by atmospheric seeing. On the other hand, they suffer from serious disadvantages including high monetary cost, lack of flexibility to upgrade or repair the instruments, and usually do not contain state-of-the-art technology by the time of launch (Kleint and Gandorfer 2015).

A particularly important difference between ground and space-based observatories, is the available aperture size. As discussed in Sect. 2.1.4, the collecting power of the telescope presents a fundamental limitation to the simultaneous angular resolution and SNR that can be achieved when imaging a dynamic solar signal (see Fig. 2.5). In this respect, the larger apertures of ground-based telescopes (currently 1.6 m versus the 0.5 m in space) provide them with an advantage position. Such a difference will be even more prominent in the near future, when the 4 m DKIST telescope under construction in Hawaii (e.g. Elmore et al. 2014) sees first light. In order to fully exploit the high SNR and spatial resolution achievable by such large apertures, new instrumental techniques—that further reduce the image aberrations and polarimetric effects introduced by atmospheric seeing—are required.

2.3.1 Description of atmospheric seeing and image motion

If an initially plane monochromatic wave propagates downwards through an atmospheric layer of thickness Δh , located at an altitude h_0 , it will experience a complex disturbance (U)—i.e. each component of the incoming \mathbf{E} is multiplied by U^{17} —given by (e.g. Saha

¹⁷Note that, the seeing disturbance do not contemplate variations of the amplitude. For polarimetry this is not an issue because (a) the air attenuation is small, (b) the portion of the sky covered by the FOV is small

2007, Sect. 5.3.1)

$$U(\mathbf{r}, t) = e^{i\delta(\mathbf{r}, t)}, \quad (2.42)$$

were the phase shifts (δ) are

$$\delta(\mathbf{r}, t) = \frac{2\pi}{\lambda} \int_{h_0}^{h_0+\Delta h} n(\mathbf{r}, t, h) dh, \quad (2.43)$$

n denotes the refractive index, t the time and \mathbf{r} the bi-dimensional position vector on the plane of the considered layer. The random fluctuations of n induce the same kind of variations in δ , which in turn aberrates (deforms) the wavefront that would reach any ground-based telescope. The consequent reduction in image quality is called *seeing* (see e.g. Saha 2007, Ch. 5).

The detailed process of image degradation by seeing is complicated and its description out of the scope of this thesis. However, two aspects are critical to ground-based polarimetry and in particular to the FSP project. Firstly, the instrumental requirements needed to reduce seeing induced spurious signals (see Sect. 3.1), are based on the temporal behavior of δ . Secondly, many image restoration techniques, such as the MOMFBD (see Sect 2.3.3), are based on a linear shift invariant model of the seeing degradation. Because of these, we only describe below some basic concepts necessary to understand how seeing is characterized, and what are the limitations and properties of the image degradation model.

The random spatial and temporal fluctuations of n , are produced by the inhomogeneities of the temperature (dominant effect in solar observations), pressure and humidity of the gases that compose the atmosphere. The source of the inhomogeneities are convection cells, wind shear and other hydrodynamic instabilities. The spatial dimensions of the fluctuations span a wide range, from the outer scale of the turbulence (tens of meters) to its inner scale (in the mm or cm level). The energy is transported towards the small scales, by the successive breaking of larger structures into smaller eddies. This scale-invariant process can be quantitatively described using the *Kolmogorov turbulence theory*.

Roddier (1981), based on the works of (Tatarski 1961) and others, combined the Kolmogorov theory with a plane-parallel atmosphere, composed of many independent thin layers, to derive the spatial correlational properties of U at the telescope aperture. The latter can be conveniently specified using the spatial coherence function of U , expressed in terms of the *Fried parameter* (r_0 , Fried 1966), as follows (e.g. Saha 2007, Sect. 5.4.2)

$$\langle U(\mathbf{r}_0)U^*(\mathbf{r}_0 + \mathbf{r}) \rangle = e^{-3.44(|\mathbf{r}|/r_0)^{5/3}}, \quad (2.44)$$

where $*$ denotes the complex conjugate. The r_0 , a.k.a coherence length, is a measure of the seeing quality and scales as

$$r_0 \propto \lambda^{6/5}. \quad (2.45)$$

Equation 2.44 can be used to derive the spatial power spectrum of δ , \mathcal{D} , due to Kolmogorov turbulence,

$$\mathcal{D}(\mathbf{k}) = 0.023r_0^{-5/3} |\mathbf{k}|^{-11/3}, \quad (2.46)$$

resulting in negligible spatial variations of the attenuation and (c) a fast variation of such a flat attenuation would only produce a modification in the polarimetric offset (thus not affecting the signal value relative to the continuum).

where \mathbf{k} is the spatial frequencies vector.

The temporal behavior of δ , due to the contribution of many dynamic atmospheric layers, is difficult to derive. A common approach due to Taylor (1938), is to consider a single phase screen (with spatial properties given by Eq. 2.46), that is frozen and moves at the local wind speed v . Then, the temporal statistics of the resulting δ at the ground, are governed by the seeing coherence time (τ_0), which relates to r_0 through

$$\tau_0 \approx \frac{r_0}{v} \propto \lambda^{6/5}. \quad (2.47)$$

The total imaging action of the seeing, can be reasonably modeled by a stochastic, linear-space-invariant system. The space invariance only holds if the *FOV* is smaller than the seeing *isoplanatic patch*, i.e. the circular area of the sky enclosed by the seeing isoplanatic angle (ϕ_0). The ϕ_0 relates to r_0 according to (e.g Saha 2007, Sect. 5.4.4)

$$\phi_0 \propto \frac{r_0}{h_0} \propto \lambda^{6/5}, \quad (2.48)$$

where h_0 is the mean effective height of the turbulence layer. As a consequence, we can write the image degradation process due to the action of both seeing and the telescope, in the spatial Fourier domain, as follows

$$\mathcal{I}(\mathbf{k}, t) = \mathcal{H}_{atm+tel}(\mathbf{k}, t) \mathcal{I}_\odot(\mathbf{k}), \quad (2.49)$$

where $\mathcal{H}_{atm+tel}(\mathbf{k}, t)$ is the instantaneous optical transfer function (OTF) of the seeing plus telescope¹⁸, and $\mathcal{I}(\mathbf{k}, t)$ and $\mathcal{I}_\odot(\mathbf{k})$ are the spatial Fourier transform of Stokes I (images) at the focus of the telescope and the Sun, respectively (refer to Fig 2.4). Note that the solar scene is assumed to be constant for the present analysis.

The above-introduced statistical properties of the seeing, translate in to properties of $\mathcal{H}_{atm+tel}(\mathbf{k}, t)$. According to the observing regime —defined by the telescope aperture (\mathbb{D}) and the exposure time (t_e)— we can distinguish the following cases (all assuming a *FOV* smaller than the isoplanatic patch, and a quasi-monochromatic observation):

1. $\mathbb{D} \ll r_0$: By definition, r_0 is equivalent to the maximum diameter of a circular aperture that would be able to operate at the diffraction limit¹⁹. Therefore, the achievable spatial resolution in this case, *is not limited by the seeing* but by the diffraction limit of the telescope, namely $1.22\lambda/\mathbb{D}$ approximately. Typical values of r_0 , for day time seeing in astronomical sites at $\lambda = 500$ nm, can be in the order of 5 cm for very bad conditions and 30 cm for excellent conditions.
2. $\mathbb{D} \gg r_0$ and $t_e \gg \tau_0$: In this *long exposure regime*, the measured image (degraded both by blurring and image motion) can be obtained by computing the average over many independent seeing realizations in Eq. 2.49 (e.g. Saha 2007, Sect. 5.4.1), i.e.

$$\langle \mathcal{I}(\mathbf{k}, t) \rangle = \langle \mathcal{H}_{atm+tel}(\mathbf{k}, t) \rangle \mathcal{I}_\odot(\mathbf{k}). \quad (2.50)$$

¹⁸In the rest of this section we assume no AO is present in the beam

¹⁹More precisely, the rms error of the wavefront, in a circular area of diameter r_0 at the ground, is approximately 1 rad or $\lambda/6$.

Roddier (1981) showed that

$$\langle \mathcal{H}_{atm+tel}(\mathbf{k}, t) \rangle = \mathcal{H}_{atmle}(\mathbf{k}) \mathcal{H}_{tel}(\mathbf{k}), \quad (2.51)$$

were $\mathcal{H}_{atmle}(\mathbf{k})$ is the long-exposure OTF of the seeing and $\mathcal{H}_{tel}(\mathbf{k})$ the (constant) telescope OTF. Moreover, he proved that $\mathcal{H}_{atmle}(\mathbf{k})$ reduces to a Gaussian OTF given by the Fourier transform of the complex disturbance coherence function (Eq. 2.44). Thus, the width of $\mathcal{H}_{atmle}(\mathbf{k})$ only depends on the overall seeing conditions, r_0 . Since $\mathbb{D} \gg r_0$, the maximum achievable spatial resolution is *seeing-limited* to $1.22\lambda/r_0$ approximately²⁰, i.e. $\langle \mathcal{H}_{atm+tel}(\mathbf{k}, t) \rangle \rightarrow \mathcal{H}_{atmle}(\mathbf{k})$. Note that if $\mathbb{D} \ll r_0$, as in the first case, then $\langle \mathcal{H}_{atm+tel}(\mathbf{k}, t) \rangle \rightarrow \mathcal{H}_{tel}(\mathbf{k})$.

3. $\mathbb{D} \gg r_0$ and $t_e \ll \tau_0$: In this *short exposure regime*, image motion does not contribute to the seeing-induced aberrations. The remaining degradation is usually called image blurring. The measured image can be computed using a single realization of $\mathcal{H}_{atm+tel}(\mathbf{k}, t)$ in Eq. 2.49 (*frozen seeing condition*). Since $\mathcal{H}_{atm+tel}(\mathbf{k}, t)$ is random, the seeing effect is studied on the energy spectral density of the measured image, i.e. (Roddier 1981)

$$\langle |I(\mathbf{k}, t)|^2 \rangle = \langle |\mathcal{H}_{atm+tel}(\mathbf{k}, t)|^2 |I_\odot(\mathbf{k})|^2 \rangle. \quad (2.52)$$

Different from the long-exposure case, the short-exposure $\langle |\mathcal{H}_{atm+tel}(\mathbf{k}, t)|^2 \rangle$ has no simple analytical expression. This was studied by Korff (1973), who proved that $\langle |\mathcal{H}_{atm+tel}(\mathbf{k}, t)|^2 \rangle$ has an asymptotic behavior that extends to the high-frequencies *up to the diffraction limit* of $\mathcal{H}_{tel}(\mathbf{k})$. The latter, i.e. that seeing-aberrated, short-exposure images retain the spatial information up to the diffraction limit, is the base of the post-facto image restoration techniques. Korff (1973) also found that the low-frequency part of $\langle |\mathcal{H}_{atm+tel}(\mathbf{k}, t)|^2 \rangle$ corresponds to the long exposure $\langle \mathcal{H}_{atm+tel}(\mathbf{k}, t) \rangle$ when an image motion compensator is used. Thus, image motion is the main responsible of the contrast reduction in the low spatial frequencies of long-exposure images. Moreover, the variance of the wavefront errors in radians squared, reduces from $1.03 (\mathbb{D}/r_0)^{5/3}$ to $0.134 (\mathbb{D}/r_0)^{5/3}$ after complete tip-tilt correction (Judge et al. 2004).

As explained above, the ratio t_e/τ_0 is critical to the spatial resolution that large telescopes (>50 cm) can reach in the presence of seeing. It is also critical to the level of spurious polarization signals introduced by the seeing (see Sect 2.3.2). Typically, τ_0 for day-time seeing is 10 to 50 ms (Löfdahl et al. 2007). Unfortunately, modern solar spectropolarimetry requires SNR values that can not be achieved with $t_e \ll 50$ ms, in any of the currently available solar telescopes. Note that the latter imposes a trade-off between SNR and spatial resolution that is in general more strict than the one imposed by the mere evolution of the solar signal, i.e. Eq 2.27 (see also Fig. 2.5). To work with longer t_e and preserve the spatial resolution, either the seeing-induced aberrations have to be compensated before the long-exposure image is acquired (path adopted by the AO community); or many short-exposure images has to be acquired and the seeing-induced aberrations removed post-facto before accumulating them (path adopted by the numeric image restoration community).

²⁰This is the reason to define the image degradation as the ratio \mathbb{D}/r_0 .

The temporal behavior of the seeing aberrations can be studied by decomposing the aberrated wavefront, using a set of orthogonal base functions called the Zernike polynomials (Rodier 1999). With each Zernike term corresponding to a different optical aberration, the temporal properties of the seeing are quantified by the temporal power spectrum of the different Zernike coefficients (Noll 1976, Hogge and Butts 1976).

The Zernike coefficients corresponding to the wavefront tilts, i.e. image motion at the focal plane, strongly contribute to the image degradation and the polarimetric spurious signals (see case 3 above). The temporal power spectrum of image motion, has been theoretically approximated (Noll 1976) and presents a decrease with the temporal frequency (f), that is $\propto f^{-2/3}$ and $\propto f^{-11/3}$ for low and high frequencies respectively (see e.g. Saha 2007, Sect. 5.5.3). The cutoff or separation between low and high frequencies is²¹ $\propto v/D$ because it determines the time a given low-altitude phase screen takes to cross the aperture. The power spectrum of image motion has been *measured* in solar observations, generally from the error signal of an image stabilization system (e.g. von der Luhe 1988, Acton et al. 1992, Lites 1987). As an example, Fig. 2.8 shows the results reported in Figure 1 of Judge et al. (2004), which include the effect of using an AO system to correct the tip-tilt terms.

Instrumental image motion (a.k.a image jitter) has the same effects on image resolution and polarimetry as seeing-induced image motion. However, due to its fundamentally different source, image jitter does not follow a Kolmogorov-based temporal power spectrum. In particular, some electro-mechanical components, e.g. active mirrors of the telescope pointing system, may introduce resonances in the power spectrum (see the spikes in Fig. 2.8) that can harm the polarimetric accuracy (see Sect 6.3).

2.3.2 Polarimetric effects in the different modulation schemes

Since polarimetry is based on differential intensity measurements, atmospheric seeing produces not only a reduction of the spatial resolution in the Stokes images, but also creates spurious signals. Such signals are usually called seeing induced crosstalk (SIC), because the combination of the seeing aberrations plus the polarimetric measurement system, produce a crosstalk between the measured Stokes parameters (e.g. Lites 1987). The amplitude of the SIC depends on the seeing conditions and the properties of the modulation technique employed in the polarimeter, among others.

Let us exemplify SIC by assuming that a temporally-modulated polarimeter, which has $1/(N_{mod}f_{mod}) \approx \tau_0$, is used to acquire a full-stokes measurement. In addition, we neglect any polarization effect introduced by the telescope and the atmosphere, and assume the true solar scene does not evolve withing the modulation period ($1/f_{mod}$). Each modulation state of such a *mid-speed polarimeter*, experiences approximately a single (or the average of only few) realizations of $\mathcal{H}_{atm+tel}(\mathbf{k}, t)$. Using Eq. 2.49 and 2.29; and dropping the position and time variables; we can write the intensity measured in modulation state number $i \in \{0, 1, \dots, N_{mod} - 1\}$ as follows

$$\hat{I}_i = \sum_{j=0}^3 O_{i,j}(H_{atm+tel}^i \star S_{\odot,j}), \quad (2.53)$$

²¹It is also strongly dependent on the seeing outer scale.

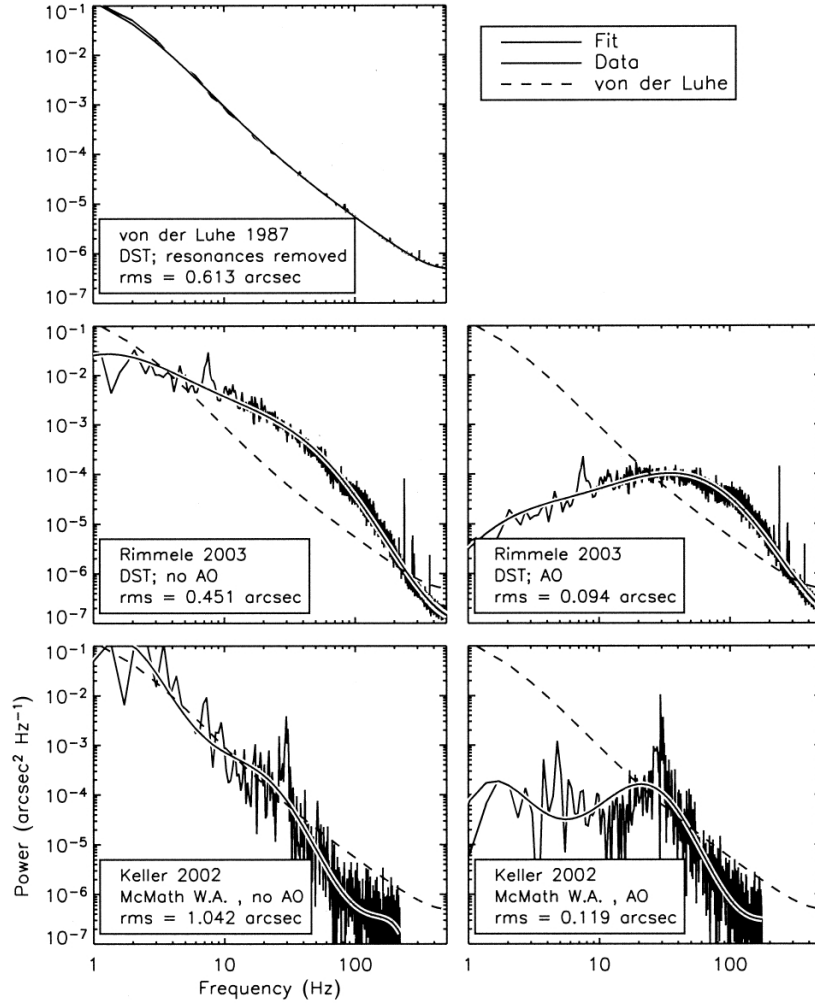


Figure 2.8. Measured power spectrum of seeing-induced image motion given in Fig. 1 of Judge et al. (2004). Each panel shows a different measured spectrum (noisy continuous), a fit (smooth continuous) and the data from the top left panel (dashed). The data were acquired either at the Dunn Solar Telescope (DST) or at the McMath-Pierce west auxiliary telescope (WA, see the insets). The panels on the left and right columns correspond to measurements without and with an AO system in the beam respectively. The action of the AO system strongly reduces the power at frequencies below ~ 30 Hz, but does not substantially modify the higher frequency components. The sharp peaks correspond to instrumental jitter due to resonances in the telescopes pointing systems, among others. The author of each measurement is identified in the corresponding inset. Copyrights Optical Society of America 2004.

where $H_{atm+tel}^i$ denote the point spread function (PSF) present during modulation state number i , \star the convolution operation, and the quantities \hat{I} , O and S_{\odot} represent bi-dimensional images. Note that, the product between images is defined to be element to element and not the matrix product.

Assuming a spatially flat O across the FOV , we can re-write Eq. 2.53 as

$$\hat{I}_i = H_{atm+tel}^i \star \sum_{j=0}^3 O_{i,j} S_{\odot,j}, \quad (2.54)$$

where the sum corresponds to the measured intensity in the absence of seeing. Demod-

ulating Eq. 2.54 using Eq. 2.31, and assuming a flat \mathbf{D} across the FOV , we obtain the following measured Stokes vector elements

$$\hat{S}_{mid,k} = \sum_{i=0}^{N_{mod}-1} \left(H_{atm+tel}^i \star \sum_{j=0}^3 D_{k,i} O_{i,j} S_{\odot,j} \right), \quad (2.55)$$

were $k \in \{0, 1, 2, 3\}$.

If the polarimeter used is a *fast polarimeter*, i.e. with $1/f_{mod} \ll \tau_0$, then we can assume the $H_{atm+tel}^i$ are the same for all the N_{mod} modulation states, i.e. $H_{atm+tel}^i = H_{atm+tel}^0$. In this case, the measurement corresponds just to the aberrated version of the true $S_{\odot,k}$, i.e. from Eq. 2.55

$$\hat{S}_{fast,k} = H_{atm+tel}^0 \star \sum_{i=0}^{N_{mod}-1} \sum_{j=0}^3 D_{k,i} O_{i,j} S_{\odot,j} = H_{atm+tel}^0 \star S_{\odot,k}. \quad (2.56)$$

Note that, generally both $\hat{S}_{mid,k}$ and $\hat{S}_{fast,k}$ differ in a given spatial position from $S_{\odot,k}$. Nonetheless, the nature of the errors is very different. $\hat{S}_{fast,k}$ results from the linear filtering of $S_{\odot,k}$ and thus, it cannot contain spatial frequency components that are not present in the original solar scene. The latter is not true for $\hat{S}_{mid,k}$. For example, consider the simple case of a solar scene with a spatially-non-flat Stokes I and a flat polarization vector —as the one detected in non-magnetic solar spectral lines— here $\mathbf{S}_{\odot}(\mathbf{r}) = S_{\odot,0}(\mathbf{r})[1, \kappa_1, \kappa_2, \kappa_3]^T$ were κ_1 , κ_2 and κ_3 are constants $\in \mathbb{R}$. The measured polarization vector, using a fast polarimeter, is in this case flat and equals to the solar value, i.e.

$$\frac{\hat{S}_{fast,k}}{\hat{S}_{fast,0}} = \frac{H_{atm+tel}^0 \star \kappa_k S_{\odot,0}}{H_{atm+tel}^0 \star S_{\odot,0}} = \kappa_k, \quad (2.57)$$

On the other hand, the $\hat{S}_{mid,k}/\hat{S}_{mid,0}$ are non-flat and contain spurious polarization signals. The latter are introduced because $S_{\odot,0}$ is also non-flat, i.e. there is *crosstalk* from Stokes I to \mathbf{p} .

Another modulation regime that we can consider is the one reached by a *slow polarimeter*, i.e. one with $1/(N_{mod}f_{mod}) \gg \tau_0$. In this case, each modulation state would experience a long-exposure PSF, which would tend to be all similar given constant seeing conditions (see case 2 in Sect 2.3.1). As a consequence, the resulting SIC reduces with respect to the mid-speed case. However, this gain comes at the expense of a strong reduction in spatial resolution.

The SIC reduction by the usage of a *dual beam system*, as well as the effect of beam imbalances, can be easily understood using the examples given in Collados (1999). Let us denote the two simultaneous intensity measurements obtained with a dual-beam system —e.g. one formed by an ideal circular polarization analyzer, a polarizing beam splitter and two independent cameras denoted up (u) and down (d)— as follows

$$\hat{I}_u(t_0) = g(I_{\odot} + \Delta I_{atm}) + g(V_{\odot} + \Delta V_{atm}), \quad (2.58)$$

$$\hat{I}_d(t_0) = (g + \Delta g)(I_{\odot} + \Delta I_{atm}) - (g + \Delta g)(V_{\odot} + \Delta V_{atm}), \quad (2.59)$$

were ΔI_{atm} and ΔV_{atm} represent the seeing-induced errors in a particular spatial location, and Δg is the uncertainty in the gain table determination after a flat fielding procedure.

The measured Stokes \hat{I} and \hat{V} are then,

$$\hat{I}_{dbeam} = \hat{I}_u(t_0) + \hat{I}_d(t_0) = (2g + \Delta g)(I_\odot + \Delta I_{atm}) - \Delta g(V_\odot + \Delta V_{atm}), \quad (2.60)$$

$$\hat{V}_{dbeam} = \hat{I}_u(t_0) - \hat{I}_d(t_0) = (2g + \Delta g)(V_\odot + \Delta V_{atm}) - \Delta g(I_\odot + \Delta I_{atm}). \quad (2.61)$$

If the dual beam system is *perfectly balanced*, i.e. $\Delta g = 0$, the crosstalks $I \leftrightarrow V$ disappear (last terms in Eq. 2.60 and 2.61) and the measured Stokes parameters are just the aberrated versions of the true values. On the other hand, given that typically $V_\odot \ll I_\odot$ (see Sect. 2.1.2), even a small Δg can severely diminish the polarimetric accuracy (see e.g. Stenflo and Povel 1985, Keller et al. 1994). In particular, since the last term on the right side of Eq. 2.60 can be neglected, the crosstalk introduced in $\hat{V}_{dbeam}/\hat{I}_{dbeam}$ is $\Delta g/(2g + \Delta g)$ which can easily be $>0.1\%$ for large sensors. In the above-presented analysis, we have neglected beam imbalances due to the wrong registration (co-alignment) of the beams on the sensors. The latter represent a strong limiting factor of the polarimetric accuracy in dual beam systems, particularly in the presence of strong spatial gradients of the signals (Lites 1987).

The last modulation scheme to analyze is the *beam exchange*. Assuming the same dual beam system that was used to acquire the measurements given in Eq. 2.58 and 2.59, is now used to take two extra measurements but exchanging the beams of the two detectors, we get

$$\hat{I}_u(t_1) = g(I_\odot + \Delta I'_{atm}) - g(V_\odot + \Delta V'_{atm}), \quad (2.62)$$

$$\hat{I}_d(t_1) = (g + \Delta g)(I_\odot + \Delta I'_{atm}) + (g + \Delta g)(V_\odot + \Delta V'_{atm}), \quad (2.63)$$

where we have assumed that both gains have not changed from $t_0 \rightarrow t_1$ and denoted with primes the new values of the seeing induced signals. The measured Stokes signals can now be obtained by the following combination of the four intensity measurements,

$$\hat{I}_{beamex} = \hat{I}_u(t_0) + \hat{I}_d(t_0) + \hat{I}_u(t_1) + \hat{I}_d(t_1), \quad (2.64)$$

$$\hat{V}_{beamex} = \hat{I}_u(t_0) - \hat{I}_d(t_0) - \hat{I}_u(t_1) + \hat{I}_d(t_1), \quad (2.65)$$

that result in

$$\hat{I}_{beamex} = (2g + \Delta g)(I_\odot + \Delta I_{atm} + \Delta I'_{atm}) + \Delta g(\Delta V_{atm} - \Delta V'_{atm}), \quad (2.66)$$

$$\hat{V}_{beamex} = (2g + \Delta g)(V_\odot + \Delta V_{atm} + \Delta V'_{atm}) + \Delta g(\Delta I'_{atm} - \Delta I_{atm}). \quad (2.67)$$

The crosstalk terms in Eq. 2.66 and 2.67 are now only dependent on the small seeing-induced signals. In particular, the error introduced by the last term of Eq. 2.67, can be kept lower than in the dual beam case, i.e. $\Delta g(\Delta I'_{atm} - \Delta I_{atm})/\hat{I}_{beamex} < 0.1\%$.

A detailed quantitative study of the SIC, when using a rotating wave-plate as modulator, was introduced by Lites (1987). He developed a formalism to include only the effects of image motion by assuming the change in the true Stokes vector, due to seeing, is given by the gradient in the true Stokes I times the image displacement. This allows the computation of the crosstalk values among all the Stokes parameters, using the measured power spectrum of seeing-induced image motion. Lites (1987) considered both single and dual beam setups, and obtained the fundamental results exemplified above, namely

- The SIC increases linearly with the rms image motion.

- The rms SIC reduces with increasing f_{mod} following roughly $1/f_{mod}$.
- The dual beam system strongly reduces the $I \rightarrow Q, U, V$ crosstalk, but does not substantially lessen the other components.
- Any imbalance in the dual beam system produces strong $I \rightarrow Q, U, V$ crosstalk.

Using the same basic formalism, Judge et al. (2004) extended the work by Lites (1987) to include FLCs and LCVRs-based modulators, and the effects of only image motion compensation by an AO system. They computed the rms SIC for the different modulation technologies, including dual-beam setups, and using different measured power spectra of image motion (with and without tip-tilt correction, see Fig. 2.8). Their main result is the quantitative confirmation that the SIC becomes irrelevant when $f_{mod} > 400$ Hz, and that tip-tilt correction by the AO strongly reduces SIC. Using simulated solar granulation, they also concluded that the AO correction is critical to perform polarimetry at high spatial resolutions (~ 0.3 arcsec).

The first quantitative estimation of SIC considering high-order seeing aberrations, and the effect of AO corrections, was done by Krishnappa and Feller (2012). They start from a high-spatial-resolution, full-Stokes, simulated snapshot of a plage region in the Sun. The simulated data is then convolved with an instantaneous seeing PSF. The latter is obtained numerically by creating frozen phase screens, from a Kolmogorov spectrum with $r_0 = 10$ cm (Eq. 2.46), and then moving them over a 1 m-telescope at a wind speed of 10 m s^{-1} . The seeing-aberrated data is convolved with the telescope PSF, and then corrected by simulating the action of an ideal AO system that can perfectly compensate up to a desired number of Zernike terms. The results from the Krishnappa and Feller (2012) simulations, corresponding to a single beam modulation scheme based on two FLCs and two SRs, are repeated in Fig. 2.9. The two main conclusions arising from them are that the SICs level is practically independent of the number of modes corrected by the AO, and that at least a $f_{mod} \approx 100$ Hz is required to effectively reduce all the SIC components down to the 10^{-4} level approximately.

2.3.3 Image restoration

Even though AO systems are regularly used in most of the state-of-the-art solar facilities to correct low-order seeing distortions, their performance is limited (see e.g. Rimmele 2000, Rimmele and Marino 2011, Berkefeld 2007, and references therein). This is mainly due to finite bandwidth of the control system, limited number of actuators in the active mirrors, accuracy of the wavefront sensing and seeing anisoplanatism²². Current efforts to solve the latter, have shown promising advances with the introduction of the multi-conjugated AO systems (e.g. Schmidt et al. 2014a,b).

In the context of this work, image restoration refers to any numeric technique used to reconstruct or repair seeing aberrated solar images post acquisition. Such techniques present some advantages with respect to the AO systems, e.g. they can correct high-order aberrations. In spite of that, the best results are obtained generally with both solutions working together. The main restoration techniques used in solar applications are different

²²Anisoplanatism (see e.g. Rimmele and Marino 2011) refers to the variation of the seeing PSF across the scene, produced because the FOV is larger than the seeing isoplanatic patch (Eq. 2.48).

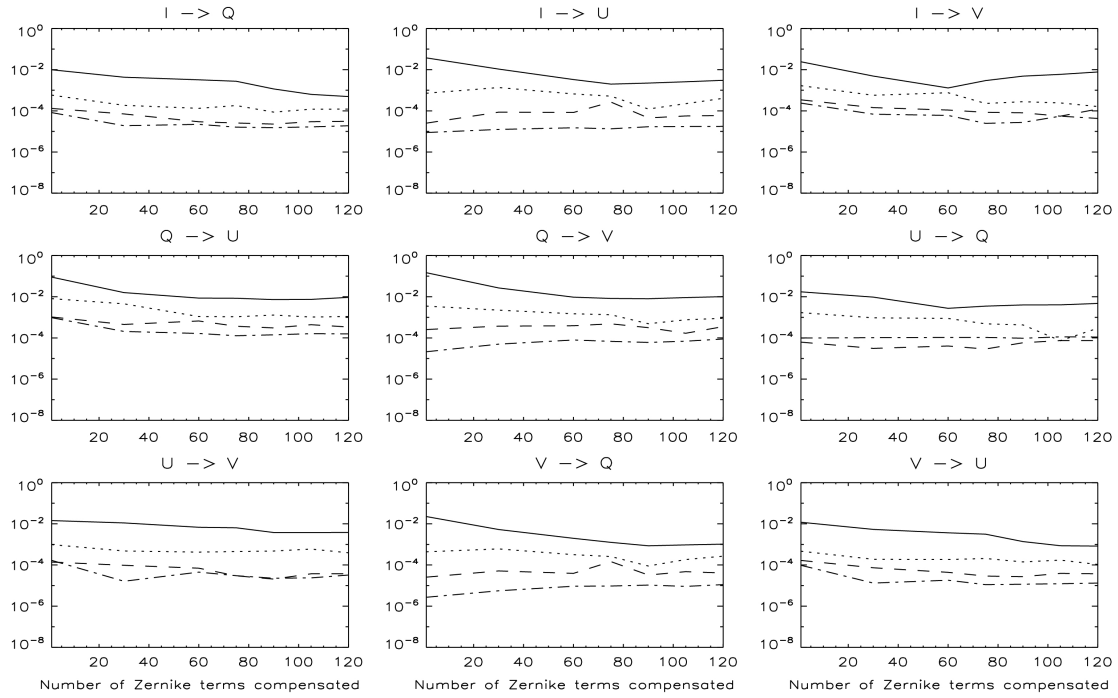


Figure 2.9. Simulated SIC considering high-order aberrations and the AO effect, given in Fig. 7 of Krishnappa and Feller (2012). Each panel shows the SIC (vertical axes) between two Stokes parameters (indicated in the titles), versus the number of Zernike terms compensated by the AO (horizontal axes), for different modulation frequencies (different line-styles). The modulation frequencies in all panels are 2.14 (continuous), 29.9 (dotted), 98.2 (dashed), and 200.7 Hz (dashed-dotted). Copyrights Optical Society of America 2012.

variants of MOMFBD (see Löfdahl 2002, for a review) and speckle imaging (SI, Keller and von der Luehe 1992).

Independently of the technique used, the model assumed for the image degradation due to seeing is linear and space-invariant (Eq. 2.49). Since neither the true solar scene (object) nor the degradation function (seeing plus telescope PSF) are known, many independent measurements of the same (constant) object are required to constrain the estimations. In order to preserve the spatial information up to the telescope diffraction limit, such measurements need to have $t_e < \tau_0$, in daylight typically $t_e \sim 10$ ms. The space invariance means that only images with a *FOVs* smaller than the seeing isoplanatic patch (see Eq. 2.48) can be restored. To deal with larger *FOVs*, the scene is usually divided in smaller patches that are restored independently.

Both MOMFBD and SI present pros and cons. Three important disadvantages of SI are (a) it does not work properly when an AO is in the beam, because it modifies the seeing statistical properties; (b) it does not allow the estimation of the degradation functions; and (c) it requires at least ~ 100 statistically independent measurements of the same object, which is difficult when considering fast evolving solar signals. On the other hand, MOMFBD requires much more computing time and perform worse with low contrast data (Löfdahl et al. 2007). The first restorations of the data acquired with FSP has been carried out using MOMFBD, thus we detail here only this technique.

The multi-frame blind deconvolution (MFBD) problem implies recovering a time-invariant object, \mathcal{I}_\odot , using only many aberrated and noisy measurements, $\{\mathcal{I}_i\}$, where $i \in$

$\{0, 1, \dots, N_{frm}-1\}$. Dropping the spatial frequency variable, we can write in the spatial Fourier domain (following Van Noort et al. 2005)

$$\mathcal{I}_i = \mathcal{H}_{atm+tel}^i \mathcal{I}_\odot + \mathcal{N}_i, \quad (2.68)$$

where \mathcal{N}_i is the Fourier transform of the noise, the OTFs can be obtained from

$$\mathcal{H}_{atm+tel}^i = \mathcal{F}\{|\mathcal{F}^{-1}\{P_i\}|^2\}, \quad (2.69)$$

and \mathcal{F} denotes the Fourier transform operator. The generalized pupil function, P_i , can be obtained from the telescope pupil transmission function (\mathbb{D}) and the pupil phase (δ_i), as follows

$$P_i = \mathbb{D} e^{i\delta_i}. \quad (2.70)$$

The δ_i describe the seeing-aberrated wavefronts. They are parametrized to reduce the number of free variables, using the following finite orthogonal expansion

$$\delta_i = \delta_{0,i} + \sum_{m=0}^{N_{mode}-1} \kappa_{i,m} \Omega_{i,m}, \quad (2.71)$$

where N_{mode} denote the number of modes used, $\kappa_{i,m}$ are the expansion coefficients and $\Omega_{i,m}$ are the orthogonal basis functions, i.e. Zernike polynomials for the tilts terms and atmospheric Karhunen-Lo  ve modes²³ for the blurring effects. The $\delta_{0,i}$ is used to include any known phase difference (diversity) with respect to another channel (see below).

The simultaneous estimation of both object and aberrations is achieved by the iterative minimization of an error metric with respect to all the coefficients $\kappa = \{\kappa_{i,m}\}$ (note that κ is different from the spatial frequency vector \mathbf{k}). The simplest metric and the fastest implementation, are obtained for Gaussian noise (Van Noort et al. 2005). In this case, the metric (\mathcal{L}) can be simplified to the least square difference between the measured \mathcal{I}_i and the estimated ones (Paxman et al. 1996), i.e.

$$\mathcal{L}(\kappa) = \sum_{\mathbf{k}} \left(\sum_{i=0}^{N_{frm}-1} |\mathcal{I}_i|^2 - \frac{|\sum_{i=0}^{N_{frm}-1} \mathcal{I}_i^* \hat{\mathcal{H}}_{atm+tel}^i|^2}{\sum_{i=0}^{N_{frm}-1} |\hat{\mathcal{H}}_{atm+tel}^i|^2 + \gamma} \right), \quad (2.72)$$

where $\hat{\mathcal{H}}_{atm+tel}^i$ are the estimated OTFs and γ is the regularization term of a simple Wiener deconvolution²⁴. Note that Eq. 2.72 does not explicitly include the unknown object²⁵, \mathcal{I}_\odot , and thus after minimization all the $\mathcal{H}_{atm+tel}^i$ are known (we call this, the *wavefront sensing step*). The derivation of the estimated object can be done after the wavefront sensing in an separate *deconvolution step*.

²³A set of optimal basis functions, that minimize the mean squared error in the truncated expansion of a random process. The expansion coefficients are independent random variables, while the basis functions are orthogonal and continuous (Rod  ier 1990).

²⁴A Wiener filter has a spectral response, $\mathcal{H}_{wiener}(\mathbf{k})$, that allows the best estimation, i.e. minimizes the mean squared error, of a random image from its blurred version. If the blurring function is $\mathcal{H}(\mathbf{k})$, then $\mathcal{H}_{wiener}(\mathbf{k}) = 1/\mathcal{H}(\mathbf{k}) \times |\mathcal{H}(\mathbf{k})|^2 / (|\mathcal{H}(\mathbf{k})|^2 + \gamma(\mathbf{k}))$. $\gamma(\mathbf{k})$ is a regularization factor, used to avoid noise amplification, given by the ratio of the noise and signal power spectra (see e.g. Saha 2007).

²⁵The second term inside the parentheses in Eq. 2.72 corresponds to the estimated version of the first term. Note it resembles the convolution of the estimated object and the estimated OTFs, where the former is in turn obtained from a Wiener deconvolution of the measurements using the estimated OTFs.

Multiple objects can be recorded at the same time, e.g. by simultaneously imaging the same solar scene using different filters in each channel. Additionally, more than one channel can be used to image the same object with different diversity $\delta_{0,i}$ (phase diversity). The restoration of each object, $\mathcal{I}_{\odot,j}$ with $j \in \{0, 1, \dots, N_{obj}-1\}$, constitutes an independent MFBD problem (Eq. 2.72). Nonetheless, any known relationship among the objects, can be translated to an equality constraint among the corresponding free coefficients, κ_j , to make the simultaneous restoration a better conditioned problem. The latter is the MOMFBD approach, developed by Löfdahl (2002) and implemented as a freeware, highly-parallel, C++ code by Van Noort et al. (2005). A MOMFBD implies then, the minimization of the weighted sum of the individual metrics (Eq. 2.72) of all the objects, namely

$$\mathcal{L}_{mo}(\kappa_{mo}) = \sum_{j=0}^{N_{obj}-1} \kappa_{obj,j} \mathcal{L}_j(\kappa_j), \quad (2.73)$$

where $\kappa_{obj,j}$ are the individual weights.

Typical wide band (WB) solar scenes require at least ~ 5 frames to run a MFBD. On the other hand, narrow band (NB) data require an increased number of frames to obtain a good restoration, due to the low SNR (Löfdahl et al. 2007). Another solution to restore NB data, is to record a simultaneous WB channel. After acquisition, both channels can be jointly restored by running a two-object MOMFBD. The latter, provided that, sub-pixel co-alignment is performed and the aberrations in both channels are the same or have a fixed, known relationship (Van Noort et al. 2005).

3 High-cadence, ground-based polarimetry

As seen in Ch. 2, the reduction of SIC and the implementation of image restoration, are critical for any ground-based polarimeter that aims to reach simultaneously high polarimetric sensitivity and high spatial resolution (a regime demanded by many challenging open questions in modern solar physics, see Sect. 2.1.4). To reduce SIC a high-modulation frequency is required. In addition, an efficient implementation of image restoration demands short exposure times. A high DC and low noise are also needed, to reach the desired SNR as fast as possible and avoid the spatial smearing produced by solar evolution and seeing. These basic requirements can be met by a high-cadence polarimeter, i.e. one that can acquire a large amount of Stokes images per second. The development of the prototype of an instrument that aims for such a regime, is the central topic of this thesis.

The present chapter begins by summarizing the general properties that define such a high-cadence polarimeter, based on the concepts introduced in Ch. 2. These are then used to explore the requirements of the camera and the polarization modulator, in order to ponder in a nutshell the different available technologies (Sect. 3.1). From the analysis above, it is found that the camera is generally the bottle neck of a high-cadence polarimeter. This is further explored by comparing the different cameras used in eight state-of-the-art, solar polarimeters that work in the visible part of the spectrum (Sect. 3.2.1). Within such a comparison, the prototype of the FSP is introduced, as a novel solar polarimeter that works in an unexploited regime of high cadence, low noise and high DC . An overview of FSP is given in Sect. 3.2, including an enumeration of its main constituent components.

As seen in Sect. 2.1.3, the IR and UV regimes are very important to diagnose the solar atmosphere, most notably the transition region and the chromosphere. In spite of this, the rest of this work focuses only on visible-polarimetry (from 400 to 700 nm approximately) in which almost all spectropolarimetric measurements have been carried out, due to a richness of Zeeman sensitive lines, allowing detailed diagnostics of the solar magnetic field. It is also the regime targeted by the FSP project. Some of the contents presented in this chapter have been literally published in Iglesias et al. (2016).

3.1 Main properties of a high-cadence polarimeter

Based on the concepts and criteria introduced in Ch. 2, we have collected in Table 3.1, the most relevant properties that define a ground-based polarimeter that simultaneously aims for high-polarimetric sensitivity and high spatial resolution.

Parameter	Value	Motive(s)	See also
Modulation	Fast, single-beam	A slow dual beam system only reduces crosstalk from Stokes I to \mathbf{p} , and may suffer from beam imbalance and misalignments. The slow, beam exchange technique also reduces only the main SIC component, in addition it harms the spatial resolution and cadence due to the combination of two independent measurements taken at different instants of time.	Sect. 2.3.2
	Full Stokes	To allow the remote sensing of all the magnetic field vector components and the detection of scattering polarization.	Sect. 2.1.2
f_{mod}	≥ 100 Hz	To reduce SIC to $\sim 10^{-4}$ (the need of this value is estimated from numeric simulations).	Fig. 2.9
	≥ 400 Hz	To practically eliminate SIC	Sect. 2.3.2
t_e	≤ 10 ms	To implement image restoration.	Sect. 2.3.3
		To improve the data simultaneity.	Sect. 2.2.3
ϵ	$\sim \epsilon_{ideal}$	To reach the required SNR faster and avoid smearing due to solar evolution and seeing.	Sect. 2.1.4, 2.3.1
		To improve SNR and thus the image restoration performance.	Sect. 2.3.3
		To reach the required SNR faster and thus improve the data simultaneity.	Sect. 2.2.3
σ_{cam}^2	$\ll \sigma_p^2$	Same as ϵ . The photon noise rms value can be low. e.g. $\sigma_p \approx 22 e^-$ rms adopting the assumptions used in Eq. 2.26; and $\lambda = 500$ nm, $D = 1.5$ m, a camera sensitivity of 80 %, $t_e = 2.5$ ms and that we are observing at a line core with an intensity equal to 10 % of the continuum intensity.	Same as ϵ
DC	~ 100 %	Same as ϵ	Same as ϵ
		To acquire a larger amount of images and thus improve the image restoration performance.	Sect. 2.3.3
$QE \times FF$	~ 100 %	Same as ϵ	Same as ϵ
Accuracy	≤ 1 %	To be able to detect polarimetric signals with amplitudes of 10^{-4} relative to the continuum, provided that the instrumental polarization is below 1 %.	Sect. 2.1.4

Table 3.1. Summary of the most relevant properties of a ground-based polarimeter that simultaneously aims for high polarimetric sensitivity ($\sim 10^{-4}$) and high spatial resolution (< 1 arcsec). Target values are given for each parameter along with their corresponding motivation.

The fast modulation and a short exposure time detailed in Table 3.1, can be fulfilled only by a high-cadence polarimeter. For the rest of this work, we use the term fast polarimeter as a synonym of high-cadence polarimeter.

3.1.1 Camera requirements

The general polarimeter properties given in Table 3.1, impose a first set of constraints on the camera specifications. The two most demanding parameters for a large sensor are the FR and σ_{cam} . The former is determined by which of the following two strategies is used to register the different modulation states (Stenflo 2013, Ch. 13):

- *Synchronous readout*: Where each modulation state is recorded by the camera in an individual frame. Thus, FR is determined by f_{mod} through:

$$FR = N_{mod} f_{mod}. \quad (3.1)$$

- *Asynchronous readout*: Where many modulation states are recorded in a single frame. This was firstly implemented by Povel et al. (1990) in the successful Zurich IMaging POLarimeter (ZIMPOL). This is, up to date, the only polarimeter that works with modulation frequencies in the 10 kHz regime. ZIMPOL has seen many improvements since its first version, and proved capable of carrying out measurements with very-high sensitivity ($\sim 10^{-5}$) although only at low spatial resolution (see Sect. 3.2.1), using a spectrograph as wavelength discriminator (see Ramelli et al. 2010, for an overview).

The heart of the ZIMPOL system is a specially modified CCD sensor. In the full-Stokes version, which employs an FLC-based modulator with $N_{mod} = 4$, three out of four rows of the sensor are shielded, so they are not photosensitive and can be used as charge storage. During operation, the modulator is synchronized with the charge transfer of the CCD, allowing the accumulation of the signals of the individual modulation states in independent rows. Since the charge transfer can be done in the μs regime, the modulation frequency is basically limited by the modulator. In this way, the sensor readout is decoupled from f_{mod} allowing to have $FR \ll f_{mod}$.

The ZIMPOL concept presents clear disadvantages regarding the resulting FR , DC , and pixel shape and size. These make the system not suitable for high spatial resolution applications (see Sect. 3.2.1).

Assuming that a synchronous readout is employed, we enumerate in the following list, the main camera properties that critically affect the performance of a fast polarimeter. We include also representative values for each parameter, only to guide the discussion of their implications on the camera technology selection. The first four points are derived from the figures given in Table. 3.1, the rest are obtained from other considerations (specified in each case).

1. $FR \geq 400$ fps : Necessary to achieve a $f_{mod} \geq 100$ Hz with $N_{mod} = 4$ (Eq. 3.1), which is the minimum required to measure the full \mathbf{S} (Sect. 2.2.1). This value of FR also guarantees $t_e < 10$ ms. Note we do not consider the case of $f_{mod} \geq 400$ Hz given in

Table 3.1. This is because the minimum resulting FR , i.e. ≥ 1600 fps, can not be achieved —simultaneously with the noise, sensor size and DC specifications listed below— even by state-of-the-art technology on scientific cameras (see e.g. Sect. 3.2.1).

2. $\sigma_{cam} < 7 e^- \text{rms}$: Imposed for the polarimeter to be photon-noise limited (see Sect. 5.5), i.e.

$$\sigma_{cam}^2 < 0.1 \sigma_p^2. \quad (3.2)$$

In most of the scientific cameras —provided that no strict power consumption constraints are imposed— the σ_d can be reduced to very low levels by cooling the sensor. Assuming this —and considering that the imposed t_e is short, further reducing the number of dark electrons— the σ_{ro} becomes the main contributor to σ_{cam} . The latter is what discourages the usage of commercial high-speed ($> \text{kHz}$) cameras, to do high-resolution solar polarimetry¹.

Moreover, the lack (until very recently) of scientific cameras with the FR , DC , sensor size and σ_{cam} specifications enumerated here; has led to the fact that most of the high-sensitivity, ground-based polarimeters currently in operation, still make use of the slow dual beam technique for SIC suppression (see Sect. 3.2.1).

3. $DC \sim 100\%$: In addition to the motives given in Table 3.1, note that, the smaller the DC the more strict the noise requirements of the camera become, i.e. for a given FR the σ_p per frame decreases with the DC , making it more difficult to fulfill Eq. 3.2.

Given the high FR imposed, an almost $\sim 100\%$ duty cycle can be obtained in large sensors (see below) only if they have the ability to read while they continue integrating. Such a characteristic is implemented only in full-frame-transfer or interline CCDs (Hoslt 1998) —by means of dedicated charge storage areas in the sensor— and in specific CMOS sensors that can store the signal in the readout node of each pixel (e.g. Lauxtermann and Leipold 2011).

4. $QE \times FF \sim 100\%$: This implies keeping $FF = 100\%$ and maximizing QE in the 400 to 700 nm wavelength range. Note that the former discourages the usage of interline CCDs or CMOS devices with complex circuitry inside the pixel structure².
5. *Shutter type = Snapshot*: In order to keep the DC as high as possible, the camera needs to be exposed during most of the duration of each modulation cycle. This implies that $t_e \approx 1/(N_{mod} f_{mod})$, therefore, the exposure of all the pixels of the sensor has to be in phase. If not, the pixels that are readout later may accumulate some

¹This is, however, the solution adopted in the high-cadence polarimeter at the Japanese Solar Flare Telescope (Hanaoka 2004, Hanaoka et al. 2003). This polarimeter uses a small (260×260 pixels), commercial camera (DALSA-CA-D6-256) that can run at 955 fps. The sensor operates at ambient temperature and has large readout noise (not reported). The main difference with respect to the regime aimed at in Table 3.1, is that the photon flux, and thus the σ_p are higher, relaxing the requirement on σ_{ro} imposed by Eq. 3.2.

²With these kind of devices a $FF = 100\%$ can still be obtained by utilizing a micro-lenses array, in order to focus the incoming light only in the photosensitive areas of each pixel. This solution presents, however, other drawbacks including misalignments between pixels and micro-lenses, and the associated increase in straylight.

of the signal corresponding to the transition state of the modulator, or to the next modulation state; resulting in a reduction of their ϵ (see Sect. 4.3.3). The latter rules out the usage of CMOS devices with rolling shutter, where the rows of the sensor are read sequentially from top to bottom. This case is exemplified in Fig. 3.1, see e.g. Piqueras (2013), Sect. 3.4.3 for a detailed analysis.

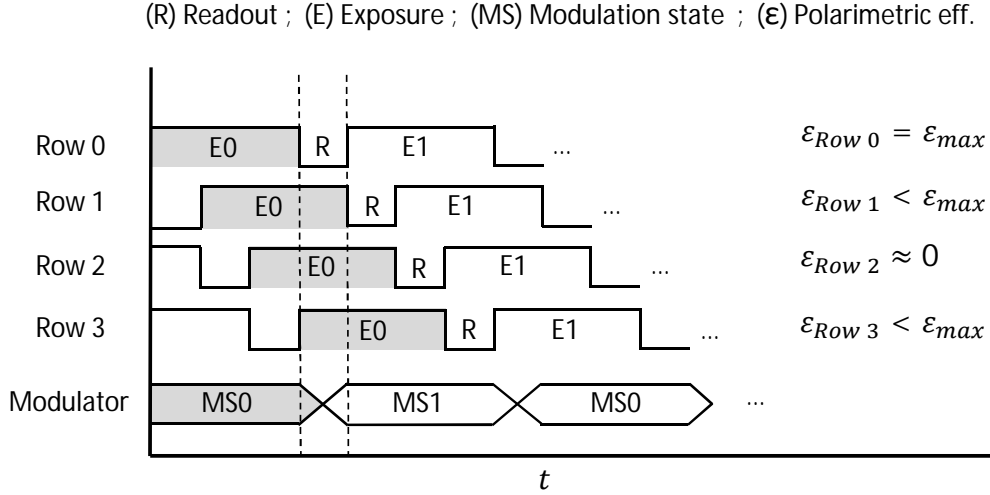


Figure 3.1. Rolling shutter implications in high-cadence polarimetry. The sketch shows the read-out timing of a simplified example, with a bistable modulator synchronized to a sensor with only four rows. The sensor is working at the highest possible FR , i.e. the first row is read immediately after the last one, and the readout time is assumed to be equal to the modulator switching time for simplicity. The synchronization is such that ensures the highest ϵ for Row 0. As a consequence, Row 2 accumulates in a single exposure approximately the same amount of signal from MS0 as from MS1, resulting in a practically null ϵ , i.e. the polarization signal can not be recovered. Row 1 and 3 have a reduced ϵ because part of their exposure occurs during the transition phase of the modulator. Note that, Row 3 is dephased almost one modulation cycle with respect to Row 0 and 1, this has to be taken into account during the demodulation in order to recover the proper polarization signals.

6. $N_{col} \times N_{row} \geq 1024 \times 1024 \text{ pixel}^2$: As pointed out by Iglesias et al. (2016):

The size and aspect ratio of the detector, directly affect the instrument FOV. In general, large detectors are required to image many common scientific targets with sub-arcsec sampling, e.g. large active regions. In combination with a spectrograph, a large aspect ratio can be an advantage, depending on the required spectral resolution and range. For filtergraph-based systems, smaller aspect ratios are commonly used.

7. $A_{pixel} \leq 20 \times 20 \mu\text{m}^2$: As explained in Iglesias et al. (2016):

Two aspects are relevant regarding pixel area. Firstly, detectors with non-square pixels have a more complex point spread function (PSF) and sample the image at different spatial frequencies in the two orthogonal

dimensions, further complicating the image restoration process. Secondly, the pixel size has to match the required spatial sampling of the—ideally diffraction limited—image. As a consequence, large pixels may require re-imaging setups of unpractical dimensions, which can also introduce further optical aberrations.

Small and square pixels are an advantage, the figure given here is just a reference adopted from the typical values used in current solar facilities (see Sect. 3.2.1).

8. $N_{ENOB} \geq 11$ ENOB: This is imposed to have a very low quantization noise (Hoslt 1998, Sect. 4.2.5), e.g.

$$\sigma_{adc}^2 = \left(\frac{2^{N_{adc}-N_{ENOB}}}{G \sqrt{12}} \right)^2 \leq 0.1 \sigma_{cam}^2, \quad (3.3)$$

where N_{ENOB} is the ADC effective number of bits (ENOB), which is smaller than the ADC resolution (N_{adc}), because it includes both the quantization noise and the contributions from the non-ideal circuitry of the ADC (IEEE 2001). Here we have assumed $2^{N_{adc}}/G = 15\,000\,e^-$ due to the short exposure times involved (see σ_p in Table 3.1).

9. $NL < 1\%$: Non-linearities in the camera introduce spurious polarimetric signals (Keller 1996). The amplitude of such artifacts is proportional to the NL and to the instrumental polarization level. The figure given here, is required to ensure the artifact level is $\sim 10^{-4}$ when the instrumental offset is $\sim 10^{-2}$, see Sect. 5.3 for further details.

From the above-detailed properties, note that σ_{cam} , $QE \times FF$ and NL are among the critical camera specifications. Since typically CCDs outperform CMOS sensors in such parameters (see Table 2.2), most of the high-sensitivity, ground-based polarimeters currently in operation employ CCD cameras (Sect. 3.2.1).

3.1.2 Polarization modulator requirements

In the following list we enumerate the main requirements of the polarization modulator derived from Table 3.1, along with their implications on the modulation technology selection.

1. $f_{mod} \geq 100$ Hz: Out of the available modulation technologies listed in Sect. 2.2.2, only the FLCs and PEMs allow to modulate above 100 Hz. However the very high modulation frequency of the PEMs rules out any demodulation by means of synchronous readout.
2. *Full stokes modulation*: A full-Stokes modulator based on PEMs has proven difficult to implement, because it requires two PEMs oscillating at the same frequency. Such a configuration is very sensitive to external perturbations (e.g. small temperature mismatches of the crystals) and thus the required phase stability can not be achieved (Gandorfer 1999).

On the other hand, full-stokes modulators based on FLCs have been successfully used in many solar polarimeters for slow (e.g. Keller et al. 2003) and in two cases for fast (Hanaoka 2004, Ramelli et al. 2010) modulation. Furthermore, FLCs can be purchased with high optical quality, and are long lasting and stable, provided UV degradation and temperature issues are controlled (see Sect. 2.2.2).

3. $N_{mod} = 4$: Modulation schemes with larger N_{mod} produce Stokes images with larger SNR (del Toro Iniesta 2003, Sect. 5.2). On the other hand, the camera FR scales linearly with N_{mod} (Eq. 3.1). Since the minimum FR imposed on the camera by the SIC considerations is already a strict requirement (see point 2 in Sect. 3.1.1), the smallest value possible for N_{mod} that allows to measure the full \mathbf{S} should be adopted³, i.e. 4 (Sect. 2.2.1).
4. $\epsilon \sim \epsilon_{ideal}$: Modulators based on two FLCs ($N_{mod}=4$) can provide $\epsilon_{total} > 80\%$, usually by means of a modulator design optimized for efficiency across a broad spectral working range (Gisler 2005, Tomczyk et al. 2010).
5. $t_s \ll 2.5$ ms: Since for a fast polarimeter the DC has to be as high as possible, the camera is likely to be exposed during both the stable states of the modulator, as well as during the transition between stable states. Thus, in order to ensure high ϵ , the modulator switching time (t_s) should be kept short (see Sect. 4.3.3), i.e.

$$t_s \ll \frac{1}{N_{mod}f_{mod}}. \quad (3.4)$$

To compute the figure given here, we assumed $N_{mod} = 4$ and $f_{mod}=100$ Hz. A typical value for t_s in FLCs is $\sim 70 \mu s$ (see Sect. 4.2.1).

Note that, considering the requirements specified above, an FLC-based polarization modulator is the best candidate to be employed in a full-Stokes, fast polarimeter.

3.2 The Fast Solar Polarimeter Prototype

The goal of the FSP project is the development of a ground-based, high-cadence polarimeter that can operate as close as possible to the regime detailed in Table 3.1, in order to acquire high-spatial-resolution and high-polarimetric-sensitivity measurements of the solar light in the visible part of the spectrum. The main science questions that the FSP project will seek to address include, among others, those listed in Sect. 2.1.4. Consequently the main design driving parameters are a target sensitivity of 10^{-4} and sub-arcsec spatial resolution (reachable only with spectropolarimetric data that is optimized for post acquisition restoration).

Based on the arguments presented in Sect. 3.1.1, it can be clearly seen that the most challenging component, required to develop such a fast polarimeter, is the camera. FSP is conceived around a novel, custom-made pnCCD camera that can provide high FR and low

³Note that, this discourages the usage of a rotating waveplate as a modulator, even if a fast rotation of the disk can be achieved. For example, the polarimeter developed by Hanaoka (2012) uses a plate rotating at 25 s^{-1} that has $N_{mod} = 8$. Thus it can only reach a $f_{mod} = 50$ Hz with a detector that has $FR=400$ fps.

σ_{cam} . In addition, following the arguments given in Sect. 3.1.2, an FLC-based polarization modulator is employed.

The FSP project started in 2012 and is divided in two stages. The first one involves the development of a prototype polarimeter, that uses a pnCCD camera that has a small ($264 \times 264 \text{ pixel}^2$) sensor, $FR \leq 800 \text{ Hz}$ and $\sigma_{cam} = 4.9 e^-_{rms}$; in a single beam configuration. The camera was manufactured by PnSensor GmbH. The principal goals of the prototype stage are (a) to assess the suitability of the pnCCD technology for its usage in high-cadence, high-sensitivity polarimetry at visible wavelengths; (b) to develop an FLC-based modulator that can provide at least $f_{mod} \geq 100 \text{ Hz}$ and $\epsilon_{tot} \geq 80 \%$ in the 400 to 700 nm wavelength range; and (c) to obtain the measurements required to evaluate the instrumental concept and its polarimetric performance. Including, most notably, the residual SIC level when operating at $f_{mod} = 100 \text{ Hz}$. The main focus of this thesis is the development of such a prototype, hereafter denote simply as FSP.

The know-how acquired with FSP shall be used to face the second stage of the project, hereafter referred to as FSP II (Sect. 7.1), which implies the development of a science ready polarimeter using a camera with a larger pnCCD sensor ($1024 \times 1024 \text{ pixel}^2$) that can run at $FR \leq 400 \text{ Hz}$. Such a sensor, and its associated electronics, is currently being developed by the MPG Semiconductor Lab. The modulator package will be the same as employed in FSP, with the difference that the larger sensor area will allow the implementation of a *high-cadence, dual-beam setup*, never tested in solar polarimetry before.

3.2.1 Cameras used in ground-based polarimeters: state-of-the-art

To better allocate the working regime of FSP among the rest of the ground-based solar polarimeters, we present in Table 3.2 (adapted from Iglesias et al. 2016), the main camera properties for the following eight state-of-the-art polarimeters that work in the visible part of the spectrum ⁴: IBIS (Cavallini 2006); VIP (Beck et al. 2010); CRISP (Scharmer et al. 2008, de la Cruz Rodríguez et al. 2015); DLSP on phase II (Sankarasubramanian et al. 2004, 2006); SPINOR (Socas-Navarro et al. 2006) ; FSP and ZIMPOL-3 (Ramelli et al. 2010, 2014). We include, in addition, the targeted properties of FSP II (see Sect. 7.1).

All the cameras listed in Table 3.2 are based on CCD sensors that have square pixels. The only exception to the latter is ZIMPOL-3, which has a pixel aspect ratio of 4 to 1 and a long dimension ($90 \mu\text{m}$) nearly six times larger than the most common value ($< 16 \mu\text{m}$). ZIMPOL-3 uses a sensor with three out of four rows covered. This demands attaching a

⁴As explained in Iglesias et al. (2016):

We excluded from this list the SOLIS/VSM (Keller et al. 2003) although is an interesting example of early high-cadence polarimetry. The initial idea of the project in 1998 was to use a pair of custom made, 1024×1024 , Sarnoff VCCD1024H cameras which had, $18 \times 18 \mu\text{m}^2$ pixel area, $46 e^-_{rms}$ readout noise and 300 fps frame rate (Keller 1998). However the system was never delivered by the manufacturer, forcing the VSM team to select an interim camera, with the Rockwell HyViSI-1024 model being chosen. The cameras were modified to have 256×1024 pixels, a 92 fps frame rate and have been operative since 2003 (Harvey et al. 2004). Due to variable-dark levels, inter-quadrant crosstalk and readout noise issues, among others, VSM was updated in 2010 to use a pair of commercial Sarnoff 1M100 cameras (Balasubramanian and Pevtsov 2011) similar to the ones used in SPINOR, hence the exclusion from our list.

Polarimeter	Camera model	A_{pixel} [μm^2]	$N_{col} \times N_{row}$ [pixel ²]	FR [fps]	σ_{ro} [e^- rms]	N_{adc} [bit]	DC [%]	f_{mod} [Hz]	Dual beam	WB channel
IBIS	KAF-1400	6.8×6.8	1024×1024	2.86	20	12	3 ¹	0.42	Yes	Yes
VIP	E2V-CCD97	16×16	512×512	29	5.4	16	100	7.25	Yes	Yes
CRISP	CAMIM100	16×16	1024×1024	37 ²	20	12	70	9.25	Yes	Yes
DLSP*	Pixel Vision Pluto	12×12	488×652	50	50	14	100	12.5	Yes	No
SPINOR*	CAMIM100-SFT	16×16	512×1024	100 ³	40	12	100	12.5	Yes	No
FSP	pnCCD	48×48	264×264	800	4.9	14	98.6	200	No	No
FSPII ⁴	pnCCD	36×36	1024×1024	400	5	16	95	100	Yes	Optional ⁵
ZIMPOL-3* ⁶	CCD55-30	22.5×90	1252×144	1.47	6	16	1.5 ¹	≥ 1000	No	No

¹ Computed for an exposure time of 10 ms.

² Although the Sarnoff CAMIM100 camera used can reach 100 fps.

³ Although the Sarnoff CAMIM100-SFT camera used can reach 190 fps.

⁴ Currently under development, we listed the expected values. See Sect. 7.1.

⁵ The camera noise is less critical due to the higher flux, thus, it can be implemented with e.g. a fast commercial CMOS camera.

⁶ Even though the CCD55-30 sensor used has frame transfer architecture, the ability of reading while integrating is not implemented resulting in an overhead readout time of about 0.66 s.

Table 3.2. Comparison of the detector-related properties for eight state-of-the-art, full-stokes, ground-based, solar polarimeters working in the visible part of the spectrum. The figures listed here are the ones reported to be used during typical polarimetric measurements, and may differ from the maximum allowed by the cameras. This is the result of design trade-offs that include, among others, the performance of the associated post-focus instruments. The polarimeters marked with an asterisk operate in spectrograph mode while the others are used in filtergraph mode. FSP has been tested in both modes. All the instruments employ CCD sensors with $FF \sim 100\%$. We have excluded QE because its value can be modified by means of sensor coatings, in order to guarantee high (>80%) figures in the desired portions of the visible spectrum. Adapted from Iglesias et al. (2016).

micro-lenses array in front of the photosensitive matrix, to focus the light on the uncovered pixels and keep $FF \approx 100\%$. The latter produces non-square pixels and requires a challenging sub-micron, alignment process between the uncovered rows and the micro lenses matrix (Gandorfer et al. 2004). FSP and FSP II also present a disadvantage with respect to their A_{pixel} , which are larger (two to three times in each dimension) than the other polarimeters (mainly due to limitations in the production process of their manufacturer).

The detector sizes of the selected polarimeters are very varied, those operating in a spectrograph mode (marked with an asterisk in Table 3.2) have non-square aspect ratios. Larger sensor areas and higher FR s constitute a trade off that depends on the readout technology and strategy, among others. Since the th pnCCD uses massive parallel readout (see Ch. 5), FSP II can reach up to half the FR of FSP with 16 times larger sensor area (see Sect. 7.1).

Taking in to account that the QE , FF , ϵ and σ_d of the selected instruments are similar⁵, we have plotted their values of FR , f_{mod} and σ_{ro} in Fig. 3.2; to better illustrate the situation of each polarimeter with respect to the high-cadence regime specified in Table 3.1. Note that, there is a clear difference between the high f_{mod} of ZIMPOL-3, which uses asynchronous readout, and the rest of the polarimeters, that have synchronous readout and thus follow Eq. 3.1. In spite of this, both groups of polarimeters are outside the parameter space that defines the ideal, high-cadence regime ($f_{mod} \geq 400$ Hz and $t_e \leq 10$ ms). The f_{mod} of the synchronous readout group—which uses $N_{mod} = 4$ to reduce the required FR , except for IBIS that has $N_{mod} = 6$ and SPINOR that has $N_{mod} = 8$ —is basically limited by their noise performance, i.e. the higher the FR the smaller the σ_p per frame, demanding lower values of σ_{ro} . On the other hand, the very low FR and DC of ZIMPOL-3 (along with the above-stated issues on A_{pixel}) make the instrument not suitable for high-spatial resolution applications.

The FSP and FSP II are located within a regime unexplored by previous solar polarimeters, see Fig. 3.2. The same is characterized by having simultaneously the shortest t_e , the lowest σ_{ro} , among the highest DC and a $f_{mod} \geq 100$ Hz that ensures $SIC \sim 10^{-4}$ (see Table 3.1). The necessity of employing a dual beam setup to further reduce SIC in such a regime depends, among others, on the specific science goals and the relative values of the artifacts introduced by residual beam imbalances and SIC . The latter is currently an open question that the FSP project aims to answer.

A discussion on what is the best strategy to reach the ideal regime shown in Fig. 3.2 is given in Ch. 7.

3.2.2 System overview

The different components that conform FSP are summarized by the block diagram in Fig.3.3, and detailed in the following list:

- *Calibration unit:* The first FSP component, that the light gathered by the solar telescope and altered by the AO system encounters, is the polarization calibration unit. This is a polarization state generator (PSG) formed by a high-quality linear polarizer and a super achromatic QWP. Both components are mounted in motorized

⁵They can also be optimized by e.g. including micro lenses, using different sensor coatings, modifying the modulator design or reducing the working temperature of the sensor

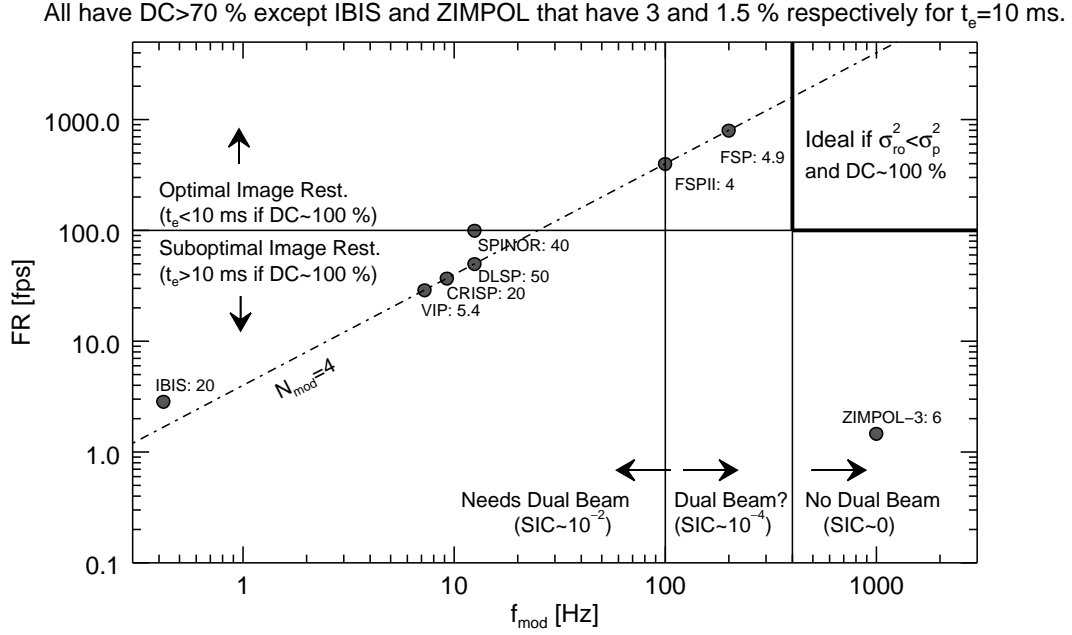


Figure 3.2. Comparison of the frame rate and modulation frequency of the solar polarimeters listed in Table 3.2. Each black dot is labeled with the name of the polarimeter it represents, and its corresponding value of σ_{ro} [e^- rms]. The horizontal continuous line at 100 fps correspond to $t_e = 10$ ms (if a $DC \approx 100\%$ is assumed), i.e the maximum typically allowed for a good image restoration assuming no WB channel is used (see Table 3.1). The vertical continuous lines are at $f_{mod} = 100$ Hz and 400 Hz to divide the regimes where SIC reduces considerably and is practically eliminated, respectively (see Table 3.1). See the text for extra details.

rotational stages that allow the modification of their optical axes, position angles. In addition, the whole ensemble is mounted on a motorized linear stage, that permits displacing the PSG in (to perform a polarimetric calibration) and out (during regular measurements) of the beam path. The \mathbf{S} generated by the PSG can be computed using the PSG Mueller matrix, which is given by (see Eq. 2.14 and 2.17)

$$\mathbf{M}_{PSG}(\theta_{ret}, \lambda) = \frac{\mathbf{M}_{ret}(\theta_{ret}, \delta(\lambda)) \mathbf{M}_{ppol}(\theta_{ppol}, k_{0^\circ}, k_{90^\circ})}{M_{ppol,0,0}(\theta_{ppol}, k_{0^\circ}, k_{90^\circ})}, \quad (3.5)$$

where we have normalized it to make $\mathbf{M}_{PSG,0,0} = 1$, because the normalized Stokes vector is the relevant quantity. The different Stokes vectors required to perform a calibration are generated by changing θ_{ret} . The values provided by the manufacturer of the optical components are $k_{0^\circ} = 0.99$, $k_{90^\circ} = 0.02$ and $\delta(\lambda)$ given in Fig. 3.4.

The polarizer position angle defines the Stokes Q direction and thus is kept fixed, i.e. $\theta_{ppol} = 0^\circ$. The rotational stages are the Owis model DMT-100, and present a repeatability of the position angle better than 0.01° . The determination of the zero for θ_{ret} and θ_{ppol} , i.e. the location of the optical axes with respect to the components glass, can typically be done with $\Delta\theta_{ret} = \pm 1^\circ$ and $\Delta\theta_{ppol} = \pm 0.1^\circ$ accuracies respectively. This introduces an error in the normalized Stokes vector generated by the

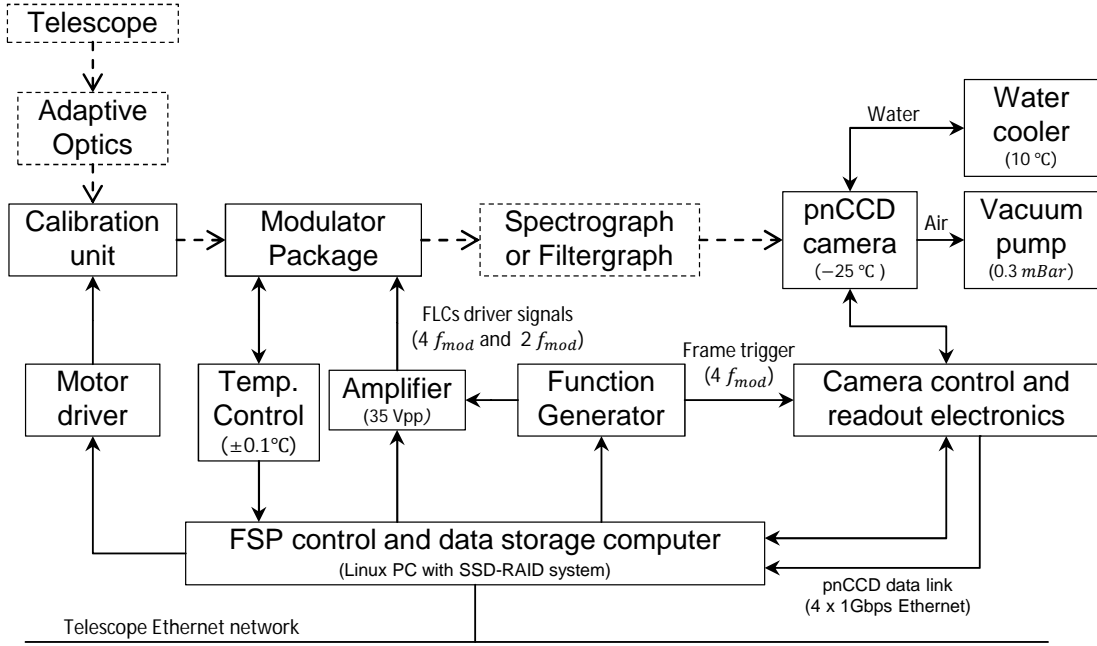


Figure 3.3. Components of the FSP as given in Fig.1 of Iglesias et al. (2016). Each box represents one or many pieces of hardware (dashed boxes do not belong to FSP itself but are required to make the observations). Some of the blocks have their typical operating parameters annotated in parentheses. The beam path is indicated by the dashed arrows. Non-labeled solid arrows represent different control, data and power connections. The communication lines required to synchronize FSP acquisition with the spatial (when the spectrograph is used) or spectral (when the filtergraph is used) scanning are not shown.

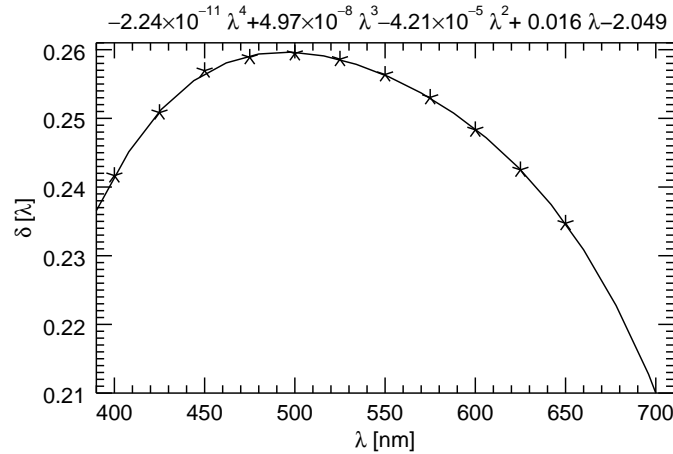


Figure 3.4. Retardance dispersion of the achromatic QWP in the PSG of FSP. The asterisks denote measurements and the continuous line correspond to the fitted polynomial described by the formula given above the frame.

PSG, that can be computed as follows

$$\begin{bmatrix} \Delta q \\ \Delta u \\ \Delta v \end{bmatrix} = \Delta \theta_{ret} \left[\left| \begin{bmatrix} \frac{\partial M_{PSG,1,0}}{\partial \theta_{ret}} \\ \frac{\partial M_{PSG,2,0}}{\partial \theta_{ret}} \\ \frac{\partial M_{PSG,3,0}}{\partial \theta_{ret}} \end{bmatrix} \right| \right]_{max} = 1.1 \begin{bmatrix} 3.55 \\ 3.55 \\ 3.35 \end{bmatrix} \times 10^{-2} \approx \begin{bmatrix} 3.9 \\ 3.9 \\ 3.7 \end{bmatrix} \%, \quad (3.6)$$

where we have used Eq. 2.8 and 3.5, replaced the above-given values for δ , k_{0° and k_{90° , considered a full rotation of the QWP and assumed the input of the PSG is weakly and polarized.

- *Modulator package*: After the calibration unit, the beam encounters the FSP modulator package, which is located as early as possible in the beam path to minimize the polarimetric influence of the other optical components, most notably the wavelength discriminator. The modulator is temperature controlled and driven with analog voltage signals, provided by an *Agilent 33502A two-channel amplifier* (fixed gain of 5). Further details on the modulator are given in Ch. 4.
- *pnCCD camera*: The modulated intensities, after being filtered by the wavelength discriminator, are recorded using the pnCCD camera. In order to reduce the dark current, the sensor is cooled down to -25°C by means of a peltier thermoelectric cooler module, and a closed water circuit (Julabo F25-ED with an operating range from -28 to 100° and an accuracy of $\pm 0.03^\circ$). In order to avoid condensation, the sensor housing is evacuated to 0.3 mbar. Further details on the camera are given in Ch. 5.
- *Function generator*: Both the modulator switching and the camera readout are triggered in synchronization by a single *Agilent 33522A, 30 MHz function generator*. Even though FSP can modulate at 200 Hz, most of the measurements were obtained at 100 Hz because that is the f_{mod} of FSP II, and thus the main regime that the prototype was designed to explore.
- *Control computer*: The instrument is controlled by a single Linux-based PC. The control computer is used (a) to configure the function generator, amplifier and camera to acquire the desired measurement; (b) to control the motorized calibration unit; (c) to record the house keeping data from the camera housing and temperature of the modulator; and (d) to record the output data of the camera. Due to the high data rate, 780 Mbit s^{-1} at 800 fps, the data is transferred by four dedicated 1 Gbit s^{-1} Ethernet connections in parallel and recorded in the control computer using a SSD-based RAID system.

4 Characterization and optimization of an FLC-based polarization modulator

The modulator package is one of the key elements of the polarimeter because its performance influences the polarimetric sensitivity and accuracy. In order to guarantee high modulation frequency and polarimetric efficiencies, special considerations have to be taken into account during the design and optimization of the modulator package.

This chapter details the development process of the FLC-based modulator used in FSP. Section 4.1 presents a description of the main design features. The optimization procedure, followed to obtain a balanced and achromatic set of polarimetric efficiencies, is detailed in Sect. 4.2 including the main characterization results of the FLCs and SRs used in the modulator. Finally, Sect. 4.3 describes the polarimetric calibration procedure—including its limitations (Sect. 4.3.1)—along with the measured behavior of the modulation matrix with respect to changes in the wavelength (Sect. 4.3.2) and modulation frequency (Sect. 4.3.3). In addition, the measured thermal properties of the FLCs are used to simulate the modulation matrix temperature dependence (Sect. 4.3.4). These results are utilized among others to derive the modulation frequency and temperature stabilization requirements, as well as to define how frequently a calibration needs to be performed.

The result of this chapter are fundamental to the development of the data reduction pipeline of the instrument, briefly described in Chapter 6. Some of the contents presented here have been published in Iglesias et al. (2016).

4.1 Main design features

The FSP modulator has a design similar to the SOLIS/VSM modulator (Keller et al. 2003). It is composed of two bistable FLCs (FLC1 and FLC2), two SRs (SR1 and SR2) and a polarizer beam splitter cube employed as linear analyzer (see Sect. 2.2.2). The main characteristics of the modulator can be appreciated in Fig. 4.1 and are listed below:

- *Housing*: The modulator housing is made of a good thermal conductor (the main block is $\text{CuZn}_{39}\text{Pb}_3 - 2.0380 - \text{MS58}$) and has large mass (7845.7 g). This is to provide high thermal inertia and low gradients, in order to facilitate the thermal control of the optical elements (see Sect. 4.3.4). The maximum dimensions of the modulator, including the rotational stage and the beam splitter cube, are $133.2 \times 125.0 \times 234.2$ mm. The optical aperture is 22 mm.

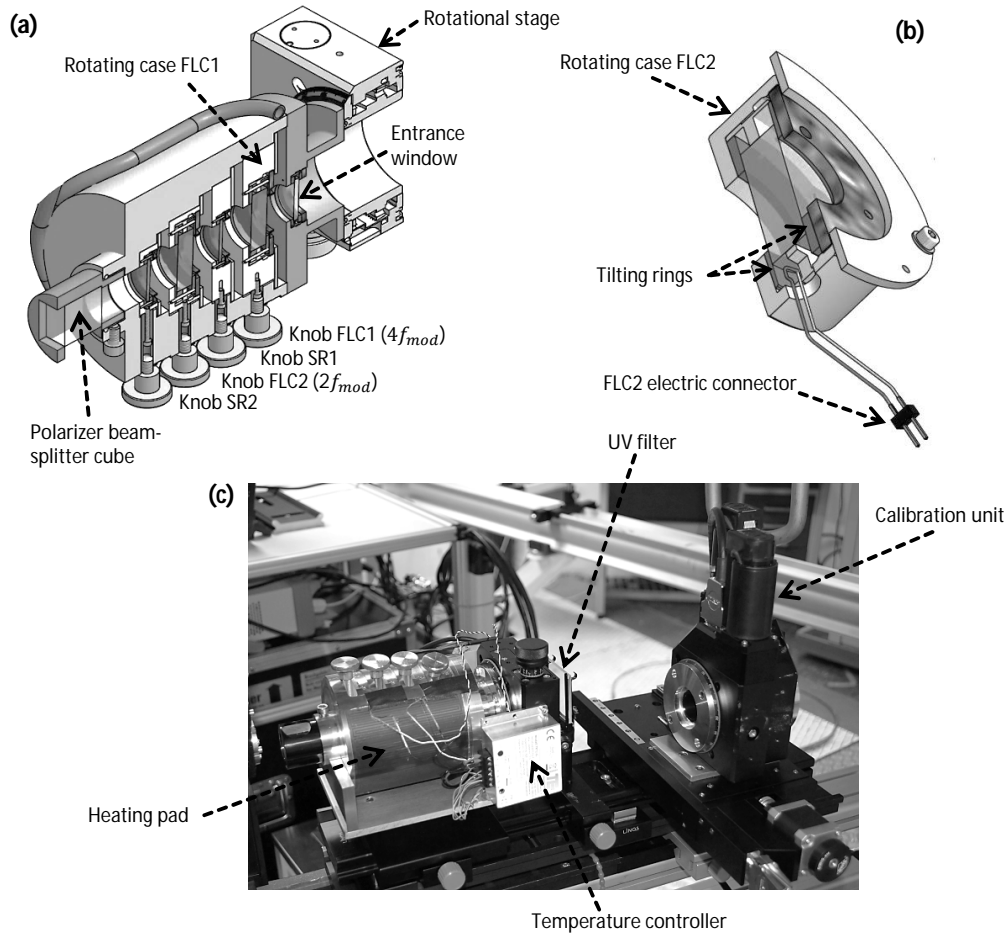


Figure 4.1. FSP modulator package. The disposition of the optical components can be seen in the CAD cross-section (a). The two FLCs and SRs are mounted in special cases that allow them to be manually rotated (by means of dedicated knobs) and introduce tilts of the optical surfaces (by means of tilting rings) to avoid multiple internal reflections (see b). The photograph (c) shows the modulator mounted behind the FSP calibration unit and a UV filter. The housing of the temperature controller electronics, and the flexible pad used for heating are also visible. Image (a) is adapted from Iglesias et al. (2016).

- *Heating pad:* The initial modulator design included an active thermal control system that can both cool and heat the modulator housing. Even though there are some minor advantages in running the modulator below ambient temperature (say at 15 °C, see Sect. 4.2.1) such thermal control has not been implemented yet and replaced by a simpler heating-only device. The modulator is heated above room temperature (36 °C), using a flexible pad heater controlled by a Pt100-based PID regulator (Telemeter Electronic model TR12-G), to ensure the required stability (better than ± 0.1 °C, see Sect. 4.3.4). The heating pad is glued to the housing and covers a large area to minimize the thermal gradients.
- *Components cases:* The FLCs and SRs are mounted in independent cases that allow the manual rotation of their optical axes ($\pm 20^\circ$), by means of independent graduated knobs that have a $\pm 0.5^\circ$ accuracy. Such a rotation capability is used during the efficiencies optimization, see Sect. 4.2. In addition, the cases impose a tilt ($2 \pm 0.3^\circ$)

to each component in order to avoid having parallel surfaces between components that can produce interference fringes due to multiple internal reflections.

- *Entrance window*: The 25 mm entrance window has an anti-reflection coating (VIS 0° [425-675nm]) that presents a reflectance lower than 0.3 % in the 400 to 700 nm wavelength range, and has a sharp increase below 400 nm. The latter contributes to reduce the UV radiation reaching the FLCs, which is further diminished by the UV filter placed before the modulator¹.
- *Beam splitter cube*: In FSP only the transmitted beam of the 25 mm polarizer beam splitter cube is used. Regarding its polarimetric action, it is equivalent to that of a partial linear polarizer (see Sect. 2.2.2) with $k_{0^\circ}=0.99$ and $k_{90^\circ}=0.02$ in the 440 to 650 nm wavelength range. The position of the beam splitter optical axis is kept parallel to the Stokes Q direction defined by the PSG. This angle can be modified by the modulator rotational stage, which is an Owis model DT100-D53 that has an accuracy of ± 30 arcsec.

Neglecting the effect of the entrance window, the polarimetric action of the modulator can be modeled by its Mueller matrix (see Eq. 2.14 and 2.17),

$$\mathbf{M}(I') = \frac{\mathbf{M}_{PPOL}\mathbf{M}_{SR2}\mathbf{M}_{FLC2}\mathbf{M}_{SR1}\mathbf{M}_{FLC1}}{M_{PPOL,0,0}}, \quad (4.1)$$

were $I' = [\theta_{FLC1}, \theta_{SR1}, \theta_{FLC2}, \theta_{SR2}, \delta_{FLC1}, \delta_{SR1}, \delta_{FLC2}, \delta_{SR2}, k_{0^\circ}, k_{90^\circ}, \Theta'_{FLC1}, \Theta'_{FLC2}]^T$ and all the position angles are measured counter clockwise from $\theta_{PPOL} = 0^\circ$ (see Sect. 4.1). We adopt Eq. 2.40 to model the retardance dispersion of the FLCs and the SRs. Each FLC has two positions of its optical axis. We define θ_{FLC1} and θ_{FLC2} for the position where the optical axis is closer to 0° . Θ'_{FLC1} and Θ'_{FLC2} are the relative deviations of the FLCs optical axes measured counter clockwise from θ_{FLC1} and θ_{FLC2} respectively. The deviations are either 0° or the value of the switching angles (Θ_{FLC1} and Θ_{FLC2}). The four possible combinations of the FLCs states define the modulation scheme, with $N_{mod}=4$ and the following 4×4 modulation matrix (see Eq. 2.30)

$$\mathbf{O}(I) = \begin{bmatrix} 1 & \mathbf{h}^T([\dots, 0^\circ, 0^\circ]^T) \\ 1 & \mathbf{h}^T([\dots, \Theta_{FLC1}, \Theta_{FLC2}]^T) \\ 1 & \mathbf{h}^T([\dots, 0^\circ, \Theta_{FLC2}]^T) \\ 1 & \mathbf{h}^T([\dots, \Theta_{FLC1}, 0^\circ]^T) \end{bmatrix}, \quad (4.2)$$

were the vector I contains all the relevant modulator parameters

$$I = [\lambda, \theta_{FLC1}, \theta_{SR1}, \theta_{FLC2}, \theta_{SR2}, \delta_{0FLC1}, \delta_{0SR1}, \delta_{0FLC2}, \delta_{0SR2}, \lambda_{0FLC1}, \lambda_{0SR1}, \lambda_{0FLC2}, \lambda_{0SR2}, C_{FLC1}, C_{SR1}, C_{FLC2}, C_{SR2}, k_{0^\circ}, k_{90^\circ}, \Theta_{FLC1}, \Theta_{FLC2}]^T. \quad (4.3)$$

Note that FLC1 is driven at twice the frequency of FLC2 (see Fig. 3.3). For future reference we assume all the wavelengths in I are expressed in nm, all the angles in deg, all the δ_0 in fractions of λ and all the C in nm^3 .

¹UV radiation is energetic enough to dissociate the organic molecules that from the liquid crystal, permanently degrading its polarimetric properties.

The two main performance features relevant to the modulator design are the achievable polarimetric *sensitivity* and *accuracy*. The first limiting factor of the polarimetric accuracy is the quality of the polarimetric calibration, i.e. what are the errors when estimating the true $\mathbf{O}(\mathbf{l})$. Such errors, are further increased with any significant variation of \mathbf{l} between the calibration and the actual science measurement. Therefore, the sensitivity of $\mathbf{O}(\mathbf{l})$ to some of the parameters in \mathbf{l} determines important calibration requirements to ensure an accuracy better than 1 %, see Sect. 4.3.

If a good accuracy is obtained, the maximization of the polarimetric sensitivity — proportional to the $\epsilon(\mathbf{l})$ derived from $\mathbf{D}(\mathbf{l})$, see Eq. 2.35— becomes the most important driver of the modulator design, see Sect. 4.2.

4.2 Efficiencies optimization

The polarimetric response of the modulator components is strongly wavelength dependent, particularly for the FLCs. Therefore, the maximization (optimization) of $\epsilon(\mathbf{l})$ can be done as follows:

- *Optimization for a narrow spectral range:* Which has the advantage that typically larger $\epsilon(\mathbf{l})$ can be obtained. This implies, however, that observations at other wavelengths have either very low $\epsilon(\mathbf{l})$ or require a modification of the modulator. The latter implies exchanging some of the optical components and/or readjusting all the position angles.
- *Optimization for an achromatic response:* This approach seeks to have simultaneously the maximum $\epsilon(\mathbf{l})$ and the flattest dispersion. Even if, for a narrow spectral range the achromatic modulator may present lower $\epsilon(\mathbf{l})$, it allows multi-wavelength observations —either simultaneous or sequentially deferred— without the need of any modification.

Since the main FSP science goals demand vector-polarimetric observations across the whole optical range, an *achromatic and balanced modulator* was selected, i.e. with a goal $\epsilon(\mathbf{l}) \rightarrow \epsilon_{bal}$ in the 400 to 700 nm wavelength range. The balance of the efficiencies (see Eq. 2.38) implies that no preference is given for circular or linear polarization, e.g. due to the longitudinal and traversal Zeeman effects respectively. In spite of this, the adjustment of the components position angles was designed to allow a fast and accurate modification. This was done to permit a minor optimization in case a specific scientific program requires higher or unbalanced $\epsilon(\mathbf{l})$ in a narrow spectral range. The latter feature has, however, not been utilized in FSP yet.

The FLCs and SRs properties strongly affect the resulting $\epsilon(\mathbf{l})$ (see Fig. 4.2). In addition, the manufacturing tolerances of the components can be large, in particular for the FLCs (e.g. $\Delta\delta_{0FLC} = \pm 10\%$), and the retardance dispersion parameters can not be precisely controlled in the manufacturing process. To minimize the effect of such manufacturing tolerances in the modulator design, we applied the procedure described in the following three sections.

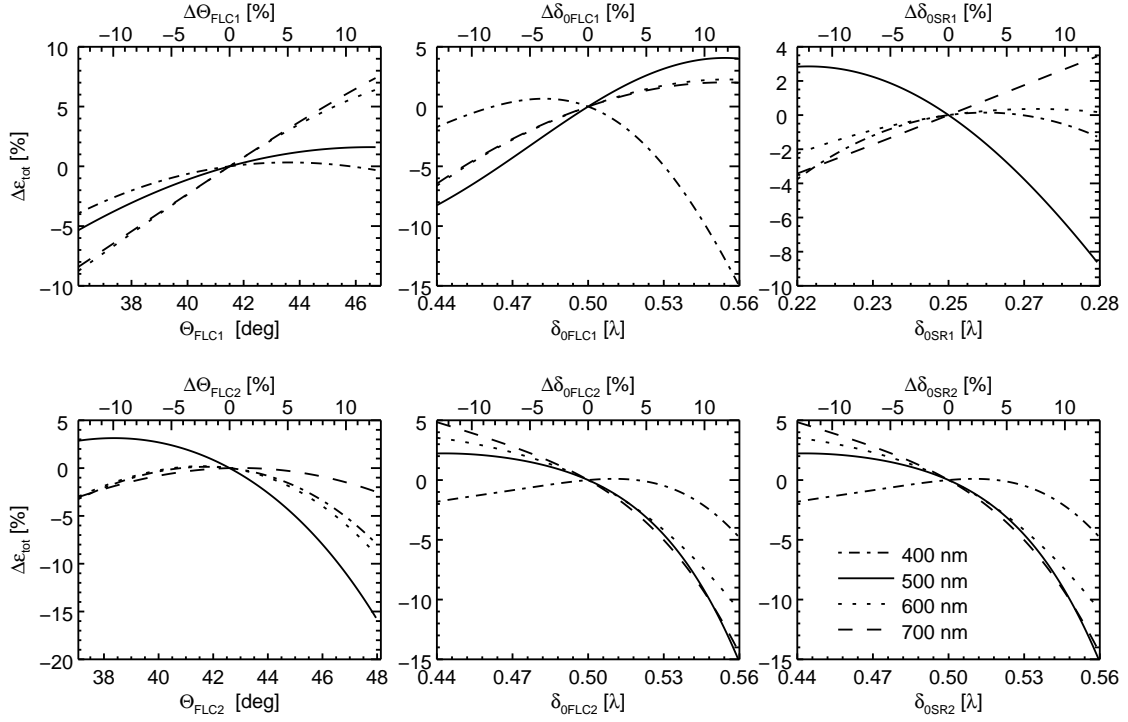


Figure 4.2. Sensitivity of the total polarimetric efficiency to variations in the FLCs switching angles and the retardances of all components. Each panel presents the simulated variation of $\epsilon_{tot}(I)$ (vertical axis) versus the change in a single modulator parameter (indicated in the label of each horizontal axis), for different wavelengths (line styles, see the legend). The modulator model employed is defined in Eq. 4.2. The model parameters corresponding to the origin in all panels, are given in Table 4.4.

4.2.1 Step 1: FLCs characterization

In the first step, two FLCs were purchased specifying a half-wave retardation at 460 nm wavelength, and a usable aperture of 25 mm. The two pieces acquired were characterized in order to determine the actual behavior of their δ_{FLC} , Θ_{FLC} and t_s with respect to changes in T , λ and the driving voltage (V).

To measure δ_{FLC} and Θ_{FLC} at a given wavelength, the FLC is placed in between two crossed linear polarizers and illuminated with quasi-monochromatic light. For each state of the FLC, the intensity resulting from such a setup, varies sinusoidally with the orientation of its position angle, following²

$$I = \kappa_0 \left\{ 1 + \cos \left[\frac{2\pi(\theta_{FLC} - \kappa_1)}{\kappa_2} \right] \right\} + \kappa_3, \quad (4.4)$$

where κ_0 , κ_1 , κ_2 and κ_3 are four constants $\in \mathbb{R}$.

An example of a measured I is given in Fig. 4.3a along with the resulting fits of the function given in Eq. 4.4 to the measurements of each state (denoted I_1 and I_2). δ_{FLC} is

²For each state, the retarder action of the FLC implies a $\delta_{FLC} \approx 180^\circ$ clockwise rotation of the incoming Stokes vector in the Poincaré sphere, around the axis defined by the FLC optical axis (see Eq. 2.17). Therefore, when illuminated with pure q , the output of the FLC is q (minimum intensity) if its optical axis is oriented in $\pm q$ direction. The output is $-q$ (maximum intensity) if the optical axis is in the $\pm u$ direction.

derived from (using the average of κ_3 of both states)

$$\delta_{FLC} = \frac{\cos^{-1}(2\kappa_3 - 1)}{2\pi}. \quad (4.5)$$

The position of the FLC optical axis (see point 2 in Sect. 2.1.2) in each state is given by the rotation angle that maximizes the corresponding output intensity at a fixed wavelength (see Fig. 4.3a). Let us call such angles $\theta_{FLC,max1}$ and $\theta_{FLC,max2}$, taken for two consecutive maxima of I_1 and I_2 respectively. Then, Θ_{FLC} is obtained from the difference $\theta_{FLC,max2} - \theta_{FLC,max1}$. In the later there is a 90° ambiguity —because the output is periodic²— that can be solved by measuring the Θ_{FLC} temperature dependence (see below).

To eliminate the ambiguity in the determination of the optical axis orientation, the FLC is fixed at $\theta_{FLC,max1}$ and an achromatic QWP is added to the setup after the first polarizer, in order to illuminate the FLC with pure circularly polarized light³. Due to the dispersion of the δ_{FLC} , the optical axis orientation in state 1 is $\theta_{FLC,max1}$ if the zero crossing of the curve $I_1(\theta_{FLC,max1}) - I_2(\theta_{FLC,max1})$ versus λ has positive slope. If not, the optical axis is oriented at $\theta_{FLC,max1} + 90^\circ$.

The main FLC characterization results are summarized in Fig. 4.3 and described below:

- *Retardance*: Fig. 4.3c and 4.3d show the measured dispersion of δ_{FLC1} and δ_{FLC2} respectively, for different T and a fixed $V_{FLC} = 11.0$ V. The values of C and λ_0 , resulting from fitting Eq. 2.40 with $\delta_0 = 0.5$ to the measurements, are reported in Table 4.1. δ_{FLC} decreases with temperature although the sensitivity is low, e.g. the (spectral) mean variation between the fitted dispersion functions at 15 and 40°C is approximately $-4 \times 10^{-4} \lambda^\circ\text{C}^{-1}$ for FLC2 (equivalent to $-0.15 \text{ \%}^\circ\text{C}^{-1}$ for the worst case $\delta_{FLC2} = 0.25\lambda$).

T_{FLC} [$^\circ\text{C}$]	C_{FLC1} $\times 10^7 [\text{nm}^3]$	λ_{0FLC1} [nm]	error $\times 10^{-3} [\lambda]$	C_{FLC2} $\times 10^7 [\text{nm}^3]$	λ_{0FLC2} [nm]	error $\times 10^{-3} [\lambda]$
15	-	-	-	1.42	439.7	7.1
22	-	-	-	1.46	438.8	6.8
30	1.48	454.4	9.0	1.41	435.8	4.9
40	1.44	451.9	6.1	1.45	434.2	7.0

Table 4.1. Measured FLCs dispersion constants. The error columns give the rms difference between the measured retardances and the fitted dispersion law (Eq. 2.40). The values with ‘-’ were not measured.

- *Switching time*: The FLCs are driven with two alternating⁴ square signals with switching time ~ 8.4 ns (and peak voltage V_{FLC}). The square, is the wave form that produces the fastest switching of the FLCs. Moreover, t_{sFLC} reduces with higher

³Note that, in this step the sense of rotation of stokes $+v$ is defined.

⁴The maximum offset component allowed in the FLCs driving voltage is 10 mV. The continuous application of a larger value may damage the device due to the migration of impurity ions towards the electric plates, and the subsequent apparition of a permanent electric field.

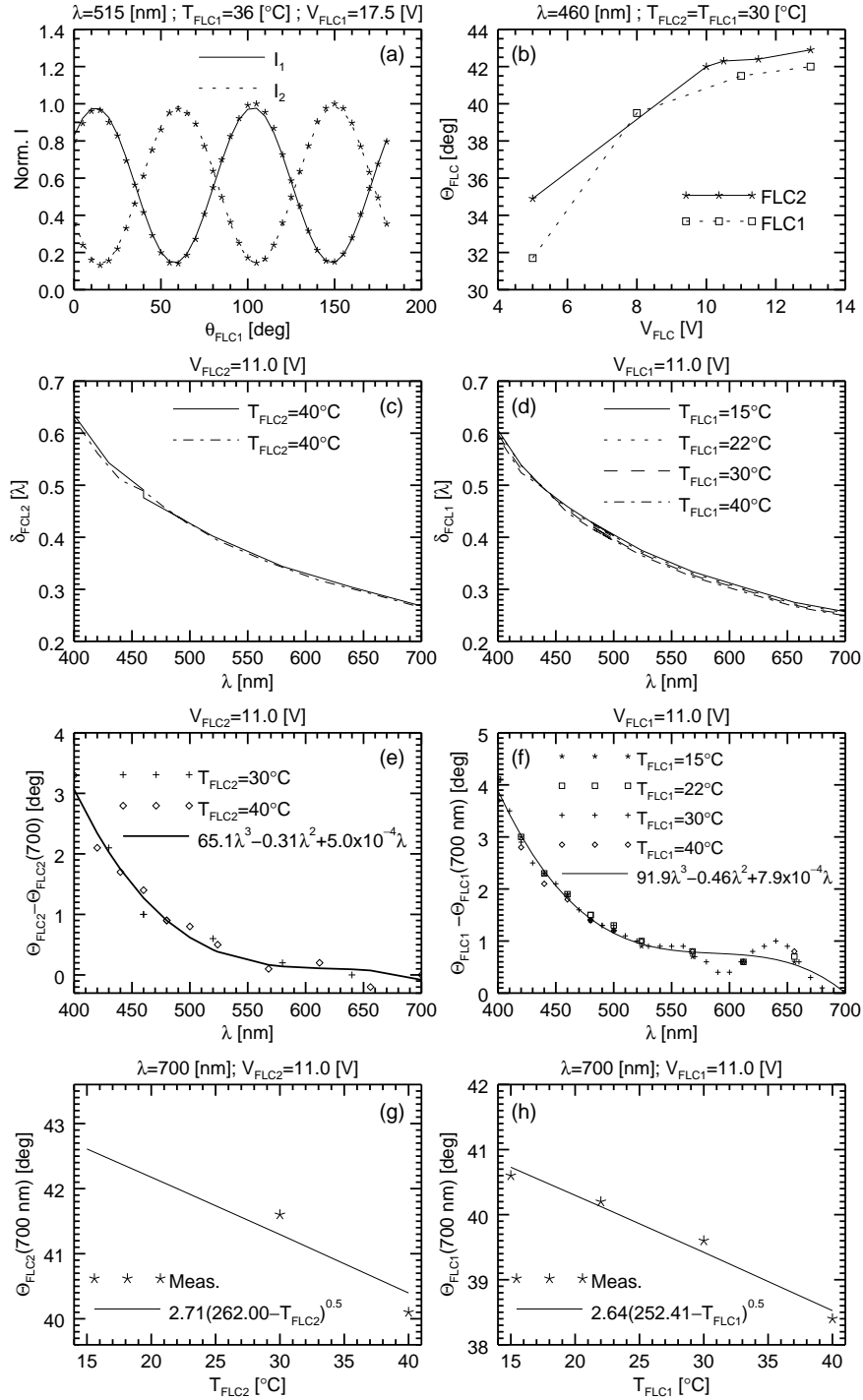


Figure 4.3. FLCs characterization results. The measurement conditions are specified in the title of each panel. (a) Variation of the output intensity versus position angle for both states of FLC1 (asterisks), along with the resulting fits of Eq. 4.4 (see legend). (b) Switching angle versus driving voltage for both FLCs (see legend). Retardance dispersion at different temperatures (see legends) for FLC2 (c) and FLC1 (d). Switching angle dispersion at different temperatures (see legends) for FLC2 (e) and FLC1 (f). In both cases the value of the switching angles at $\lambda = 700 \text{ nm}$ has been subtracted. The latter are shown in (g) and (h) for FLC2 and FLC1 respectively, along with the fitted temperature variation laws. See the text for extra details.

V_{FLC} ($t_{sFLC} \propto \Theta_{FLC}/E$), as reflected by the measurements given in Table. 4.2. t_{sFLC} is defined as the difference between the time instants where the output intensity is 10 % and 90 % of the stable state value, when the FLC is placed between crossed polarizers.

V_{FLC}	t_{sFLC1}	t_{sFLC2}
[V]	[μ s]	[μ s]
5	157.0	131.0
10	75.0	73.0
13	58.6	63.0

Table 4.2. Measured FLCs switching time at $T_{FLC} = 40^\circ\text{C}$, $\lambda = 460\text{ nm}$ and a driving frequency of 1 kHz.

- *Switching angle:* Θ_{FLC} increases with V_{FLC} (see Fig. 4.3b), in this respect driving the FLCs at higher voltages is desired (also to reduce t_s , see above). The maximum allowed voltage for the purchased FLCs is 25 V, thus, we adopted $V_{FLC1} = V_{FLC2} = 17.5\text{ V}$ (note in Fig. 4.3b that the variation begins to flatten off above $\sim 11\text{ V}$).

The measured dispersion of Θ_{FLC1} and Θ_{FLC2} are presented in Fig. 4.3e and 4.3f respectively, for different T and a fixed $V_{FLC} = 11.0\text{ V}$. For each temperature, the corresponding value of Θ_{FLC} at $\lambda = 700\text{ nm}$ has been subtracted from all the measurements to show that the temperature dependence of Θ_{FLC} is approximately wavelength independent⁵. The subtracted Θ_{FLC1} and Θ_{FLC2} are given in Fig. 4.3g and 4.3h respectively, along with the fitted temperature variation law (Eq. 2.41). Since for FLC1 only two temperatures were measured, the fit was restricted to have $d\Theta_{FLC1}/dT = d\Theta_{FLC2}/dT$ for $T_{FLC1} = T_{FLC2} = 36^\circ\text{C}$, namely⁶ $-0.09\text{ deg }^\circ\text{C}^{-1}$.

- *Transmission:* Both FLCs present a measured transmittance above 80 % in the 440 to 700 nm wavelength range. From 400 to 440 nm the transmittance is still above 40 %.

4.2.2 Step 2: First optimization and SRs characterization

The measured properties of the FLCs were used to compute a first set of optimum θ for all the components and the values of δ_{SR1} and δ_{SR2} . The optimization, performed using the software developed by Gisler (2005), minimizes the squared differences between the ϵ of the modulator model given by Eq. 4.2 and ϵ_{bal} (Eq. 2.38), in the 400 to 700 nm wavelength range. Since the modulator model does not include the dispersion of Θ_{FLC1} and Θ_{FLC2} ⁵, we used the values at 460 nm, $T = 36^\circ\text{C}$ and $V_{FLC} = 17.5\text{ V}$, i.e. 41.5° and 42.6° respectively⁷. After this first optimization, two 25 mm SRs were purchased

⁵The physical effect that produces the variation of Θ_{FLC} with λ measured here, is not reported in the literature and needs further investigation.

⁶This value is low compared to the typical temperature dependence in FLCs, e.g Feller (2002) found $d\Theta_{FLC}/dT \approx -0.5\text{ deg }^\circ\text{C}^{-1}$.

⁷Measured in a separate characterization campaign and thus not shown in Fig. 4.3.

specifying the values of δ_{SR1} (quarter-wave plate at 488 nm) and δ_{SR2} (half-wave plate at 532 nm) found. The acquired components were characterized to determine the actual dispersion of their retardances (see Table 4.3) and location of their optical axes.

T_{SR} [°C]	C_{SR1} $\times 10^6 [\text{nm}^3]$	λ_{0SR1} [nm]	error $\times 10^{-3} [\lambda]$	C_{SR2} $\times 10^6 [\text{nm}^3]$	λ_{0SR2} [nm]	error $\times 10^{-3} [\lambda]$
25	2.39	510.76	1.0	5.50	517.67	17.7

Table 4.3. Measured SRs dispersion constants. The error columns give rms difference between the measured retardances and the fitted dispersion law (Eq. 2.40).

4.2.3 Step 3: Final optimization and results

The measured dispersions of the SRs were used to run a second optimization, this time specifying only the θ of all the components as free parameters. The final measured properties used in the modulator model, along with the optimum position angles found are listed in Table 4.4. A comparison of the measured (see Sect. 4.3) and modeled optimum efficiencies is given in Fig. 4.4. Note that the agreement between the model and measurements is good (errors are $<10\%$), considering that the dispersion of Θ_{FLC1} and Θ_{FLC2} are not considered in the former. Another potential error source is the limited accuracy when setting the optimum position angles found in the modulator. This is due to the limited accuracy during the initial determination of the components' optical axes ($\pm 1^\circ$, see Sect. 4.2.1) and when rotating their mechanical cases ($\pm 0.5^\circ$). This effect is, however, only in the percentage level according to simulated sensitivity values of the total polarimetric efficiencies (see Table 4.5).

Property	FLC1	SR1	FLC2	SR2	PPOL	Unit
Θ	41.5	-	42.6	-	-	°
δ_0	0.5	0.25	0.5	0.5	-	λ
λ_0	451.9	510.8	434.2	517.7	-	nm
$C (x10^7)$	1.46	0.24	1.43	0.55	-	nm^3
k_{0°	-	-	-	-	0.99	-
k_{90°	-	-	-	-	0.02	-
Opt. θ	-71.8	26.7	-41.5	64.8	0	°

Table 4.4. Properties of the optical components in FSP modulator. These parameters defined the model (Eq. 4.2) used to derive the optimum position angles (given in the last row). See the text for extra details.

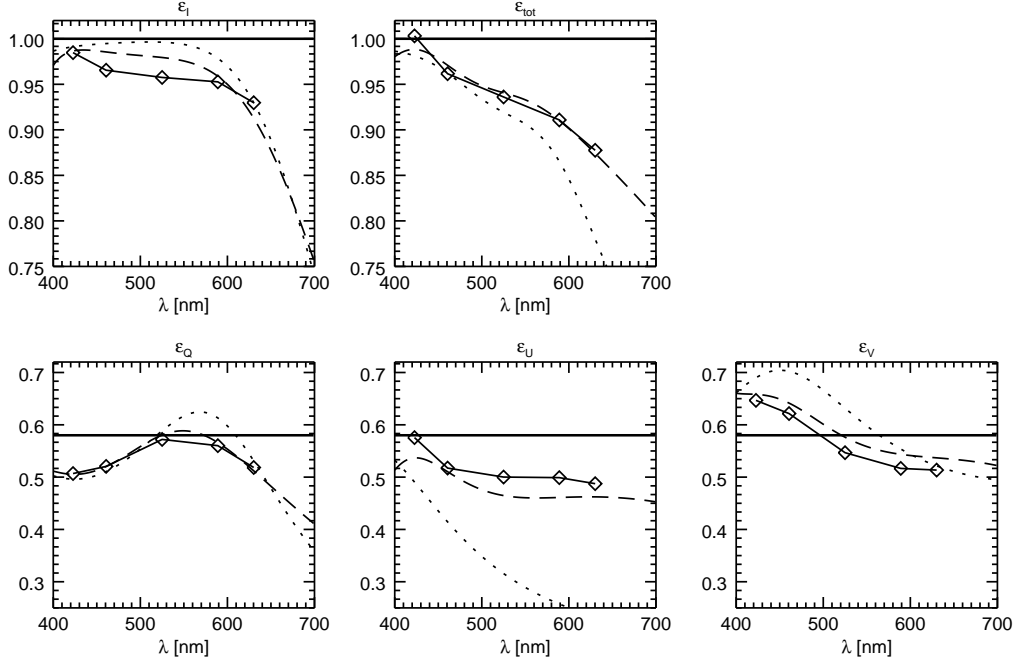


Figure 4.4. Measured (diamonds) and modeled FSP polarimetric efficiencies. The results of the modulator model—used to compute the optimum position angles, see Table 4.4—is shown with dashed lines. To emphasize the necessity of a proper description of the retardances’ dispersion, we also present the results of the same modulator model, except that all C were set to zero (dotted). The horizontal continuous lines represent the polarimetric efficiencies of an ideal and perfectly balanced modulator (Eq. 2.38). Adapted from Iglesias et al. (2016)

	θ_{FLC1}	θ_{SR1}	θ_{FLC2}	θ_{SR2}	θ_{PPOL}	Unit
$d\epsilon_{tot}/d\theta$	4.3	5.3	13.7	17.2	8.6	10^{-3} deg^{-1}

Table 4.5. Sensitivity of the total polarimetric efficiency to variations in the position angles. The table gives the simulated maximum values of $d\epsilon_{tot}/d\theta$ in the 400 to 700 nm wavelength range, assuming one element is rotated at a time. The model used is defined in Table 4.4.

4.3 Polarimetric calibration

In order to estimate \mathbf{O} , a series of N_{cal} calibration measurements are acquired using as input the Stokes vectors generated by the PSG (see Eq. 3.5 and 2.29),

$$\hat{\mathbf{I}}_{cal,j} = \mathbf{O} \begin{bmatrix} 1 \\ \mathbf{M}_{PSG,1,0}(\theta_{ret,j}, \lambda) \\ \mathbf{M}_{PSG,2,0}(\theta_{ret,j}, \lambda) \\ \mathbf{M}_{PSG,3,0}(\theta_{ret,j}, \lambda) \end{bmatrix} + \mathbf{N}_j = \mathbf{O} \mathbf{s}_{PSG,j} + \mathbf{N}_j, \quad (4.6)$$

where $j \in \{0, 1, \dots, N_{cal} - 1\}$, \mathbf{s}_{PSG} is the normalized Stokes vector and \mathbf{N}_j represent the noise in measurement number j . In Eq. 4.6 we have dropped the output intensities of the PSG because they do not affect the retrieved \mathbf{O} , as long as they are the same for all the N_{cal} measurements (see Sect. 4.3.1). Since the noise is random (not known) and the true calibration Stokes vectors may differ from \mathbf{s}_{PSG} due to errors in the PSG model; only

an estimation of \mathbf{O} can be obtained. If the noise is neglected in Eq. 4.6, and the N_{cal} measurements are grouped using block matrices, the estimated (measured) \mathbf{O} , $\hat{\mathbf{O}}$, can be computed as follows (see e.g. Beck et al. 2005a, for a derivation),

$$\hat{\mathbf{O}}^T = \begin{bmatrix} \mathbf{s}_{PSG,0}^T \\ \mathbf{s}_{PSG,1}^T \\ \vdots \\ \mathbf{s}_{PSG,N_{cal}-1}^T \end{bmatrix}^{-1} \begin{bmatrix} \hat{\mathbf{I}}_{cal,0}^T \\ \hat{\mathbf{I}}_{cal,1}^T \\ \vdots \\ \hat{\mathbf{I}}_{cal,N_{cal}-1}^T \end{bmatrix}. \quad (4.7)$$

If $N_{cal} = 4$, the inverse in Eq. 4.7 can be directly computed (given properly chosen \mathbf{s}_{PSG}) because the matrix is squared and non-singular. In practice $N_{cal} > 4$ is used, and $\hat{\mathbf{O}}$ is obtained in a least square fashion by computing the inverse in Eq. 4.7 using the SVD pseudo-inverse. Note that, each row of $\hat{\mathbf{O}}$ has to be normalized (divided by the element in the first column) in order to match the definition given in Eq. 4.2.

The measured calibration Stokes vectors are then obtained using the estimated demodulation matrix, $\hat{\mathbf{D}}$, as follows

$$\hat{\mathbf{S}}_{cal,j} = \hat{\mathbf{O}}^{-1} \hat{\mathbf{I}}_{cal,j} = \hat{\mathbf{D}} \hat{\mathbf{I}}_{cal,j}. \quad (4.8)$$

A typical set of FSP calibration measurements (with $N_{cal} = 18$) are given in Fig. 4.5. Since the uncertainty in θ_{ret} of the PSG can introduce a large error in \mathbf{s}_{PSG} (see Eq. 3.6), we leave its value as a free parameter to fit by minimizing the residuals of the calibration measurements, namely the $\Delta \mathbf{s}_{cal,j} = \hat{\mathbf{s}}_{cal,j} - \mathbf{s}_{PSG,j}$ given in Fig. 4.5⁸. The $\hat{\mathbf{O}}$ derived from the measurements in Fig. 4.5 is shown in Table 4.6.

$$\begin{bmatrix} 1.000 & 0.200 & 0.791 & 0.557 \\ 1.000 & -0.606 & -0.788 & -0.090 \\ 1.000 & 0.150 & 0.034 & -0.976 \\ 1.000 & 0.970 & -0.152 & 0.129 \end{bmatrix}$$

Table 4.6. Example FSP modulation matrix at $\lambda = 630.2$ nm. The figures correspond to the average over the sensor area.

Any difference between the $\hat{\mathbf{O}}$ estimated in the calibration and the true \mathbf{O} present during the acquisition of the science data will harm the instrument polarimetric accuracy. Let us denote the true modulation matrix at the time of the calibration as $\mathbf{O}(\mathbf{I}_{cal})$, and assume it was estimated with no errors, i.e. $\hat{\mathbf{D}}(\mathbf{I}_{cal}) = \mathbf{O}^{-1}(\mathbf{I}_{cal})$. Then, the Stokes vector acquired during a measurement where the modulation matrix has changed a small amount $\Delta \mathbf{O}$, can be expressed as follows,

$$\hat{\mathbf{S}} = \hat{\mathbf{D}}(\mathbf{I}_{cal})[\mathbf{O}(\mathbf{I}_{cal}) + \Delta \mathbf{O}]\mathbf{S}. \quad (4.9)$$

⁸The minimization is done in a least square sense, i.e. minimizing the rms $\Delta \mathbf{s}_{cal}$ with respect to a (constant for all j) error in $\theta_{ret,j}$ (this requires evaluating Eq. 3.5, 4.7 and 4.8 for each iteration of the minimization). This procedure, detailed in Beck et al. (2005b), can also be used to fit the δ of the PSG. We do not do it here because the measured δ (Fig. 3.4) has proven to be accurate enough, i.e. fitting it does not considerably reduced the calibration residuals.

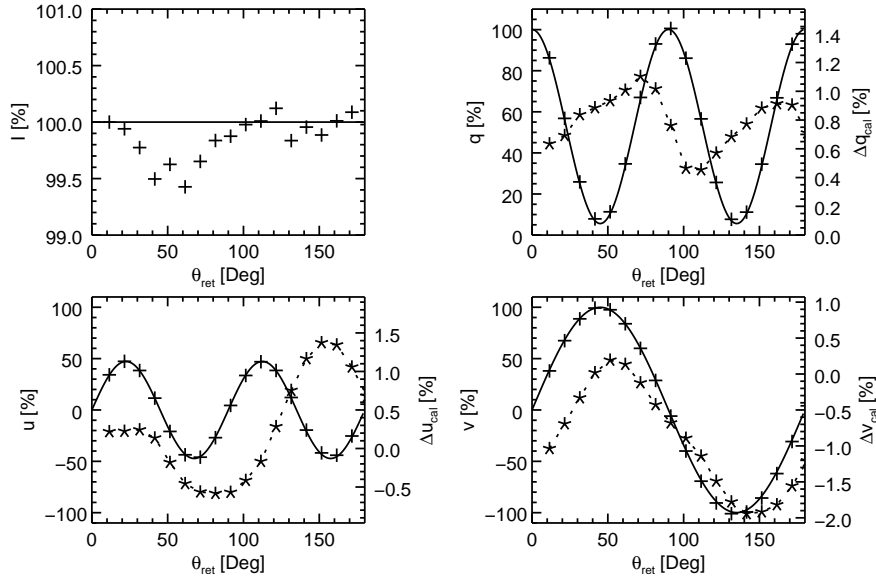


Figure 4.5. Example FSP calibration measurements at $\lambda = 630.2$ nm. Both the modeled (continuous line) and measured (+ symbols) normalized Stokes parameters are shown for each position angle of the retarder in the PSG (referring to the left scale). The difference (residuals) are denoted with asterisks (referring to the right scale). The measurements correspond to the average values over the sensor area. The fitted value of θ_{ret} for the retarder in the PSG is 1.51° . The values of I are normalized to the first calibration position.

$\Delta \mathbf{O}$ can be produced by a variation in any of the elements of \mathbf{I} , either because they were intentionally modified —e.g. in a typical filtergraph-based line scan, the calibration is acquired in a single spectral point such as line continuum and used to demodulate all the measurements— or because they present spurious variations (e.g. the temperature-induced change of Θ_{FLC}).

We have collected in Table 4.7 the maximum allowed values for $\Delta \mathbf{O}$, that keep the errors (defined with respect to the $\Delta \mathbf{O} = 0$ case) in the measured $\hat{\mathbf{s}}$ of Eq. 4.9 below 1×10^{-4} . Since such errors are multiplicative, they scale approximately with the value of the instrumental polarization⁹. Therefore, we show in Table 4.7 two tables that assume two typical instrumental polarization levels, namely 1 % and 5 %. Note that, all the elements in the first column of $\Delta \mathbf{O}$ are zero because the modulation matrix is normalized.

In the rest of the present section (except Sect. 4.3.1) we use the figures in Table 4.7, as a reference to evaluate the errors introduced by the variations of common variables that affect the FSP modulation matrix. This is done to derive the maximum allowed variations of λ before a new calibration is required and the stability criterion for the modulation frequency and the modulator temperature.

4.3.1 Spatial dependence

The modulation matrix presents variations across its aperture due to the spatially variable properties of the SRs, FLCs and the beam splitter cube in the modulator. In FSP the

⁹We are considering here the measurement of a weak ($\ll 1$ %) solar signal. Therefore, the instrumental polarization level dominates the value of \mathbf{S} in Eq. 4.9. Moreover, in general it also determines the offset or zero polarization level, because the solar continuum is practically unpolarized close disk center.

$$\begin{bmatrix} - & 0.032 & 0.032 & 0.032 \\ - & 0.020 & 0.020 & 0.020 \\ - & 0.012 & 0.012 & 0.012 \\ - & 0.020 & 0.020 & 0.020 \end{bmatrix} \begin{bmatrix} - & 0.006 & 0.006 & 0.006 \\ - & 0.004 & 0.004 & 0.004 \\ - & 0.002 & 0.002 & 0.002 \\ - & 0.004 & 0.004 & 0.004 \end{bmatrix}$$

Table 4.7. Maximum allowed variations of the modulation matrix elements. The tables present the absolute value of $\Delta\mathbf{O}$ that produces an error equal to 1×10^{-4} in the retrieved q , u or v of Eq. 4.9. Two cases are given, firstly using $\mathbf{S} = [1, 0.01, 0.01, 0.01]$ (leftmost table) and secondly $\mathbf{S} = [1, 0.05, 0.05, 0.05]$ (rightmost table), e.g. due to 1 % and 5 % instrumental polarization respectively. We also assume that only one element varies at a time, that $\mathbf{O}(\mathbf{I}_{cal})$ is the one given in Table 4.6, that $\hat{\mathbf{D}}(\mathbf{I}_{cal}) = \mathbf{O}^{-1}(\mathbf{I}_{cal})$ and that all the elements in the first column of $\Delta\mathbf{O}$ are zero.

modulator is located close to a focal plane to avoid FLCs-induced image jitter (see Sect. 6.4.5). As a consequence, \mathbf{O} may vary across the FOV . If this is the case, and the same (spatially averaged) $\hat{\mathbf{D}}$ is used to demodulate (Eq. 4.8) all the pixels in the image (*scalar demodulation*), then a non-flat error is introduced. In FSP such errors are at the $\sim 1\%$ level, this can be seen by looking at the calibration residuals in Fig. 4.5 where a scalar demodulation was used, see also below.

To eliminate the errors introduced when performing a scalar demodulation, a *field dependent demodulation* has to be applied, i.e. Eq. 4.8 is solved independently for each pixel using the corresponding $\hat{\mathbf{O}}$. Unfortunately, this is not possible with the calibration technique used here because the spatial variations of the estimated $\hat{\mathbf{O}}$ —obtained using Eq. 4.7—are dominated by the errors introduced by the violation of the assumption of constant output intensities of the PSG¹⁰, see Fig. 4.6. Feller (2007) developed a technique to eliminate the errors introduced by a variable illumination during calibration. Such a technique, which involves taking extra calibration measurements to estimate not only the 16 elements of \mathbf{O} but also the N_{cal} input intensities, is planned to be implemented for FSP in the near future. This will allow the application of a field dependent demodulation with the subsequent increase in polarimetric accuracy (e.g. to eliminate the residual gradients present in Fig. 4.6c).

4.3.2 Spectral dependence

The measured dispersion of the FSP modulation matrix is shown in Fig. 4.7 (for a plot of the associated efficiencies see Fig. 4.4). Let us estimate the maximum variations of each element as the maximum measured slopes, given in the titles of each panel. Then, the comparison (in particular element {2, 1}) with the figures in Table 4.7 determines that a new polarimetric calibration has to be acquired for changes in the wavelength that are larger than ~ 1 nm and ~ 0.1 nm considering 1 % and 5 % instrumental polarization respec-

¹⁰ The assumption of constant output intensities of the PSG implies that its input Stokes I , Q and U , are constant during the calibration time. The acquisition of all the N_{cal} calibration takes ~ 5 min to complete. While Q and U do not change much in this time scale—because the changes in the instrumental polarization are negligible— I cannot be considered constant. In particular, because the calibrations were acquired using the telescope in flat field mode, i.e. with the pointing moving around the solar disk center (see Sect 6.1.1). The latter, added to the intrinsic contrast of solar granulation ($\sim 10\%$), results in a temporal variation of the individual pixels illumination.

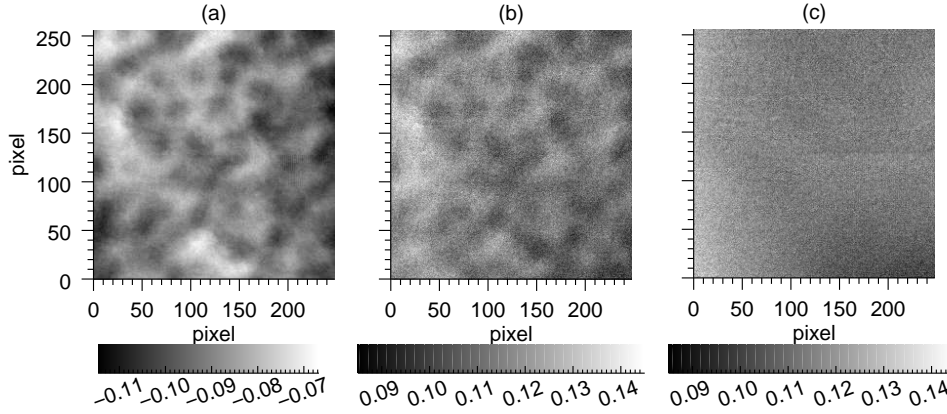


Figure 4.6. Spatial variation of the FSP modulation matrix due to errors during calibration. Image (a) shows element $\{1, 3\}$ of the $\hat{\mathbf{O}}$ given in Table 4.6. The spatial variations seen here are not present in the real \mathbf{O} , they are the errors introduced by the fluctuations of the input intensity during the calibration (e.g. due to the solar granulation contrast combined with the telescope movement imposed during calibration). The latter can be seen for example when comparing the Stokes u (corresponding to measurement $j = 3$ in Fig. 4.5) obtained using a field dependent demodulation (b) and a scalar demodulation (c), which is the technique used in this work. The remaining spatial variations present in (c) are due to changes in \mathbf{O} (plus any artifact introduced by the camera). See the text for extra details.

tively. Note that, the typical line width is less than ~ 0.1 nm justifying the acquisition of a single calibration, at say the continuum spectral point, to calibrate all the measurements of a filtergraph-based line scan.

4.3.3 Modulation frequency dependence

In order to maximize DC and due to the high FR , FSP does not use a shutter in front of the pnCCD camera¹¹. The two main consequences are that frame transfer effects may appear (this is discussed in Sect. 5.2) and that there is signal accumulated during the modulator switching time. The latter produces a reduction of the SNR in the measured polarimetric signals and a reduction of the ϵ .

The only variable components in the modulator are the FLCs, which present a smooth transition between the two positions of their optical axes (see Dubreuil et al. 2010, for a high temporal resolution measurement of \mathbf{M}_{FLC} during switching). Therefore, the variation of the modulator Mueller matrix is determined by the FLCs switching time. Since at $V_{FLC} = 17.5$ V, $t_{sFLC} \approx 50 \mu s$ (obtained from an extrapolation of the values in Table 4.2), i.e. it corresponds only to 4 % of the modulation state duration at the highest $f_{mod} = 200$ Hz; the reduction of ϵ_{tot} with increasing f_{mod} is small (see Fig. 4.8).

The required long term stability (in the hours range) of f_{mod} , to keep the errors produced by the associated change of the modulation matrix below 1×10^{-4} , is approximately 1 Hz for an instrumental polarization ≤ 5 %. The latter can be estimated from the measured

¹¹ A mechanical shutter reduces DC when continuously operating at 400 Hz, moreover the fastest designs usually involve a non-global exposure. An optoelectronic solution introduces extra optical components contributing to a lower throughput, among others. Using no shutter also reduces hardware and error sources because no extra synchronizations are required.

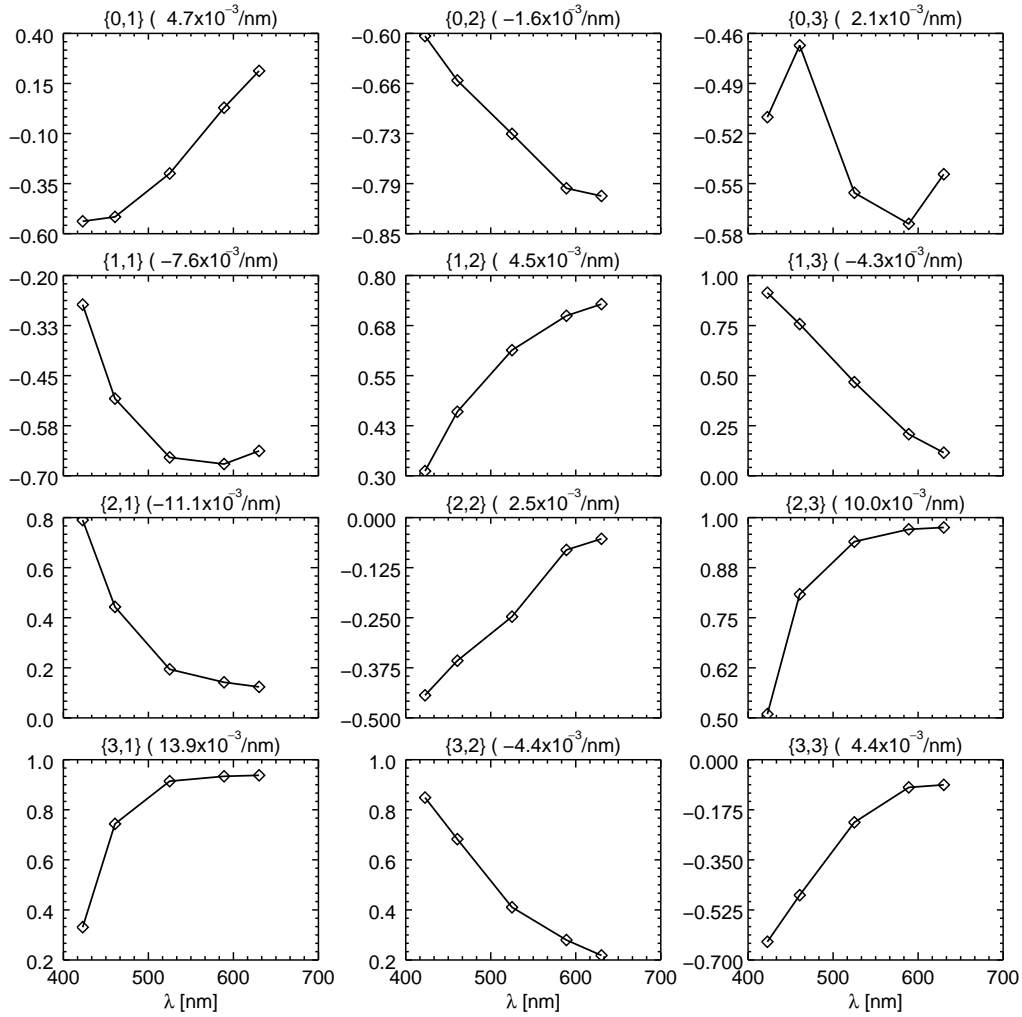


Figure 4.7. Measured dispersion of the FSP modulation matrix. The first column of the matrix (with all elements equal to one) is not shown here. The maximum slope of each curve is given in parentheses in the title of the respective panel. All figures correspond to the averages over the sensor area.

changes (in particular element $\{2, 1\}$) of $\hat{\mathbf{O}}$ versus f_{mod} shown in Table 4.8, and the figures given in Table 4.7. The stability specified above is easily satisfied by the function generator that produces the FLCs driving signals (see Sect. 3.2.2), which presents a long term variation of the output frequency of ± 2 ppm of the set value ± 15 pHz.

4.3.4 Thermal dependence

A change in the modulator temperature modifies the FLCs switching angles (see Sect. 4.2.1) and thus the modulation matrix. We can estimate this effect by combining the modulator model defined in Table 4.4, with the fitted temperature variation laws for both Θ_{FLC1} (Fig. 4.3h) and Θ_{FLC2} (Fig. 4.3g).

Table 4.9 shows the maximum variations of each element in \mathbf{O} derived from such an estimation, assuming that $T_{FLC1} = T_{FLC2}$. Note that, from a comparison (in particular element $\{2, 1\}$) of the figures in Table 4.9 and those given in Table 4.7, we can conclude

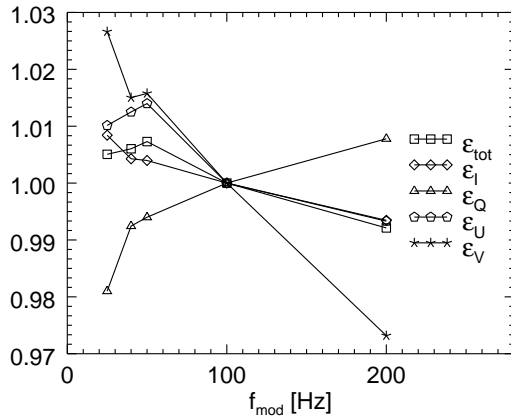


Figure 4.8. Measured variation of the FSP polarimetric efficiencies (see legend) with modulation frequency at $\lambda = 525$ nm. Each curve has been normalized to the 100 Hz point.

-	0.024	0.004	0.002
-	0.002	0.004	-0.003
-	-0.025	0.006	-0.010
-	0.017	0.013	0.010

Table 4.8. Variation of the FSP modulation matrix with modulation frequency. The figures give the maximum measured change of each element in $\hat{\mathbf{O}}$ for f_{mod} in the 20 to 200 Hz range and $\lambda = 525$ nm, expressed in daHz^{-1} .

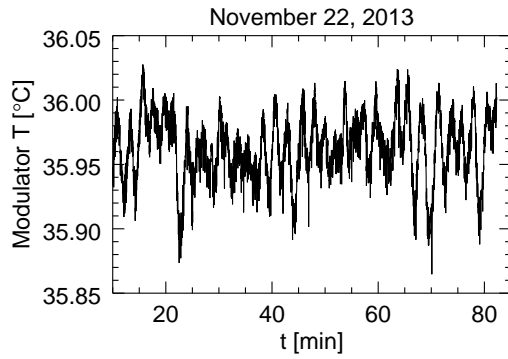


Figure 4.9. Measured modulator housing temperature, during a typical observation at the VTT. The series shown here has a mean of 35.96°C , a standard deviation of 0.025°C and a maximum deviation from the mean of 0.099°C .

-	0.000	0.000	0.000
-	0.006	0.006	0.004
-	0.005	0.001	0.005
-	0.005	0.005	0.001

Table 4.9. Simulated thermal variation of the FSP modulation matrix. The table gives the maximum absolute derivative with respect to T_{FLC} (expressed in $^\circ\text{C}^{-1}$), for λ from 400 to 700 nm and T_{FLC} from 15 to 40°C . See the text for extra details.

that a long term (in the hours range) stability of the modulator housing temperature of $\Delta T \approx 0.1^\circ\text{C}$ is sufficient to keep the inaccuracies produced by the variations of \mathbf{O} below 1×10^{-4} (assuming constant thermal gradients). Fig. 4.9 presents the thermal stability achieved with the current thermal control system (see Sect. 4.1).

5 Characterization and optimization of a pnCCD camera for fast imaging polarimetry

As emphasized in Chapter 3, the bottle neck of a synchronous, high-cadence polarimeter, is the camera used to detect the modulated intensities. Particularly critical are its total noise, frame rate and duty cycle. In addition, differential artifacts, i.e. varying from exposure to exposure, are likely to appear as a polarimetric spurious signal and thus, are also relevant for high-sensitivity polarimetry.

This chapter introduces the pnCCD camera that was custom made to be used in FSP (Sect. 5.1). In Sect. 5.2.2 the synchronization between camera and the polarization modulator is selected and the general expression for the signal acquisition, including that collected during the shutter-less frame transfer, is presented (Sect. 5.2). The latter allows the development of a post-facto numeric technique to eliminate the smearing introduced during frame transfer, in the presence of strongly polarized sources. A characterization of the camera performance with emphasis on its usage for imaging polarimetry is also presented. This includes assessing the polarimetric effects of gain non-linearities and residual offsets (Sect. 5.3), and characterizing the different noise sources (Sect. 5.5); including readout (Sect. 5.4.4), dark (Sect. 5.4.5) and most notably the common mode noise (Section 5.4.1). Finally, a brief discussion of the photon-noise limited regime in polarimeters (Sect. 5.5) helps to emphasize the advantages of a low noise camera such as the one used in FSP. Some of the contents of the present chapter have been literally published in Iglesias et al. (2015) and Iglesias et al. (2016).

5.1 Design and specifications

The pnCCD camera used in FSP employs a fully-depleted, back-illuminated CCD sensor commonly called pnCCD. pnCCDs are part of a family of devices that have been invented since their basic working principle, the sideward depletion¹, was introduced in 1983 (see Castoldi and Guazzoni 2012, for an historical review). Sideward depletion strongly increased the CCDs QE , and considerably reduced their output capacitance (even for large

¹In a nutshell, the sideward depletion consists of fully depleting an e.g. n-type semiconductor wafer by sandwiching it with two p^+ implants. The two junctions are reversed biased with increasing voltages until their depletion regions merge in the interior of the n-type substrate. This technique allows full depletion with bias voltages that are four times lower than previously needed in a conventional p^+nn^+ structure (Lechner et al. 2004).

area devices) among others. The later, in addition, particularly pushed the development of high-performance readout electronics that has low σ_{ro} and high FR , including, the very important introduction of the on-chip amplifier.

The first pnCCD was demonstrated in 1988 for X-ray spectroscopy (Strueder et al. 1988). Since then, many of the most successful developments and applications of this kind of sensors to astrophysics, have been done at the Max Planck institute for extraterrestrial physics and the semiconductor lab of the Max Planck Society, initially together with PNSensor GmbH. They developed the first versions of the pnCCD sensor and readout ASIC—the CMOS amplifier and multiplexer (CAMEX)—employed in FSP, for X-ray imaging in the successful XMM-Newton space mission launched in 1999 (Strueder et al. 2000). Further improvements were made for another X-ray application in space on board of the ROSITA mission (Meidinger et al. 2003). The high QE and FR with low σ_{ro} of the above-named pnCCD systems, have also promoted their usage for imaging in optical and near IR wavelengths since 2006 (Hartmann et al. 2006). Particularly suitable applications were found in astronomy either as main imager or as wavefront sensor for AO systems (see Ihle et al. 2012, and references therein).

The above-named benefits on FR and σ_{ro} of the pnCCD (further detailed below), are clearly in line with the camera requirements of a high-cadence solar polarimeter (see Sect. 3.1.1). The latter has triggered the development of FSP, which constitutes the first application of a pnCCD to solar polarimetry.

5.1.1 pnCCD sensor and readout electronics

The basic internal structure of the three-phase pnCCD sensor used in the FSP camera is presented in Figs. 5.1a and b. The main detector features, that are most relevant to its application in a high-cadence polarimeter, are enumerated below. See Table 3.2 for further detector properties, and also Ihle et al. (2008) and Hartmann et al. (2006).

1. *Fully depleted, back illuminated pnCCD*: The fully depleted volume of the sensor increases its QE in the whole optical range. The photocharges generated by higher energy photons (with short penetration depths) are more likely to reach the accumulation region—located at the electron potential minimum at around $8\mu\text{m}$ of the front side—because the bulk of the sensor is devoid of free charges for recombination and the electric field in its interior is large. This permits having a back illuminated device with thicker substrate (compared to usual CCDs), which in turn greatly improves the efficiency in detecting lower energy photons (with high penetration depths). The back illumination also allows to reach $FF = 100\%$; to avoid etaloning in applications with very narrow spectral bandwidth, like solar spectropolarimetry; and to have a thin and homogeneous entrance window which has low absorption and—along with the reduced reflectivity when depositing anti-reflecting coatings on it—contributes to further increase the QE in the blue (see Fig. 5.1c). The buried transfer channel contributes to a low *charge transfer inefficiency* ($<5 \times 10^{-5}$). In addition, the fully depleted volume and large pixels, among other properties, allow the sensor to reach FWC up to $1 \times 10^5 e^-$ (although this is not a critical parameter because modern solar polarimetry is generally photon starved, see Sect 2.1.4).

2. *Column parallel readout and split frame transfer architecture*: The sensor presents channel parallel readout, i.e. every semi-column has independent readout circuitry (see below) and is read in parallel. The readout is split and each half of the light sensitive area is quickly transferred to a shielded frame storage after each exposure (see Sect. 5.2 for further details on this process). The two above-named technologies (plus the fast readout of the CAMEX, see below) allow the sensor to reach simultaneously high *FR* and *DC* (see Table 3.2).
3. *On chip amplifiers plus CAMEX readout ASICs*: Each semi-column of the sensor ends in a low-noise, on-chip JFET amplifier. The output of each on-chip amplifier is in turn bonded to a single channel of the readout ASICs, the CAMEX (see Herrmann et al. 2008, Hartmann et al. 2006). Each CAMEX has 132 readout channels that are read in parallel and then multiplexed to two analog serial outputs (64 channels per output). A single readout channel of the CAMEX is conformed among others by (a) a current source to bias the pnCCD on-chip amplifier; (b) a first JFET low noise amplification stage; (c) a second amplification stage, with 8-fold correlated double sampling for noise reduction²; (d) a sampling and hold stage that allows starting the amplification of the next CCD row while the multiplexing of the current row is still in progress (further increasing the *FR*); and (e) a serializer. The CAMEX also features fully programmable gains and digital to analog converters and reference voltages, for the internal generation of the bias voltages of each stage (eliminating the need of many external power supply lines). The above-named characteristics of the readout CAMEX plus the low noise figures of the on-chip amplifier (possible due to the low output capacitance of the fully depleted channel) are the main causes of the very low σ_{ro} (Sect. 5.4.4) and *NL* (Sect. 5.3).
4. *Others*: The light sensitive area of the CCD sensor in FSP is small³, i.e. $N_{col} \times N_{row} = 248 \times 256 \text{ pixel}^2$ (see point 6 in Sect 3.1.1). Note that, 8 additional columns and 4 rows are covered by an aluminum shield in each side of the light sensitive area. The shielded columns are used to filter the common mode artifact (see Sect. 5.4.1). The shielded rows help to prevent stray light in the adjacent rows of the frame storage areas. The *image area* of the sensor is $12.7 \times 12.7 \text{ mm}^2$.

5.1.2 pnCCD camera

An overview of the pnCCD camera system, including housing, main connections and associated readout electronics rack is given in Fig. 5.2 (see Ihle et al. 2012, for a description of a similar system). The sensor is located in an evacuated compartment of the camera housing, and is cooled down using two two-stage Peltier elements that are pre-cooled using a cool water circuit. The maximum dimensions of the camera housing are $170 \times 165.8 \times 227.9 \text{ mm}$. The 8 analog outputs of the CAMEX are connected to one

²This means that the output of the first amplifier stage is sampled eight times after the reset, and another eight times after the charges are read. The samples before and after the reset are then subtracted one to one and the eight resulting values averaged to form the output signal, see also footnote 15 in Sect. 2.2.4.

³We used $N_{col} \times N_{row} = 264 \times 264 \text{ pixel}^2$ in Table 3.2 because this are the amount of pixels read in every exposure.

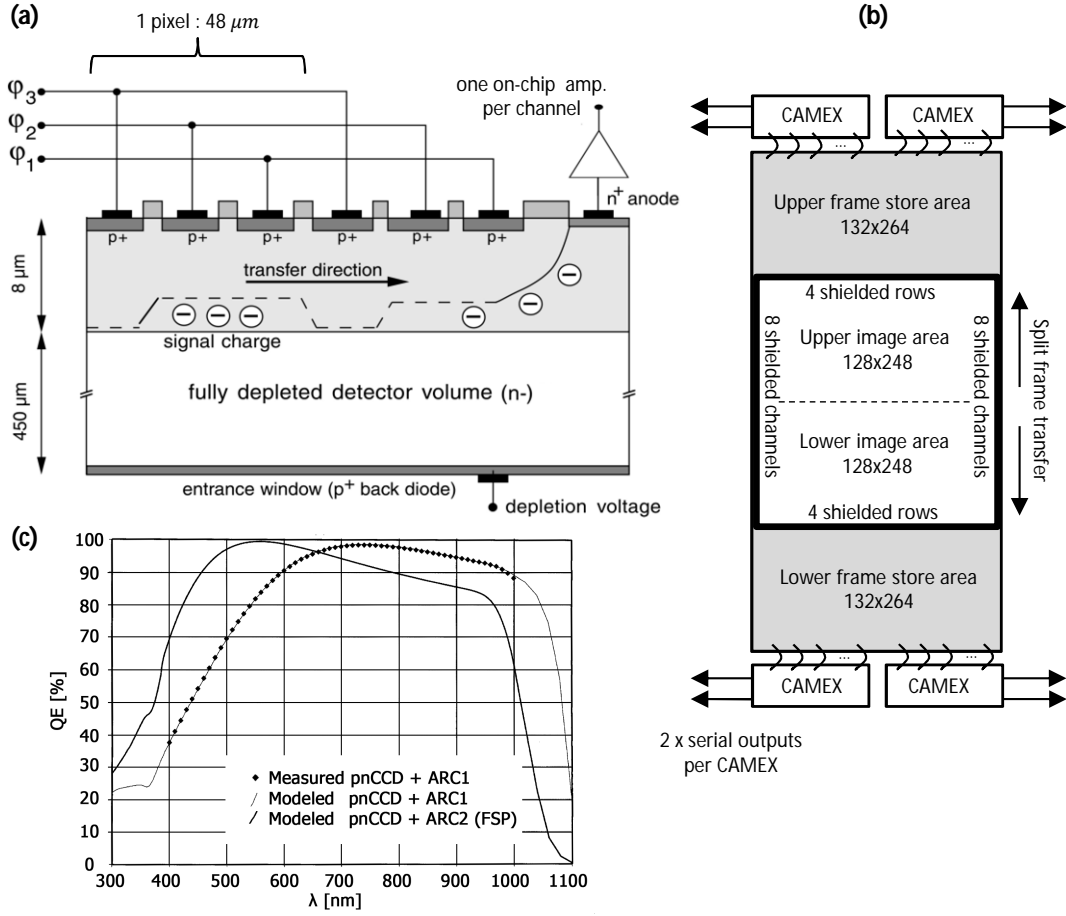


Figure 5.1. pnCCD sensor used in FSP. (a) Schematic cross section of a portion of one sensor channel. (b) Array structure, including the light-sensitive image area and the shielded frame store area. (c) Sensor QE , including the measured and simulated values with two different anti-reflecting coatings (the one used in FSP is ARC2). See the text for extra details. Images (a) and (b) were adapted from Ihle et al. (2012).

ADC each, which have $N_{adc}=14$ bit and are located in four boards of the external rack (see further details in Sect. 3.2.2).

5.2 Camera-modulator synchronization and camera calibration

The frame acquisition of the pnCCD camera and the switching of the modulator (i.e. of the FLCs) need to be synchronized (see Sect. 3.1.1). In FSP, the synchronization strategy was determined to facilitate the post-facto correction (given in Sect 5.2.1) of the smearing produced by the shutter-less operation (see Sect. 4.3.3) of the frame transfer pnCCD. The smearing is introduced because the sensor is permanently illuminated, and thus, the charge wells keep collecting signal while they are being transferred to the frame store area after each exposure (see e.g. Hoslst 1998).

We will define the signal (expressed in DN) read in pixel $\{x,y\}$ of frame No. n , $\hat{I}_{x,y}^n$,

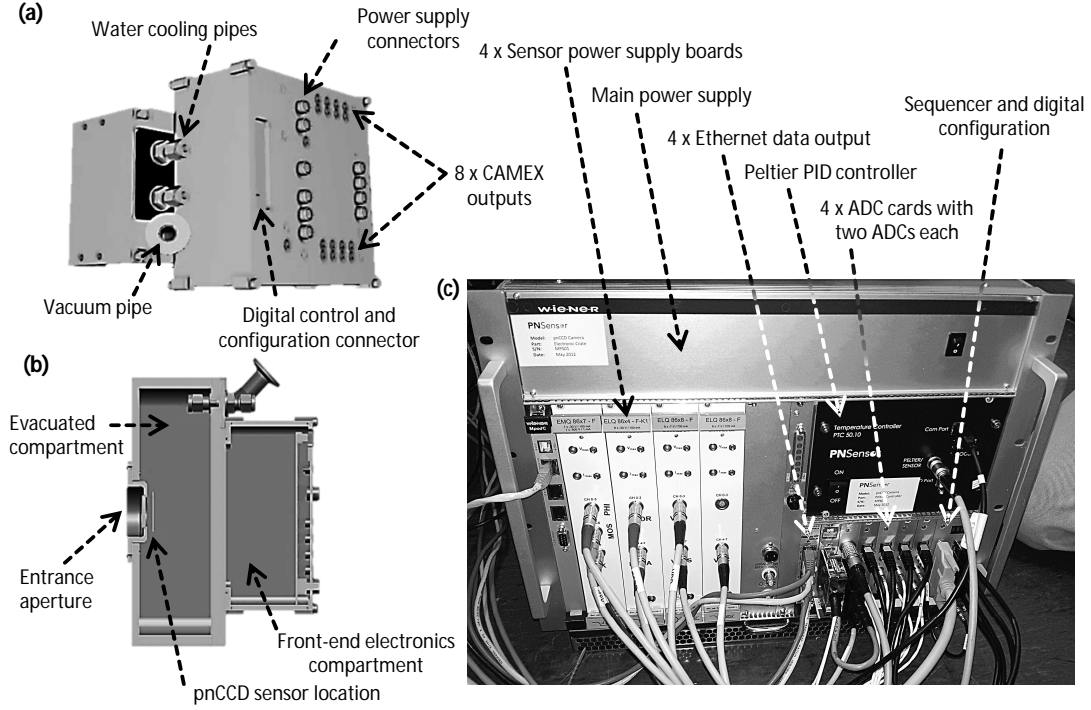


Figure 5.2. pnCCD camera system used in FSP. The camera housing and main connectors — including the water cooling and vacuum lines— can be seen in the CAD rendering (a). The internal divisions, i.e. one evacuated compartment that contains the image sensor and one separated compartment to secure part of the front-end electronics, can be appreciated in the rendered CAD cross section (b). A large portion of the front-end electronics —including the sensor power supplies, the eight ADCs, the Peltier cooler controller and the sequencer among others— is located in an external 19-inch rack (c).

using the following pnCCD camera calibration expression,

$$\hat{I}_{x,y}^n = \bar{I}_{x,y}^n + \bar{I}_{d,x,y} + I_{off,x,y} + N_{p,x,y}^n + N_{d,x,y}^n + N_{ro,x,y}^n + N_{cm,y}^n, \quad (5.1)$$

where $\bar{I}_{x,y}^n$ and $\bar{I}_{d,x,y}$ are the *smeared signals* due to the photon and dark charges respectively, $I_{off,x,y}$ is the digital offset of the camera, $N_{p,x,y}^n$ is the photon noise, $N_{d,x,y}^n$ is the dark noise, $N_{ro,x,y}^n$ is the read out noise and $N_{cm,x,y}^n$ is the signal due to the common mode artifact. Note that we have separated the different sources in the right hand side of Eq. 5.1 in their signal (deterministic values equal to the ensemble average of the corresponding random processes) and noise (random processes) components. To describe the statistical properties of all these terms, let us define the time and space sample average operators (unbiased estimators of the corresponding expected values) as $\langle \rangle_n$ and $\langle \rangle_{xy}$ respectively. In addition we denote the time and space sample variances (unbiased estimators of the corresponding variances) as $\sigma_{(n)}^2$ and $\sigma_{(xy)}^2$ respectively. In Eq. 5.1 we have assumed, considering time and space samples large enough, the following (which are further discussed in the rest of the chapter):

- Dark current and offset do not change in time: $\langle \bar{I}_{d,x,y}^n \rangle_n = \bar{I}_{d,x,y}$ and $\langle I_{off,x,y}^n \rangle_n = I_{off,x,y}$. We define the *bias or dark corrected signal* as $\hat{I}_{x,y}^n - \bar{I}_{d,x,y} - I_{off,x,y}$.
- All the noises are time and space uncorrelated, thus all cross covariances between N terms are null.

- $\langle N_{p,x,y}^n \rangle_n = \langle N_{d,x,y}^n \rangle_n = \langle N_{ro,x,y}^n \rangle_n = \langle N_{cm,y}^n \rangle_n = \langle N_{p,x,y}^n \rangle_{xy} = \langle N_{d,x,y}^n \rangle_{xy} = \langle N_{ro,x,y}^n \rangle_{xy} = 0$.
- The common mode is random in n and y but it is constant for a given row (x), thus $\langle N_{cm,x,y}^n \rangle_x = N_{cm,y}^n$ and $\langle N_{cm,y}^n \rangle_y = 0$. Note that this makes possible its correction and thus we call it noise when referring to its n and y behavior, and artifact when referring to its x behavior. We define the *common mode corrected signal* as $\hat{I}_{x,y}^n - N_{cm,y}^n$.

In the remaining part of the present chapter we elaborate on all the terms in the right hand side of Eq. 5.1, in order to characterize their value for the pnCCD camera, quantify their polarimetric effect and/or study their correction techniques when relevant. Most of such results were obtained for a frame rate of 400 fps (because it is the FR of FSP II) and a conversion gain of 8.7 (because it is the maximum allowed by the camera and provides the best SNR). In addition, this is the regime for all the measurements shown in Ch. 6. Note, however, that the methods utilized in this chapter can be applied to a different regime without modifications.

5.2.1 Frame transfer model

The camera-modulator synchronization can be appreciated in Fig. 5.3, which details the acquisition of a single pixel in row No. y of frame No. n . The position $y=0$ corresponds to the first non-shielded row of the lower image area of the sensor (see Fig. 5.1.b). Note, however, that the following analysis is the same for the upper image area and any semi-column of the sensor⁴ (thus we drop the x coordinate). The upper sketch of Fig. 5.3 illustrates the position of charge well No. y during the duration of the frame acquisition, i.e. between time instants t_n and t_{n+1} with $1/FR = t_{n+1} - t_n$. The lower sketch shows the temporal variation of the photo-charges flux generated at pixel No. y , $i_y(t)$. The switching of $i_y(t)$ (lasting t_s) is produced by the action of the modulator on the incoming beam. The switching of the FLCs' optical axes are smooth and (approximately) symmetric with respect to their inflection points (Dubreuil et al. 2010), therefore we have adopted the same transition profile for $i_y(t)$. Moreover, we consider the flux to be constant between transitions, with value i_y^n and i_y^{n+1} for frames No. n and $n+1$ respectively. The black boxes denote the frame transfers, which last $N_{row}t_t/2 \approx 34 \mu s$, with t_t being the period of the charge transfer clock. We have *delayed the camera trigger* (beginning of each frame transfer) with respect to the beginning of the modulator switching (at the end of t_e), in order to ensure that the full frame transfer takes place during a phase of stable illumination.

In the scenario described above, charge well No. y acquires both photon and dark (thermal) charges during (a) a fraction of the first frame transfer that takes place after exposing frame No. $n-1$ —where the initially empty charge well moves from position $N_{row}/2 - 1$ to $y+1$ —, (b) the exposure time (t_e) of frame No. n —where the charge well is static at position y —, (c) the switching time (t_s)—where the charge well is also static at position y —, and (d) a fraction of the second frame transfer that takes place during frame No. $n+1$, where the charge well moves from position $y-1$ to 0. For

⁴We neglect charge transfer inefficiencies (see Sect. 5.1.1), pixel blooming and any crosstalk between semi-columns. The latter is partially justified by the pnCCD detector (visible) PSF, which according to Ihle et al. (2008) has a full width at half maximum (FWHM) lower than $24 \mu m$ (half the pixel size).

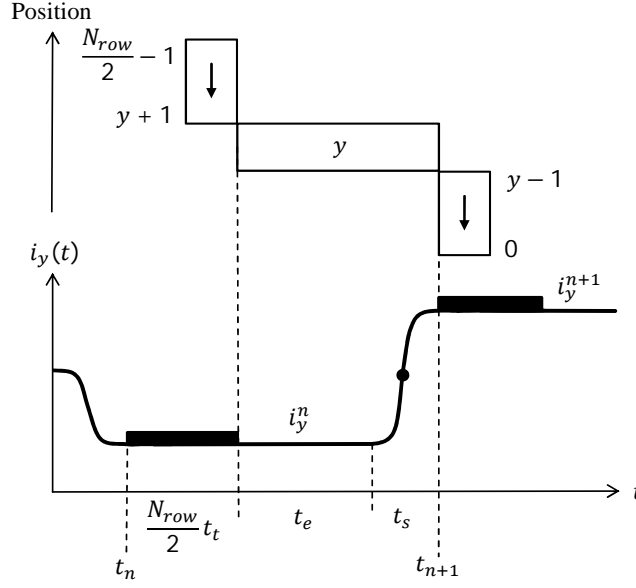


Figure 5.3. Frame transfer and camera-modulator synchronization. The upper sketch shows the position of charge well No. y in a semi-column of the pnCCD lower image area, during the acquisition of frame No. n (which lasts $t_{n+1} - t_n = 1/FR = 2.5$ ms). The lower image illustrates the temporal variation of the photo-charges flux at pixel No. y , $i_y(t)$. We consider a smooth switching (lasting $t_s \approx 100 \mu s$) of the modulator with a profile that is symmetric with respect to its inflection point (black dot). Moreover, the flux is assumed constant between transitions for all pixels, i.e. during the exposure time (t_e) and the frame transfers (black boxes with duration $N_{row}t_t/2 \approx 34 \mu s$). The camera trigger (beginning of frame transfer) is delayed with respect to the beginning of the modulator switching (at the end of t_e) to facilitate the post-facto numeric correction of the smearing. See the text for extra details. Image adapted from Iglesias et al. (2015).

the particular case in which the sensor illumination is approximately constant between consecutive frames, the smearing signal accumulated during (a) and (d) is also constant in time. Powell et al. (1999), see also Ruyten (1999), developed a numeric technique to eliminate, post-acquisition, the smearing signal introduced in such a *constant illumination regime*.

If the light entering the modulator is strongly polarized, e.g. in the presence of strong instrumental polarization, large Zeeman signals from solar active regions or during polarimetric calibration, the intensity of consecutive frames may vary considerably. In such a *highly variable illumination regime*, the technique by Powell et al. (1999) can not be used. We reformulated the smearing model (Iglesias et al. 2015) to consider the variable illumination profile shown in Fig. 5.3, by writing the $\bar{I}_{x,y}^n$ and $\bar{I}_{d,x,y}$ in Eq. 5.1 as (recall that we dropped the x coordinate)

$$\bar{I}_y^n = G_y \left[\kappa_1 t_t \sum_{j=y+1}^{N_{row}/2-1} i_j^n + t_e i_y^n + \frac{1}{2} t_s (i_y^n + i_y^{n+1}) + \kappa_2 t_t \sum_{j=0}^{y-1} i_j^{n+1} \right], \quad (5.2)$$

and

$$\bar{I}_{d,y} = G_y \left[i_{d,y}(t_e + t_s) + t_t \sum_{\substack{j=0 \\ j \neq m}}^{N_{row}/2-1} i_{d,j} + t_t \sum_{j=-N_{row}/2+y}^{-1} i_{d,j} + t_{ro} \sum_{j=-N_{row}/2}^{-N_{row}/2+y-1} i_{d,j} \right], \quad (5.3)$$

respectively. Note that G_y is the pnCCD conversion gain and that the optical gain of the setup (which is treated in Sect. 5.4.5) is not relevant because of how i_y^n was defined. The terms in the right hand side of Eq. 5.2 are due to the signal acquired during the above-mentioned stages, i.e. (a), (b), (c) and (d) for the first to the last term respectively. The specific form of the third term is due to the assumed symmetry of the i_y^n transition profile (Fig. 5.3). The ad hoc coefficients κ_1 and κ_2 were included to facilitate experimental tuning of the model, e.g. to contemplate possible differences in the photocharge-generation efficiencies of the static and transferring clocking states, compensate the effects of synchronization errors between the pnCCD readout and flux switching (see below), etc. Analogously, the first term in the right hand side of Eq. 5.3 is due to stages (b) and (c), and the second term due to (a) and (d). The third and fourth terms represent the dark signal acquired when the charge wells are transported inside the frame store area (Fig. 5.1), during the readout process (with readout clock period t_{ro}). In the latter we have considered the position index y to be negative, from -1 (corresponding to the row of the frame store area next to the image area) to $-N_{row}/2$ (corresponding to the row of the frame store area next to the readout nodes).

If we assume that the differences in G_y among the pixels in a semi-column are small⁵, and define the unsmeared signal acquired during t_e as

$$I_y^n = G_y t_e i_y^n, \quad (5.4)$$

and the smearing parameters α , δ_1 and δ_2 as

$$\alpha = \frac{t_s}{2t_e}, \quad \delta_1 = \frac{\kappa_1 t_t}{t_e} \quad \text{and} \quad \delta_2 = \frac{\kappa_2 t_{ro}}{t_e}. \quad (5.5)$$

Then we can write Eq. 5.2 in matrix form as follows,

$$\bar{\mathbf{I}}^n = \mathbf{A} \mathbf{I}^n + \mathbf{B} \mathbf{I}^{n+1}, \quad (5.6)$$

where the smeared and unsmeared semi-columns are given by $\bar{\mathbf{I}}^n = [\bar{I}_0^n, \bar{I}_1^n, \dots, \bar{I}_{N_{row}/2-1}^n]^T$ and $\mathbf{I}^n = [I_0^n, I_1^n, \dots, I_{N_{row}/2-1}^n]^T$ respectively, and the frame transfer matrices \mathbf{A} and \mathbf{B} are defined as

$$\mathbf{A} = \begin{bmatrix} 1 + \alpha & \delta_1 & \dots & \delta_1 \\ 0 & 1 + \alpha & \dots & \delta_1 \\ \vdots & \vdots & \ddots & \vdots \\ 0 & 0 & 0 & 1 + \alpha \end{bmatrix} \quad \text{and} \quad \mathbf{B} = \begin{bmatrix} \alpha & 0 & \dots & 0 \\ \delta_2 & \alpha & \dots & 0 \\ \vdots & \vdots & \ddots & \vdots \\ \delta_2 & \delta_2 & \delta_2 & \alpha \end{bmatrix}. \quad (5.7)$$

⁵Recall that in the pnCCD there is one readout channel per semi-column. This assumption can be avoided if desired just by working with all the images expressed in electrons, i.e. dividing each pixel by its corresponding conversion gain.

Eq. 5.6 evidences that the frame transfer with highly variable illumination introduces not only the obvious spatial correlation between the pixels of the considered semi-column, but also a temporal correlation between the semi-column in frames n and $n+1$ (see Iglesias et al. 2015). In the present analysis we have considered the delay of the camera trigger to be exactly the modulator switching time (t_s). In practice, however, we have not measured t_s ⁶ and thus we have imposed a *camera-modulator trigger delay* of 100 μ s, to ensure that it is longer than the $t_{sFLC} \approx 50 \mu$ s (Sect. 4.2.1). A $t_s < 100 \mu$ s may produce a slight reduction of the polarimetric efficiencies and of the smearing correction quality. Therefore, the accurate measurement of t_s and tuning of the camera-modulator trigger delay remains as future work.

5.2.2 Frame transfer correction

For a given set of smeared semi-columns, $\bar{\mathbf{I}} = [(\bar{\mathbf{I}}^0)^T, (\bar{\mathbf{I}}^1)^T, \dots, (\bar{\mathbf{I}}^{N_{frm}-1})^T]^T$ with $N_{frm} \geq 2 \in \mathbb{N}$, and considering that the matrices \mathbf{A} and \mathbf{B} are triangular, the desmearing can be efficiently done by solving iteratively Eq. 5.6 from pixel No. $N_{row}/2 - 1$ to 0 and frame No. $N_{frm} - 1$ to 0, provided the final condition $\mathbf{I}^{N_{frm}}$ is known.

The $\bar{\mathbf{I}}$ are estimated from the measured intensities after correcting for the common mode artifact and subtracting the smeared dark frame, i.e. neglecting the noise contributions in Eq. 5.1 we can write (recovering the x coordinate)

$$\bar{I}_{x,y}^n \approx \hat{I}_{x,y}^n - \bar{I}_{d,x,y} - I_{off,x,y} - N_{cm,y}^n. \quad (5.8)$$

On the other hand, the difficulties in obtaining $\mathbf{I}^{N_{frm}}$ can be avoided after considering that the homogeneous solution of Eq. 5.6, i.e.⁷ $(-\mathbf{A}^{-1}\mathbf{B})^n \mathbf{I}^{N_{frm}} = \mathbf{H}^{N_{frm}-n} \mathbf{I}^{N_{frm}}$, is highly damped, see Fig. 5.4. Therefore, the error introduced by assuming that $\mathbf{I}^{N_{frm}} = \bar{\mathbf{I}}^{N_{frm}-1}$, can be reduced to negligible levels provided a few frames at the end of the series are dropped.

The desmearing algorithm operates on many smeared semi-columns that are noisy (recall that we neglected the noise when writing Eq. 5.8). Therefore, the noise in the individual corrected images is larger than the noise in the individual input images. To study the overall conditioning (error propagation) of the algorithm, we can write the solution to Eq. 5.6 for all n as follows

$$\mathbf{I} = \mathbf{U}\bar{\mathbf{I}} + \mathbf{H}\mathbf{I}^{N_{frm}}, \quad (5.9)$$

where the block-matrices \mathbf{H} and \mathbf{U} are

$$\mathbf{H} = [(\mathbf{H}^{N_{frm}})^T, (\mathbf{H}^{N_{frm}-1})^T, \dots, (\mathbf{H}^1)^T]^T \quad (5.10)$$

and

$$\mathbf{U} = \begin{bmatrix} \mathbf{A}^{-1} & \mathbf{H}^1 \mathbf{A}^{-1} & \mathbf{H}^2 \mathbf{A}^{-1} & \dots & \mathbf{H}^{N_{frm}-1} \mathbf{A}^{-1} \\ \mathbf{0} & \mathbf{A}^{-1} & \mathbf{H}^1 \mathbf{A}^{-1} & \dots & \mathbf{H}^{N_{frm}-2} \mathbf{A}^{-1} \\ \vdots & \vdots & \vdots & \ddots & \vdots \\ \mathbf{0} & \mathbf{0} & \mathbf{0} & \dots & \mathbf{A}^{-1} \end{bmatrix}, \quad (5.11)$$

⁶The modulator t_s can be larger than t_{sFLC} of the individual FLCs if, for example, their driving signals are slightly out of phase, or the switching profiles are not exactly symmetric or equal.

⁷Here we use upper scripts of time independent matrices to denote exponentiation. Recall that the contribution of the final condition to the general solution of a difference equation, is given by the homogeneous solution.

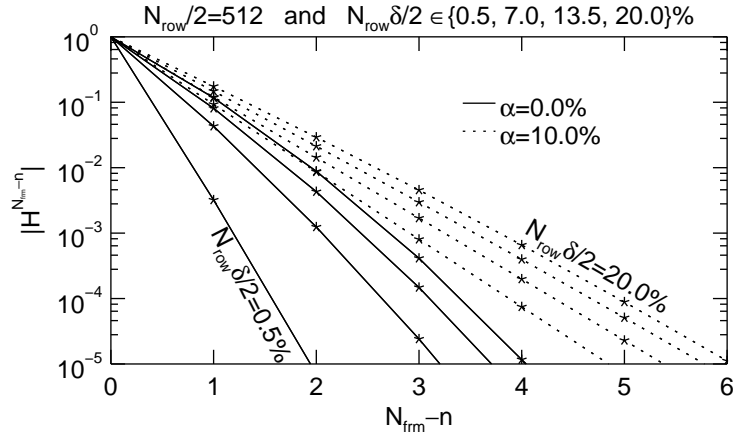


Figure 5.4. Errors in the desmeared images due to uncertainties in the final condition of Eq. 5.6. The plot shows the euclidean norm of the homogeneous solution, $|\mathbf{H}^{N_{frm}-n}|$, versus the index of the desmeared frame. The curves in each set, continuous for $\alpha = 0.0\%$ and dotted for $\alpha = 10.0\%$, correspond to $N_{row}\delta/2 = 0.5, 7.0, 13.5$ and 20.0% from left to right respectively. The figures were computed using $\delta_1 = \delta_2 = \delta$ and $N_{row}/2 = 512$ (the value for the FSP II sensor), although they are practically insensitive to N_{row} for $N_{row} \gg 1$. $N_{row}\delta/2$ is the ratio of the total transfer time to the exposure time (for the pnCCD working at 400 fps, $N_{row}\delta/2 = 1.8\%$ and $\alpha = 2\%$). Image adapted from Iglesias et al. (2015)

respectively, and $\mathbf{0}$ is the $N_{row}/2 \times N_{row}/2$ null matrix. If we neglect the contributions of $\mathbf{H}\mathbf{I}^{N_{frm}}$ (Fig. 5.4), the propagation of the relative errors (NSR) in $\bar{\mathbf{I}}$ when applying Eq. 5.9, is upper bounded by the condition number of \mathbf{U} ⁸. From Fig. 5.5, it can be seen that the condition number of \mathbf{U} for the pnCCD working at $FR = 400$ fps is ~ 1.01 , thus only a $\sim 1\%$ increase of the NSR in the images is expected after applying the desmearing algorithm.

If the Stokes vector at the input of the FSP modulator is constant in time, the measured intensities repeat cyclically every $N_{mod} = 4$ images. In this case, Eq. 5.6 can be solved for a single period of the input, $\bar{\mathbf{I}} = [(\bar{\mathbf{I}}^0)^T, (\bar{\mathbf{I}}^1)^T, (\bar{\mathbf{I}}^2)^T, (\bar{\mathbf{I}}^3)^T]^T$, without the need of a final condition. The corresponding desmearing expression can be written in block matrix as,

$$\mathbf{I} = \tilde{\mathbf{U}}^{-1} \bar{\mathbf{I}}, \quad (5.12)$$

where the $2N_{row} \times 2N_{row}$, block circulant matrix (de Mazancourt and Gerlic 1983) $\tilde{\mathbf{U}}$ is,

$$\tilde{\mathbf{U}} = \begin{bmatrix} \mathbf{A} & \mathbf{B} & \mathbf{0} & \mathbf{0} \\ \mathbf{0} & \mathbf{A} & \mathbf{B} & \mathbf{0} \\ \mathbf{0} & \mathbf{0} & \mathbf{A} & \mathbf{B} \\ \mathbf{B} & \mathbf{0} & \mathbf{0} & \mathbf{A} \end{bmatrix}. \quad (5.13)$$

Note that, Eq. 5.12 is linear and thus *it can be applied after averaging any number of periods*, reducing this way the computational load. The numeric inversion of $\tilde{\mathbf{U}}$ is not a problem because it has to be done only once. On the other hand, the product in the right side of Eq. 5.12 may be computationally expensive because it has to be performed

⁸The ratio of the largest to the smallest singular values of \mathbf{U} (Press et al. 2007a).

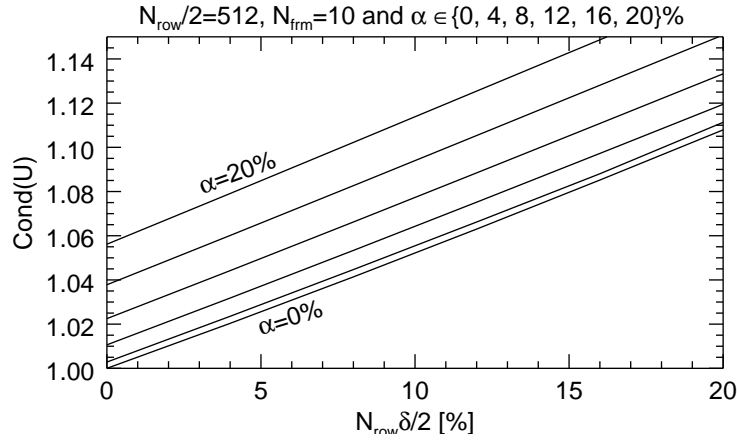


Figure 5.5. Error propagation in the desmearing algorithm. The plot shows the condition number of \mathbf{U} , i.e. the upper limit for the propagation of the relative errors of $\tilde{\mathbf{I}}$ in Eq. 5.9, versus the parameters product $N_{row}\delta/2$. The curves correspond to $\alpha = 0, 4, 8, 12, 16$ and 20% from bottom to top respectively. The figures were computed using $\delta_1 = \delta_2 = \delta$, $N_{row}/2 = 512$, $N_{frm} = 10$ and different values of α (although they are practically insensitive to N_{row} and N_{frm} for $N_{row} \gg 1$ and $N_{frm} \gg 1$). As expected, the restoration becomes monotonically worse conditioned for increasing δ and α (for the pnCCD working at 400 fps, $N_{row}\delta/2=1.8\%$ and $\alpha=2\%$). Image adapted from Iglesias et al. (2015)

once per image column. The latter is important to FSP II due to the larger sensor area, therefore, its optimization remains as future work⁹.

For a given α and δ , the relative error introduced by the smearing in the fainter pixels increases with the contrast of the corresponding semi-column and with the ratio of the semi-column intensity in the two consecutive frames considered (given by the polarization degree of the incoming Stokes vector). The latter produces that, even for a fixed incoming \mathbf{S} , the artifact level is differential, i.e. varies among the four intensity images of a given modulation cycle. Therefore, after demodulation, the smearing will appear as a polarimetric artifact, i.e. not only in the retrieved I but also in Q , U and V . This can be seen in the example shown in the first row of Fig. 5.6a. The same presents the four modulated intensities—after applying Eq. 5.8 and averaging several modulation cycles—acquired with FSP, when measuring a USAF target illuminated by pure linearly polarized light (generated by the FSP calibration unit). Such an example constitutes an extreme case because the contrast is large, the illumination between consecutive frames can vary up to ~ 10 times ($|\mathbf{p}| \approx 100\%$), and the frame rate is high ($FR=700$ fps). In the second row of Fig. 5.6a, we show the results of the desmearing algorithm given in Eq. 5.12 when applied to the images in the first row. The quality of the desmearing can also be seen in the cross sections plotted in Fig. 5.6b and c.

⁹Two possible approaches to do this are (a) finding only an approximate solution iteratively by first guessing \mathbf{I}^0 and (b) using the fact that $\tilde{\mathbf{U}}^{-1}$ is also block circulant and band dominant (Vescovo 1997) to implement an efficient multiplication algorithm.

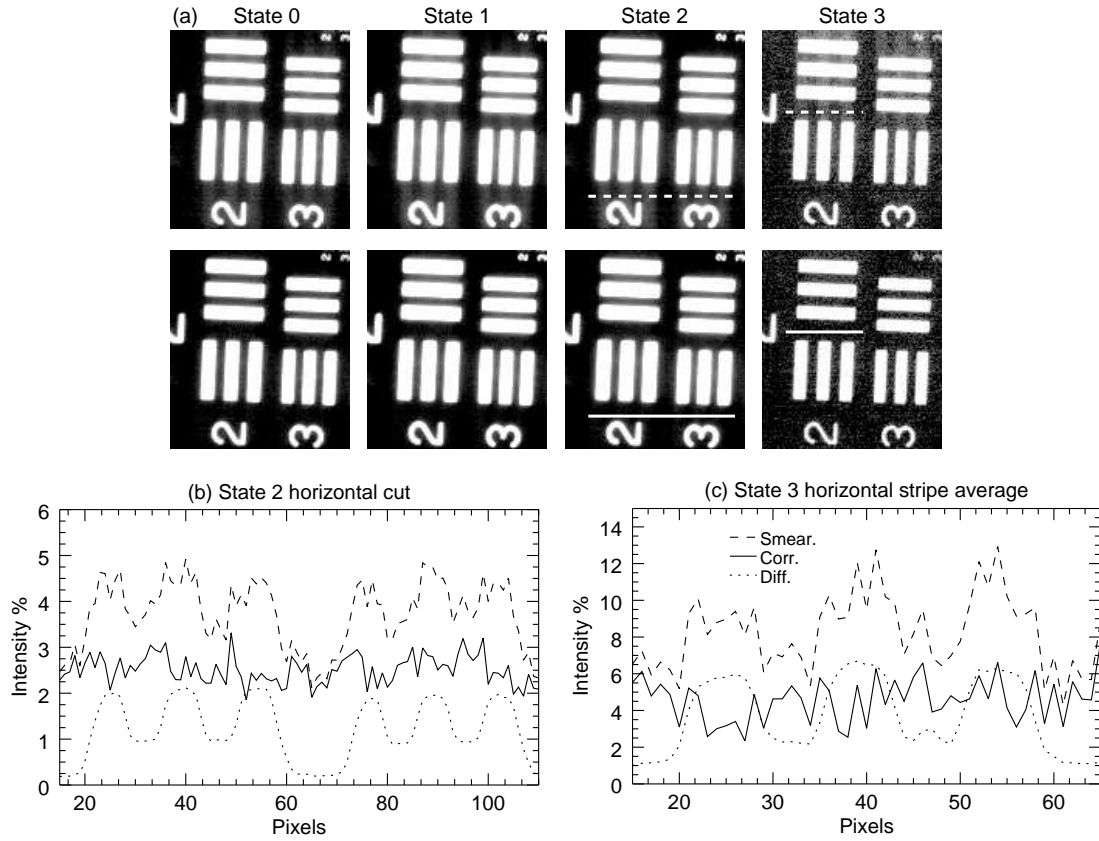


Figure 5.6. Frame transfer artifact correction. The first row of image (a) shows the four modulated intensities (only a fraction of the sensor area) after averaging several modulation cycles, acquired with FSP working at 700 fps, when measuring a USAF target illuminated with constant, linearly polarized light. The mean values of the bright areas in the images are 1950, 2828, 2825, and 297 DN for States 0 to 3, respectively. The white lines in State 2 mark the location of the horizontal cuts shown in (b). Analogously, the white lines in State 3 indicate the center of the vertical average of a 4-pixel-wide horizontal stripe presented in (c). The second row in image (a) shows the result of the smearing correction (Eq. 5.12). In both (b) and (c) the values for the smeared (dashed) and corrected (continuous) images, as well as their difference (dotted), are given in percentage of the mean value in the bright areas of the corresponding smeared image. Adapted from Iglesias et al. (2015).

5.3 Gain and linearity

The most common technique to measure the camera conversion gain and linearity is the photon transfer curve. There are few variants of such a technique (see Bohndiek et al. 2008, for a description and a comparison) which can be applied in case the camera response is expected to present large ($>10\%$) non-linearities, e.g. as seen in some CMOS sensors. Here we use a *mean-variance analysis* because the pnCCD response is linear to a very high degree ($<1\%$, see below). The procedure we followed is described below:

1. A fast LED light source —driven by a 400 Hz rectangular signal of variable duty cycle (DC_{LED}), synchronized with the frame readout— is used to linearly vary the input intensity of the camera. For each DC_{LED} value, 400 frames (spanning 1 s) are recorded. This is repeated many times (~ 20) to minimize the long term variation of

the illumination and reduce the uncertainty in the estimated values.

2. Assuming a time invariant conversion gain, we can write the temporal variance of the dark and common mode corrected signal in pixel $\{x, y\}$ of frame No. n , $\hat{I}_{corr,x,y}^n$, as follows (see Eq.5.1 and 5.2)

$$\sigma_{corr,x,y,(n)}^2 = G_{x,y} \langle \hat{I}_{corr,x,y}^n \rangle_n + \sigma_{d,x,y,(n)}^2 + \sigma_{ro,x,y,(n)}^2, \quad (5.14)$$

and obtain $G_{x,y}$ from a linear fit, see Fig. 5.7. Note that we have not probed the whole dynamic range, which goes up to $\sim 12\,000$ DN, because during normal observations at the telescope, the signal per resolution element rarely exceeds ~ 5000 DN ($581\,e^-$).

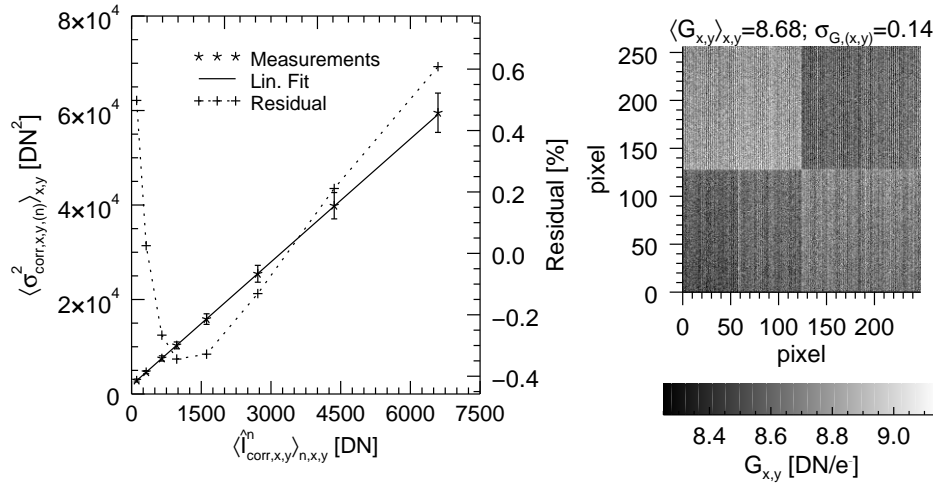


Figure 5.7. Measured pnCCD camera gain. The leftmost plot shows the spatially averaged, photon transfer curve (referring to the left scale) along with a linear fit and the corresponding residuals (referring to the right scale, see legend and Eq. 5.14). The rightmost image presents the conversion gains derived for each pixel of the sensor, as well as their spatial average and standard deviation (title). Note that the dominant spatial variations of $G_{x,y}$ are due to the differences in each CAMEX (four quadrants) and in each readout channel (semi-columns).

Non-linearities (NL) in the camera response are important for high-sensitivity polarimetry. They can introduce artifacts that depend on the measured Stokes I —and thus are non-flat across the FOV —and that scale with the instrumental polarization (Keller 1996). To study this, we measured the camera NL in the lower part of the dynamic range, see Fig. 5.8. Let us assume that the camera response presents a spurious second order term (the simplest form of NL) and in addition that the dark correction is not perfect. Then, we can express the dark and common mode corrected intensity as follows (dropping the pixel indices and neglecting noise and smearing, see Eq. 5.1 and 5.4),

$$\hat{I}_{corr}^n = \kappa_{NL} (I^n)^2 + I^n + \Delta I_{off}, \quad (5.15)$$

where κ_{NL} is the second order coefficient and ΔI_{off} is the residual offset term (both assumed time constant).

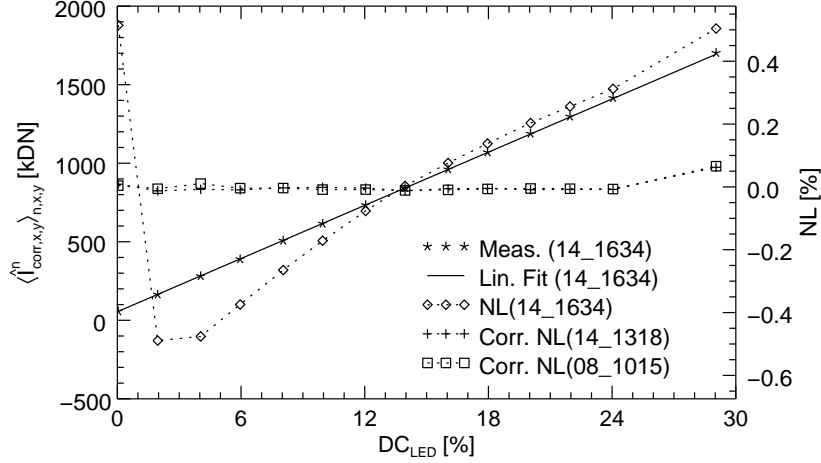


Figure 5.8. Measured pnCCD non-linearities. The plot shows the mean detected signal (referring to the left scale) versus the duty cycle of the LED lamp used to illuminate the sensor (horizontal axis); along with a linear fit and the associated non-linearity (referring to the right scale) for a measurement acquired on the date 2015.07.14 at 16:34 (see the legend). The NL are rather constant and thus they can be reduced by calibration. Here we present the resulting NL of two extra measurements—one on the same day at 13:18 and the other one taken on 2015.07.08 at 10:15 (see legend)— after subtracting the residuals from 14_1634.

Let us call the Stokes vector at the input of the modulator $\mathbf{S} = I[1, k_{inst}, k_{inst}, k_{inst}]^T$ (with $k_{inst} \in \mathbb{R}$ due to instrumental polarization). Then, by demodulating the \hat{I}_{corr}^n in Eq. 5.15, we can write the error introduced by a non-zero κ_{NL} and ΔI_{off} as,

$$\Delta \mathbf{S} = \hat{\mathbf{S}}_{corr} - \mathbf{S} = \kappa_{NL} \mathbf{D} (\mathbf{O}\mathbf{S})^2 + \Delta I_{off} \mathbf{D}[1, 1, 1, 1]^T, \quad (5.16)$$

where the square is done element-wise. Using the \mathbf{O} given in Table 4.6 and $\mathbf{D} = \mathbf{O}^{-1}$, we have computed the errors in the normalized Stokes V (Δv , which is larger than Δq and Δu) obtained from Eq. 5.16, for different κ_{NL} (assuming $\Delta I_{off} = 0$, Fig. 5.9.a), ΔI_{off} (assuming $\kappa_{NL} = 0$, Fig. 5.9.b), and values of the input \mathbf{S} . In addition, using the results of a second order fit to the measurements in Fig. 5.8, we estimated the values of κ_{NL} and ΔI_{off} for the pnCCD camera, see Fig. 5.9c and d respectively. Note that, the lower right quadrant of the sensor has clearly larger NL and presents a worse dark correction. The column-wise variation suggests a defective or wrongly configured readout CAMEX (see Sect. 6.4).

From a comparison of say the spatial mean plus two sigma values of ΔI_{off} (~ 5 DN) with the curves in Fig. 5.9b, it can be stated that the errors can be kept $\sim 1 \times 10^{-4}$ provided that $\kappa_{inst} \approx 1\%$. On the other hand, by comparing the mean plus two sigma value of κ_{NL} ($\sim 2.5 \times 10^{-5} \text{ DN}^{-1}$) with Fig. 5.9a, we can see that even for $\kappa_{inst} = 1\%$ the errors are few times above 1×10^{-4} . This situation can be improved by calibrating the sensor NL , which is possible thanks to the stable sensor response, see Fig. 5.8. By using this technique the value of κ_{NL} can be easily reduced by one order of magnitude, leading to errors below 1×10^{-4} for $\kappa_{inst} = 1\%$. Such a NL correction has not been implemented in the FSP reduction routines and remains as future work.

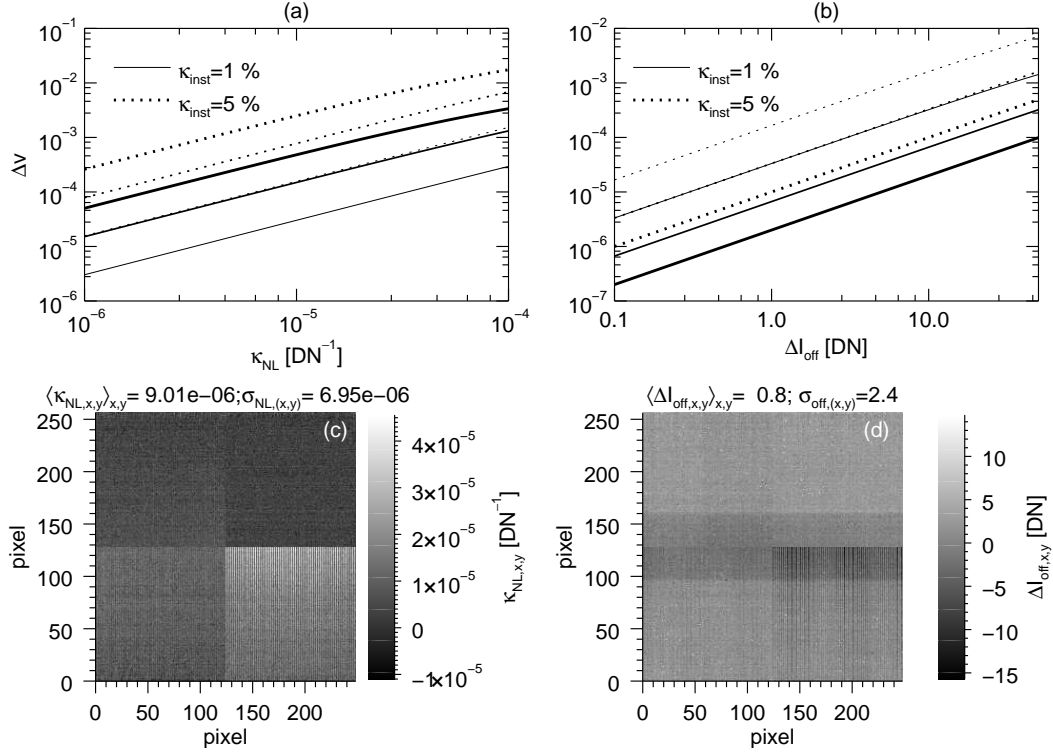


Figure 5.9. Polarimetric error introduced in the retrieved normalized Stokes V by second-order non-linearities (κ_{NL} , image a) and residual offsets (ΔI_{off} , image b), calculated using Eq. 5.16. In both (a) and (b) the figures were computed for two levels of instrumental polarization (κ_{inst} , see legends) and three values of the incoming intensity I , namely 300 (thinnest lines), 1500 (mid thickness lines) and 5000 DN (thickest lines). The measured values of κ_{NL} and ΔI_{off} for the pnCCD camera are given in images (c) and (d) respectively (along with their spatial means and standard deviations in the titles). See the text for extra details.

5.4 Camera noise

5.4.1 Common mode correction

Typically in CCDs the readout is done serially, by transferring the charges from each vertical register to an horizontal transfer register ending in a readout stage. Phenomena like interferences, artifacts in the clocking signals or variation of the bias voltages, among others, affect the readout stage and tend to increase the readout noise of the camera. Differently, the pnCCD sensor has a parallel channel readout implemented by four CAMEXs (Fig. 5.1b). All the readout channels located in each CAMEX share, among others, the bias circuitry and timing lines. Therefore, phenomena such as those named above introduce spurious signals (denoted here as common mode artifact) that affect simultaneously and equally all the readout stages belonging to a single CAMEX. The common mode artifact manifests itself as an additive offset that is equal for all the pixels in the same semi-row of the sensor ($N_{cm,y}^m$, see Eq. 5.1) and varies from frame to frame. The latter implies that the common mode appears (with equal spatial properties) in the polarimetric images, and, considering that it dominates the noise of dark images, it has to be reduced in order to do high-sensitivity, narrow-band polarimetry.

The post-facto correction of the common mode implies estimating and subtracting

$N_{cm,y}^n$ in every semi-row (y) and frame (n). Such estimation can be done only by using channels that contain no photon signals. In optical applications, this requires shielding few vertical registers of the sensor¹⁰, as done in the pnCCD camera (Fig. 5.1b). For the pixels associated to a single CAMEX, we can express the estimated common mode signal, \hat{N}_{cm} , as the average of N_{xs} shielded columns $\{xs_0, xs_1, \dots, xs_{N_{xs}-1}\}$ computed *after the image has been dark corrected*, as follows (see Eq. 5.1)

$$\hat{N}_{cm,y}^n = \frac{1}{N_{xs}} \sum_{x=x_{s0}}^{xs_{N_{xs}-1}} (N_{p,x,y}^n + N_{d,x,y}^n + N_{ro,x,y}^n) + N_{cm,y}^n = \Delta N_{cm,y}^n + N_{cm,y}^n, \quad (5.17)$$

where $\Delta N_{cm,y}^n$ represents the residual common mode which is not zero, because N_{xs} is generally too small for the sum of the noises to get sufficiently close to its expected value of $0 e^-$ -rms. The common mode correction reduces then to (see Eq. 5.1)

$$\begin{aligned} \hat{I}_{corr,x,y}^n &= \hat{I}_{dark-corr,x,y}^n - \hat{N}_{cm,y}^n \\ &= \hat{I}_{x,y}^n - \bar{I}_{d,x,y} - I_{off,x,y} - \hat{N}_{cm,y}^n \\ &= \bar{I}_{x,y}^n + N_{p,x,y}^n + N_{d,x,y}^n + N_{ro,x,y}^n - \Delta N_{cm,y}^n. \end{aligned} \quad (5.18)$$

In order to have a good correction, the minimum N_{xs} required has to produce an rms residual common mode noise, $\sigma_{\Delta cm,x,y}^2$, that is small compared to the other sources of camera noise, i.e. $\sigma_{\Delta cm,x,y}^2 \ll \sigma_{d,x,y}^2 + \sigma_{ro,x,y}^2$. For the pnCCD sensor used in the FSP prototype a large $N_{xs}=8$ was foreseen, in order to help estimating the minimum value required to achieve a good correction, and help in the design of the larger sensor for FSP II¹¹. We investigated this by (a) acquiring 4648 dark frames —at $FR = 400$ fps and $T_{CCD} = -25^\circ\text{C}$ — in order to eliminate $\bar{I}_{x,y}^n$ and $N_{p,x,y}^n$ from Eq. 5.18; (b) applying dark correction to each frame by doing $\hat{I}_{dark-corr,x,y}^n = \hat{I}_{x,y}^n - \langle \hat{I}_{x,y}^n \rangle_n$; and (c) correcting for common mode each frame by applying the first expression in Eq. 5.18, using different N_{xs} . The results of this analysis are presented in Fig. 5.10. As can be appreciated there, the common mode dominates over all the noise sources in the individual frames (see Fig. 5.10a). As a consequence, even the correction using a single shielded channel ($N_{xs} = 1$), reduces considerably the artifact level (see the plot in Fig. 5.10c). The correction is exponentially less effective with increasing N_{xs} and thus, using $N_{xs} = 3$ already reduces the noise in the images by 85 %. Another important aspect, which cannot be addressed using dark frames, is the fact that for illuminated frames the shielded channel that is closest to the image area is exposed to considerable amounts of stray light. As a consequence, it cannot be used for common mode correction. For this reason we adopted $N_{xs} = 7$ for the correction of all the data presented in this work.

¹⁰Initially, the pnCCD was used for X-ray imaging in astrophysical applications (Sect. 5.1). In this case, the common mode correction does not require shielded channels, because the X-ray detections are spatially sparse and thus much of the sensor is not illuminated in each exposure.

¹¹Having a large N_{xs} has not only the drawback of a reduced usable sensor area, but also presents serious routing problems for the design of a larger pnCCD, which requires more than two CAMEXs to read each half of the sensor.

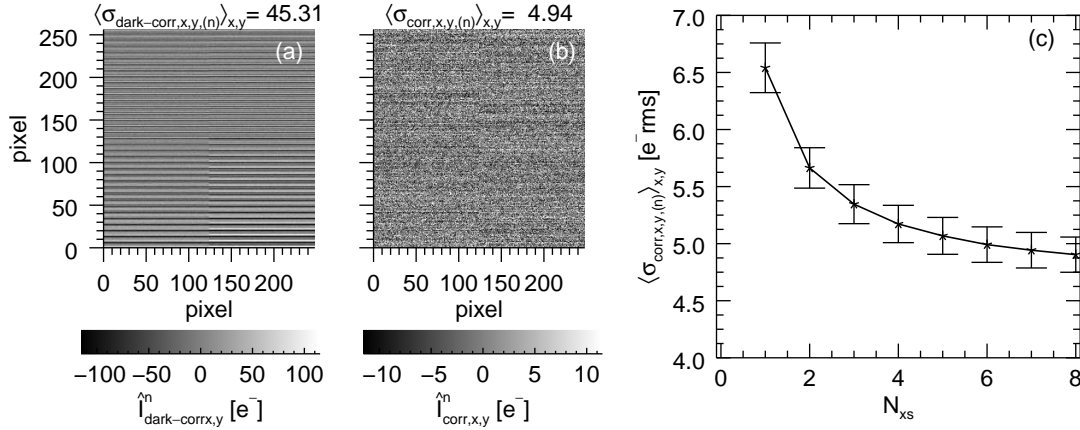


Figure 5.10. Common mode artifact correction. A single bias-corrected, dark frame is shown before (a) and after (b) the common mode correction (using $N_{xs}=7$ shielded channels of the pnCCD). The plot in (c) presents the spatial average of the temporarily-estimated (using 4648 dark frames), rms noise of the individual pixels, $\sigma_{\text{corr},x,y,(n)}$, versus the number of shielded channels used for common mode correction. The error bars denote the spatial standard deviation of $\sigma_{\text{corr},x,y,(n)}$. A conversion gain of $G = 8.68 \text{ DN}/e^-$ was used. See the text for extra details.

5.4.2 Total camera noise

For the case of $N_{xs} = 7$, the mean total camera noise can be estimated from the corresponding value of $\langle \sigma_{\text{corr},x,y,(n)} \rangle_{x,y}$ found in Fig. 5.10, namely (dropping the pixel indexes)

$$\sigma_{cam} = \sqrt{\sigma_d^2 + \sigma_{ro}^2 + \sigma_{\Delta cm}^2} = 4.94 \pm 0.16 e^- \text{rms}. \quad (5.19)$$

Note that, in this definition of σ_{cam} we do not include *PRNU* (dark frames were used and the noises were estimated for each pixel individually) because its residual value depends on the quality of the flat fielding procedure (Sect. 6.1.1). Analogously, we do not include the residual FPN after dark correction (the noises were estimated for each pixel individually) because per frame it is well below the other noise values in Eq. 5.19. The latter can be seen by computing the temporal average of the spatially estimated total noise in the corrected dark frames used to produce Fig. 5.10, i.e. $\langle \sigma_{\text{corr},(x,y)} \rangle_n = 4.94 \pm 0.02 e^- \text{rms}$, which is equal to $\langle \sigma_{\text{corr},x,y,(n)} \rangle_{x,y}$ given in Eq. 5.19.

5.4.3 Exposure time stability

A difference in the exposure times of the four modulation states, introduces an artificial polarimetric offset (flat across the *FOV*, see e.g. Martinez Pillet 2007), which is generally not critical because (a) the signals are measured with respect to the nearest continuum spectral point, and (b) the polarimetric offset is generally dominated by the instrumental polarization. Since many modulation states are usually averaged to increase *SNR*, only a difference in the mean values of the exposure times will produce a polarimetric offset in the accumulated Stokes images. On the other hand, random variations of the exposure time (jitter) only increases the noise in the accumulated images. When writing Eq. 5.1 we did not contemplate the noise introduced by such a jitter. This is because in FSP the camera frame transfer is triggered by the function generator that drives the modulator

(see Sect. 3.2.2), which is very stable (see Sect. 4.3.3). Each frame of the pnCCD camera carries a $1\text{ }\mu\text{s}$ accuracy time stamp. For example, in a series of 28426 frames acquired with $FR=400$ fps, we measured a mean frame acquisition period (time difference between consecutive time stamps) of 2.500 ms with a standard deviation of $2.53\text{ }\mu\text{s}$.

5.4.4 Readout and quantization noise

The noise in common-mode-corrected, dark frames —temporally estimated for each pixel using many frames— can be decomposed as follows

$$\begin{aligned}\sigma_{corr,x,y,(n)}^2 &= \sigma_{d,x,y,(n)}^2 + \sigma_{ro,x,y,(n)}^2 + \sigma_{\Delta cm,x,y,(n)}^2 \\ &= G_{x,y}^2 i_{d,x,y} \left[t_e + t_s + t_t (N_{row} - y) + t_{ro} y \right] + \sigma_{ro,x,y,(n)}^2 + \sigma_{\Delta cm,x,y,(n)}^2 \quad (5.20) \\ &= G_{x,y}^2 i_{d,x,y} t_{tot} + \sigma_{ro,x,y,(n)}^2 + \sigma_{\Delta cm,x,y,(n)}^2,\end{aligned}$$

where we have used the last equality in Eq. 5.18 (assuming $\bar{I}_{x,y}^n = 0$); and Eq. 5.3, assuming that $i_{d,x,y}$ of the pixels in a single column are approximately the same. t_{tot} is the total lifetime of the charge wells during each acquisition, which depends on the y coordinate of the considered pixel. The most common technique to measure the readout noise of the camera involves acquiring many 'zero-exposures' frames, i.e. with t_{tot} short enough to make the dark noise contribution (first term in the right hand side of Eq. 5.20) negligible. Note that, in frame transfer CCDs, the minimum possible t_{tot} is $t_t (N_{row} - y) + t_{ro} y$. For cameras with large $\sigma_{ro,x,y,(n)}$, fast readout and frame transfer (small t_{ro} and t_t), usually the minimum t_{tot} is small enough to allow and accurate measurement of $\sigma_{ro,x,y,(n)}$. In the pnCCD, however, this is not the case and thus we measured $\sigma_{ro,x,y,(n)}$ by acquiring frames with the charge transfer direction reversed, i.e. no charges are deposited in the readout capacitance. This is practically equivalent to do $t_{tot} = 0$ ms at the expense of loosing any dependence of $\sigma_{ro,x,y,(n)}$ on y . The latter is not a problem because each semi-column of the sensor has its own readout channel. We acquired 1000 frames in such a reversed transfer mode for different frame rates, and computed $\sigma_{corr,x,y,(n)} = \left(\sigma_{ro,x,y,(n)}^2 + \sigma_{\Delta cm,x,y,(n)}^2 \right)^{1/2}$, see Fig. 5.11. Note that, $\sigma_{corr,x,y,(n)}$ does not depend on FR because the readout is done at a fixed frequency (t_{ro} is constant).

The ADCs used to digitalize the analog outputs of the CAMEX have a resolution of $N_{adc} = 14$ bit with $N_{ENOB} = 10$ ENOB. Therefore, the contribution of the quantization noise (see Eq. 3.3) to the readout noise is small, i.e. $N_{adc}=0.53\text{ }e^-$ rms for a conversion gain of $G=8.68\text{ DN}/e^-$.

5.4.5 Dark noise, offset and dynamic range

Comparing the measured mean value of $\sigma_{corr,x,y,(n)}$ at $FR=400$ fps shown in Fig. 5.11 with Eq. 5.19, it is evident that the total camera noise is dominated by the readout (plus residual common mode) noise for the normal working temperature of $T_{CCD} = -25\text{ }^\circ\text{C}$. Moreover, a rough estimation of the dark noise in this regime is $\sqrt{4.94 - 4.93} = 0.31\text{ }e^-$ rms. Since the total lifetime of the charge wells (t_{tot} , see Eq. 5.20) depends on the y (row) coordinate, and t_{ro} ($\sim 8.66\text{ }\mu\text{s}$) is larger than t_t ($\sim 0.26\text{ }\mu\text{s}$), the pixels located near the center of the image will accumulate on average more dark charges.

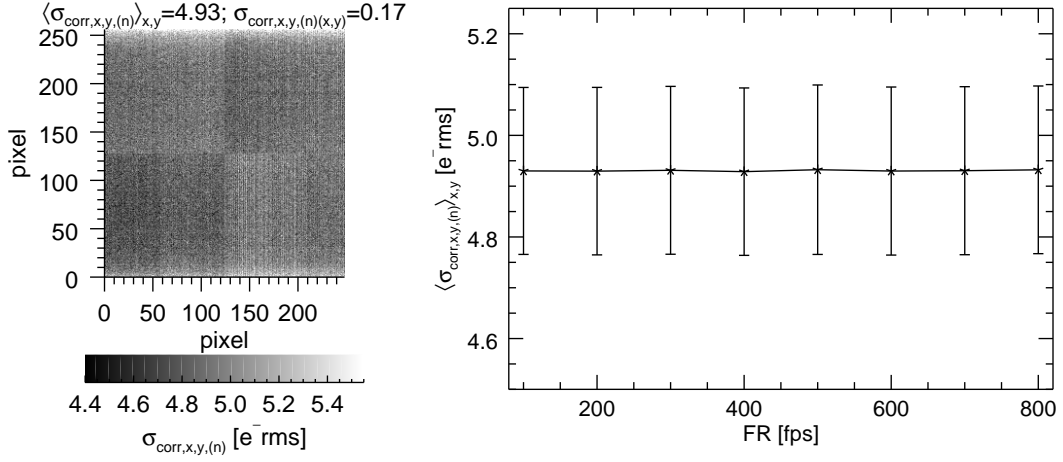


Figure 5.11. Measured readout plus residual common mode noise of the pnCCD camera. The leftmost image shows the temporally-estimated noise in 1000, common-mode and bias corrected dark frames. The frames were acquired at a frame rate of $FR=400$ fps, and with the charge transfer direction reversed in order to avoid any contribution from thermal charges. The same procedure was repeated for different FR , the resulting mean values of the noises are shown in the rightmost plot. See the text for extra details.

A typical bias frame used for dark correction at $FR=400$ fps is presented in Fig. 5.12, including its time stability. From the latter it can be seen that the bias of the lower right (LR) quadrant presents a slightly worse time stability than the upper left quadrant (UL, which is similar to the other quadrants), i.e. the standard deviations of the curves for LR and UL are 7.6 and 5.3 DN respectively. This may be the reason for the increased residual offsets detected in the LR quadrant in Fig. 5.9d, although its confirmation requires further investigation. Note that the bias frame shown in Fig. 5.12 presents few (~ 16) hot pixels (with values from 300 up to 3000 DN above the spatial mean). The source of such pixels has not been identified, however, they are filtered out during data reduction.

Using the spatial mean value of the bias frame given in Fig. 5.12, $\langle \hat{I}_{\text{dark},x,y}^n \rangle_{n,x,y}$, and the previously found $G=8.68 \text{ DN}/e^-$ and $\sigma_{\text{cam}}=4.94 e^- \text{rms}$; we can estimate the *dynamic range per frame* of the pnCCD camera to be $(2^{N_{\text{adc}}} - \langle \hat{I}_{\text{dark},x,y}^n \rangle_{n,x,y}) / (G\sigma_{\text{cam}}) = 285$.

5.5 Photon-noise limited regime

As discussed in Sect. 2.1.4, solely the photon-noise imposes severe constraints on the achievable SNR when doing high-resolution, imaging spectropolarimetry of dynamic solar signals. Therefore, reducing any noise contribution from the camera or modulator is very important. To illustrate this, let us express the required number of Stokes images (N_{stk} , i.e. four times the number of intensity frames) that need to be averaged, in order to achieve a desired noise level in the *normalized* Stokes parameter $i \in \{I, q, u, v\}$ (σ_i) as follows

$$N_{\text{stk}} = \frac{\kappa_{\text{int}}}{\epsilon_i^2 N_{\text{mod}} \sigma_i^2 \langle \bar{I}^n \rangle_n} \left(1 + \frac{\sigma_{\text{cam}}^2}{\sigma_p^2} \right), \quad (5.21)$$

where $\kappa_{\text{int}} = 1 e^-$; $\langle \bar{I}^n \rangle_n$ is expressed in e^- , i.e. we redefined $\langle \bar{I}^n \rangle_n \rightarrow \langle \bar{I}^n \rangle_n / G$ (see

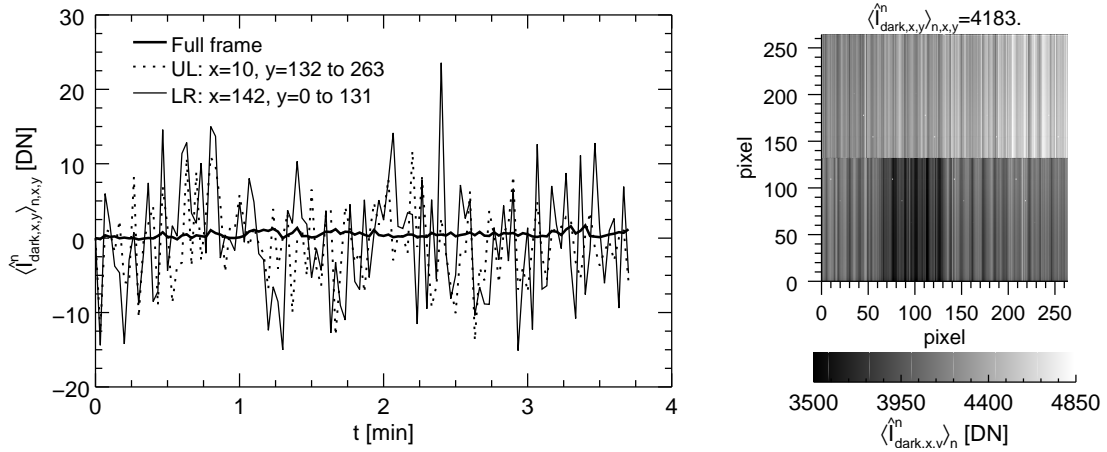


Figure 5.12. Bias frame of the pnCCD camera operating at $FR=400$ fps and $T_{CCD} = -25^\circ\text{C}$. The plot on the left shows the temporal variation of the spatial mean value of the bias frame. Each bias frame was computed by averaging 800 (spanning 2 s) dark frames. The three curves correspond to the spatial mean calculated over the whole sensor area, one semi-column in the upper left (UL) quadrant, and one semi-column in the lower right (LR) quadrant (see legend). The initial value at $t=0$ min, was subtracted from the three curves. The rightmost image presents the bias frame resulting from averaging all the 89600 (spanning 3.73 min) dark frames in the series. See the text for extra details.

Eq. 5.2); we have dropped the pixel indexes; assumed that the images have been dark and common mode corrected; and used Eq. 5.1 and 2.35. From Eq. 5.21 is easy to see that the required N_{stk} (which defines the integration time) scales quadratically with the relative changes in the modulator's polarimetric efficiencies, and thus efficiency maximization is crucial (see Sect. 4.2). Analogously, having a low camera noise compared to the photon noise of the individual frames is very important due to the quadratic dependence of N_{stk} with σ_{cam} , see Fig. 5.13. For example, if $\sigma_{cam} = \sigma_p$, twice the integration time is required compared to the case where $\sigma_{cam} \approx 0$. Note that, in the latter case, N_{stk} scales linearly with the relative changes of $\langle \bar{I}^n \rangle_n$, which are given by any property that affects the amount of collected photons by the camera, most notably QE , FF and DC .

From the linear dependence of the relative increase (with respect to the $\sigma_{cam} = 0$ case) of N_{stk} with the ratio $\sigma_{cam}^2/\sigma_p^2$ given by Eq. 5.21, we can define the *photon-noise limited* regime. Considering acceptable an increase of the integration time of 10% to reach the goal σ_i , then, the minimum mean intensity per frame is the one that produces $\sigma_{cam}^2/\sigma_p^2 = 0.1$, i.e.

$$\langle \bar{I}^n \rangle_{n,pn-limit} = 10\sigma_{cam}^2. \quad (5.22)$$

For the case of the pnCCD camera this value corresponds to $\langle \bar{I}^n \rangle_{n,pn-limit} = 244 e^-$ (see Eq. 5.19). As an example, consider the next fastest polarimeter in Fig. 3.2, SPINOR which has $FR=100$ fps and a $\sigma_{ro}=40 e^-$ rms. Assuming the best-case scenario where $\sigma_{cam} = \sigma_{ro}$, SPINOR has $\langle \bar{I}^n \rangle_{n,pn-limit} = 16000 e^-$. Moreover, the relative increase in the integration time required to reach any goal σ_i given any $\langle \bar{I}^n \rangle_n$, is for SPINOR 66.6 times larger than that of FSP.

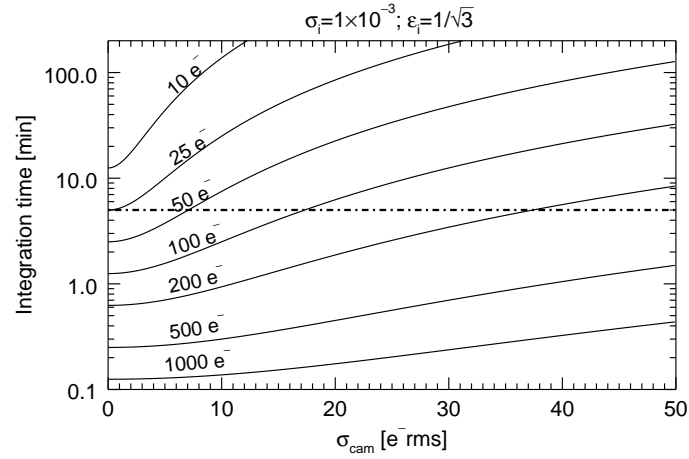


Figure 5.13. Integration time required to achieve a noise level of 1×10^{-3} in the normalized Stokes images, versus the total camera noise for different intensity levels ($\langle \bar{I}^n \rangle_n$, annotated over each continuous curve). Note that the vertical axis is in logarithmic scale. The figures were computed using Eq. 5.21, assuming a frame rate of 400 fps and the parameters shown in the title (note that for a given frame rate, the integration time is independent of N_{mod}). The horizontal dotted line indicates the typical lifetime of solar granulation (5 min). As an example, in the VTT we obtained (working at the diffraction limit) a $\langle \bar{I}^n \rangle_n$ of ~ 12 and $\sim 300 e^-$ for the line core of Ca I 422.7 nm and the continuum near Fe I 630.2 nm respectively (see Ch. 6). See also Table 3.2 for typical values of σ_{ro} (which generally dominates σ_{cam}) in solar polarimeters.

6 First light measurements

After integration of the main FSP components in the laboratory, the instrumental concept was tested in five first-light campaigns. These were carried out using the 68 cm, German VTT located in El Teide observatory, Tenerife, between the years 2013 and 2015.

The present chapter describes some of the results of such observations, along with the most relevant tasks that were carried out in order to obtain the final data sets. The emphasis is put on the data reduction pipeline (Section 6.1), for the reason that its realization requires understanding the main components of the system and thus, is in close relationship with the results obtained in Chapters 4 and 5. One example observation is given for FSP working in spectrograph mode (Section 6.2) and two for the case of filtergraph (Section 6.3). In addition, we present the results of the firsts applications of MOMFBD to filtergraph-based FSP measurements, including a short overview of the different ways in which the restoration of the data can be approached. The results of the presented measurements are used to assess the performance of the polarimeter, including the achieved polarimetric sensitivity and residual levels of SIC (Section 6.4). Some of the contents of the present chapter have been published in Iglesias et al. (2016).

6.1 Data acquisition and reduction

In the following sections we describe in a nutshell the most important data reduction steps, required to process FSP data. The same steps are applied for measurements carried out with a spectrograph or with a filtergraph unless explicitly stated. A typical measurement involves the acquisition of (a) science measurements, with modulated intensities $\hat{\mathbf{I}}$; (b) flat field measurements, with modulated intensities $\hat{\mathbf{I}}_{flat}$; (c) dark measurements, with intensities $\hat{\mathbf{I}}_{dark}$; and (d) polarimetric calibration measurements, with modulated intensities $\hat{\mathbf{I}}_{cal}$.

6.1.1 Intensity calibration

The first step involves the calibration of the modulated intensities acquired with the pnCCD camera. This requires the following

1. *Science data acquisition:* Given a goal noise in the normalized Stokes vectors of the science images, σ , the required number of Stokes measurements (N_{stk}) can be derived from Eq. 5.21.
2. *Missing frames and phase detection:* Since the synchronization of camera and modulator is crucial to allow the demodulation of the acquired intensities, every single

missing frame has to be carefully identified (using the time stamps, see Sect. 5.4.3) and the full modulation cycle removed. Another critical aspect is the definition of which of the four modulation states is considered the first one. Such a first state has to be the same in all data sets, including the calibration measurements. One drawback of the pnCCD camera design was that the identification of the modulation states corresponding to each frame was not implemented. Therefore a workaround that includes an initial overexposure was used. This issue was taken into consideration when designing the new FSP II camera.

3. *Dark correction:* Before or after the science images have been acquired, the dark measurements are carried out. The number of dark frames required, $N_{frm-dark}$, can be computed from $\sigma_{cam}/\sqrt{N_{frm-dark}} \ll \sigma$ and Eq. 5.19. Then, the science images are dark corrected by doing $\hat{I}_{corr0,x,y}^n = \hat{I}_{x,y}^n - \langle \hat{I}_{dark,x,y}^n \rangle_n$ (see Eq. 5.1).
4. *Common mode correction:* Each frame is common mode corrected by applying Eq. 5.18. After this, the shielded channels of the sensor are cropped from all frames to obtain $\hat{I}_{corr1,x,y}^n$.
5. *Frame transfer correction:* The smearing is eliminated from each modulation state (set of four intensity frames) by applying Eq. 5.12 to each column of $\hat{I}_{corr1,x,y}^n$. This results in the desmeared intensities $\hat{I}_{corr2,x,y}^n$. Note that Eq. 5.12 assumes a periodic signal, i.e. a constant input Stokes vector. If this is not the case, Eq. 5.6 has to be used (iteratively solved) instead.
6. *Flat fielding:* The acquisition of the flat field is done by randomly moving the telescope in a quiet region of the Sun, around the same longitude as the science observations, and disabling the AO correction. Since the telescope motion has a fixed velocity, the faster the camera, the more frames have to be acquired to ensure the proper smearing of the solar structures in the background. From a noise point of view, the number of flat frames required, $N_{frm-flat}$, can be obtained from $\sqrt{(\sigma_{cam}^2 + I_{flat})/N_{frm-flat}} \ll \sigma$, where I_{flat} is the mean intensity in the flat images.

The corrected (after undergoing steps 2 to 5) flat field data, $\hat{I}_{flat-corr2,x,y}^n$, are used to eliminate the spatial variations of the gain table in the science data by doing $\hat{I}_{corr3,x,y}^n = \hat{I}_{corr2,x,y}^n * \langle \hat{I}_{flat-corr2,x,y}^n \rangle_{n,x,y} / \langle \hat{I}_{flat-corr2,x,y}^n \rangle_n$. This procedure takes into account both the spatial variations of the detector G and the optical gain of the setup. In addition, since the average of all frames (independently of the modulation state) of $\hat{I}_{flat-corr2,x,y}^n$ is used, no polarized components of the flat field can be corrected using this technique. When using a spectrograph, the spectral lines are present in the flat field¹ complicating the correction of the pixels located in the lines. To cope with this, the spectral lines are numerically removed from $\langle \hat{I}_{flat-corr2,x,y}^n \rangle_n$ by interpolating in the wavelength dimension. When observing with a multi-etalon filtergraph in telecentric configuration (Sect. 2.2.3), as for the measurements presented in Sect. 6.2, the flat field is usually dominated by the etalons errors. Therefore we acquire and apply an independent flat field for each spectral point. Given a spatially constant spectral content of the incoming intensity during flat fielding, variations in

¹Moving the spectral lines out of the *FOV* implies retuning the spectrograph setup which would modify the flat field and produce an erroneous correction.

the etalon cavities (optical path length) and reflectance across their aperture, produce a spatial variation of the transmission profiles. The transmission profile of the multi-etalon setup can vary in amplitude, width and spectral location. While all these phenomena produce a spatial fluctuation of the output intensity, the flat fielding process described above can correct only for local changes of the amplitude and not for spectral shifts of the transmission profiles. The latter, however, are higher-order errors that can be corrected in an extra step (not described here, see de la Cruz Rodríguez et al. 2015) if required.

7. *Image restoration:* In this step, the modulated intensities ($\hat{I}_{corr3,x,y}^n$) can be optionally restored by using a MOMFBD, this is detailed in Sect. 6.1.5. Note that the flat fielding procedure described in the previous step, only affects the resulting Stokes I images. Thus it could also be applied after the polarimetric demodulation only on Stokes I . We have done it in the 6th step, however, because it is required if the intensity images are restored before demodulation.

6.1.2 Polarimetric calibration

The polarimetric calibration is done as explained in Sect. 4.3. We typically record $N_{cal} = 18$ independent calibration inputs, see Fig. 4.5. When working with a filter-graph, the calibration is acquired in the nearest continuum spectral position (see Sect. 4.3.2) and with the telescope moving in flat field mode, to ensure an unpolarized and flat input for the PSG. This, however, contributes to increasing the input intensity fluctuations (see foot note 10 on Sect. 4.3.1), which complicates the implementation of a field dependent demodulation, see Sect 4.3.1. When working with a spectrograph, the calibration is performed covering the same spectral range as the science data. The spectral lines are excluded (due to the low SNR) when computing the spatial mean to obtain a scalar demodulation matrix (Sect 4.3.1). The estimated demodulation matrix, $\hat{\mathbf{D}}$, is used to demodulate the science data by doing $\hat{\mathbf{S}}_{x,y} = \hat{\mathbf{D}}\hat{\mathbf{I}}_{corr3,x,y}$ for each modulation cycle.

6.1.3 Frame accumulation and polarimetric normalization

After demodulation, the N_{stk} Stokes images acquired are normalized (Eq. 2.11) and accumulated to reduce noise. The accumulation and normalization operations do not commute and thus an order of application has to be selected. Considering Stokes Q , the two possible options are $\langle \hat{Q}_{x,y}^n / \hat{I}_{x,y}^n \rangle_n$ and $\langle \hat{Q}_{x,y}^n \rangle_n / \langle \hat{I}_{x,y}^n \rangle_n$. Out of these two options, only the latter is an asymptotically (for $N_{stk} \rightarrow \infty$) unbiased estimator for the ratio of the expectation values, $Q_{x,y}/I_{x,y}$ (see Fig. 6.1). The second order approximation to the expected value of both estimators is (see van Kempen and van Vliet 2000),

$$\mathcal{E}\left(\left\langle \frac{\hat{Q}_{x,y}^n}{\hat{I}_{x,y}^n} \right\rangle_n\right) = \frac{Q_{x,y}}{I_{x,y}} + \kappa_{bias} \quad \text{and} \quad \mathcal{E}\left(\frac{\langle \hat{Q}_{x,y}^n \rangle_n}{\langle \hat{I}_{x,y}^n \rangle_n}\right) = \frac{Q_{x,y}}{I_{x,y}} + \frac{\kappa_{bias}}{N_{stk}}, \quad (6.1)$$

where $\kappa_{bias} = (Q_{x,y}1[DN] - \sigma_{Q,I,x,y}^2)/I_{x,y}^2$, \mathcal{E} represents the expectation value operator and $\sigma_{Q,I,x,y}^2$ is the covariance between $Q_{x,y}$ and $I_{x,y}$. Note that $I_{x,y}$ is in the denominator of κ_{bias} , this produces a crosstalk from Stokes I which is spatially non-flat and increases for short exposure times.

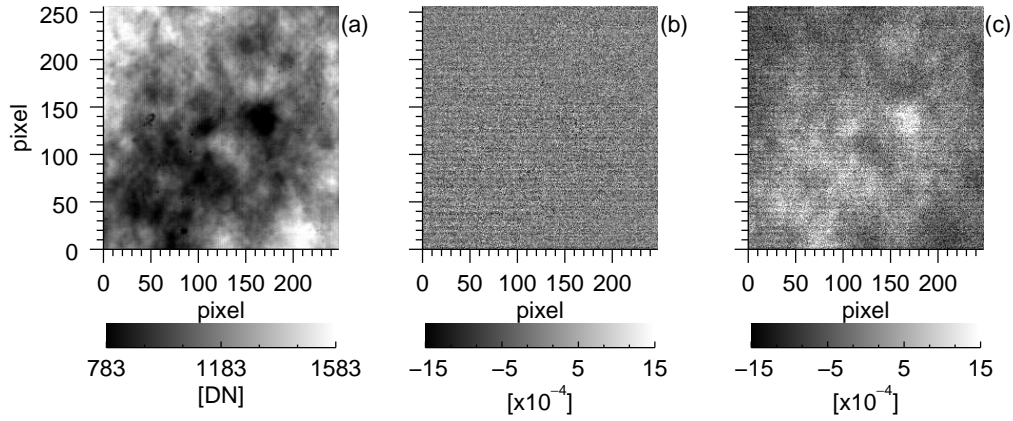


Figure 6.1. Frame accumulation and polarimetric normalization. Image (a) shows the averaged Stokes I of near 5×10^4 (8.3 min) measurements, $\langle \hat{I}_{x,y}^n \rangle_n$, acquired with FSP in filtergraph mode and with the modulator package disconnected, i.e. no polarization signal is expected. No flat fielding was applied and thus the contrast of $\langle \hat{I}_{x,y}^n \rangle_n$ is practically dominated by the etalons cavity errors. The difference of the artifact introduced by the κ_{bias} term of Eq. 6.1, is evident in the Stokes images that where accumulated and then normalized ($\langle \hat{Q}_{x,y}^n \rangle_n / \langle \hat{I}_{x,y}^n \rangle_n$, image b) and vice versa ($\langle \hat{Q}_{x,y}^n / \hat{I}_{x,y}^n \rangle_n$, image c). Adapted from Iglesias et al. (2016).

6.1.4 Instrumental polarization

The modulation matrix estimated during the polarimetric calibration includes the polarimetric action any optical element that is placed in between the PSG and the polarization analyzer of the modulator². During the observations presented in this chapter we placed the PSG immediately in front of the modulator (see Fig. 4.1c). Therefore, after all the reduction steps presented in Sect. 6.1.1, 6.1.2 and 6.1.3 have been applied, the measured Stokes vector ($\hat{\mathbf{S}}$) corresponds to the one present at the input of the modulator, i.e. the basic data reduction block of Fig. 2.4 is complete. The next step implies correcting for the polarimetric action of any optical element, located in between the modulator and the telescope entrance aperture, in order to estimate the Stokes vector there, $\hat{\mathbf{S}}_{tel}$, i.e. solving

$$\hat{\mathbf{S}} = \mathbf{M}_{AO+tel} \hat{\mathbf{S}}_{tel}, \quad (6.2)$$

where the AO plus telescope Mueller matrix, \mathbf{M}_{AO+tel} , is usually found by a combination of measurements (by placing a PSG as close as possible to the telescope aperture) and modeling (to extrapolate the measured values to e.g. different times of the day, where the telescope configuration is modified or different wavelengths). The details of such instrumental calibration are out of the scope of this work. Moreover, all the data presented here has not been subject to this kind of instrumental calibration because a working polarimetric model of the VTT and its AO system valid for optical wavelengths, was not available during the first light campaigns where, in addition, most of the efforts were focused on assessing FSP performance. As a workaround, when required we used an heuristic correction of the instrumental polarization which implies assuming that the \mathbf{M}_{AO+tel} is constant

²Due to this the best is to locate the PSG as early in the beam as possible. Note that, the polarimetric actions of the optical elements located after the analyzer are not relevant, as long as they can be considered constant within a modulation cycle period. This is because the input Stokes vector is encoded in the intensity of the output beam.

across the FOV , its vector \mathbf{h} (see Eq. 2.10) is small (no strong depolarization effects are present), its matrix \mathbf{R} is predominantly a rotation matrix (retarder effects are strong) and its vector \mathbf{v} is not null (polarizing effects are present). Under these assumptions, the action of \mathbf{M}_{AO+tel} can be modeled as a rotation followed by a translation of the incoming \mathbf{p}_{tel} . Therefore, the instrumental polarization can be removed by first subtracting spatially flat offsets to make the continuum spectral points in the \hat{Q}/\hat{I} , \hat{U}/\hat{I} and \hat{V}/\hat{I} images equal to zero (invert the translation); and the applying a spatially flat rotation of the polarization vector until no correlation among \hat{Q}/\hat{I} , \hat{U}/\hat{I} and \hat{V}/\hat{I} is evidently present (invert the rotation).

6.1.5 Image restoration with MOMFBD

In Fig. 2.4 the basic data reduction block is separated from the post processing block, which is just illustrative. Ideally, all the reduction steps should be applied to the data following the optical path in reverse order. Thus, image restoration should be the last correction to be implemented, i.e. after instrumental polarization corrections. In practice, however, image restoration can be applied before the polarimetric demodulation if one aims for additional SIC reduction. Moreover some instrumental effects are entangled with the seeing aberrations (and thus with the restoration step), e.g. the wavelength shifts introduced by etalon errors when used in telecentric configuration (see point 6 in 6.1.1). As a consequence, when using a very accurate model of the image forming system, the reduction of the data becomes a complex problem linked to a specific filtergraph setup, which is out of the scope of this work. Great efforts are currently being put to elaborate such a detailed data reduction which is necessary to do high-resolution, high-sensitivity solar spectropolarimetry with Fabry-Pérot filtergraphs from the ground, see e.g. the work by de la Cruz Rodríguez et al. (2015). Here we present only few basic approaches to restore filtergraph-based FSP data using a MOMFBD. The MOMFBD algorithm (Sect. 2.3.3) requires two main steps. Firstly the *wavefront sensing* or estimation of the seeing OTFs, which involves the minimization of Eq. 2.73 to get the coefficients of the expansion in Eq. 2.71 for each object. Secondly, the *deconvolution step* which requires applying a Wiener deconvolution (see footnote 24 in Sect 2.3.3) to solve Eq. 2.68 and estimate the true solar scene. The modulated intensities acquired with FSP at $FR = 400$ fps have an exposure time (2.5 ms) that is about four times shorter than the typical seeing coherence time $\tau_0 \approx 10$ ms (corresponding to $r_0=10$ cm and a wind speed of 10 m s^{-1}). In addition, only a single narrow-band channel (object) is available³. The aforementioned properties of FSP data allow different approaches to perform the MOMFBD, each of which presents different pros and cons according to the specific case under consideration, in particular the SNR in the individual Stokes images, the quality of the flat fielding process and the seeing conditions. We describe only three of such approaches in Table 6.1. For brevity we denote the flat-field-corrected intensity image ($\hat{\mathbf{I}}_{corr3}$) in modulation state $i \in \{0, 1, 2, 3\}$ of modulation cycle $k \in \{0, 1, \dots, N_{stk} - 1\}$ as \hat{I}_i^k . Analogously the derived Stokes vector (Sect. 6.1.2) no. k is written $\hat{\mathbf{S}}^k$. Note that four different objects (Obj. 0 to 3) need to be defined to separate the four modulation states of FSP. If all the frames would be used

³This is not ideal. The implementation of a WB channel can be done at high frame rates using a commercial camera because photon noise is dominating in each frame. Performing the wavefront sensing step using such a high SNR frames will provide better results than using only narrow band images.

Approach	$\mathcal{H}_{atm+tel}$	Obj. 0	Obj. 1	Obj. 2	Obj. 3
AP1	0	\hat{I}_0^0	\hat{I}_1^0	\hat{I}_2^0	\hat{I}_3^0
	1	\hat{I}_0^1	\hat{I}_1^1	\hat{I}_2^1	\hat{I}_3^1
		...			
AP2	0	\hat{I}_0^0	-	-	-
	1	-	\hat{I}_1^0	-	-
	2	-	-	\hat{I}_2^0	-
	3	-	-	-	\hat{I}_3^0
	4	\hat{I}_0^1	-	-	-
	5	-	\hat{I}_1^1	-	-
		...			
AP3	0	\hat{I}^0	\hat{Q}^0/\hat{I}^0	\hat{U}^0/\hat{I}^0	\hat{V}^0/\hat{I}^0
	1	\hat{I}^1	\hat{Q}^1/\hat{I}^1	\hat{U}^1/\hat{I}^1	\hat{V}^1/\hat{I}^1
		...			

Table 6.1. Different approaches to restore FSP data with MOMFBD. In the first approach (AP1) the modulated intensities are restored assuming the same realization of the seeing for the four modulation states (each treated as a separate object). Therefore, for each modulation cycle, the MOMFBD code will use a single fitted $\mathcal{H}_{atm+tel}$ to deconvolve the four intensities. On the other hand, in the second approach (AP2) a different seeing realization is assumed for each modulation state. Thus the MOMFBD code will fit a different $\mathcal{H}_{atm+tel}$ and use it to deconvolve each modulated intensity. The remaining option (AP3) implies restoring the data after the polarimetric demodulation and normalization, assuming the same $\mathcal{H}_{atm+tel}$ for all the Stokes parameters of each measurement.

to solve a single MFBF problem, the changes introduced by the modulation would be misinterpreted as seeing induced changes leading to a wrong wavefront sensing. Below we list the main pros and cons of each approach.

- *AP1*: This approach is suitable to restore measurements of faint signals because intensity images are used, which have larger SNR than the normalized Stokes \hat{Q} , \hat{U} and \hat{V} . In addition AP1 is not very sensitive to residual gain table artifacts (non-flat multiplicative terms) because the same $\mathcal{H}_{atm+tel}$ is used to restore the four modulated intensity frames of each modulation cycle (an assumption that does not hold for bad seeing conditions where $\tau_0 \leq 2.5$ ms), and thus there is no significant relative spatial shift introduced between the frames. As a consequence residual gain table artifacts, e.g. non-corrected interference fringes, will not tend to appear after demodulation in the normalized Stokes \hat{Q} , \hat{U} and \hat{V} images. For the same reason, AP1 does not modify the levels of SIC per modulation cycle. Note that this approach requires the modulated intensity images to be flat fielded as described in step 6 of Sect. 6.1.1.
- *AP2*: For each modulation cycle independent $\mathcal{H}_{atm+tel}$ are fitted and used to demodulate each of the four intensities. Therefore AP2 introduces relative numerical shifts among the frames. This means that residual gain table artifacts will tend to appear in the normalized Stokes \hat{Q} , \hat{U} and \hat{V} images after demodulation. On the other hand, this also means that AP2 may reduce (if the restoration is good) the SIC levels by compensating the differential seeing aberrations present among the modulated intensities. AP2 also requires the intensity images to be flat fielded as

described in step 6 of Sect. 6.1.1.

- *AP3*: In this approach the restoration is applied after polarimetric demodulation⁴. In principle the normalization step should be done first to avoid introducing artifacts due to residual gain table effects in the Stokes images. However, if many images are used, the issues presented in Sect. 6.1.3 may complicate this. The *SNR* in the normalized Stokes \hat{Q} , \hat{U} and \hat{V} images is typically low (e.g. Sect 6.3.1), and thus they tend to spoil the wavefront sensing step (that is why fitting an independent $\mathcal{H}_{atm+tel}$ for each normalized Stokes parameter is not generally done). Since a single $\mathcal{H}_{atm+tel}$ is fitted per Stokes measurement, a solution to the latter is to reduce the object weights (see Eq. 2.73) of the polarimetric images or even set them to zero, i.e. $K_{obj,1} = K_{obj,2} = K_{obj,3} = 0$, to use only Stokes *I* to perform the wavefront sensing step. Even assuming a good wavefront sensing, the low *SNR* in the normalized Stokes images also complicates the estimation of the regularization parameter in the Wiener deconvolution step (see footnote 24 in Sect 2.3.3). *AP2* does not require the flat fielding to be applied before demodulation (as in step 6 of Sect. 6.1.1), it can be done only for Stokes \hat{I} after the demodulation is complete.

6.2 Measurements in spectrograph mode

The first-light campaign of FSP was carried out at the German Vacuum Tower Telescope (VTT⁵) during June 2013, using the echelle (Sect. 2.2.3) spectrograph (see e.g. Dörr et al. 2012). The VTT has an aperture of 68 cm (providing an angular resolution of $\Delta\alpha=0.180$ arcsec at $\lambda=500$ nm), a focal length of 45.64 m, an image plate scale of 4.59 arcsec mm⁻¹ at the primary focus, and it is equipped with the Kiepenhauer Institute Adaptive Optics System (KAOS, see von der Luehe et al. 2003). KAOS can compensate up to ~30 modes (26 are regularly used) in close loop with a ~100 Hz bandwidth, and has a Shack-Hartmann wavefront sensor that operates in visible wavelengths (500 to 600 nm). The pre-dispersed echelle spectrograph of VTT presents a resolving power of 1.2×10^6 , e.g. $\Delta\lambda=4.2$ mÅ at $\lambda=500$ nm.

This first FSP campaign was aimed at testing the basic instrument functionality and at evaluating the polarimetric sensitivity that can be achieved in low spatial and high spectral resolution measurements. The most important components of the instrumental setup are summarized in Fig. 6.2. We performed different spatial scans of solar active regions to measure Zeeman signals (Sect. 2.1.2) in the Fe I 630.2 nm and Fe I 525.0 nm spectral lines, and found that the instrument performed as expected in such a high *SNR* regime (see e.g. Fig. 2.3). In addition, we acquired faint scattering polarization signals (Sect. 2.1.2) near the solar limb in the Ca I 422.7 nm, Na I *D*₂ 589.0 nm and Sr I 460.7 nm spectral lines. This kind of measurements require high polarimetric sensitivity and —considering that they have been measured and reported in the literature, see Fig. 2.2— they are useful for instrument validation. In the following section we report, as an example, the results of the Ca I measurements. A discussion of the results is given in Sect. 6.4.

⁴Note that, the deconvolution and polarimetric demodulation operations commute only if the demodulation matrix is spatially flat.

⁵See Schroeter et al. (1985) or <http://www.kis.uni-freiburg.de/en/observatories/vtt/> for updated information.

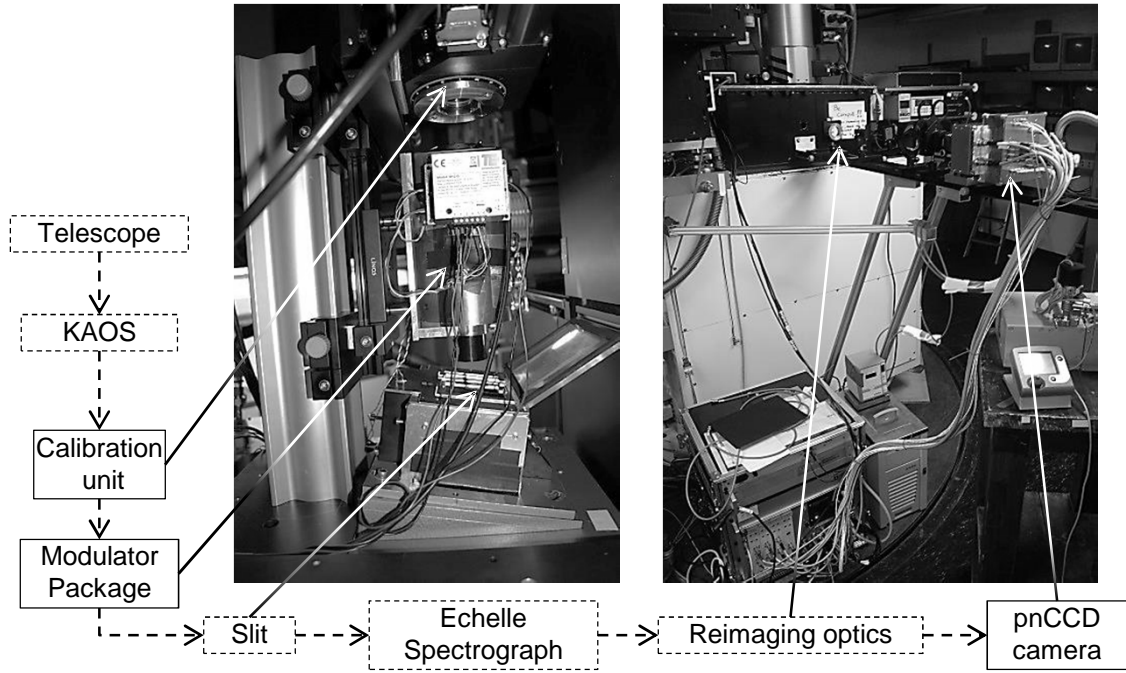


Figure 6.2. FSP setup during the first light measurements with the VTT echelle spectrograph. The boxes denote the main components located in the beam path (marked with dashed arrows). The boxes with continuous borders belong to FSP. The two photographs show the real devices associated to some of the boxes (indicated with continuous arrows). These include the modulator package (left photo) vertically mounted on top of the box containing the spectrograph entrance slit, and the pnCCD camera (right photo) mounted at an output port of the echelle spectrograph.

6.2.1 Low SNR regime: Second solar spectrum of Ca I

To record the second solar spectrum of Ca I, the slit was located near the solar limb —at $\mu \approx 0.15^6$ — where the scattering signals are stronger (Sect. 2.1.2). In addition, we oriented the slit (which matched the Stokes Q orientation of FSP) tangential to the solar limb in order to maximize the Stokes Q signal. As mentioned in Sect. 6.2, we aimed for high spectral but low spatial resolution which allowed us to use long integration times in order to explore the high polarimetric sensitivity regime of FSP⁷. Therefore, a large spatial sampling ($\Delta\alpha_{\text{samp}}$) was used, see Table 6.2. Moreover KAOS was not correcting the wavefronts because the low contrast near the limb does not allow its proper functioning. The measured values of scattering polarization and the achieved polarimetric sensitivity are presented in Fig. 6.3.

6.3 Measurements in filtergraph mode

Filtergraph-based measurements are the main goal of FSP because high spatial resolution in combination with high sensitivity are required when trying to estimate the smallest and

⁶ μ is equal to the cosine of the angle between the LOS and the normal of the solar surface.

⁷Since the gradient in Stokes I images is large due to the presence of the absorption spectral lines, the system is sensitive to instrumental image motion which can introduce polarimetric crosstalk. The high modulation frequency of FSP helps to reduce such a crosstalk.

Prop.	μ	FOV	$\Delta\alpha_{samp}$	$\Delta\lambda_{samp}$	λ_0	f_{mod}	Int. time
Value	0.15	72×3.7	0.8	17	422.7	25	4.98
Unit	-	arcsec $\times\text{\AA}$	arcsec pixel $^{-1}$	m \AA pixel $^{-1}$	nm	Hz	min

Table 6.2. Data specification of the Ca I second solar spectrum measured with FSP.

faintest polarimetric signals (see Sect. 2.1.4). The filtergraph campaigns of FSP were carried out at the VTT during November 2013 and March and June 2014, using the Triple Etalon Solar Spectrometer (TESOS, Tritschler et al. 2002, von der Luehe and Kentischer 2000, Kentischer et al. 1998). TESOS uses three Fabry-Pérot etalons (Sect 2.2.3) to achieve a resolving power of 300 000, e.g. $\Delta\lambda=17\text{ m\AA}$ at $\lambda=500\text{ nm}$, and high transmission. During the filtergraph campaigns we address the key questions required to evaluate the FSP instrumental concept, including (a) the residual levels of SIC when modulating at 100 Hz under average seeing conditions, (b) what are the polarimetric sensitivity and spatial resolution achievable at the VTT when using a frame rate of 400 fps for typical solar targets and (c) what is the performance of a narrow band MOMFBD restoration of FSP data for typical solar targets. The most important components of the adopted instrumental setup are summarized in Fig. 6.4. One relevant aspect of the setup at the VTT is that the mechanical bond between the floor supporting TESOS and the KAOS tank is relatively poor. This means that vibrations affecting TESOS will tend to introduce relative shifts between the beam and the pnCCD camera, and thus appear as image motion. In our November 2013 campaign, the water pump used to precool the pnCCD camera (Sect. 3.2.2) was located near the TESOS optical table, and thus the weak vibrations produced by the electric motors were sufficient to introduce strong image motion (few pixels) at frequencies of 50 Hz and above. Such image motion induced polarimetric crosstalks (Sect. 2.3.2) in the order of $\sim 5 \times 10^{-3}$. In the 2014 campaigns this was solved by simply relocating the water pump far away from the TESOS optical table.

In Sect. 6.3.1 and 6.3.2 we present two measurement examples corresponding to two different regimes, i.e. low and high SNR , which help to answer the above-stated questions (b) and (c). A discussion of these results is given in Sect. 6.4. The filtergraph measurements that provide evidence to answer question (a) are treated in Sect. 6.4.5.

6.3.1 Low SNR regime: Fe I scan of the quiet sun

To explore the ability of FSP to detect faint and small scale polarimetric signals, we configured TESOS to perform $N_{scn}=40$ scans of two spectral points, one in each wing of the Fe I 630.2 nm spectral line. The details of such a scan, acquired during June 2014 in a quiet region at the center of the solar disk, are given in Table 6.3. We define the wall time as the time interval between the acquisition of the first and the last frame accumulated in a given spectral point. DC_{scn} is the fraction of the total scan time that the instrument spends collecting signal photo-charges (independently of the spectral point)⁸. The measured Stokes parameters in each wing are presented in Fig. 6.5. In addition, Fig.

⁸The synchronization between FSP and TESOS was not optimal contributing to make DC_{scn} much lower than the pnCCD camera DC . Therefore in this scan we only measured two spectral points to minimize the smearing of the signals due to solar evolution.

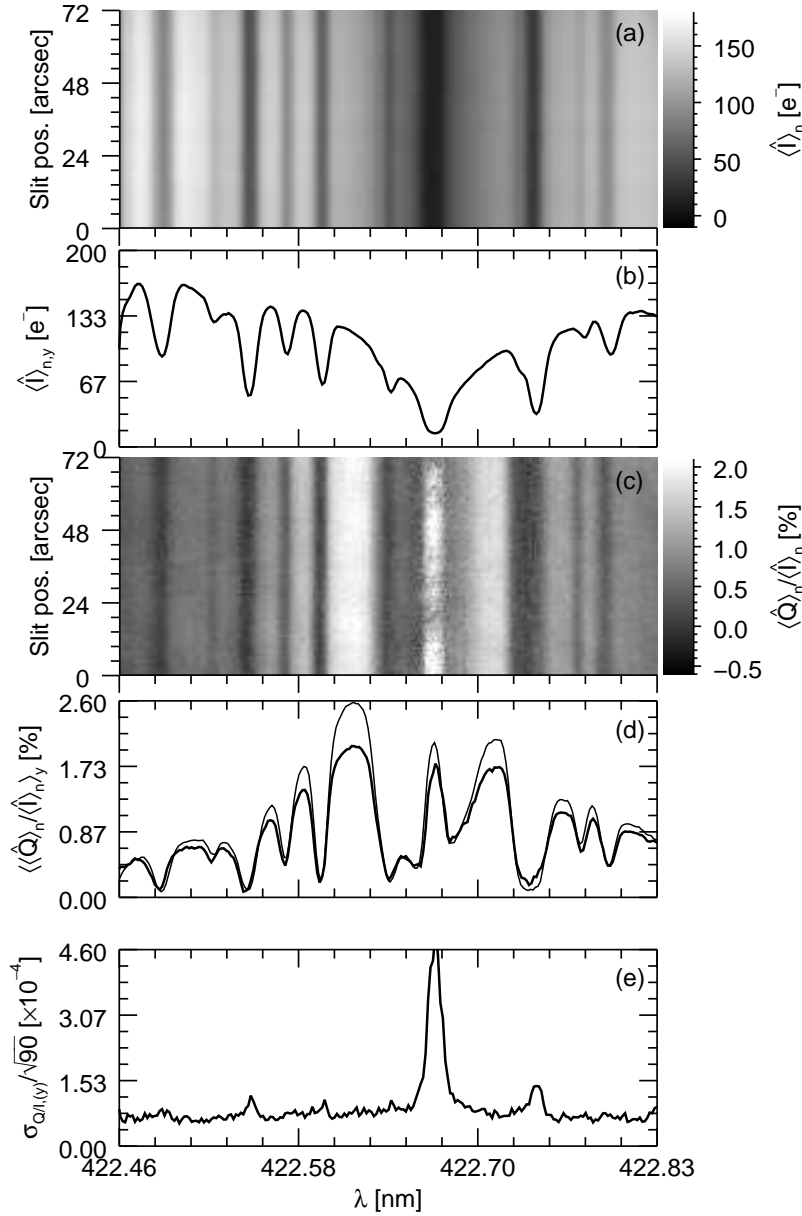


Figure 6.3. Ca I second solar spectrum measured with FSP. The averages of several measurements (covering 4.98 min wall time) are shown for Stokes I (a), including its spatial average (b), and the normalized Stokes Q (c) also including its spatial average (thick line in image d). Due to reimaging limitations, only a fraction of the pnCCD sensor ($90 \times 222 \text{ pixel}^2$) was illuminated. For comparison, we also plotted in (d) the measurements acquired with ZIMPOL at $\mu \approx 0.10$ and reported in Gandorfer (2002) (thin line). The differences between both measurements are due to the different μ values employed in the observations. The rms noise of (d), estimated from (c) along the spatial dimension, is presented in (e). The largest peak in the estimated noise is not due to the lower photo-charges flux reaching the camera in that spectral region (only about $12 e^-$ per pixel per frame) but produced by residual structures in the spatial dimension clearly visible in (c). The average value of the curve in (e) excluding figures larger than 2×10^{-4} is 8×10^{-5} . See Table 6.2 for extra details.

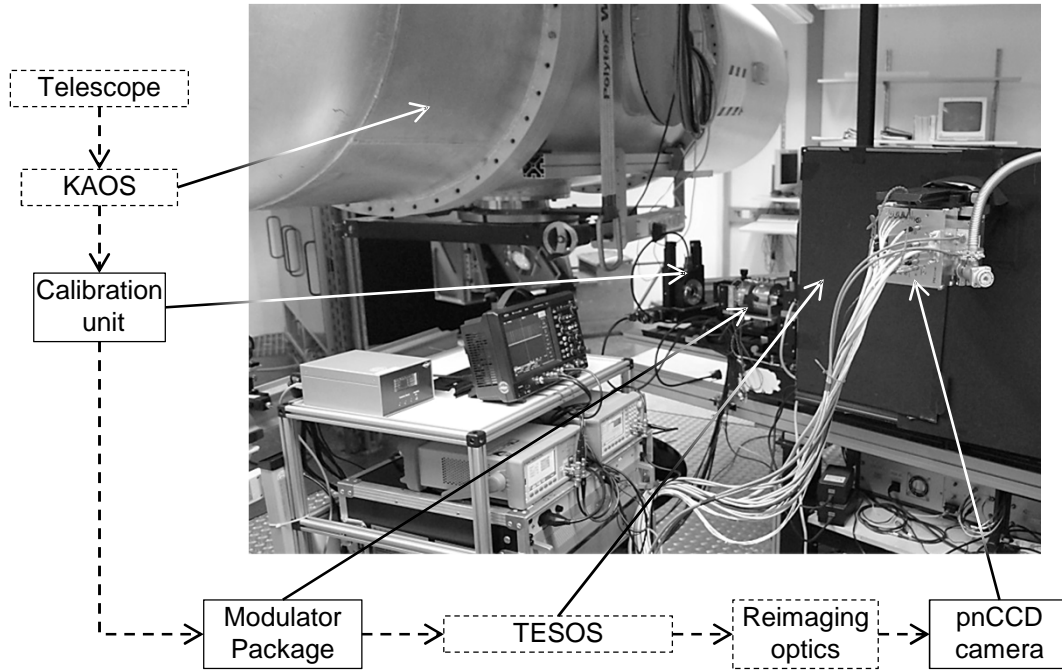


Figure 6.4. FSP setup during the first light measurements with the TESOS filtergraph at the VTT. The boxes denote the main components located in the beam path (marked with dashed arrows). The boxes with continuous borders belong to FSP. The photograph shows the real devices associated to some of the boxes (indicated with continuous arrows). At the output of KAOS (mounted inside the metallic tank), a 45° mirror redirects the beam to the FSP calibration unit and modulator package, which are located in front of TESOS (black box). The beam path was modified inside the TESOS housing to allocate the reimaging optics and mount the pnCCD camera.

6.6 shows the MOMFBD restored version of the frames acquired in the -80 mÅ spectral point, performed using AP1 (see Table 6.1).

Prop.	Value	Unit
Target heliocentric coordinates	0,0	arcsec,arcsec
FOV	19.7×20.4	arcsec ²
$\Delta\alpha_{\text{samp}}$	0.08	arcsec pixel ⁻¹
$\Delta\lambda_{\text{samp}}$	21	mÅ pixel ⁻¹
λ_0	630.2	nm
Spectral points (meas. from λ_0)	-80, 80	mÅ
f_{mod}	100	Hz
DC_{scn}	53	%
N_{scn}	40	%
Total int. time per spectral point	0.95	min
Total wall time per spectral point	3.99	min

Table 6.3. Data specification for the Fe I scan of the quiet sun measured with FSP. See the text for extra details.

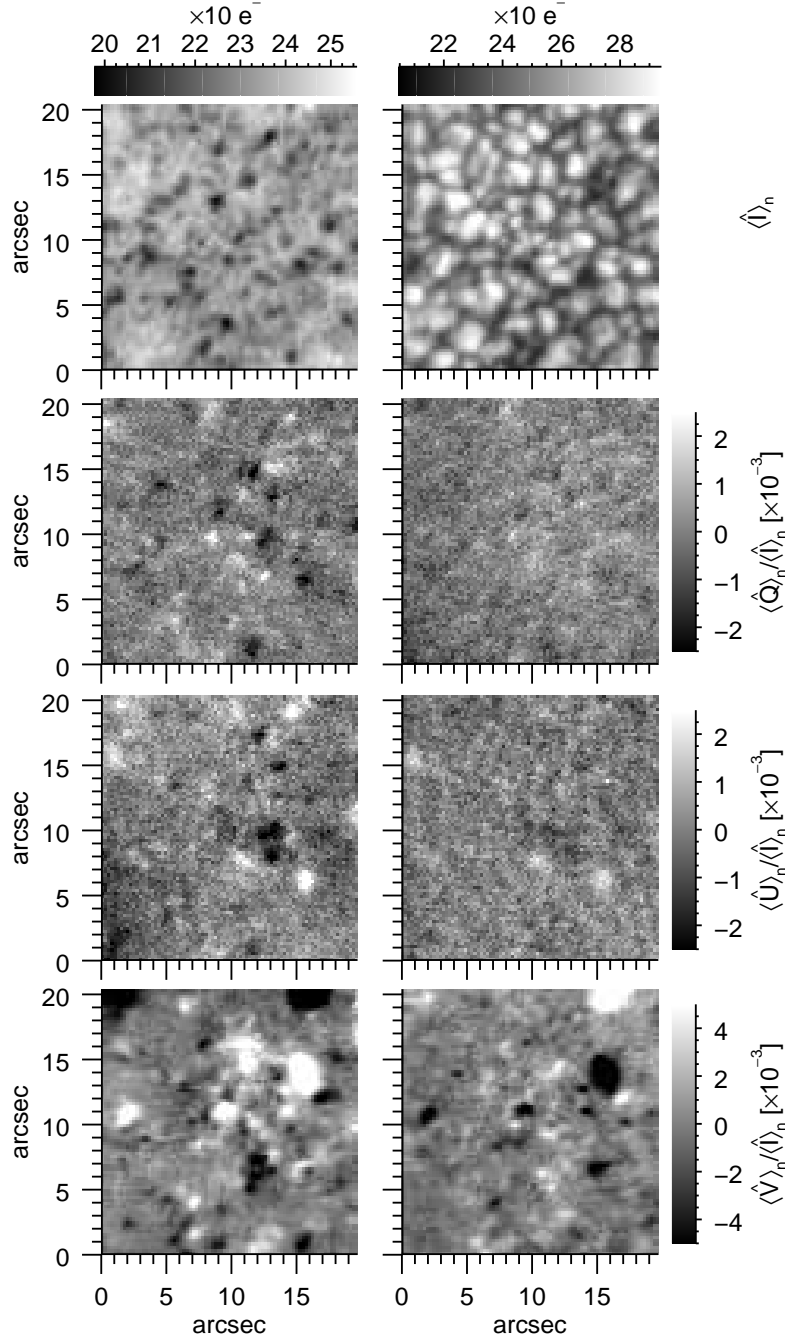


Figure 6.5. Quiet Sun scan of the Fe I 630.2 nm spectral line. Averaged Stokes parameters (images in each row, see the titles on the right margin) for the two measured spectral points, namely -80 (images in the leftmost column) and 80 mÅ (images in the rightmost column) from the line core. All images have been binned using a $3 \times 3 \text{ pixel}^2$ window. The rms noises in the -80 mÅ images are 3.0 , 3.6 and 3.1×10^{-4} for the normalized Stokes Q , U and V respectively. The noise (assumed spatially white) was estimated from the average value of the power spectrum of the non-binned images (using no apodization). See Table 6.3 for extra details.

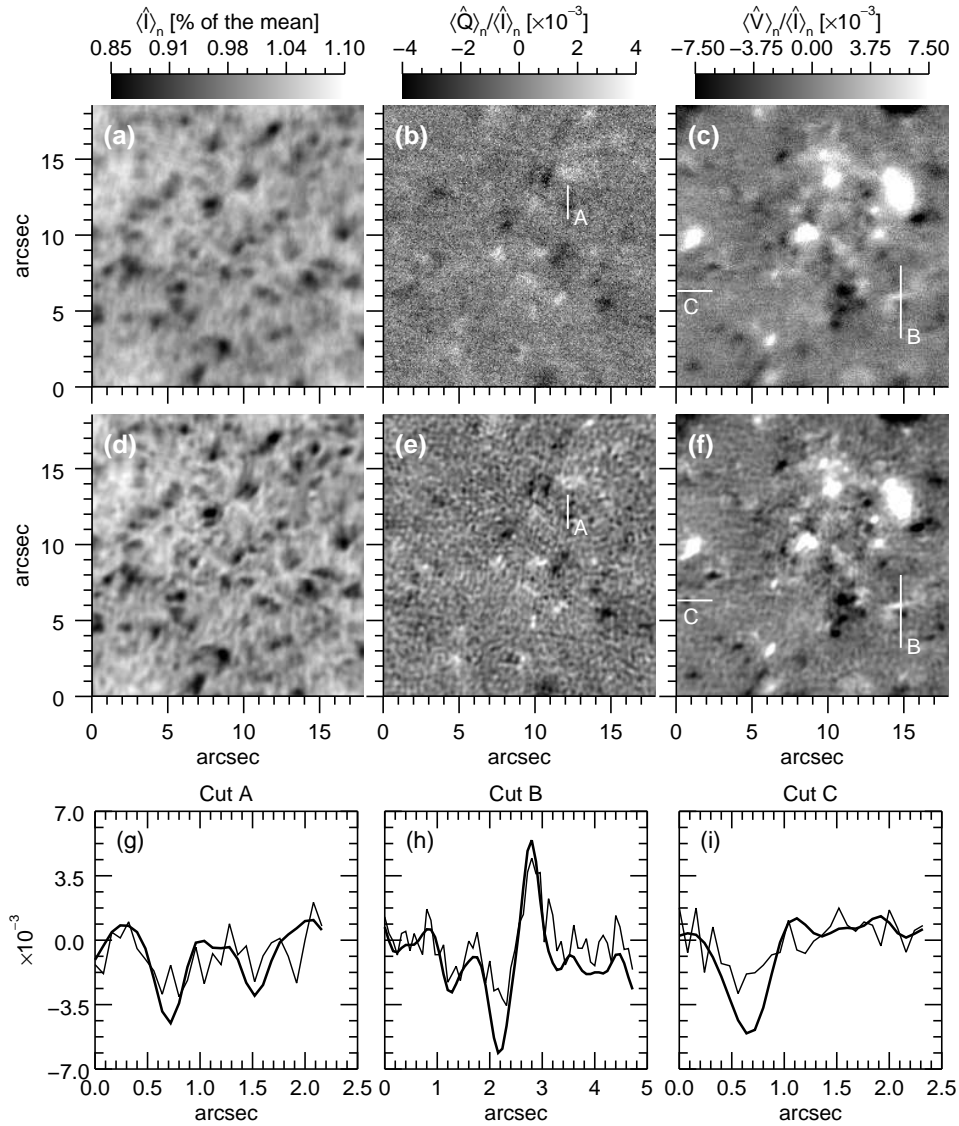


Figure 6.6. MOMFBD restored quiet Sun scan of the Fe I 630.2 nm spectral line. Images (a), (b) and (c) correspond to the averaged Stokes I , normalized Q and normalized V respectively, shown in Fig. 6.5. Images (d), (e), and (f) are the MOMFBD restored versions of (a), (b) and (c) respectively. Note the improvement in spatial resolution and in the signal levels, which can be appreciated in the values across the three selected cuts marked with white lines in images (b), (c), (e) and (f), and plotted in (g), (h) and (i). The thick lines in such plots correspond to the restored images, while the thin lines to the averaged data. See the text for extra details.

6.3.2 High SNR regime: Fe I scan of an active region

The high-cadence of FSP allows also the study of fast evolving, strong (due to the low SNR achievable) solar signals. To explore this we scanned with TESOS five spectral points (integrating only ~ 2 s in each) of the Fe I 630.2 nm line, targeting a small solar active region (pore). The details of the scan are given in Table 6.4. The measured Stokes parameters are presented in Fig. 6.7 and their corresponding MOMFBD restored versions (performed using AP2, see Table 6.1) in Fig. 6.8. A detail of the original and restored versions is shown in Fig. 6.9.

Prop.	Value	Unit
Target	AR12096	
Target heliocentric coordinates	-428,-194	arcsec,arcsec
FOV	19.7×20.4	arcsec ²
$\Delta\alpha_{samp}$	0.08	arcsec pixel ⁻¹
$\Delta\lambda_{samp}$	21	mÅ pixel ⁻¹
λ_0	630.2	nm
Spectral points (meas. from λ_0)	-280,-80,80,-40,40	mÅ
f_{mod}	100	Hz
DC_{scan}	62	%
Int. time per spectral point	1.89	s
Wall time per spectral point	3.04	s

Table 6.4. Data specification for active region scan in Fe I measured with FSP.

6.4 Performance evaluation

The first-light measurements reported in the previous sections allow a first assessment of the FSP performance, this is discussed in the present section.

6.4.1 pnCCCd camera issues

The major issues we found with the pnCCD camera, which should be solved for the optimal functioning of FSP II are

- *Interference fringes:* Even though the entrance window of the pnCCD camera (Fig. 5.2) is wedged, interference fringes appear in the acquired images, which were identified to come from the camera. This can be either due to internal reflections in the entrance window or reflections between the window and the sensor surface⁹. Such fringes were strongly variable in time within intervals of ~ 5 s. This variation is slower than the FSP modulation frequency and thus fringes do not appear in the polarimetric images. However, they could not be properly removed by flat fielding of the intensity images. The fringes make the image restoration process more difficult because they are at a fixed location from frame to frame and introduce considerable power in the images at high spatial frequencies. This produce a wrong wavefront estimation and/or the apparition of fringes in the restored Stokes images (e.g. the central area in Fig. 6.6e and f). To minimize these effects we filtered the fringes by masking their corresponding frequency components in the spectrum of the individual frames (using a Wiener local filter).
- *Camera-modulator phase detection:* The pnCCD camera does not allow tagging the individual frames with their corresponding modulation state, a necessary condition to preserve the phase between the calibration and science measurements, See point 2 in Sect. 6.1.1. As a workaround we have developed a method that implies over-

⁹The anti-reflective coating of the sensor and entrance window makes this option unlikely though.

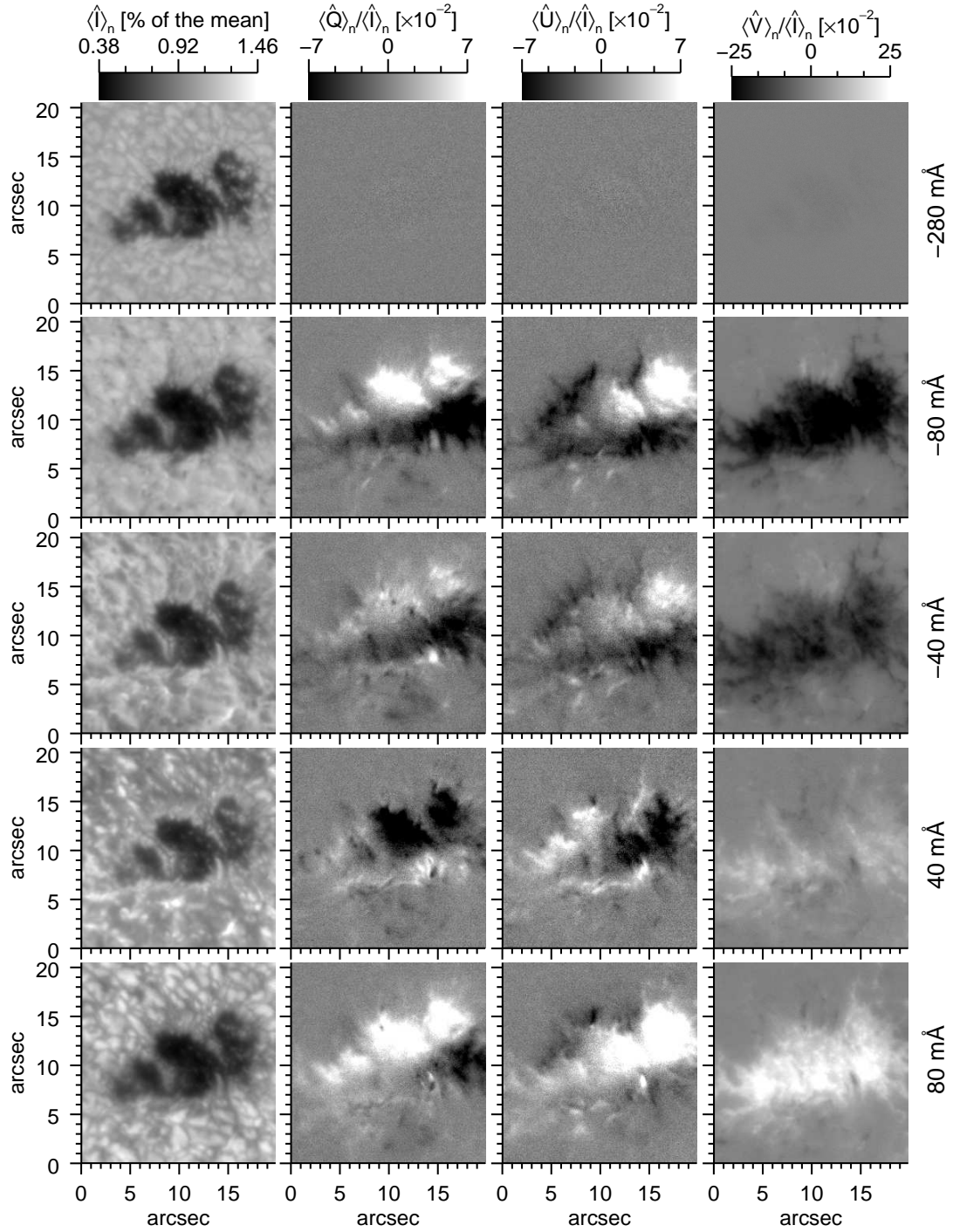


Figure 6.7. Active region scan of the Fe I 630.2 nm spectral line measured with FSP. Average of 189 (1.89 s) Stokes measurements (images in each column, see the title of the color bars) for the five spectral positions (images in each row, see the titles on the right margin) of the scan detailed in Table 6.4. The rms noise in the -280 mÅ images is 4.1 , 4.8 and 3.8×10^{-3} for the normalized Stokes Q , U and V respectively.

exposing (and thus loosing) the first tens of frames of each measurement, which reduce the effective DC .

- *Deviant CAMEX*: The linearity (see Fig. 5.9) and bias (Sect. 5.4.5) measurements

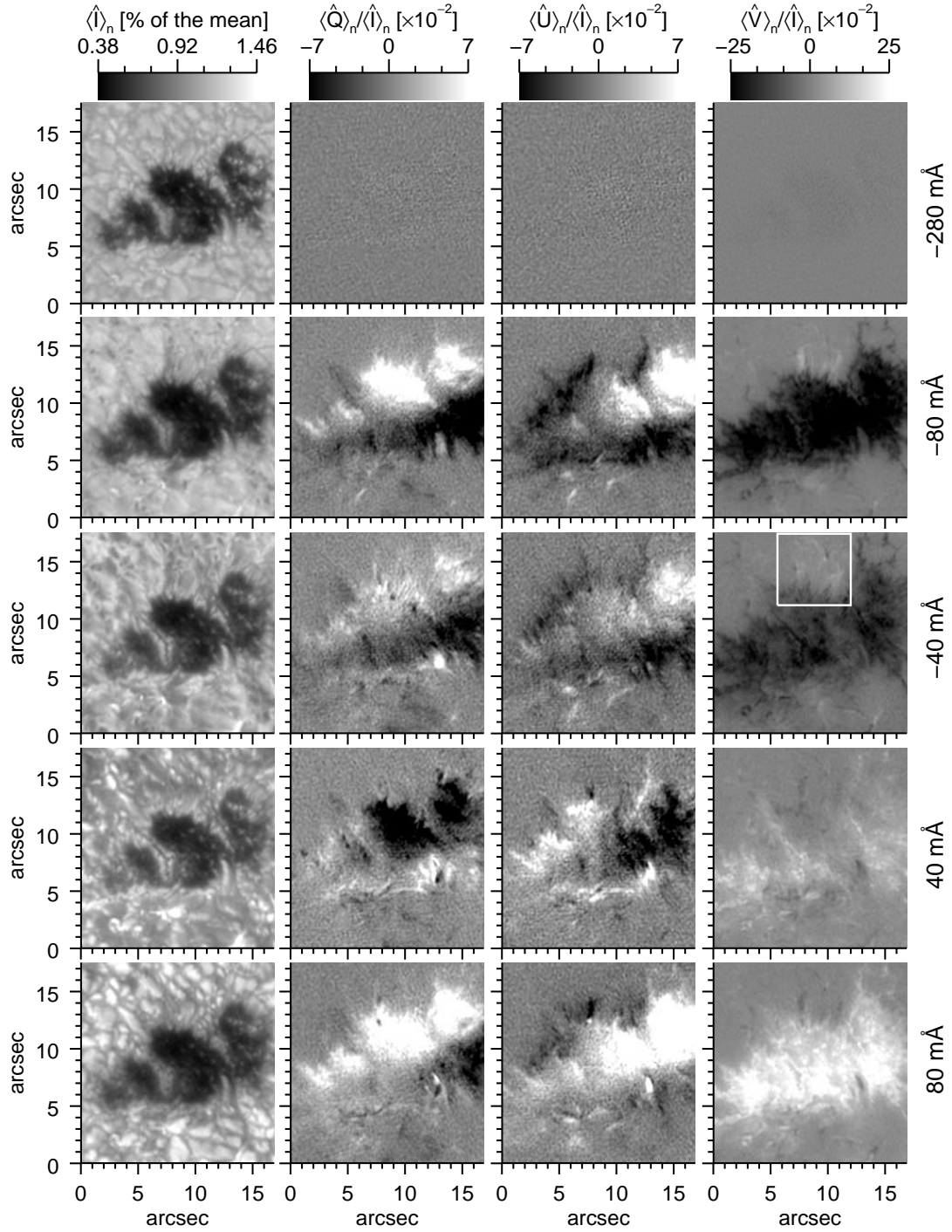


Figure 6.8. MOMFBD-restored version of the images shown in Fig. 6.7. The white rectangle delimits the detail presented in Fig. 6.9. See the text for extra details.

of the sensor revealed that the lower right CAMEX chip (Fig. 5.1) behaves differently. The corresponding sensor quadrant shows a column-wise artifact in some of the measurements involving very low light levels. The origin of this issue is not completely understood so far. The most plausible reason is that this particular CAMEX has slightly deviating specifications e.g. due to error in the biasing circuitry. A detailed analysis of this effect has been delayed to a late stage, because it

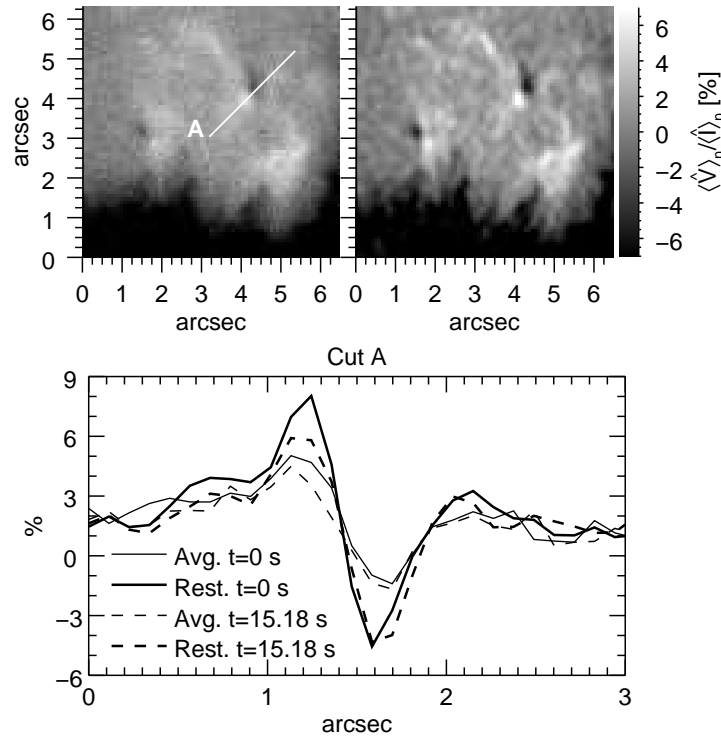


Figure 6.9. Detail of the MOMFBD-restored scan of the Fe I 630.2 nm spectral line. The two images show a detail (delimited by the white rectangle in Fig. 6.8) of the averaged (leftmost image, see Fig. 6.7) and MOMFBD-restored (rightmost image, see Fig. 6.8) normalized Stokes V corresponding to the -40 mÅ spectral point. The increase of the detected signal due to the restoration, can be appreciated in the bottom plot that presents the values across cut A (marked by a white line) for both images (continuous lines, see legend). In the same a plot we also included the values for the same cut through a normalized Stokes V image taken at a later time (dashed lines, see legend). The time difference between both measurements is 15.18 s, see Table 6.4.

was not critical for the evaluation of the instrumental concept using the prototype. For the science-ready FSP II camera, all the 16 different readout ASICs (see Sect. 7.1) have to be carefully tested for such effects to guarantee the same performance over the entire sensor.

6.4.2 Image restoration and signal amplitude

The restoration of FSP measurements using a MOMFBD improves the spatial resolution and, more importantly, considerably increases the detected signal level. In the small ($\sim 1 \text{ arcsec}$) bipolar region shown in Fig. 6.6h, the differences in the detected peak to peak amplitude of Stokes V , between the simple average and the restored version, is $3.5 \pm 0.2 \times 10^{-3}$. This exemplifies that avoiding the dilution of the signals is a key requirement to detect faint, small-scale sources. Simply accumulating frames to reduce noise does not help to measure fainter *solar* signals, if the detected amplitudes decrease

with time due to the spatial smearing produced by seeing¹⁰.

The application of AP1 (see Table 6.1) to restore low SNR measurements, as the one given in Fig. 6.6, showed that the wavefront sensing step of the MOMFBD provides stable estimations when using only narrow-band data. Note, however, that the MOMFBD merit function (Eq. 2.72) assumes Gaussian noise and that such an assumption is not satisfied for low-light-level and high-contrast observations (Van Noort et al. 2005). The usage of a wide-band channel would further improve the quality of the wavefront sensing. On the other hand, the noise amplification produced during the deconvolution step can counter balance the gain in signal level for scenes with low SNR , i.e. there is a trade-off between the noise amplification given by the bandwidth of the regularization filter (see e.g. footnote 24 in Sect. 2.3.3) and the spatial resolution of the estimated object. This is the case of Stokes Q in Fig. 6.6e which presents a lower gain in SNR after restoration than Stokes V in Fig. 6.6f, even though the same OTFs were used to deconvolve both sets of images. After the wavefront sensing is done, the estimation of the object with known degradation functions constitutes a multi-frame deconvolution problem. To improve the aforementioned results, multi-frame deconvolution techniques that are particularly designed to deal with (Poissonian) noisy images should be applied. Such techniques (see e.g. Starck et al. 2002) avoid the division in Fourier space (and thus the noise amplification at high frequencies) by using a maximum-likelihood approach, where the object is firstly guessed and then iteratively estimated with increasing accuracy by minimizing a given error metric¹¹.

The high frame rate and duty cycle of the pnCCD camera provide a large amount of frames. The increased amount of frames make the MFBD problem better constrained which tend to compensate for the ill-conditioning produced by the low SNR of the individual frames, producing a more reliable sensing of the wavefronts even for short periods of time. Since the restoration quality strongly depends on the seeing conditions, contrast of the solar scene and SNR of the individual frames, one way to verify the previous statement is to artificially reduce the camera frame rate. To do this we simply picked one out of nine frames from a set of modulated intensities acquired at $FR = 400$ fps. After demodulation, the resulting data is equivalent to a measurement acquired at a mid-speed of $FR_{mid} = 44.4$ fps and a $DC_{mid} = 11.0\%$. We applied this technique to 192×4 frames corresponding to the -40 mÅ spectral point of the scan shown in Fig 6.7. We then applied AP2 (see Table 6.1) to restore both the original and derived data sets and compared the restoration quality (see Fig. 6.10). Note that, the reduced number of frames available for the restoration in the derived data set—only 21 instead of the 192 per modulation state of the original data set—produces a worse restoration (compare images e and f) even when the individual intensity measurements have the same exposure time and SNR (~ 13.9 , compare b and c). Moreover, clear artifacts can be found in the restored Stokes parameters (compare images e and f) which are due to SIC and/or caused by the AP2 restoration process.

¹⁰See also the simulations by Krishnappa and Feller (2012), discussed at the end of Sect. 2.3.2, where they report a strong increase in the detected polarimetric signal with increasing number of corrected Zernike terms by an AO system (particularly up to 30 Zernike terms).

¹¹For example, the maximum-likelihood approach leads to the Richardson-Lucy algorithm (Richardson 1972) when Poissonian noises are assumed. In the non multi-frame approach, the estimated object can be found for iteration n using a single frame, i , by doing (see Eq. 2.68), $I_{\odot}^{n+1} = [\mathcal{H}_{atm+tel}^* \star I_i / (\mathcal{H}_{atm+tel}^i \star I_{\odot}^n)] I_{\odot}^n$.

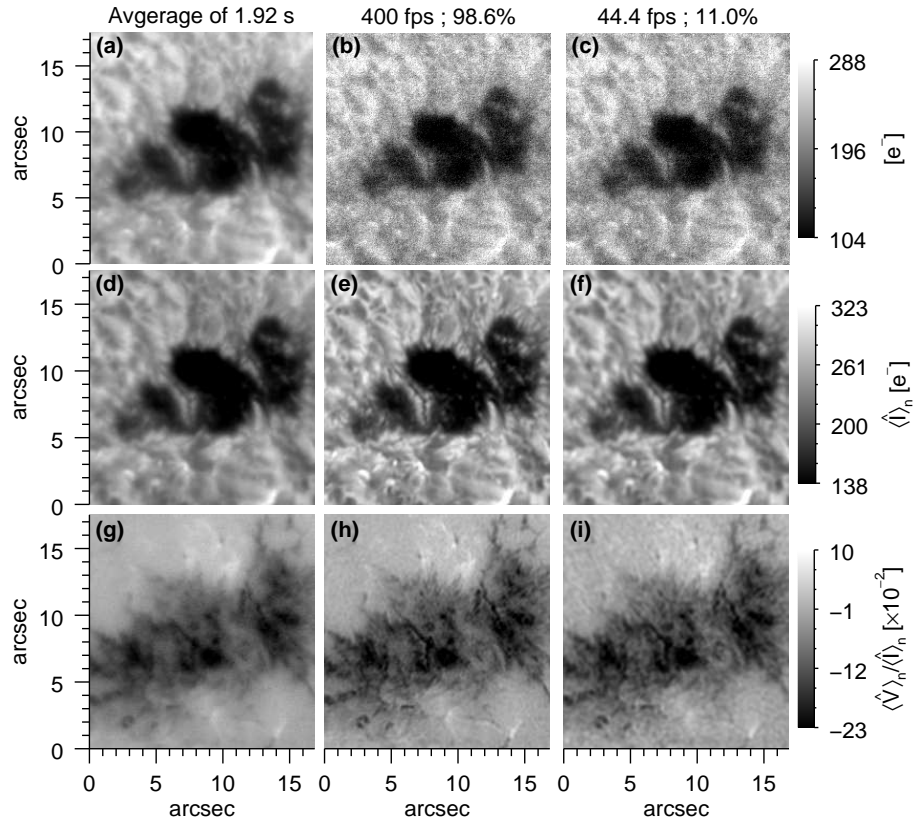


Figure 6.10. Effects of FSP cadence and duty cycle when restoring a time series lasting 1.92 s of the -40 m\AA spectral point of the scan shown in Fig 6.7, using MOMFBD. The first column presents the average of the 192 measurements including, one modulated intensity (a), Stokes I (d), and normalized Stokes V (g). The second column illustrates the results of the AP2 (see Table 6.1) restoration. Both a single modulated intensity (b) and two of the resulting Stokes parameters (e and h) are shown. The third column gives the outcome of the same restoration, run on the data set that has a reduced frame rate (44.4 fps) and duty cycle 11.0 %, including a single modulated intensity (c) and two of the restored Stokes parameters (f and i). Image adapted from Iglesias et al. 2016. See the text for extra details.

The possibility to obtain such a high-cadence set of restored full-Stokes measurements is a clear advantage when studying small-scale, fast-evolving, strong solar signals. For example in the small (~ 1 arcsec) bipolar region shown in Fig. 6.9, the detected peak to peak Stokes V value increases to $6.1 \pm 0.8 \%$ after MOMFBD restoration. Moreover, the measured temporal reduction (after 15.18 s) of the peak to peak values are 0.3 ± 0.8 and $2.3 \pm 0.8 \%$ for the averaged and restored versions respectively.

6.4.3 Polarimetric sensitivity

The non-ideal polarimetric and photometric efficiencies, and the presence of artifacts are the major factors that cause a polarimeter to depart from the ideal photon limited trade-off between SNR and spatial resolution imposed by the evolving solar scene (see Fig. 2.5). The high polarimetric efficiencies (see Fig. 4.4), camera sensitivity (see Sect. 5.1.1 and Fig. 5.1c), duty cycle (see Table 3.2 and Sect. 5.1.1) and low camera noise (see Sect. 5.4.2) allow FSP to reach the goal polarimetric sensitivity faster than other instruments.

These are the main properties that permitted the detection of the small-scale (0.24 arcsec spatial sampling), quiet-Sun signals with a sensitivity of $\sim 3.5 \times 10^{-4}$ after integrating 0.95 min (about a fifth of the typical solar granulation life-time) with a flux of only about $230 e^- \text{ pixel}^{-1} \text{ frame}$, see Fig. 6.5. The detection was further improved by the increase in signal levels obtained by image restoration. On the other hand the main potential sources of artifacts are the modulator and the polarimetric calibration procedure, the pnCCD camera and the residual levels of SIC. We found that the modulator and calibration artifacts can be suppressed to the level of 1×10^{-4} , provided that the instrumental polarization level is not larger than $\sim 1 \%$ (see Sect. 4.3). Analogously, we found that the pnCCD camera introduces no major polarimetric artifact besides those mentioned in Sect. 6.4.1 (see Sect. 5.2 and 5.3). These statements are further supported by the results reported in Sect 6.4.5 and the low-spatial-resolution measurements of the second solar spectrum given in Fig. 6.3. The latter reach a polarimetric sensitivity of $\sim 8 \times 10^{-5}$ in the spatially-averaged, normalized Stokes Q , without clear signs of instrumental artifacts and with good agreement with the ZIMPOL results.

6.4.4 Measurements of the magnetically insensitive 557.6 nm line

In order to estimate the level of SIC, no solar signal has to be present in the Stokes images¹². One of the best ways to achieve this is by measuring polarization in magnetic lines with null Landé factor to ensure the absence of Zeeman signals. If, in addition, a target located near the center of the solar disk is chosen, the scattering polarization signals are also practically ruled out, resulting in flat Stokes Q , U and V images with non-zero offsets due to instrumental polarization. The combination of a non-flat Stokes I with such a flat Q , U and V in this kind of measurement, makes it ideal to detect any SIC from Stokes I to Q , U and V . We measured the Fe I 557.6 nm line (which has $g=0$) in a quiet region of the Sun during a short campaign in April 2015. Such measurements are presented in Fig. 6.11. As can be appreciated in the Stokes images of row (c), there is a clear artifact affecting Stokes Q and U . Such an artifact is not present in the measurements given in row (a), which were acquired under the same conditions, except that the modulator was disconnected. The latter means that no actual modulation is taking place and thus no polarimetric signal should be measured. The actual source of the aforementioned artifact has not been identified and remains as future work. In spite of this we list and discuss below the main possible sources.

- *Modulator induced image motion:* The combination of a non-normal beam incidence on the FLCs (see the tilting rings in Fig. 4.1) and a change in their refractive index, between the two states of their optical axes, introduces a deflection of the output beam. Such a deflection may produce in turn image motion which is synchronized with the frame acquisition, and thus any derived artifact will be systematically repeated every modulation cycle appearing even after accumulating many Stokes images. Modulation induced image motion has been reported to appear in other polarimeters (see e.g. Hanaoka 2006). One solution to this problem is to locate the modulator package near a focal plane in order to minimize the image

¹²For example in measurements of the quiet Sun, both SIC and transversal Zeeman signals tend to appear near the borders of the granules where the gradient of Stokes I is maximum.

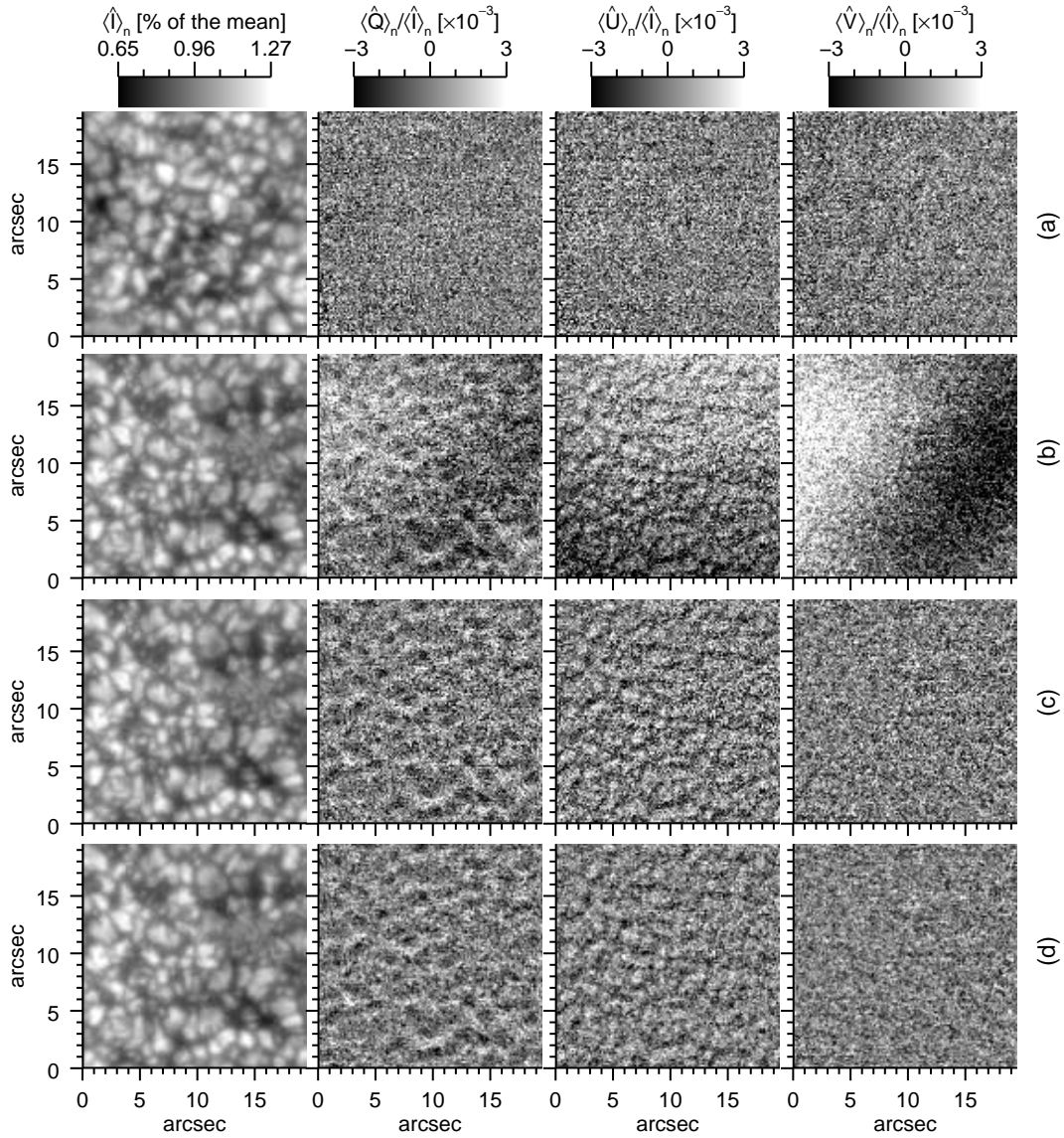


Figure 6.11. Measurements of the non-magnetic 557.6 nm line. (a) ~ 10 s average acquired with the modulation disconnected. (b) ~ 10 s average acquired with the modulation running. (c) same as (b) after subtracting from each image its smoothed version (using a 40×40 pixel² window). (d) same as (c) except that the images were realigned before the polarimetric demodulation, using sub-pixel cross-correlation among consecutive frames. Such a realignment reduced the temporal power spectrum of the Stokes Q and U time series, by approximately one order of magnitude. The original plate scale of the images is 0.08 arcsec pixel⁻¹ in both directions, however they have been binned using a 2×2 pixel² window. The standard deviations of the normalized Stokes Q , U and V images in row (a), are 1.2 , 1.4 and 1.3×10^{-3} respectively.

motion introduced by the beam deflection¹³. We have not quantified the beam deflection, if any, introduced by the FSP modulator package. However the artifacts seen in row (c) of Fig. 6.11 are not likely to be produced by this effect because the center of the modulator was located at only ~ 15 cm from a focal plane (\ll than the

¹³In principle image motion can not be eliminated because the two FLCs in the modulator can not be in the same focal plane at the same time.

telescope focal length of 45 m); the realignment of the images before demodulation shown in row (d), does not considerably reduce the artifact level; and no artifact is visible at the same level in the measurements presented in Fig. 6.5.

- *SIC*: Another possible source of the artifacts seen in row (c) of Fig. 6.11 is residual seeing induced crosstalk. This option is unlikely because of the following. Firstly, note that the measurements acquired with the modulation package disconnected are still sensitive to these effects, i.e. the only difference with respect to a regular measurement is that O does not depend on i in Eq. 2.53. However, the artifacts are not present in the images shown in row (a). Secondly, the correlation coefficients of the Stokes Q , U and V images in row (c) with respect to the Stokes I image, are larger (-0.28, 0.23 and -0.05 respectively) than the correlation coefficients of the absolute values of the same Stokes Q , U and V with respect to the modulus of the gradient of Stokes I (-0.03, 0.01 and -0.01 respectively). In case of SIC, the opposite is expected. Finally, the realignment of the images before demodulation shown in row (d), does not considerably reduce the artifact level (which also rules out jitter induced crosstalk due to e.g. a resonance peak in the residual motion of the AO tip-tilt correction mirror).
- *Stray light*: A third potential source of the artifacts under discussion is the presence of stray light. This means that the measured Stokes vector, $\hat{\mathbf{S}}_{stray}$ is the sum of the vector measured in absence of stray light, $\hat{\mathbf{S}}$, plus a spatially uncorrelated term due to possibly polarized stray light, $\Delta\hat{\mathbf{S}}$. We can write the measured normalized Stokes parameter $k \in \{Q, U, V\}$ as follows,

$$\frac{\hat{S}_{stray,k}}{\hat{S}_{stray,0}} = \frac{1}{1 + \Delta\hat{S}_0/\hat{S}_0} \left(\frac{\hat{S}_k}{\hat{S}_0} + \frac{\Delta\hat{S}_k}{\hat{S}_0} \right). \quad (6.3)$$

Note that, even if the stray light is unpolarized ($\Delta\hat{S}_k = 0$) it will introduce crosstalk from Stokes I in the Q , U and V images, by means of the multiplicative term in the right side of Eq. 6.3. Such a crosstalk can explain the artifacts in row (c) of Fig. 6.11 which correlate with Stokes I (see the previous bullet). Moreover a wavelength-dependent polarized stray light term, can also account for the large scale gradients seen in row (d) which are not present in the measurements acquired at other wavelengths.

6.4.5 Spatial resolution and seeing induced crosstalk

The present section has been extracted from Iglesias et al. 2016 with minor changes and an adapted notation.

Quantifying the amplitude of SIC in narrow-band, diffraction-limit-sampled, Stokes images recorded at high modulation frequency, is difficult because the artifact is normally hidden by the photon noise and any possible solar signal. Moreover if image averaging is used to reduce photon noise, the SIC artifact is smeared and thus its level also reduces, see Sect. 2.3 and e.g. Lites 1987, Hanaoka 2004. Let us discriminate the *spatially estimated* power in the image of the normalized Stokes parameter $i \in \{Q, U, V\}$, after averaging N_{stk}

measurements as follows,

$$\sigma_{tot}^2(i, N_{stk}, f_{mod}, I_{rms}) = \frac{\sigma_i^2}{N_{stk}} + \sigma_{art}^2(i, N_{stk}, f_{mod}, I_{rms}) + \sigma_{sig}^2(i, N_{stk}), \quad (6.4)$$

where we have neglected any fixed pattern noise that cannot be reduced by image averaging. $\sigma_i = (\sigma_{cam}^2 + \sigma_p^2)^{1/2} / (\epsilon_i \sqrt{N_{mod}} \langle \hat{I} \rangle)$ is the noise in the individual normalized Stokes images (see Eq. 2.35); $\sigma_{art}(i, N_{stk}, f_{mod}, I_{rms})$ includes the power due to SIC and other artifacts (see below) in Stokes parameter i , where we made explicit its dependence with respect to N_{stk} , to the modulation frequency, f_{mod} , and to the rms contrast values of the Stokes I images averaged, I_{rms} ; and $\sigma_{sig}(i, N_{stk})$ is the averaged signal power of the actual solar scene. To be able to reliably detect solar polarimetric signals, one needs to obtain after averaging, a value of the signal to artifact and noise ratio, $SANR(i, N_{stk}) = \sigma_{sig}(i, N_{stk}) / [\sigma_i^2 / (N_{stk}) + \sigma_{art}^2(i, N_{stk}, f_{mod}, I_{rms})]^{1/2}$, that is large enough given a predefined criterion. Note that the above-described approach is of practical relevance only for the cases where the portion of the FOV covered by signal and by artifact are similar, so that their spatial rms values are equally representative of their peaks values.

As an application of the above-expressed ideas, let us consider the case of quiet Sun measurements, of particular importance for FSP given its science goals. One way to achieve $\sigma_{sig}(i, N_{stk}) = 0$ in Eq. 6.4 and still be sensitive to SIC, is to use measurements acquired with the modulator package deactivated (see Sect. 6.4.5). In addition, since SIC not only depends on modulation frequency, but also on the instantaneous seeing conditions and contrast of the solar scene (Judge et al. 2004); we use the following procedure to reduce the influence of the latter two. We start with a set of 45989 (7.66 min wall time) quiet Sun measurements acquired at 100 Hz with the FSP modulator package deactivated. We then derived two new sets that have modulation frequencies of 20 and 11.1 Hz, by picking one out of five and one out of nine frames respectively, from the set of measured intensities at 100 Hz (as done in Sect. 6.4.2). After demodulation, the 20 and 11.1 Hz data sets are equivalent to measurements taken at those frequencies with duty cycles of 19.7 and 11 % respectively. The advantages of this method are that practically the same solar scene, seeing conditions and values of σ_i are present in the three data sets. The measured values for Stokes I and normalized Stokes Q corresponding to the original and derived measurements are shown in Fig. 6.12 for different values of N_{stk} . The qualitative results also apply to Stokes U and V , which are not presented here.

Firstly, note that SIC is evident in the single measurements, i.e. $N_{stk}=1$, of the 20 and 11.1 Hz cases (images c and d respectively) while not being above the noise level for the 100 Hz image (b). Moreover, the artifact tends to have larger amplitudes towards the borders of the FOV because the AO corrections of the wavefront are worse away from the system's locking point —located approximately at the center of the image— due to seeing anisoplanatism (see Sect. 2.3.3). The reduction of the SIC with increasing modulation frequency, can be also appreciated in Fig. 6.13, where the artifact level in the individual Stokes Q measurements,

$$\sigma_{art}(Q, 1, f_{mod}, I_{rms}) = \sqrt{\sigma_{tot}^2(Q, 1, f_{mod}, I_{rms}) - \sigma_Q^2}, \quad (6.5)$$

is plotted for all the frames —thus including a variety of instantaneous seeing conditions— in the three data sets versus Stokes I rms contrast. To obtain the artifact level, we assume it can only introduce power at spatial frequencies that are below the diffraction

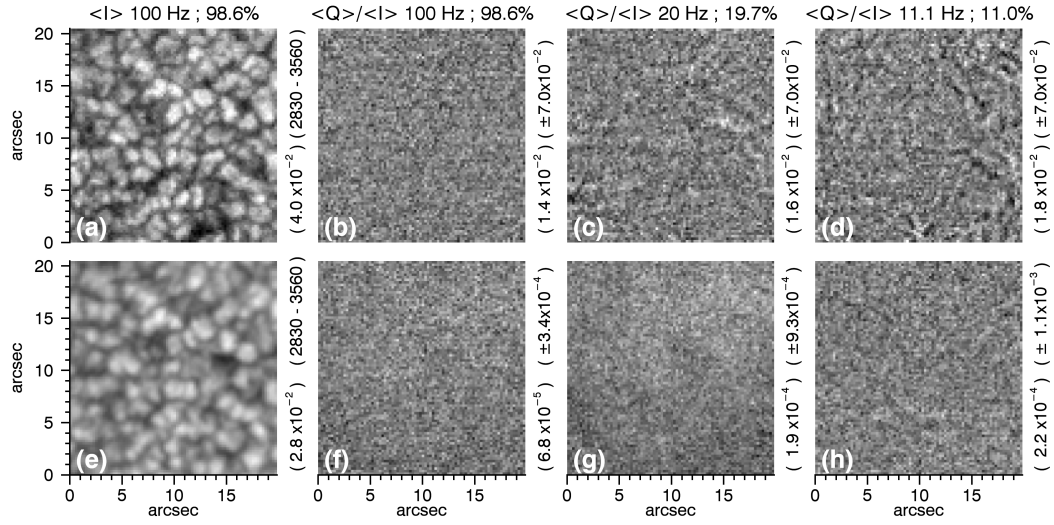


Figure 6.12. Seeing induced crosstalk in normalized Stokes Q image, for different modulation frequencies, duty cycles (labeled on top of each column) and number of averaged measurements (rows). These quiet Sun images were acquired with FSP modulator package disconnected, in which situation no solar polarization signal is expected, using the VTT/TESOS filtergraph tuned to the continuum at -280 m\AA from the line core of Fe I, 630.2 nm . The upper row presents Stokes I (a) and the normalized Stokes Q (b, c and d) of a single measurement. The lower row shows the results after averaging 45989 (e and f), 9160 (g) and 5060 (h) Stokes images, all covering 7.66 min wall time approximately. The 20 and 11.1 Hz cases, were obtained by eliminating intermediate intensity measurements from the 100 Hz case before demodulation, see the text for details on this procedure. The original plate scale of the images is $0.08 \text{ arcsec pixel}^{-1}$ in both directions, however they have been binned using a $3 \times 3 \text{ pixel}^2$ window. The figures in parentheses on the right border of each image denote its gray scale range (upper panels) and standard deviation, or rms contrast for Stokes I , computed across the sensor area (lower panels). Image extracted from Iglesias et al. 2016.

limit, and that σ_Q is white noise. Then, σ_Q can be estimated by the average value of the power located at spatial frequencies beyond the diffraction limit. This estimation of $\sigma_{\text{art}}(Q, 1, f_{\text{mod}}, I_{\text{rms}})$ includes not only SIC contributions but also any other source of colored noise.

Secondly, from the second row in Fig. 6.12, note that SIC has been smeared out to very low levels in the 20 and 11.1 Hz cases (g and h respectively) due to image accumulation. This suggests that SIC artifact is less critical for low-spatial resolution measurements; where, in addition, any small-scale solar signal would also be smeared (compare the contrast of images a and e). If, however, a high spatial resolution is aimed for, reducing the SIC below the photon noise level in the individual measurements is crucial¹⁴. The latter is also exemplified by Fig. 6.14 where the resulting Stokes I and normalized Stokes Q , corresponding to the average of 1.16 min wall time of the data sets with 100 and 11.1 Hz modulation frequency, are presented along with their respective MOMFBD restored versions (using AP1, see Table 6.1). In the plain averages, both the spatial resolution and the SIC levels are lower because signal (images a and b) and artifact has been smeared out

¹⁴Note that this becomes more difficult when the photon flux reaching the detector increases, e.g. by taking sub-diffraction-limited images with a larger aperture.

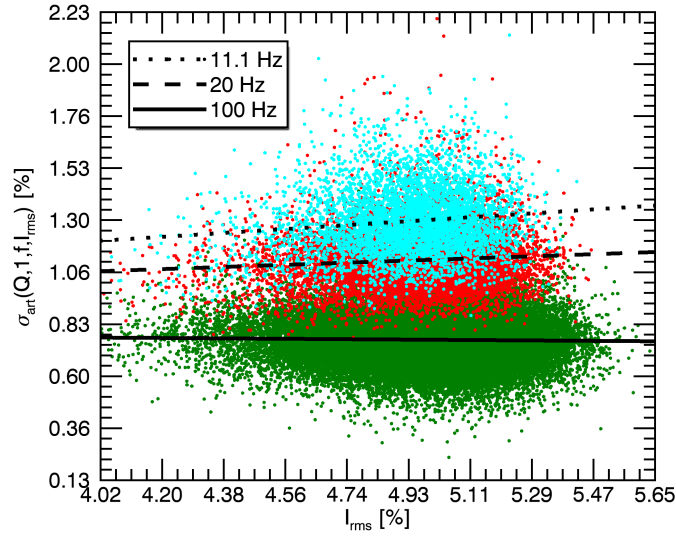


Figure 6.13. Measured artifact level in individual Stokes Q measurements (see Eq. 6.5) versus Stokes I rms contrast, for the data sets presented in Fig. 6.12. Each dot gives the value of a single measurement acquired at a modulation frequency of 100 (green), 20 (red) and 11.1 Hz (cyan). The black lines represent linear fits to the 100 (continuous), 20 (dashed) and 11.1 Hz (dotted) datasets. Image extracted from Iglesias et al. 2016.

(images e and f). Thus, the benefits of a higher modulation frequency are less prominent. If image restoration is applied to preserve spatial resolution (see images c and d), and any possible small-scale polarimetric signal, then the SIC is also preserved producing a clear difference between the artifact levels of the cases with 100 and 11.1 Hz modulation frequency. The benefits of a combined high modulation frequency, high cadence and high duty cycle—to obtain simultaneously high-spatial resolution (through image restoration) and low SIC—are then demonstrated by images c and g.

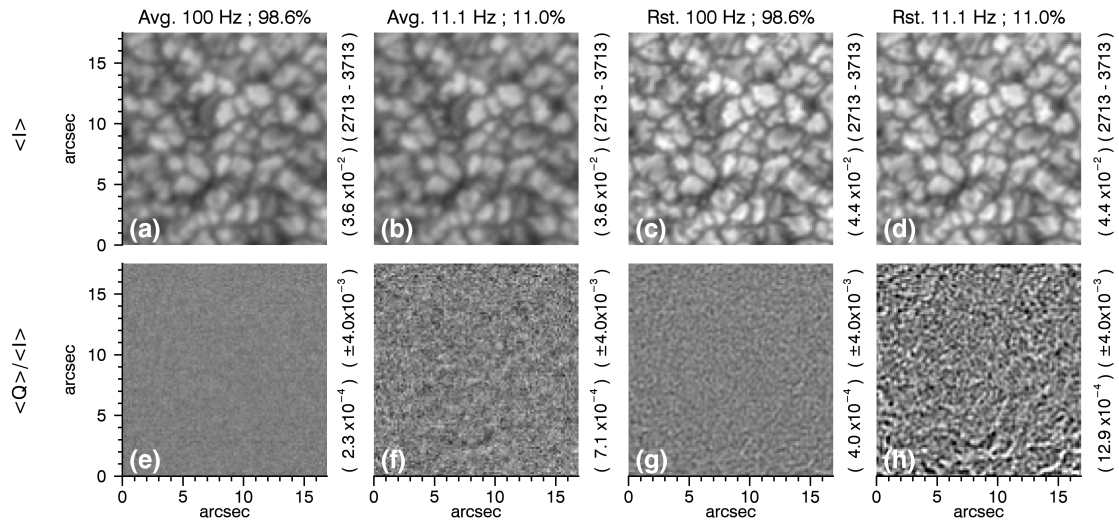


Figure 6.14. Effects of the modulation frequency, duty cycle and image restoration (labeled on top of each column) on the SIC level in Stokes Q images. The Stokes I (upper row) and the normalized Stokes Q (bottom row) are shown for the data sets with 100 and 11.1 Hz modulation frequency presented in Fig. 6.12. Both a plain average, covering 1.16 min wall time (a, b, e and f), and the corresponding MOMFBD-restored versions (c, d, g and h) are presented. The original plate scale of the images is $0.08 \text{ arcsec pixel}^{-1}$ in both directions, however they have been binned using a $2 \times 2 \text{ pixel}^2$ window. The figures in parentheses on the right border of each image, denote its gray scale range (upper panels) and standard deviation, or rms contrast for Stokes I , computed across the images (lower panels). Image extracted from Iglesias et al. 2016.

7 Concluding remarks and prospects

In this thesis we have tackled the instrumental challenges that arise when developing a ground-based, high-cadence solar polarimeter. This work is focused on a specific instrument, the prototype of the FSP. However many of the methods and techniques we employed or developed, are of relevance to high-cadence polarimetry in general.

Any practical polarimeter that aims to measure the full Stokes vector (a requirement to e.g. remotely probe the full magnetic field vector), employs a form of temporal modulation. Therefore, we started by summarizing the main effects of atmospheric seeing on temporally-modulated imaging polarimetry, namely the reduction of spatial resolution and the introduction of SIC. After describing the cons of the dual-beam (beam imbalances), beam-exchange (extra measurements required) and asynchronous-readout solutions, we derived the most important properties of a single-beam, synchronous polarimeter that aims to reduce SIC and optimize image restoration. These properties were translated in to a set of general requirements for the camera and modulator, that were in turn used to evaluate the pros and cons of the different available technologies. This showed that based on reliability, performance and technology maturity an FLC-based modulator is the best current alternative for full-Stokes, high-cadence modulation. In addition, it showed that the bottle neck of a synchronous polarimeter are the frame rate and noise of the scientific camera employed.

The latter motivated the development of the FSP prototype, which is described in this work. We have integrated, characterized and optimized an FLC based polarization modulator, supporting the fact that a model-based design procedure can be satisfactorily used to obtain achromatic polarimetric efficiencies. By comparing the required stability of the modulation matrix with the characterization results, we derived the calibration requirements in terms of the maximum changes allowed in wavelength, modulator housing temperature, and driving frequency. In addition we characterized a custom-made pnCCD camera never used in polarimetry before, and proved its suitability to do high-cadence, high-sensitivity solar polarimetry from the ground. We selected a specific synchronization between camera and modulator, which allowed us to develop an accurate model of the image acquisition including the signals acquired during the shutter-less frame transfers, and the strong variations on the sensor illumination that can be present when doing polarimetry. The latter was used to develop a numeric technique for correcting image smearing post-acquisition. The main properties of the pnCCD camera were characterized and its polarimetric effects addressed when relevant. These include the effects of non-linearity, residual offsets, common-mode noise (where the minimum number of channels for the correction was derived) and readout noise.

We have preformed all the necessary steps to acquire the first-light measurements of the integrated FSP prototype at the VTT solar telescope. These include the development

of the reduction routines and acquisition of measurements working with both a spectrograph and filtergraph. These measurements allowed us to assess the suitability of the FSP instrumental concept. We found that the superior sensitivity, noise, duty cycle of the pnCCD camera, together with the high polarimetric efficiencies of the modulator are crucial to acquire the extremely photon-starved measurements required by many science cases. In addition, the high cadence and duty cycle of FSP proved crucial to allow the restoration of the images by means of a MOMFBD, using only narrow-band data which have low SNR . The restoration improved not only the spatial resolution of the Stokes images, but also increased the signal levels. With FSP we measured scattering polarization with a polarimetric sensitivity of 8×10^{-5} , and detected sub-arcsec bipolar patches of linear polarization at the 1×10^{-3} level using the TESOS filtergraph.

We studied the residual level of SIC using non-modulated filtergraph measurements. We found that at a modulation frequency of 100 Hz, if no image restoration is used, SIC is below the 7×10^{-5} noise level after averaging ~ 8 min of quiet-Sun Stokes images. If the signal is preserved by using a MOMFBD restoration, then SIC is also preserved increasing its level. After restoring 1.16 min of quiet-Sun measurements acquired with FSP, we found artifacts at the 4×10^{-4} noise level only in the edges of the images where the AO performance is reduced due to seeing anisoplanatism.

There are a set of open questions and tasks that arise from the above-mentioned work, and demand further investigation during the next phase of the FSP project. We list the most relevant below.

- The dispersion of the FLC's switching angles that we measured should be verified and, in the positive case, included in the modulator model.
- Reducing the instrumental polarimetric offset is crucial to lower the level of the artifacts introduced by various camera and modulator related effects (e.g. detector non-linearities, instability of the modulation matrix, etc.). A simple option to compensate the instrumental offsets is to modify the exposure times of the different modulation cycles. This solution will be implemented in FSP II.
- The calibration procedure has to be modified to contemplate variations of the input illumination, in order to allow the implementation of a spatially-dependent demodulation.
- The calibration of the pnCCD non-linearities has to be implemented.
- The tuning of the camera-modulator triggering delay has to be done.
- The synchronization between FSP and the scanning feature of the post focus instrument, has to be optimized in order to fully exploit the high duty cycle of FSP.
- The modulator induced jitter, if any, should be properly characterized to assess whether the modulator can be used further away from a focal plane, which would reduce the variation of the modulation matrix across the FOV and may be advantageous in terms of physical constraints for specific setups.
- The source of the observed artifacts in the 556.7 nm line should be identified in order to allow a more accurate estimation of the residual SIC levels.

- Multi-frame deconvolution algorithms that are better than a Wiener filter to deconvolve very low SNR images, have to be investigated in order to improve the image restoration results.

Let us end this section by discussing Fig. 3.2. As can be appreciated there, the ideal regime in terms of SIC reduction corresponds to a modulation frequency, f_{mod} , beyond 400 Hz. Reaching such a high f_{mod} with a synchronous, full-Stokes polarimeter implies operating the camera at least at a $FR=1600$ fps. This solution is clearly not desirable because the resulting very low photon noise would impose a serious constraint on the camera readout noise, in order to be photon noise limited. Moreover, there is no clear advantage in terms of image restoration because the exposure time (~ 0.6 ms) is much shorter than the typical 10 ms coherence time of the seeing. In this sense trying to further push the synchronous approach beyond FSP II does not look like a good alternative. A better solution should be trying to implement an asynchronous polarimeter using a different technique than that used in ZIMPOL in order to reach $f_{mod} \geq 400$ Hz while keeping $FR=100$ fps, a low readout noise and a high QE , FF and DC . A promising technology to implement this alternative solution are the active pixel sensors where the charges corresponding to the different modulation states can be accumulated separately within the pixel structure. One version of such detectors, the DEPFET/Infinipix, are currently being investigated at the semiconductor lab of the Max Planck Society in collaboration with the Max Planck institute for Solar System Research. Note that many science cases do not require reaching the ideal regime discussed above. Therefore many highly demanded measurements can still be done if the residual SIC can be reduced to about 1×10^{-4} , as done with FSP for specific conditions.

7.1 The Fast Solar Polarimeter II

The next phase in the FSP project, FSP II, implies the development of a science-ready polarimeter. The modulator package and calibration unit used in the prototype will be also employed in FSP II. The camera will be replaced by a larger 1024×1024 pixel² pnCCD (see Table 3.2 for details) currently under development at the semiconductor lab of the Max Planck Society. The camera will provide a larger FOV while keeping the 100 Hz modulation frequency and low noise. To achieve this, 16 readout ASIC of a new type are used, the so called VERITAS-1 (Porro et al. 2013). The larger FOV allows the implementation of a high-cadence, dual-beam system which has never been operated before. If no beam exchange is used, the performance of the dual-beam setup strongly depends on the ability of the flat fielding procedure to effectively suppress beam imbalances. In addition the larger image size increases the data rate from 47 to 800 MBs^{-1} . This would demand the creation of data mining routines and the optimization of data reduction algorithms (e.g. smearing correction) in order to minimize processing time and storage. One important aspect related to the latter is the necessity of storing all the recorded frames, which is strongly determined by the selected image restoration approach.

Acronyms

ADC	Analog to digital converter (p. 27)
AO	Adaptive optics (p. 2)
ASIC	Application specific integrated circuit (p. 27)
CAMEX	CMOS amplifier and multiplexer (p. 76)
CCD	Charge-coupled device (p. 3)
CDS	Correlated double sampling (p. 29)
CMOS	Complementary metal-oxide-semiconductor (p. 3)
ENOB	Effective number of bits (p. 50)
FLC	Ferro-electric liquid crystal (p. 3)
FPGA	Field programmable gates array (p. 27)
FPN	Fixed pattern noise (p. 29)
FSP	Fast Solar Polarimeter (p. xii)
FSP II	Fast solar polarimeter II (p. 52)
FWHM	Full width at half maximum (p. 80)
HWP	Half-wave plate (p. 12)
IR	Infra red (p. 16)
JFET	Junction field-effect transistor (p. 77)
KAOS	Kiepenhener institute Adaptive Optics System (p. 103)
LC	Liquid crystal (p. 12)
LCVR	Liquid crystal variable retarder (p. 23)
LED	Light emitting diode (p. 86)
LOS	Line of sight (p. 14)
MFBD	Multi-frame blind deconvolution (p. 41)
MOMFBD	Multi-object multi-frame blind deconvolution (p. 2)
NB	Narrow band (p. 43)
OTF	Optical transfer function (p. 34)
PEM	Piezo-elastic modulator (p. 23)
pnCCD	Pn-type CCD (p. 3)
PSF	Point spread function (p. 37)
PSG	Polarization state generator (p. 54)
QWP	Quarter-wave plate (p. 12)
rms	Root mean squared (p. 31)
SI	Speckle imaging (p. 41)
SIC	Seeing induced crosstalk (p. xvi)
SR	Static retarder (p. 24)
SVD	Singular value decomposition (p. 22)
TESOS	Triple Etalon SOLar Spectrometer (p. 105)

Acronyms

UV	Ultra violet (p. 16)
VTT	Vacuum Tower Telescope (p. 5)
WB	Wide band (p. 43)
ZIMPOL	Zurich IMaging POLarimeter (p. 47)

Nomenclature

$\mathbb{1}$	Identity matrix of the appropriate dimensions (p. 10)
A	Polarimetric efficiencies matrix (p. 22)
A	First frame transfer matrix coefficient (p. 82)
α	Frame transfer coefficient (p. 82)
A_{pixel}	Pixel area (p. 30)
B	Magnetic field (p. 13)
B	Second frame transfer matrix coefficient (p. 82)
c_2	Short form for $\cos(2\theta)$ (p. 10)
C	Coefficient in the dispersion law of the FLC retardance (p. 24)
χ	Azimuthal angle of the magnetic field vector defined with respect to the Stokes Q direction (p. 14)
C_{T1}	First coefficient in the temperature dependence law of the FLC switching angle (p. 24)
C_{T2}	Second coefficient in the temperature dependence law of the FLC switching angle (p. 24)
D	Demodulation matrix (p. 21)
D	Demodulation matrix element (p. 21)
\mathbb{D}	Telescope aperture (p. 19)
\mathbb{D}	Telescope pupil transmission function (p. 42)
DC	Duty cycle (p. 4)
DC_{scn}	Scan duty cycle (p. 105)
$DCNU$	Dark current non-uniformity (p. 29)
Δ	Used to denote an interval or change in a quantity (p. 14)
δ	Phase of a wave (p. 8)
δ	Retardance (p. 11)
δ	Frame transfer coefficient (p. 82)
$\Delta\lambda$	Spectral resolution (p. 17)
$\Delta\alpha$	Angular resolution (p. 17)
Δt	Temporal resolution (p. 17)
$\Delta\lambda_z$	Zeeman splitting (p. 14)
E	Electric field (p. 7)
E	Electric field component (p. 8)
ϵ	Polarimetric efficiencies vector (p. 21)
ϵ	Polarimetric efficiency (p. 21)
\mathcal{E}	Expected value operator (p. 99)
f	Temporal frequency (p. 36)
FF	Filling factor (p. 30)

f_{mod}	Modulation frequency (p. 23)
FOV	Field of view (p. 25)
FR	Frame rate (p. 30)
\mathcal{F}	Fourier transform operator (p. 42)
FWC	Full well charge (p. 30)
G	Conversion gain (p. 30)
g	Landé factor of an atomic transition (p. 14)
g	Gain of an optical system (p. 9)
γ	Wiener filter parameter (p. 42)
γ	Inclination angle of the magnetic field vector defined with respect to the line of sight (p. 14)
Γ	Solar spectral irradiance (p. 19)
H	Point spread function (p. 37)
\mathbf{h}	Diattenuation vector (p. 9)
\mathcal{H}	Optical transfer function (p. 34)
h	Altitude (p. 32)
\mathbf{H}	Matrix coefficient of the homogeneous solution of the frame transfer equation (p. 83)
$\hat{\mathbf{D}}$	Measured or estimated demodulation matrix (p. 69)
$\hat{\mathbf{O}}$	Measured or estimated modulation matrix (p. 69)
$\hat{\mathbf{s}}$	Measured or estimated normalized Stokes vector (p. 69)
\hat{I}	Measured or estimated Stokes I parameter (p. 16)
$\hat{\mathbf{I}}$	Measured or estimated vector of intensities (p. 21)
\hat{N}_{cm}	Measured or estimated common mode artifact (p. 90)
\hat{Q}	Measured or estimated Stokes Q parameter (p. 99)
\hat{S}	Measured or estimated Stokes vector element (p. 21)
$\hat{\mathbf{S}}$	Measured or estimated Stokes vector (p. 16)
\hat{U}	Measured or estimated Stokes U parameter (p. 101)
\hat{V}	Measured or estimated Stokes V parameter (p. 39)
i	Charges flux produced in a CCD (p. 80)
I	Stokes I parameter (p. 8)
\bar{I}	Smeared Stokes I parameter (p. 79)
$\bar{\mathbf{I}}$	Vector of smeared Stokes I parameters (p. 82)
i_d	Dark current (p. 30)
\mathcal{I}	Fourier transform of Stokes I (p. 34)
I_{off}	Digital offset of the camera (p. 79)
\mathbf{I}	Vector of intensities (p. 82)
j	Total angular momentum quantum number (p. 13)
k	Wave number (p. 8)
k_{0°	Transmittance of a partial linear polarizer along its optical axis (p. 11)
k_{90°	Transmittance of a partial linear polarizer along a direction orthogonal to its optical axis (p. 11)
κ	Used for general proportionality constants or coefficients (p. 12)
$\boldsymbol{\kappa}$	A vector of constants κ (p. 42)
\mathbf{k}	Spatial frequencies vector (p. 34)
\mathcal{L}	Error metric (p. 42)

\mathbf{l}	Vector containing the modulator parameters (p. 61)
λ	Wavelength (p. 11)
l	Orbital angular momentum quantum number (p. 14)
\mathbf{M}	Mueller matrix (p. 9)
M	Mueller matrix element (p. 9)
μ	Cosine of the angle between the LOS and the normal of the solar surface (p. 104)
N	Noise (p. 79)
n	Refractive index (p. 33)
n	Discrete time or frame number (p. 78)
\mathcal{N}	Fourier transform of the noise (p. 42)
\mathbb{N}	Set of the integers numbers (p. 83)
N_{adc}	ADC resolution (p. 30)
N_{cal}	Number of calibration measurements (p. 68)
N_{cm}	Signal due to the common mode artifact (p. 79)
N_{col}	Number of columns of an image sensor (p. 30)
N_d	Dark noise (p. 79)
n_e	Extraordinary refractive index (p. 11)
N_{ENOB}	ADC effective number of bits (p. 50)
N_{frm}	Number of frames (p. 42)
NL	Non-linearity (p. 30)
N_{mod}	Number of modulation states (p. 21)
N_{mode}	Number of modes used in a MFBD (p. 42)
n_o	Ordinary refractive index (p. 11)
N_{obj}	Number of objects used in a MOMFBD (p. 43)
N_p	Photon noise (p. 19)
N_{ro}	Read out noise (p. 79)
N_{row}	Number of rows of an image sensor (p. 30)
N_{scn}	Number of scans (p. 105)
NSR	Noise to signal ratio (p. 18)
N_{stk}	Number of Stokes frames (p. 93)
\mathbf{N}	Noise vector (p. 68)
N_{xs}	Number of shielded channels used for common mode correction (p. 90)
\mathbf{O}	Modulation matrix (p. 21)
O	Modulation matrix element (p. 37)
Ω	Orthogonal basis functions used in a MFBD (p. 42)
ω	Angular temporal frequency (p. 8)
P	Generalized pupil function (p. 42)
\mathbf{p}	Polarization vector (p. 9)
π	Principal Zeeman component (p. 14)
Φ	Photon or photo-electron flux (p. 19)
ϕ_0	Seeing isoplanatic angle (p. 34)
$PRNU$	Photon response non-uniformity (p. 30)
q	Short form for Q/I (p. 9)
Q	Stokes Q parameter (p. 8)
QE	Quantum efficiency (p. 19)
\mathbf{R}	Rotation matrix (p. 9)

r_0	Fried parameter (p. 33)
\mathbb{R}	Set of the real numbers (p. 10)
\mathbf{r}	Bi-dimensional position vector (p. 33)
\mathbf{S}	Stokes vector (p. 8)
S_0	Alternative form for Stokes I parameter (p. 9)
S_1	Alternative form for Stokes Q parameter (p. 9)
\mathbf{s}	Normalized Stokes vector (p. 68)
S_2	Alternative form for Stokes U parameter (p. 9)
s_2	Short form for $\sin(2\theta)$ (p. 10)
S_3	Alternative form for Stokes V parameter (p. 9)
S	Stokes vector element (p. 37)
σ	Standard deviation or rms value (p. 21)
σ_b	Blue Zeeman component (p. 14)
σ_r	Red Zeeman component (p. 14)
σ_{adc}	Quantization noise rms value (p. 30)
σ_{cam}	Total camera noise rms value (p. 31)
σ_d	Dark noise rms value (p. 30)
σ_p	Photon noise rms value (p. 19)
σ_{ro}	Read out noise rms value (p. 30)
SNR	Signal to noise ratio (p. 3)
T	Temperature (p. 24)
t	Time (p. 8)
τ_0	Seeing coherence time (p. 34)
t_e	Exposure time (p. 34)
θ	Scattering angle relative to the propagation direction of the incoming beam (p. 12)
θ	Position angle of the optical axis of a given optical component relative to the Stokes Q direction (p. 11)
θ	Rotation angle of a reference frame rotation (p. 10)
Θ	FLC switching angle (p. 24)
t_{ro}	Period of the CCD charge readout clock (p. 82)
t_s	Switching time (p. 51)
t_t	Period of the CCD charge transfer clock (p. 80)
t_{tot}	Total life time of the charge wells in the pnCCD (p. 92)
u	Short form for U/I (p. 9)
U	Stokes U parameter (p. 8)
\mathbf{U}	Matrix coefficient of the particular solution of the frame transfer equation (p. 83)
$\tilde{\mathbf{U}}$	Matrix coefficient of the periodic solution of the frame transfer equation (p. 84)
v	Short form for V/I (p. 9)
V	Stokes V parameter (p. 8)
v	Speed (p. 18)
V	Voltage (p. 63)
\mathbf{v}	Polarizance vector (p. 9)
v_{los}	Line of sight velocity (p. 16)
x	Horizontal position or column number (p. 78)
ξ	Modulus of the complex modulating amplitude of a quasi-monochromatic wave (p. 8)

xs	Horizontal position or column number of the shielded pnCCD channels (p. 90)
y	Vertical position or row number (p. 78)

Bibliography

- Acton, D. S., Sharbaugh, R. J., Roehrig, J. R., Tiszauer, D., 1992, Wave-front tilt power spectral density from the image motion of solar pores, *Applied Optics*, 31, 4280–4284
- Almeida, J. S., González, M. M., 2011, The magnetic fields of the quiet sun, in *ASP conference Series*, (Eds.) J. Kuhn, et al., vol. 437, p. 451
- Balasubramaniam, K. S., Pevtsov, A., 2011, Ground-based synoptic instrumentation for solar observations, in *Solar Physics and Space Weather Instrumentation IV*, vol. 8148, pp. 09–18
- Beck, C., Schlichenmaier, R., Collados, M., Bellot Rubio, L., Kentischer, T., 2005a, A polarization model for the German Vacuum Tower Telescope from in situ and laboratory measurements, *Astronomy and Astrophysics*, 443, 1047–1053
- Beck, C., Schmidt, W., Kentischer, T., Elmore, D., 2005b, Polarimetric Littrow Spectrograph - instrument calibration and first measurements, *Astronomy and Astrophysics*, 437, 1159–1167
- Beck, C., Bellot Rubio, L. R., Kentischer, T. J., Tritschler, A., del Toro Iniesta, J. C., 2010, Two-dimensional solar spectropolarimetry with the KIS/IAA visible imaging polarimeter, *Astronomy and Astrophysics*, 520, A115
- Bello González, N., Kneer, F., 2008, Narrow-band full Stokes polarimetry of small structures on the Sun with speckle methods, *Astronomy and Astrophysics*, 480, 265–275
- Berkefeld, T., 2007, Solar adaptive optics, in *Modern solar facilities - advanced solar science*, (Eds.) F. Kneer, K. G. Puschmann, A. D. Wittmann, p. 107
- Bianda, M., Solanki, S. K., Stenflo, J. O., 1998, Hanle depolarisation in the solar chromosphere, *Astronomy and Astrophysics*, 331, 760–770
- Bigas, M., Cabruja, E., Forest, J., Salvi, J., 2006, Review of {CMOS} image sensors, *Microelectronics Journal*, 37, 433 – 451, ISSN 0026-2692
- Bohndiek, S. E., Cook, E. J., Arvanitis, C. D., Olivo, A., Royle, G. J., Clark, A. T., Prydderch, M. L., Turchetta, R., Speller, R. D., 2008, A CMOS active pixel sensor system for laboratory- based x-ray diffraction studies of biological tissue, *Physics in Medicine and Biology*, 53, 655–672
- Born, M., Wolf, E., 1999, *Principles of Optics*

- Bothmer, V., Daglis, I. A., 2007, *Space Weather: Physics and Effects*, Environmental Sciences, Springer-Verlag Berlin Heidelberg
- Castoldi, A., Guazzoni, C., 2012, Sideward depletion: A novel detector family pushes the performance of the integrated front end to new heights, *Solid-State Circuits Magazine*, IEEE, 4, 46–54, ISSN 1943-0582
- Cavallini, F., 2006, IBIS: a new post-focus instrument for solar imaging spectroscopy, *Solar Physics*, 236, 415–439
- Collados, M., 1999, High resolution spectropolarimetry and magnetography, in *Third Advances in Solar Physics Euroconference: Magnetic Fields and Oscillation*, (Eds.) B. Schmieder, A. Hofmann, J. Staude, vol. 184 of ASP Conference Series, pp. 3–22
- de la Cruz Rodríguez, J., Löfdahl, M. G., Sutterlin, P., Hillberg, T., Rouppe van der Voort, L., 2015, CRISPRED: A data pipeline for the CRISP imaging spectropolarimeter, *ApJ*
- de Mazancourt, T., Gerlic, D., 1983, The inverse of block-circulant matrix, *IEEE Transactions on Antennas and Propagation*, AP-31, 808–810
- del Toro Iniesta, J. C., 2003, *Introduction to Spectropolarimetry*, Cambridge University Press
- del Toro Iniesta, J. C., Collados, M., 2000, Optimum Modulation and Demodulation Matrices for Solar Polarimetry, *Applied Optics*, 39, 1637–1642
- Doerr, H.-P., Kentischer, T. J., Steinmetz, T., Probst, R. A., Franz, M., Holzwarth, R., Udem, T., Hänsch, T. W., Schmidt, W., 2012, Performance of a laser frequency comb calibration system with a high-resolution solar echelle spectrograph, in *Modern Technologies in Space- and Ground-based Telescopes and Instrumentation II*, vol. 8450 of SPIE, p. 84501G
- Dubreuil, M., Rivet, S., Le Jeune, B., Dupont, L., 2010, Time-resolved switching analysis of a ferroelectric liquid crystal by snapshot Mueller matrix polarimetry, *Optics Letters*, 35, 1019
- Elmore, D. F., Rimmele, T., et al., 2014, The Daniel K. Inouye Solar Telescope first light instruments and critical science plan, in *Society of Photo-Optical Instrumentation Engineers (SPIE) Conference Series*, vol. 9147 of Society of Photo-Optical Instrumentation Engineers (SPIE) Conference Series, p. 7
- Feller, A., 2002, *Achromatic Polarization Modulation with Ferroelectric Liquid Crystals*, Diploma thesis, ETH Zurich
- Feller, A., 2007, *Instrument System for Imaging Spectro-Polarimetry*, Ph.D. thesis, ETH Zurich
- Fried, D. L., 1966, Optical Resolution Through a Randomly Inhomogeneous Medium for Very Long and Very Short Exposures, *Journal of the Optical Society of America* (1917-1983), 56, 1372

- Gandorfer, A., 2000, The Second Solar Spectrum: A high spectral resolution polarimetric survey of scattering polarization at the solar limb in graphical representation. Volume I: 4625 Å to 6995 Å
- Gandorfer, A., 2002, The Second Solar Spectrum: A high spectral resolution polarimetric survey of scattering polarization at the solar limb in graphical representation. Volume II: 3910 Å to 4630 Å
- Gandorfer, A., 2005, The Second Solar Spectrum: A high spectral resolution polarimetric survey of scattering polarization at the solar limb in graphical representation. Volume III: 3160 Å to 3915 Å
- Gandorfer, A. M., 1999, Ferroelectric retarders as an alternative to piezoelectric modulators for use in solar stokes vector polarimetry, *Optical Engineering*, 38, 1402–1408
- Gandorfer, A. M., Steiner, H. P. P., Aebersold, F., Egger, U., Feller, A., Gisler, D., Hagenbuch, S., Stenflo, J. O., 2004, Solar polarimetry in the near UV with the Zurich Imaging Polarimeter ZIMPOL II, *Astronomy and Astrophysics*, 422, 703–708
- Gisler, D., 2005, Instrumentierung für hochpräzise Vektorpolarimetrie in der Astronomie, Ph.D. thesis, ETH-Zurich
- Gisler, D., Feller, A., Gandorfer, A. M., 2003, Achromatic liquid crystal polarisation modulator, in *Polarimetry in Astronomy*, (Ed.) S. Fineschi, vol. 4843 of Society of Photo-Optical Instrumentation Engineers (SPIE) Conference Series, pp. 45–54
- Goldstein, D., 2003, *Polarized Light, Revised and Expanded*, Optical Engineering, CRC Press, second edn.
- Hanaoka, Y., 2004, Ferroelectric Liquid Crystal Polarimeter for High-cadence H α Imaging Polarimetry, *Solar Physics*, 222, 265–278
- Hanaoka, Y., 2006, High-Precision Imaging Polarimetry in the H α Line, in *Astronomical Society of the Pacific Conference Series*, (Eds.) R. Casini, B. W. Lites, vol. 358 of Astronomical Society of the Pacific Conference Series, p. 185
- Hanaoka, Y., 2012, Polarimeter with a high-speed rotating waveplate for the solar observation, in *Society of Photo-Optical Instrumentation Engineers (SPIE) Conference Series*, vol. 8446 of Society of Photo-Optical Instrumentation Engineers (SPIE) Conference Series, p. 70
- Hanaoka, Y., Noguchi, M., Sakurai, T., Ichimoto, K., 2003, High-Speed H α Camera and the Real-Time Image Processing System for Solar Observations, in *Innovative Telescopes and Instrumentation for Solar Astrophysics*, (Eds.) S. L. Keil, S. V. Avakyan, vol. 4853 of Society of Photo-Optical Instrumentation Engineers (SPIE) Conference Series, pp. 576–583
- Hanle, W., 1924, Über magnetische Beeinflussung der Polarisation der Resonanzfluoreszenz, *Zeitschrift für Physik*, 30, 93–105

- Hartmann, R., Buttler, W., Gorke, H., Herrmann, S., Holl, P., Meidinger, N., Soltau, H., Strüder, L., 2006, A high-speed pnCCD detector system for optical applications, *Nuclear Instruments and Methods in Physics Research A*, 568, 118–123
- Harvey, J. W., Keller, C., Cole, L., Roy, T., Jaksha, D., 2004, High-speed cameras and solar observing, in *Telescopes and Instrumentation for Solar Astrophysics*, (Eds.) S. Fineschi, M. A. Gummin, vol. 5171 of *Proceedings of the SPIE*, pp. 258–268
- Herrmann, S., Buttler, W., Hartmann, R., Meidinger, N., Porro, M., Strueder, L., 2008, Camex readout asics for pnccds, in *Nuclear Science Symposium Conference Record*, 2008. NSS '08. IEEE, pp. 2952–2957, ISSN 1095-7863
- Hoffman, A., Loose, M., Suntharalingam, V., 2005, *CMOS Detector Technology*, *Experimental Astronomy*, 19, 111–134
- Hogge, C. B., Butts, R. R., 1976, Frequency spectra for the geometric representation of wavefront distortions due to atmospheric turbulence, *IEEE Transactions on Antennas and Propagation*, 24, 144–154
- Hoslst, G. C., 1998, *CCD Arrays Cameras and Displays*, chap. 3.3.3, SPIE Optical Engineering Press
- Howell, S. B., 2006, *Handbook of CCD Astronomy*
- IEEE, 2001, *IEEE Standard for Terminology and Test Methods for Analog-To-Digital Converters*, IEEE Std 1241-2000, pp. i–
- Iglesias, F. A., Feller, A., Nagaraju, K., 2015, Smear correction of highly variable, frame-transfer CCD images with application to polarimetry, *Applied Optics*, 54, 5970
- Iglesias, F. A., Feller, A., Nagaraju, K., Solanki, S. K., 2016, High-resolution, high-sensitivity, ground-based solar spectropolarimetry with a new fast imaging polarimeter, *Astronomy and Astrophysics*, 590, A89
- Ihle, S., Hartmann, R., Downing, M., Struder, L., Deiries, S., Gorke, H., Hermann, S., Kanbach, G., Papamastourakis, J., Soltau, H., Stefanescu, A., 2008, Optical test results of fast pnccds, in *Nuclear Science Symposium Conference Record*, 2008. NSS '08. IEEE, pp. 3351–3356, ISSN 1095-7863
- Ihle, S., Ordavo, I., Bechteler, A., Hartmann, R., Holl, P., Liebel, A., Meidinger, N., Soltau, H., Strüder, L., Weber, U., 2012, A compact high-speed pnCCD camera for optical and x-ray applications, in *Society of Photo-Optical Instrumentation Engineers (SPIE) Conference Series*, vol. 8453 of *Society of Photo-Optical Instrumentation Engineers (SPIE) Conference Series*, p. 1
- Janesick, J., Andrews, J. T., Elliott, T., 2006, Fundamental performance differences between CMOS and CCD imagers: Part 1, in *Society of Photo-Optical Instrumentation Engineers (SPIE) Conference Series*, vol. 6276 of *Society of Photo-Optical Instrumentation Engineers (SPIE) Conference Series*, p. 0

- Janesick, J., Andrews, J., Tower, J., Grygon, M., Elliott, T., Cheng, J., Lesser, M., Pinter, J., 2007, Fundamental performance differences between CMOS and CCD imagers: Part II, in Society of Photo-Optical Instrumentation Engineers (SPIE) Conference Series, vol. 6690 of Society of Photo-Optical Instrumentation Engineers (SPIE) Conference Series, p. 3
- Janesick, J. R., 2001, Scientific charge-coupled devices
- Janesick, J. R., Elliott, T., Andrews, J., Tower, J., Pinter, J., 2013, Fundamental performance differences of CMOS and CCD imagers: part V, in Society of Photo-Optical Instrumentation Engineers (SPIE) Conference Series, vol. 8659 of Society of Photo-Optical Instrumentation Engineers (SPIE) Conference Series, p. 2
- Judge, P. G., Elmore, D. F., Lites, B. W., Keller, C. U., Rimmele, T., 2004, Evaluation of seeing-induced cross talk in tip-tilt-corrected solar polarimetry, *Appl. Opt.*, 43, 3817–3828
- Keller, C., 1996, Recent progress in imaging polarimetry, in *Solar Polarization*, (Eds.) J. Stenflo, K. Nagendra, pp. 243–252, Springer Netherlands, ISBN 978-94-010-6586-3
- Keller, C. U., 1998, SOLIS: a modern facility for synoptic solar observations, in *Advanced Technology Optical/IR Telescopes VI*, vol. 3352, pp. 732–741
- Keller, C. U., von der Luehe, O., 1992, Solar speckle polarimetry, *Astronomy and Astrophysics*, 261, 321–328
- Keller, C. U., Deubner, F.-L., Egger, U., Fleck, B., Povel, H. P., 1994, On the strength of solar intra-network fields, *Astronomy and Astrophysics*, 286, 626–634
- Keller, C. U., Harvey, J. W., the SOLIS Team, 2003, The SOLIS Vector-Spectromagnetograph, in *Solar polarization 3*, vol. 307 of ASP Conference Series, p. 13
- Kentischer, T. J., Schmidt, W., Sigwarth, M., Uexkuell, M. V., 1998, TESOS, a double Fabry-Perot instrument for solar spectroscopy, *Astronomy and Astrophysics*, 340, 569–578
- Kleint, L., Gandorfer, A., 2015, Prospects of solar magnetometry - from ground and in space, *Space Science Review*
- Korff, D., 1973, Analysis of a method for obtaining near-diffraction-limited information in the presence of atmospheric turbulence, *Journal of the Optical Society of America* (1917-1983), 63, 971
- Krishnappa, N., Feller, A., 2012, Precision in ground-based solar polarimetry: simulating the role of adaptive optics, *Appl. Opt.*, 51, 7953–7961
- Lauxtermann, S., Leipold, D., 2011, Backside Illuminated CMOS Snapshot Shutter Imager on 50 um Thick High Resistivity Silicon, in 2011 INTERNATIONAL IMAGE SENSOR WORKSHOP, p. 32

- Lechner, P., Hartmann, R., Holl, P., Lutz, G., Meidinger, N., Porro, M., Richter, R., Schaller, G., Schopper, F., Soltau, H., Strüder, L., Treis, J., 2004, State-of-the-art silicon detectors for X-ray spectroscopy, in International Centre for Diffraction Data 2004, *Advances in X-ray Analysis*, vol. 47
- Lites, B., Akin, D., Card, G., Cruz, T., Duncan, D. W., Edwards, C. G., Elmore, D. F., Hoffmann, C., Katsukawa, Y., Katz, N., Kubo, M., Ichimoto, K., Shimizu, T., Shine, R. A., Streander, K. V., Suematsu, A., Tarbell, T. D., Title, A. M., Tsuneta, S., 2013, The Hinode Spectro-Polarimeter, *Solar Physics*, 283, 579–599
- Lites, B. W., 1987, Rotating waveplates as polarization modulators for stokes polarimetry of the sun: evaluation of seeing-induced crosstalk errors, *Appl. Opt.*, 26, 3838–3845
- Löfdahl, M. G., 2002, Multi-frame blind deconvolution with linear equality constraints, in *Image Reconstruction from Incomplete Data II*, (Eds.) J. Bones, M. Fiddy, R. Millane, vol. 4792, pp. 146–155
- Löfdahl, M. G., van Noort, M., Denker, C., 2007, Solar image restoration, in *Modern Solar Facilities - Advanced Solar Science*, (Eds.) F. Kneer, K. G. Puschmann, A. D. Wittmann, Universitätsverlag, Göttingen
- Magnan, P., 2003, Detection of visible photons in CCD and CMOS: A comparative view, *Nuclear Instruments and Methods in Physics Research A*, 504, 199–212
- Martinez Pillet, V., 2007, Instrumental Approaches to Magnetic and Velocity Measurements in and out of the Ecliptic Plane, in *ESA Special Publication*, vol. 651 of ESA Special Publication
- Martínez Pillet, V., del Toro Iniesta, J., Álvarez-Herrero, A., et al., 2011, The imaging magnetograph experiment (IMaX) for the sunrise balloon-borne solar observatory, *Solar Physics*, 268, 57–102, ISSN 0038-0938
- Meidinger, N., Bonerz, S., Braeuninger, H. W., Eckhardt, R., Englhauser, J., Hartmann, R., Hasinger, G., Holl, P., Krause, N., Lutz, G., Pfeffermann, E., Richter, R. H., Soltau, H., Strueder, L., Truemper, J. E., 2003, Frame store PN-CCD detector for the ROSITA mission, in *X-Ray and Gamma-Ray Telescopes and Instruments for Astronomy.*, (Eds.) J. E. Truemper, H. D. Tananbaum, vol. 4851 of Society of Photo-Optical Instrumentation Engineers (SPIE) Conference Series, pp. 1040–1047
- Noll, R. J., 1976, Zernike polynomials and atmospheric turbulence, *Journal of the Optical Society of America* (1917-1983), 66, 207–211
- Paxman, R. G., Seldin, J. H., Loefdahl, M. G., Scharmer, G. B., Keller, C. U., 1996, Evaluation of Phase-Diversity Techniques for Solar-Image Restoration, *The Astrophysical Journal*, 466, 1087
- Piqueras, J., 2013, Design and optimization of a space camera with application to the PHI solar magnetograph, Ph.D. thesis, International Max Planck Research School for Solar System Science

- Porro, M., Bianchi, D., et al., 2013, Veritas: A 128-channel asic for the readout of pnccds and depfet arrays for x-ray imaging, spectroscopy and xfel applications, *IEEE Transactions on Nuclear Science*, 60, 446–455
- Povel, H., Aebersold, H., Stenflo, J. O., 1990, Charge-coupled device image sensor as a demodulator in a 2-D polarimeter with a piezoelastic modulator, *Applied Optics*, 29, 1186–1190
- Powell, K., Chana, D., Fish, D., Thompson, C., 1999, Restoration and frequency analysis of smeared CCD images, *Applied Optics*, 38, 1343–1347
- Press, W. H., Teukolsky, S. A., Vetterling, W. T., Flannery, B. P., 2007a, *Numerical Recipes 3rd Edition: The Art of Scientific Computing*, chap. 2.6, p. 69, Cambridge University Press
- Press, W. H., Teukolsky, S. A., Vetterling, W. T., Flannery, B. P., 2007b, *Numerical Recipes 3rd Edition: The Art of Scientific Computing*, Cambridge University Press
- Ramelli, R., Balemi, S., Bianda, M., Defilippis, I., Gamma, L., Hagenbuch, S., Rogantini, M., Steiner, P., J., S. O., 2010, ZIPOL-3: a powerful solar polarimeter, in *Proc. SPIE 7735, Ground-based and Airborne Instrumentation for Astronomy III*
- Ramelli, R., Gisler, D., Bianda, M., Bello Gonzalez, N., Berdyugina, S., Soltau, D., 2014, First successful deployment of the zimpol-3 system at the gregor telescope, in *Ground-based and Airborne Instrumentation for Astronomy V*, (Eds.) S. K. Ramsay, I. S. McLean, H. Takami, vol. 9147 of *Proc. of SPIE*, pp. 3G1–3G8
- Reiners, A., 2012, Observations of cool-star magnetic fields, *Living Reviews in Solar Physics*, 9
- Richardson, W. H., 1972, Bayesian-Based Iterative Method of Image Restoration, *Journal of the Optical Society of America (1917-1983)*, 62, 55
- Rimmele, T., Marino, J., 2011, Solar adaptive optics, *Living Rev. Solar Phys.*, 8
- Rimmele, T. R., 2000, Solar adaptive optics, in *Adaptive Optical Systems Technology*, (Ed.) P. L. Wizinowich, vol. 4007 of *Society of Photo-Optical Instrumentation Engineers (SPIE) Conference Series*, pp. 218–231
- Roddier, F., 1981, The effects of atmospheric turbulence in optical astronomy, *Progress in optics*. Volume 19. Amsterdam, North-Holland Publishing Co., 1981, p. 281-376., 19, 281–376
- Roddier, F. (Ed.), 1999, *Adaptive Optics in Astronomy*, Cambridge University Press
- Roddier, N., 1990, Atmospheric wavefront simulation using Zernike polynomials, *Optical Engineering*, 29, 1174–1180
- Ruyten, W., 1999, Smear correction for frame transfer charged-coupled-device cameras, *Optics Letters*, 24, 878–880

- Saha, S. K., 2007, Diffraction-Limited Imaging with Large and Moderate Telescopes
- Sankarasubramanian, K., Lites, B., Gullixson, C., Elmore, D., Hegwer, S., Streander, K., Rimmele, T., Fletcher, S., Gregory, S., Richards, K., Rousset, E., 2004, The Diffraction Limited Spectro-Polarimeter: A new instrument for high resolution solar polarimetry., in *Telescopes and Instrumentation for Solar Astrophysics*, (Eds.) S. Fineschi, M. A. Gummin, vol. 5171, pp. 207–218
- Sankarasubramanian, K., Lites, B., Gullixson, C., Elmore, D., Hegwer, S., Streander, K., Rimmele, T., Fletcher, S., Gregory, S., Sigwarth, M., 2006, The diffraction limited spectro-polarimeter, in *Solar Polarization 4*, (Eds.) R. Casini, B. W. Lites, vol. 358 of ASP Conference Series
- Sascha, T., 2014, Polarization and polarimetry: A review, *Journal of The Korean Astronomical Society*, 47, 15–39
- Scharmer, G., Narayan, G., Hillberg, T., de la Cruz Rodríguez, J., Löfdahl, M. G., Kiselman, D., Sutterlin, P., van Noort, M., Lagg, A., 2008, CRISP spectropolarimetric imaging of penumbral fine structure, *ApJ*, 689, L69–L72
- Schmidt, D., Berkefeld, T., Heidecke, F., Fischer, A., von der Lüh, O., Soltau, D., 2014a, GREGOR MCAO looking at the Sun, in *Society of Photo-Optical Instrumentation Engineers (SPIE) Conference Series*, vol. 9148 of Society of Photo-Optical Instrumentation Engineers (SPIE) Conference Series, p. 1
- Schmidt, D., Gorceix, N., Zhang, X., Marino, J., Coulter, R., Shumko, S., Goode, P., Rimmele, T., Berkefeld, T., 2014b, The multi-conjugate adaptive optics system of the New Solar Telescope at Big Bear Solar Observatory, in *Society of Photo-Optical Instrumentation Engineers (SPIE) Conference Series*, vol. 9148 of Society of Photo-Optical Instrumentation Engineers (SPIE) Conference Series, p. 2
- Schroeter, E. H., Soltau, D., Wiehr, E., 1985, The German solar telescopes at the Observatorio del Teide, *Vistas in Astronomy*, 28, 519–525
- Socas-Navarro, H., Elmore, D., Pietarila, A., Darnell, A., Lites, B., Tomczyk, S., Hegwer, S., 2006, SPINOR: visible and infrared spectro-polarimetry at the national solar observatory, *Solar Physics*, 235, 55–73
- Solanki, S., 2003, Sunspots: An overview, *Astronomy and Astrophysics Review*, 11, 153–286
- Starck, J. L., Pantin, E., Murtagh, F., 2002, Deconvolution in Astronomy: A Review, *The Publications of the Astronomical Society of the Pacific*, 114, 1051–1069
- Stenflo, J., 1982, The Hanle effect and the diagnostics of turbulent magnetic fields in the solar atmosphere, *Solar Physics*, 80, 209–226
- Stenflo, J., 1994, *Solar Magnetic Fields*, vol. 189 of *Astrophysics and Space Science Library*, Springer Netherlands, ISBN 978-90-481-4387-0

- Stenflo, J., 1999, Solar magnetism and the second solar spectrum: Future directions, in Polarization, (Eds.) K. N. Nagendra, J. O. Stenflo, vol. 243 of Astrophysics and Space Science Library, pp. 1–16
- Stenflo, J., 2013, Solar magnetic fields as revealed by Stokes polarimetry, *Astronomy and Astrophysics Review*, 21, 66
- Stenflo, J., Keller, C., 1997, The second solar spectrum. A new window for diagnostics of the Sun., *Astronomy and Astrophysics*, 321, 927–934
- Stenflo, J. O., Povel, H., 1985, Astronomical polarimeter with 2-d detector arrays, *Appl. Opt.*, 24, 3893–3898
- Stix, M., 2002, *The Sun*, Astronomy and Astrophysics Library, Springer Berlin Heidelberg, second edn.
- Strueder, L., Lutz, G., Sterzik, M., Holl, P., Kemmer, J., 1988, First tests with fully depleted pn-CCD's, *IEEE Transactions on Nuclear Science*, 35, 372–376
- Strueder, L., Meidinger, N., Pfeffermann, E., Hartmann, R., Braeuninger, H. W., Reppin, C., Briel, U. G., Hippmann, H., Kink, W., Hauff, D., Krause, N., Aschenbach, B., Hartner, G. D., Dennerl, K., Haberl, F., Stoetter, D., Kemmer, S., Truemper, J. E., Lutz, G., Richter, R. H., Solc, P., Eckhardt, R., Kendziorra, E., Kuster, M., von Zanthier, C., Holl, P., Viehl, A., Krisch, S., Kemmer, J., Soltau, H., 2000, X-ray pn-CCDs on the XMM Newton Observatory, in *X-Ray Optics, Instruments, and Missions III*, (Eds.) J. E. Truemper, B. Aschenbach, vol. 4012 of Society of Photo-Optical Instrumentation Engineers (SPIE) Conference Series, pp. 342–352
- Tatarski, V. I., 1961, *Wave Propagation in Turbulent Medium*, McGraw-Hill
- Taylor, G. I., 1938, The Spectrum of Turbulence, *Proceedings of the Royal Society of London Series A*, 164, 476–490
- Tomczyk, S., Casini, R., de Wijn, A. G., Nelson, P. G., 2010, Wavelength-diverse polarization modulators for stokes polarimetry, *Appl. Opt.*, 49, 3580–3586
- Tritschler, A., Schmidt, W., Langhans, K., Kentischer, T., 2002, High-resolution solar spectroscopy with TESOS - Upgrade from a double to a triple system, *Solar Physics*, 211, 17–29
- Trujillo Bueno, J., Shchukina, N., Asensio Ramos, A., 2004, A substantial amount of hidden magnetic energy in the quiet Sun, *Nature*, 430, 326–329, astro-ph/0409004
- van Kempen, G., van Vliet, L., 2000, Mean and variance of ratio estimators used in fluorescence ratio imaging, *Cytometry*, 39, 300–305, ISSN 1097-0320
- Van Noort, M., Der Voort, L., LÃ¶fdahl, M., 2005, Solar image restoration by use of multi-frame blind de-convolution with multiple objects and phase diversity, *Solar Physics*, 228, 191–215, ISSN 0038-0938

- Vescovo, R., 1997, Inversion of block-circulant matrices and circular array approach, *IEEE Transactions on Antennas and Propagation*, 45, 1565–1567
- von der Luehe, O., Kentischer, T., 2000, High spatial resolution performance of a triple fabry-pérot filtergraph, *Astronomy and Astrophysics Supplement Series*, 146, 499–506
- von der Luehe, O., Soltau, D., Berkefeld, T., Schelenz, T., 2003, Kaos: Adaptive optics system for the vacuum tower telescope at teide observatory
- von der Luhe, O., 1988, Measurements of characteristics of image motion with a solar image stabilizing device, *Astronomy and Astrophysics*, 205, 354–360
- Woolfson, M., 2000, The origin and evolution of the solar system, *Astronomy and Geophysics*, 41, 12

Acknowledgements

This PhD thesis results from the work I have carried out during the past years at the Max-Planck-Institute for Solar System Research, in Göttingen, Germany. Numerous people have supported me along this path.

First I would like to thank Prof. Harald Michalik who generously accepted me as a PhD student and gave me valuable feedback to shape this thesis. I am also in debt with Prof. Sami K. Solanki for his support and efficient guidance. In addition, I would like to thank the members of the SLAM group for contributing to create such a great working and learning environment. Special thanks go to Alex Feller, who mentored me during this years and taught me almost everything I know about solar polarimetry, always with the kindness that characterizes him. I have carried out this work within the International Max Planck Research School in Solar System Science (IMPRS), efficiently coordinated by Sonja Schuh to whom I am also grateful. Finally, I would like to acknowledge Hebe Cremades for making possible my admission to the IMPRS. I dedicate this thesis to my friends, family and to my beloved partner María Belén Tomaselli: Thank you for almost a decade of the finest companionship, I love you.

Curriculum Vitae and publications

Name	Francisco Andrés Iglesias
Date of birth	7 November 1984
Place of birth	Mendoza (Argentina)
E-Mail	franciscoaiglesias@hotmail.com

Education

1998-2003	Instituto técnico ENET N°5 (Argentina) Mechanical technician
2004-2010	Universidad Tecnológica Nacional, FRM (Argentina) Electronics technician
2004-2012	Universidad Tecnológica Nacional, FRM (Argentina) Dipl.-Ing. in Electronics. Thesis: <i>Implementation of a fast Kalman filter core in FPGA</i>
2012-2016	Technische Universität Braunschweig (Germany) PhD thesis under the International Max Planck Research School (IMPRS) on Solar System Science

Publications

Iglesias, F. A., Feller, A., Nagaraju, K. and Solanki, S. K., 2016, *High-resolution, high-sensitivity, ground-based solar spectropolarimetry with a new fast imaging polarimeter*, *Astronomy and Astrophysics*, Volume 590, A89

Iglesias, F. A., Feller, A. and Nagaraju, K., 2015, *Smear correction of highly-variable, frame-transfer-CCD images with application to polarimetry*, *Applied Optics*, Volume 54, Issue 19 p. 5970.

Cremades, H., Iglesias, F. A., St. Cyr, O. C.; Xie, H., Kaiser, M. L. and Gopalswamy, N., 2015, *Low-Frequency Type-II Radio Detections and Coronagraph Data Employed to Describe and Forecast the Propagation of 71 CMEs/Shocks*, *Solar Physics*, Volume 290, Issue 9, pp.2455-2478.

Iglesias, F. A., Feller, A., Nagaraju, K. and Solanki, S. K., 2016, *Fast Solar Polarimeter: Prototype characterization and first results*, *ASP Conference Series*, Volume 504, p. 325.

Feller, A., Iglesias, F. A., Nagaraju, K., Solanki, S. K. and Ihle, S., 2014, *Fast Solar Polarimeter: Description and First Results*, *ASP Conference Series*, Volume 489, p. 271

Iglesias, F. A., and Demmaties, D., 2013, *Kalman filter core implementation in FPGA*, edUTecNe Ed. in <http://www.edutecne.utn.edu.ar>

Selected conference contributions

Iglesias, F. A., Feller, A., Nagaraju, K. and Solanki, S. K., 2014, *The Fast Solar Polarimeter*, Poster, Polarimetric Techniques and Technology workshop, Leiden (Netherlands)

Iglesias, F. A., Feller, A., Nagaraju, K., Solanki, S. K. and Ihle, S., 2013, *Design and performance characterization of the Fast Solar Polarimeter*, Poster, SPW7, Kunming (China)

Cremades, H., Iglesias, F. A., St Cyr, O. C., Kaiser, M. L., Xie, H. and Quirk, C. A., 2011, *A Descriptive-Predictive Model of CME Propagation based on Multi-Instrument Data*, AGU fall Meeting 2011, San Francisco (USA)

Iglesias F. A., Generale, S., Noguera, A. and Generale, N., 2011, *Estimation of the coverage area of a UHF antenna in a complex environment through the software Radio Mobile and validation with in situ measurements*, Poster, 6° EnIDI, Mendoza (Argentina)

Iglesias, F. A., Cremades, H., St. Cyr, O., C., Kaiser, M., 2009, *Space weather and CMEs kinematic in the inner corona*. 5° EnIDI. Mendoza (Argentina)